

# Dissertation

submitted to the  
Combined Faculties for the Natural Sciences and for Mathematics  
of the Ruperto-Carola University of Heidelberg, Germany  
for the degree of Doctor of Natural Sciences

Put forward by  
**M.Sc. Axel Donath**  
born in Landau / Pfalz, Germany  
Oral examination: May 30<sup>th</sup>, 2018



University of Heidelberg

Department of Physics and Astronomy

The Galactic Gamma-ray Source Population  
between 10 GeV and 50 TeV

*1. Referee*    **Prof. Dr. Werner Hofmann**  
Particle Physics and High-Energy Astrophysics  
Max Planck Institute for Nuclear Physics

*2. Referee*    **Prof. Dr. Stefan Wagner**  
ZAH, Landessternwarte  
University of Heidelberg

*Supervisors*    Werner Hofmann and Christoph Deil

**Axel Donath**

*The Galactic Gamma-ray Source Population between 10 GeV and 50 TeV*

PhD Thesis, March 26<sup>th</sup>, 2018

Reviewers: Prof. Dr. Werner Hofmann and Prof. Dr. Stefan Wagner

Supervisors: Werner Hofmann and Christoph Deil

**University of Heidelberg**

*Particle Physics and High-Energy Astrophysics, div. Hofmann*

Max Planck Institute for Nuclear Physics

Department of Physics and Astronomy

Saupfercheckweg 1

69117 and Heidelberg

# Abstract

This work studies the population of Galactic gamma-ray sources between 10 GeV and 50 TeV. In the first part the data taken by the H.E.S.S. Galactic Plane Survey (HGPS) above  $\sim 200$  GeV is re-analysed using a Poisson Maximum Likelihood based detection method. In this process a catalog of gamma-ray sources as well as a model of the large-scale emission in the Galaxy is created. In total 78 individual sources are detected, of which 31 can be clearly identified. For the remaining objects possible associations with known pulsar wind nebulae, supernova remnants and energetic pulsars are listed. The investigation of the whole source population reveals a variety of objects, that cover a size range from point source up to radii  $\sim 1^\circ$ . The measured fluxes range from 0.6% to 103% of the flux of the *Crab Nebula*. The analysis of the longitude, latitude and  $\text{Log } N - \text{Log } S$  distribution of the sources shows a picture of the population that is compatible with the distribution of energetic pulsars, supernova remnants and CO Gas in the Galaxy. The completeness of this picture is currently limited by the sensitivity of the telescopes. In the second part of this work the results from the HGPS analysis are systematically compared to high energy observations of the *Fermi*-LAT satellite. For this purpose images in three energy bands are computed (10 - 30 GeV, 30 -100 GeV und 100 - 2000 GeV) from the *Fermi*-LAT data and combined into colored RGB images. The qualitative comparison of the images as well as image-based flux profiles against the HGPS measurement shows good agreement in many regions. Individual regions with differences are then discussed in detail. The systematic measurement of fluxes of HGPS sources in the range between 10 GeV and 2 TeV yields significant emission for 55 objects, among 9 objects previously not known as GeV sources. A detailed examination of those cases shows source confusion on the GeV side as limiting factor for the detection.



# Zusammenfassung

Die vorliegende Arbeit befasst sich mit der Population von Quellen hochenergetischer Gammastrahlung in der Milchstraße im Energiebereich zwischen 10 GeV und 50 TeV. Im ersten Teil werden die Daten, die im Verlauf des *H.E.S.S. Galactic Plane Survey (HGPS)* oberhalb von  $\sim 200$  GeV aufgenommen wurden, mit einer *Poisson-Wahrscheinlichkeit* basierten Detektionsmethode neu analysiert. Dabei wird sowohl ein einheitlicher Katalog von lokalisierten Quellen als auch ein Modell der großskaligen Emission in der Galaxie erstellt. Insgesamt werden 78 individuelle Objekte detektiert, von denen sich 31 eindeutig bereits bekannten astronomischen Objekten zuordnen lassen, für die übrigen Quellen werden mögliche Assoziationen mit bekannten Pulsarwindnebeln, Supernovaüberresten und energetischen Pulsaren gelistet. Die Untersuchung der gesamten Population zeigt eine Vielfalt an Quellen, die in ihrer Größe von Punktquellen bis zu ausgedehnten Objekten mit Radien  $\sim 1^\circ$  reichen. Die gemessenen Helligkeiten decken einen Bereich von 0.6% bis 103% der Helligkeit des Krebsnebels ab. Die Analyse der Longituden-, Latituden- und  $\log N - \log S$ -Verteilung liefert ein Bild der Gesamtpopulation, das mit der Verteilung von Pulsaren, Supernovaüberresten und CO Gas in der Galaxie kompatibel, aber zum gegenwärtigen Zeitpunkt in seiner Vollständigkeit noch durch die Empfindlichkeit der Teleskope beschränkt ist. Im zweiten Teil der Arbeit werden die Ergebnisse der HGPS Analyse systematisch gegen Hochenergie-Beobachtungen des *Fermi-LAT* Satelliten verglichen. Dazu werden aus den *Fermi-LAT* Daten Karten in drei Energiebändern (10 - 30 GeV, 30 - 100 GeV und 100 - 2000 GeV) berechnet und zu RGB Bildern kombiniert. Der qualitative Vergleich sowohl der Bilder als auch bildbasierter Flussprofile gegen den HGPS zeigen eine gute Übereinstimmung. Einzelne abweichende Regionen werden im Detail diskutiert. Die systematische Messung von Flüssen im Bereich 10 GeV bis 2 TeV für alle HGPS Quellen ergibt für 55 Objekte signifikante GeV Emission, von denen 9 bisher nicht als GeV Quellen bekannt waren. Eine genauere Betrachtung dieser Fälle zeigt Quellkonfusion als den limitierenden Faktor bei der GeV Detektion.



# Contents

<b>1</b>	<b>Introduction</b>	<b>1</b>
1.1	The Multiwavelength Milky Way . . . . .	1
1.2	Gamma-Ray Astronomy . . . . .	4
1.2.1	Instruments . . . . .	4
1.2.2	Galactic Gamma-Ray Sources . . . . .	5
1.3	Gamma-ray Astrophysics . . . . .	8
1.3.1	Particle Acceleration . . . . .	8
1.3.2	Leptonic Emission . . . . .	10
1.3.3	Hadronic Emission . . . . .	12
1.4	Gamma-ray Data Analysis . . . . .	12
1.4.1	High Level Data Model and Data Formats . . . . .	12
1.4.2	Poisson Maximum Likelihood Fitting . . . . .	13
1.4.3	Open Source Software <i>Gammapy</i> . . . . .	14
<b>2</b>	<b>The H.E.S.S. Galactic Plane Survey</b>	<b>17</b>
2.1	Introduction . . . . .	19
2.1.1	Literature Overview . . . . .	20
2.1.2	Survey Region Overview . . . . .	20
2.2	H.E.S.S. Instrument and Dataset . . . . .	22
2.2.1	Instrument . . . . .	22
2.2.2	Observation Selection . . . . .	22
2.2.3	Event Reconstruction and Selection . . . . .	23
2.2.4	Point Spread Function . . . . .	24
2.2.5	Sky Maps . . . . .	25
2.3	Catalog Analysis Method . . . . .	28
2.3.1	Sources not Reanalyzed . . . . .	30
2.3.2	Large-Scale Emission Model . . . . .	31
2.3.3	Regions of Interest . . . . .	32
2.3.4	Multi-Gaussian Source Emission Model . . . . .	34
2.3.5	Component Selection and Classification . . . . .	36
2.3.6	Source Characterization . . . . .	37
2.3.7	Source Spectra . . . . .	39
2.3.8	Source Association . . . . .	43
2.3.9	Statistical False Detection Rate . . . . .	44
2.3.10	Method Discussion . . . . .	46

2.4	Results	48
2.4.1	Source Associations and Identifications	48
2.4.2	Longitude and Latitude Distribution	51
2.4.3	Flux and Size Distribution	53
2.4.4	Log N - Log S Distribution	55
2.4.5	Distribution in the Milky Way and Survey Horizon	57
2.4.6	Comparison with Previous VHE Publications	57
<b>3</b>	<b>The H.E.S.S. Galactic Plane Survey compared to <i>Fermi</i>-LAT Observations</b>	<b>61</b>
3.1	Introduction	62
3.1.1	Literature Overview	62
3.1.2	GeV Milky Way and HGPS Region	63
3.2	<i>Fermi</i> -LAT Instrument and Datasets	64
3.2.1	Instrument	64
3.2.2	Event Selection and PSF	64
3.2.3	Diffuse Emission Model	67
3.2.4	3FHL Catalog	68
3.2.5	Sky Maps	70
3.3	Analysis Methods	72
3.3.1	RGB Flux Images	72
3.3.2	Longitude and Latitude Flux Profiles	74
3.3.3	Spectral Flux Points	75
3.4	Results	76
3.4.1	Survey RGB Images	76
3.4.2	Survey Longitude Flux Profiles	79
3.4.3	Survey Latitude Flux Profiles	81
3.4.4	Source Associations	82
3.4.5	GeV Source Candidates	83
3.4.6	Shell-Type SNR Candidates	86
3.4.7	Examples of Typical Source Classes	88
<b>4</b>	<b>Summary and Outlook</b>	<b>93</b>
4.1	Summary	93
4.2	Outlook	95
<b>A</b>	<b>Tables</b>	<b>99</b>
<b>B</b>	<b>Survey Images</b>	<b>117</b>
<b>C</b>	<b>Individual source images and SEDs</b>	<b>133</b>

# List of Figures

1.1	MWL Image of the Milky Way . . . . .	3
1.2	Sensitivities of Current and Future Gamma-ray Instruments . . . . .	4
1.3	Examples of Shell-Type SNRs Observed in VHE Gamma-rays . . . . .	6
1.4	Examples of PWNe Observed in VHE Gamma-rays. . . . .	7
1.5	Fermi Acceleration Mechanism . . . . .	9
1.6	Example SED for a Leptonic Emission Model . . . . .	11
1.7	Example SED for a Hadronic Emission Model . . . . .	11
2.1	HGPS Region, Flux and Exposure Image in All-Sky Context . . . . .	21
2.2	HGPS Sensitivity Image and Longitude Profile . . . . .	24
2.3	HGPS Energy Threshold Longitude Profile . . . . .	26
2.4	Illustration of Adaptive Ring Background Method . . . . .	27
2.5	HGPS Source Catalog Model Construction Method . . . . .	29
2.6	HGPS Large-Scale Emission Model . . . . .	33
2.7	HGPS Residual Significance Distribution . . . . .	36
2.8	Illustration of Reflected Region Background Method . . . . .	41
2.9	HGPS Mean Number of False Detections . . . . .	45
2.10	HGPS Probability of One False Detection . . . . .	45
2.11	HGPS Comparison of Source Flux Measurements . . . . .	47
2.12	HGPS Identified Sources Summary Pie Chart . . . . .	49
2.13	HGPS Sources Latitude Distribution . . . . .	51
2.14	HGPS Sources Longitude Distribution . . . . .	52
2.15	HGPS Sources Flux and Size Distributions . . . . .	54
2.16	HGPS Sources Spectral Index Distribution . . . . .	55
2.17	HGPS Sources Log N – Log S Distribution . . . . .	56
2.18	HGPS Identified Sources Location in the Galaxy . . . . .	58
3.1	<i>Fermi</i> -LAT 3FHL All-Sky Image and HGPS Region . . . . .	65
3.2	<i>Fermi</i> -LAT Observed Counts Spectrum . . . . .	66
3.3	<i>Fermi</i> -LAT PSF Energy Dependence . . . . .	67
3.4	<i>Fermi</i> -LAT Galactic Diffuse Model All-Sky Image . . . . .	68
3.5	<i>Fermi</i> -LAT RGB Example Point Source . . . . .	74
3.6	Flux Points Method Check against 3FHL Analysis . . . . .	76
3.7	<i>Fermi</i> -LAT and HGPS Longitude Flux Profile . . . . .	80
3.8	<i>Fermi</i> -LAT and HGPS Latitude Flux Profile . . . . .	81
3.9	RGB Image and Spectrum of <i>HESS J1708-443</i> . . . . .	89

3.10	RGB Image and Spectrum of <i>HESS J1507-622</i>	89
3.11	RGB Image and Spectrum of <i>HESS J1534-571</i>	90
3.12	RGB Image and Spectrum of <i>HESS J1646-458</i>	91
B.1	HGPS Flux Image	118
B.2	HGPS Model Flux Image	119
B.3	HGPS Large Scale Model and Discarded Components Flux Image	120
B.4	HGPS Residual $\sqrt{TS}$ Image	121
B.5	HGPS Sources and MWL Associations (1 of 4)	122
B.6	HGPS Sources and MWL Associations (2 of 4)	123
B.7	HGPS Sources and MWL Associations (3 of 4)	124
B.8	HGPS Sources and MWL Associations (4 of 4)	125
B.9	HGPS Cut-out Regions, Exclusion Regions and Modeling ROIs	126
B.10	<i>Fermi</i> -LAT RGB Flux Image	127
B.11	<i>Fermi</i> -LAT RGB 3FHL Model Flux Image	128
B.12	<i>Fermi</i> -LAT RGB 3FHL Model Residual Flux Image	129
B.13	HGPS $\sqrt{TS}$ Image	130
B.14	CTA Simulated $\sqrt{TS}$ Image (Ring Background)	131
B.15	CTA Simulated $\sqrt{TS}$ Image (Template Background)	132
C.1	RGB Image and Spectrum of <i>HESS J1026-582</i>	134
C.2	RGB Image and Spectrum of <i>HESS J1632-478</i>	134
C.3	RGB Image and Spectrum of <i>HESS J1702-420</i>	134
C.4	RGB Image and Spectrum of <i>HESS J1746-308</i>	135
C.5	RGB Image and Spectrum of <i>HESS J1813-178</i>	135
C.6	RGB Image and Spectrum of <i>HESS J1843-033</i>	135
C.7	RGB Image and Spectrum of <i>HESS J1848-018</i>	136
C.8	RGB Image and Spectrum of <i>HESS J1852-000</i>	136
C.9	RGB Image and Spectrum of <i>HESS J1858+020</i>	136
C.10	RGB Image and Spectrum of <i>HESS J1534-571</i>	137
C.11	RGB Image and Spectrum of <i>HESS J1731-347</i>	137
C.12	RGB Image and Spectrum of <i>HESS J1912+101</i>	137

# List of Tables

2.1	HGPS Sources with Parameters Taken from Previous Publications . . .	31
2.2	HGPS Sources Association Summary . . . . .	48
2.3	HGPS Sources Firm Identifications . . . . .	50
3.1	<i>Fermi</i> -LAT 3FHL Source Classes Summary Table . . . . .	70
3.2	<i>Fermi</i> -LAT Images – Energy Bands and Counts Statistics . . . . .	71
3.3	<i>Fermi</i> -LAT Images – Flux and PSF Summary . . . . .	72
A.1	HGPS Source Catalog Morphological Results . . . . .	100
A.2	HGPS Source Catalog Spectral Results . . . . .	104
A.3	HGPS Sources 3FHL Associations . . . . .	108
A.4	HGPS Sources GeV Flux Points . . . . .	112



# Introduction

” *Wie es heißt, sind manche Sterne schon gestorben, die wir sehen Vielleicht zieh ´n wir im Dunkeln allein, wie du weißt, sind aus der Ferne die Dinge meist schwer zu versteh ´n, und wir bestaunen den funkelnden Schein, kalt, kalt, ist das Licht, das uns erreicht, und so alt, alt und es geht nicht verlor ´n es geht nichts verlor ´n, es geht nicht verlor ´n siehst du ihr Licht strahlt gleich hell bei Nacht und am Tag ihre Abwesenheit und Schönheit ist seltsam und selten und Worte hilflos und Trost braucht viel Zeit kalt, kalt ist das Licht das und erreicht, und so alt, alt, und es geht nichts verlor ´n, es geht nichts verlor ´n*

— **Dota Kehr**  
(Deutsche Liedermacherin)

## 1.1 The Multiwavelength Milky Way

In dark nights, when looking at the night sky, a faint whitish band becomes visible extending from East to West. It consists of approximately 100 to 300 billions single stars bounded by gravity in a disk-shaped structure, that altogether form our home galaxy: the *Milky Way*. Viewed from within, the sheer number makes it impossible for the human eye to distinguish the individual stars, giving the Milky Way its characteristic linear and blurred, milky appearance on the sky it is named after.

Already in ancient Greece the Milky Way was recognized as a structure on the night sky: the word *Galaxy* or *Galaxias* (from greek γαλα, milk) likewise refers to its milky look. The philosopher and astronomer *Demokrit* already assumed that it consists of individual stars, but it was only in the beginning of the modern age, in 1610, that *Galileo Galilei* rediscovered and confirmed this assumption by first observations with a telescope.

Since then the structure and composition of the Milky Way has always been a topic of great interest for astronomers. One of the first systematic observations (or *survey*) of the Milky Way in the optical was conducted by *Wilhelm Herschel*, who derived a morphological model of the Galaxy by counting the number of stars in the sky. In the 20th century the rapid progress of detector technologies enabled astronomers to extend their observations to other parts of the electromagnetic spectrum. In the 1930s *Karl Jansky* first discovered radio waves emanating from the Milky Way and laid the foundation for the new field of radio astronomy. Other disciplines such as infrared or microwave astronomy followed. The beginning of space flight in the 1960s gave access to wavelength ranges not directly observable from the earth such as UV radiation, X-rays and gamma-rays.

The exploration of other wavelengths in the past  $\sim 80$  yrs not only completed our existing picture of the Milky Way but also lead to surprising discoveries such as the radio source *Sagittarius A\**, which is likely associated to a putative black hole in the Galactic center, *Pulsars*, rapidly spinning neutron stars that emit pulsating radio waves or more recently the *Fermi Bubbles*, a giant bubble-like, gamma-ray emitting structure found above and below the Galactic plane. In this tradition gamma-ray astronomy extends the multiwavelength picture of the Milky Way to the highest energies. The high energy (HE) and very high energy (VHE)  $> 100$  GeV range gives access to the non-thermal Galaxy, high energetic phenomena related to supernova explosions, surroundings of black holes, annihilating putative dark matter halos and the origin of cosmic rays.

Figure 1.1 summarizes our present picture of the Milky Way in different wavelength ranges from radio up to GeV gamma-ray emission. It illustrates impressively that different parts of the electromagnetic spectrum reveal different physics of our Galaxy. While many regions in the optical (third panel from the bottom) are obscured by the interstellar dust, the picture changes in the *near-infrared* band (fourth panel from the bottom) where the dark, obscured regions disappear and the global structure of the Galaxy becomes visible. Viewed *edge-on* the Milky Way shows a distinctive disc and bulge component as well as spiral arm features. The contrary picture to the optical is delivered by the distribution of molecular  $H_2$  (fourth panel from the top). The density of  $H_2$  gas in the Galaxy is estimated from the intensity of carbon monoxide (CO)  $J=1-0$  spectral line emission. It traces the dense regions of the Milky Way, where star forming takes place. The lowermost panel of Fig. 1.1 shows the gamma-ray intensity measured by the EGRET instrument in the range between 300 MeV to 30 GeV. In this energy range the Galaxy is dominated by diffuse emission which, in this energy range, mostly results from decay of pions, that are produced in collisions of cosmic rays with the interstellar medium. Distinct spots of bright emission are associated to high-energy gamma-rays from the Crab, Geminga, and Vela pulsars.

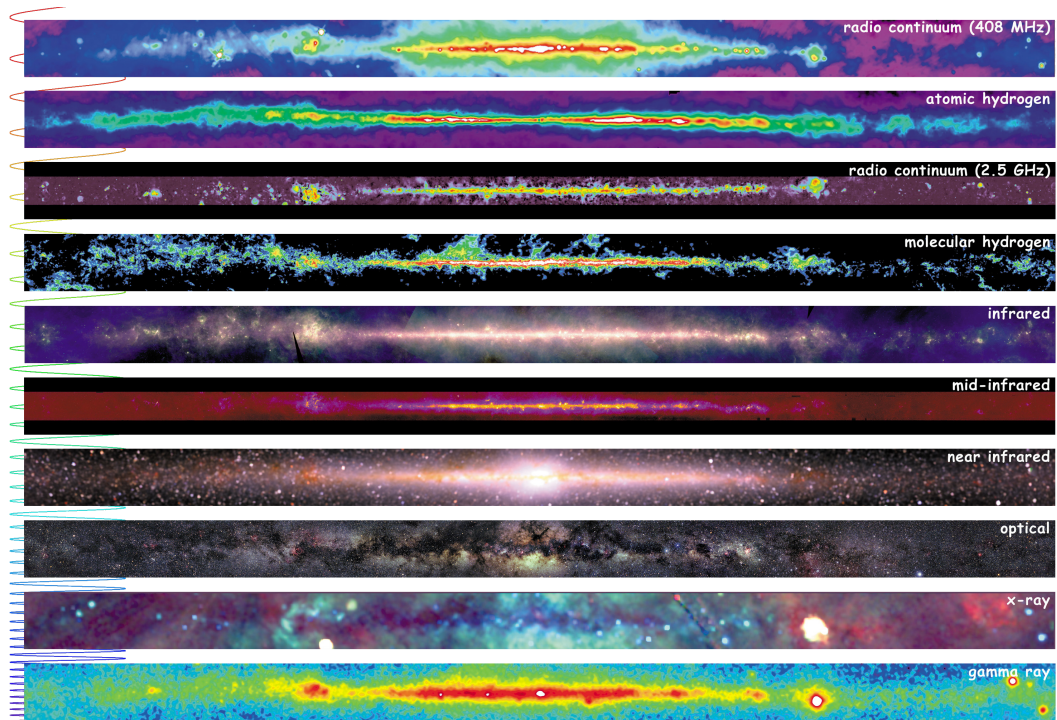


**Fig. 1.1.:** The Milky Way observed in different energy bands, from radio to gamma radiation. Image and description taken from NASA, 2012.

**Radio Continuum:** intensity of radio continuum emission (408 MHz) from surveys with ground-based radio telescopes Jodrell Bank Mark I and Mark IA, Bonn 100-meter, and Parkes 64-meter.

**Atomic Hydrogen:** column density of atomic hydrogen, derived on the assumption of optically thin emission, from radio surveys of the 21-cm transition of hydrogen.

**Radio Continuum:** intensity of radio continuum emission (2.5 GHz) from hot, ionized gas and high-energy electrons from surveys with both the Bonn 100-meter, and Parkes 64-meter radio telescopes.

**Molecular Hydrogen:** column density of molecular hydrogen inferred from the intensity of the  $J = 1 - 0$  (115 GHz) spectral line of carbon monoxide.

**Infrared:** composite mid-and far-infrared intensity observed by the Infrared Astronomical Satellite (IRAS) in 12, 60, and 100 micron wavelength bands.

**Mid Infrared:** mid-infrared emission observed by the SPIRIT III instrument on the Midcourse Space Experiment (MSX) satellite.

**Near Infrared:** composite near-infrared intensity (1.25, 2.2, and 3.5 micron) observed by the Diffuse Infrared Background Experiment (DIRBE) instrument on the Cosmic Background Explorer (COBE).

**Optical:** Intensity of visible light from a photographic survey (0.4 - 0.6 micron).

**X-Ray:** composite X-ray intensity (0.25 , 0.75, and 1.5 keV) observed by the Position-Sensitive Proportional Counter (PSPC) instrument on the Röntgen Satellite (ROSAT) .

**Gamma Ray:** intensity of high-energy gamma-ray emission (0.3 - 30 GeV) observed by the Energetic Gamma-Ray Experiment Telescope (EGRET) instrument on the Compton Gamma-Ray Observatory (CGRO).

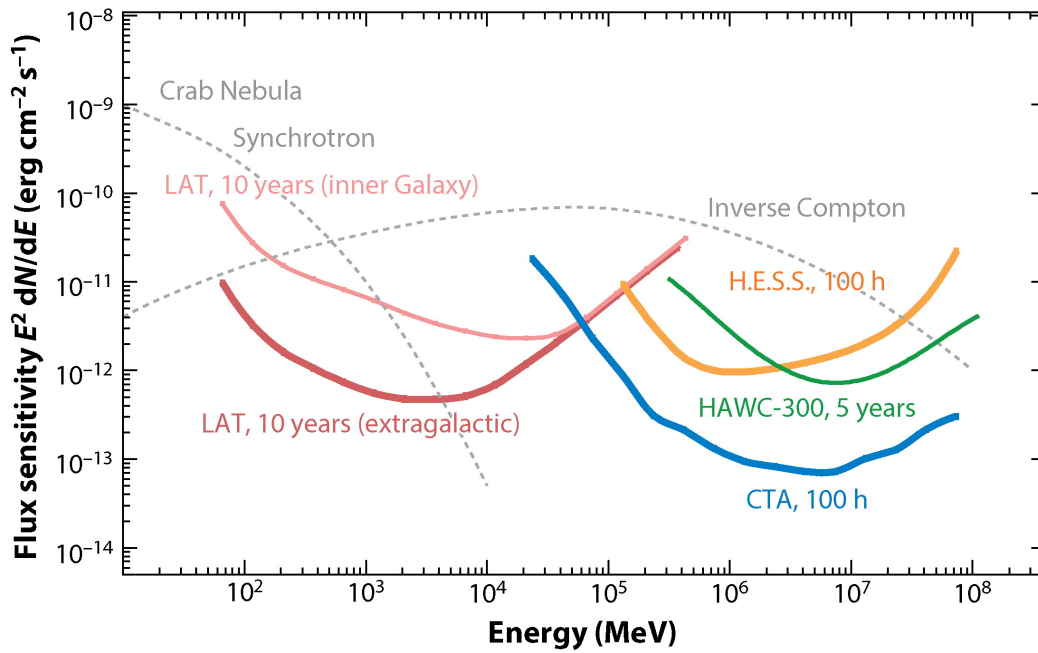


**Fig. 1.2.:** Flux sensitivities of current and future gamma-ray instruments for detection of point sources with a minimum a significance of  $5\sigma$ . The *Fermi*-LAT sensitivity is shown for 10 yrs of observation time, for the Galactic as well as extragalactic sky. The yellow line shows the sensitivity of H.E.S.S. instrument for 100 h of observation. The gray dashed line shows the synchrotron as well IC component of *Crab Nebula* SED. Figure taken from Funk (2015).

## 1.2 Gamma-Ray Astronomy

### 1.2.1 Instruments

Gamma-ray astronomy relies on the detection of single gamma-ray events and reconstruction of their arrival direction and energy. As the earth's atmosphere is not transparent to gamma radiation, a direct detection of cosmic gamma-ray particles is only possible from space based observatories. Those instruments typically measure the tracks of electron and positron pairs, created in the interaction of incoming gamma-rays with multiple layers of high-Z foils (*pair production*). The multi layer architecture allows for reconstruction of the arrival direction and an additional calorimeter for measurement of the energy deposit. The installation of these particle detectors on satellites limits the size and consequently the effective detection area to  $<1 \text{ m}^2$ . This makes them usable only in the MeV to GeV energy range. The detectors typically have a large field of view (FOV) in the order of 2 steradian and a high live time, which makes them ideal all-sky survey instruments.

Ground based observatories use indirect methods based on the detection of air showers. A primary gamma-ray photon that enters the atmosphere will interact with the air particles and trigger a cascade of secondary particles, which in turn interact

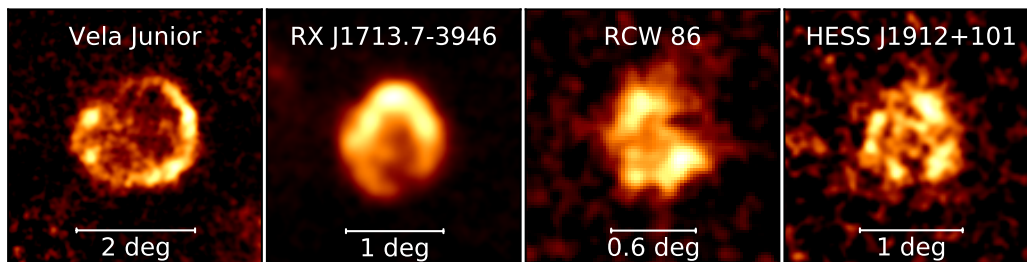
with other air particles and create an air shower. As the particles travel faster than the speed of light in the air medium, the particles emit Cherenkov light, which is visible in the optical as ultra short ( $\sim 10$  ns) blue flashes. This Cherenkov light can be imaged from the ground using optical telescopes with fast photomultiplier cameras. The stereoscopic observation of the particle shower allows for a reconstruction of the direction and energy of the primary gamma-ray particle. The current generation of these Imaging Atmospheric Cherenkov Telescopes (IACTs) have a small FOV ( $< 5$  deg), but they have large effective detection areas in the order of up to  $10.000 \text{ m}^2$ . This makes them ideal instruments for pointed observations in the TeV gamma-ray range. Instruments of this type in operation are the H.E.S.S., MAGIC and VERITAS telescopes. A more detailed review of IACTs can be found e.g. in Völk and Bernlöhr (2009).

Figure 1.2 compares the flux sensitivities for the detection of point sources<sup>1</sup> and energy ranges of current and future gamma-ray instruments. The energy range between 200 MeV and 200 GeV is covered by the *Fermi*-LAT instrument. The difference in sensitivity between observations of the inner Galaxy and the extragalactic sky is mainly caused by the increased level of diffuse background emission from the Galaxy. The very high energy range  $> 200$  GeV is currently covered by the H.E.S.S. telescopes and at energies  $> 10$  TeV the High-Altitude Water Cherenkov (HAWC) observatory takes over.

## 1.2.2 Galactic Gamma-Ray Sources

Most types of Galactic gamma-ray sources are related to late stages of stellar evolution. When a massive star ( $\sim 8 - 50$  solar masses) runs out of nuclear fuel and the burning process stops, it cannot longer maintain its hydrostatic equilibrium and collapses driven by gravitation. During the collapse the stellar material is compressed and heated and turns into neutrons via *Photodisintegration* and *Electron Capture*. The collapse stops when the core reaches a stable state, in which the equilibrium is maintained by the degeneration pressure of the neutrons. This leaves a compact spinning object called *Neutron Star* or *Pulsar* (PSR). The outer envelopes of the star bounds back from the massive core and are driven outwards again with velocities in the order of  $\sim 5 \cdot 10^3$  km/s. When the ejected stellar material hits the interstellar medium, an outwards moving shock wave is formed, which is denoted as *Supernova Remnant* (SNR). The pulsars are typically highly magnetized and generate a strong wind of relativistic charged particles mostly consisting of electrons and positrons. Those particles interact with magnetic and ambient photon fields and thus emit non-thermal radiation via the IC process and synchrotron emission. The emission is

<sup>1</sup>Sensitivity in gamma-ray astronomy is defined as the minimal flux of a point source to be detected with a certain significance (typically  $5\sigma$ ) in a given observation time.



**Fig. 1.3.:** Examples of shell-type SNRs observed in VHE gamma-rays.

observable as Pulsar Wind Nebula (PWN). A detailed review of the physics of core collapse SN can be found in Woosley and Janka (2005).

Supernovae are extreme events, where energies in the order of  $10^{51}$  erg are released in a very short time. For this reason SNe and their left overs provide an obvious environment for the production of VHE gamma-rays. The rate of core collapse SN in the Milky Way is currently estimated at  $\sim 2/100$  yrs (Diehl et al., 2006). Given that TeV gamma-ray sources are typically young objects with ages in the order of  $\sim 10^4$  yrs, we can expect a total number of a few hundreds up to a thousand of those objects in the Galaxy.

### Supernova Remnants

Supernova remnants have early been discussed as sources of cosmic rays (Ginzburg and Syrovatskii, 1964), based on mainly two arguments: First they can provide the necessary amount of energy for the production of VHE cosmic rays and the acceleration of the cosmic rays can be well explained by the mechanism of *diffusive shock acceleration* (Blandford and Eichler, 1987). A first direct evidence of the acceleration of charged particles to energies beyond 100 TeV in shock waves of SNRs was found by the H.E.S.S. telescopes by observing the shell-like morphology of RX J1713.7-3946 in TeV gamma-rays (Aharonian et al., 2004b).

Figure 1.3 shows four examples of shell-type SNRs observed in TeV gamma-rays. The SNRs have in common a pronounced shell-like structure, which clearly shows the VHE gamma-ray emission originates from the shock front region. The SNRs have diverse morphologies and sizes with brighter emission spots and different widths of the shell structure. Funk (2015) defined three main types of gamma-ray SNRs, depending on their age. The youngest objects ( $<1000$  yrs) such as *Tycho SNR* or *Cas A* show small gamma-ray fluxes, but with hard spectra in the GeV as well as TeV range. The slightly older shell-type objects ( $\sim 2000$  yrs) such as *Vela Junior* or have very hard GeV spectra with  $\Gamma \sim 1.5$ , that peak in the few TeV range and cut off above  $\sim 10$  TeV. The mid-aged SNRs ( $\sim 20,000$  yrs), typically interacting with molecular clouds, such as *W44* or *IC443* show spectra with a peak in the few GeV range and

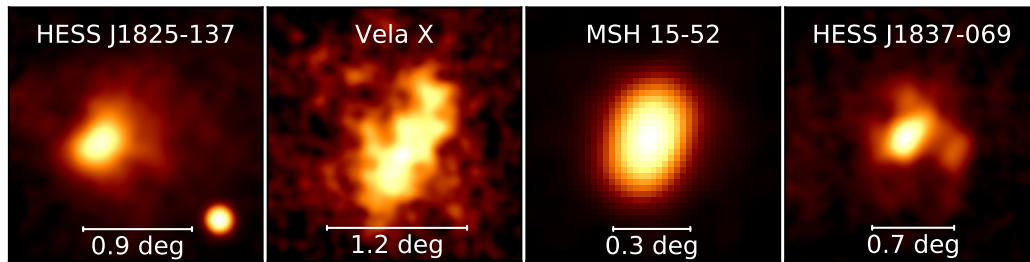


**Fig. 1.4.:** Examples of PWNe observed in VHE gamma-rays.

are faint in the TeV range. A more detailed review of *Supernova Remnants at High Energy* can be found in Reynolds (2008).

### Pulsars and Pulsar Wind Nebulae

Pulsed gamma-ray emission from the Crab and Vela pulsar was first detected by the SAS-2 instrument (Thompson et al., 1975; Kniffen et al., 1974) in the MeV energy range. With the latest observations from the *Fermi*-LAT instrument the number of identified gamma-ray pulsars has grown to > 143 objects in the Galaxy. Gamma ray pulsars appear as variable point-like sources that emit pulsed emission. Their spectrum typically cuts off in the range of a few GeV. A detailed review on gamma-ray pulsars is given by Caraveo (2014).

Unpulsed gamma-ray emission from the Crab Nebula was first detected by the Whipple telescope (Weekes et al., 1989) in the TeV range. Later e.g. Aharonian et al. (1997) delivered theoretical model predictions for the IC gamma-ray fluxes of X-ray synchrotron nebulae around pulsars. In the first H.E.S.S. Galactic Plane Survey (Aharonian et al., 2006f) PWNe were then found to be a common source class of TeV gamma-ray emission.

Figure 1.4 shows four examples of identified PWNe observed in VHE gamma-rays. Characteristic for those objects is their extension and center-filled morphology, with a bright core and fainter emission towards the tails. Beside this common properties PWNe show diverse shapes and sizes, with strong elongation, fragmentation or core and halo emission components. For the object *HESS J1825-137* an energy dependent morphology was found by Aharonian et al. (2006d), with a softening of the spectral index with increasing distance from the pulsar position. A more detailed overview of the *The Evolution and Structure of Pulsar Wind Nebulae* can be found in Gaensler and Slane (2006).

## Other Galactic gamma-ray Sources

While PWNe and SNRs are clearly the most common gamma-ray sources in the Galaxy, there are also other types of objects. One of the less frequent types are gamma-ray binary systems such as *LS 5039* or the *PSR B1259-63*. In TeV gamma-rays those binaries typically appear as point-like, highly variable sources. Two common models exist to explain the origin of the gamma-ray emission. The first one involves a microquasar system with a stellar mass black hole accreting material from a companion star, where the gamma-ray emission is produced in the relativistic jets of the microquasar. The second model involves a pulsar whose particle wind interacts with the stellar wind of its massive companion star (Dubus, 2013).

Another special case is the gamma-ray source in the Galactic center, that is likely associated to the radio source *Sgr A\**. It appears as a bright point-like source surrounded by diffuse ridge-like emission. The Galactic center source has recently been shown to accelerate protons up to PeV energies (HESS Collaboration et al., 2016).

## 1.3 Gamma-ray Astrophysics

### 1.3.1 Particle Acceleration

The production of VHE gamma-rays via the IC process or pion decay requires high energetic primary particles. Those high energies can be reached by accelerating charged particles in a mechanism named *diffusive shock acceleration*. This process was first proposed generally by Fermi (1949) and later adapted to explain diffusive particle acceleration in shock fronts of SNRs e.g. by Blandford and Eichler (1987).

The mechanism of first order Fermi acceleration is illustrated in Fig. 1.5. In the upstream as well as downstream region of the moving shock turbulent magnetic fields are present, that cause a diffuse (or isotropic) motion of the particle in both regions. Viewed from the unshocked (upstream) reference frame the particle in the unshocked region is at rest on average. As the shock approaches, the particle crosses diffusively the shock front into the downstream region, which approaches with  $3/4U$ . This way the particle can gain energy in collisions with the downstream material. Now at higher energy, its motion is again isotropized in the downstream region, such that it is at rest on average. Viewed from the downstream reference frame it is now the unshocked region, that approaches with  $3/4U$ . Again the particle can gain energy by diffusively crossing the shock front in the other direction. It can be shown that for an ideal relativistic gas, the net energy gain for such a shock crossing cycle is  $\Delta E/E \propto \frac{U}{c}$  (Longair, 2011).

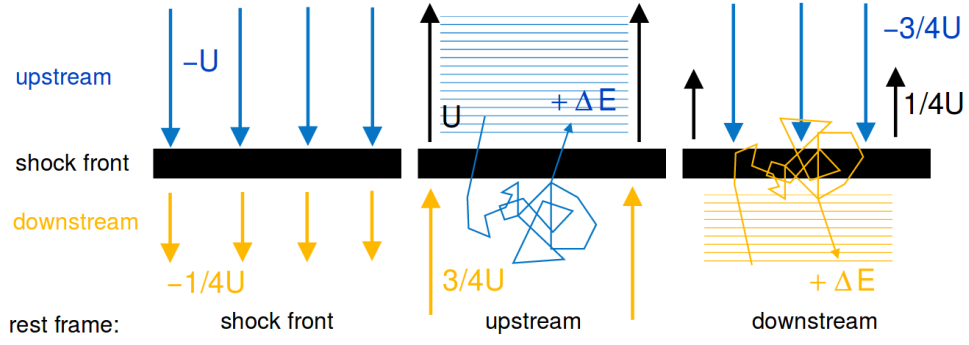


**Fig. 1.5.:** Illustration of first order diffusive particle acceleration in a shock wave for three different reference frames. The shock front is shown as black bars propagates with velocity  $U$ . The up- and downstream region are marked in blue and yellow respectively. The arrows indicate the moving directions of the material streaming towards and away the shock front. Figure taken from Funk (2005).

It can be also shown that the particle energy spectrum resulting from such an acceleration process follows a power law, with a typical index of  $\alpha \sim 2$ :

$$\frac{dN}{dE} \propto E^{-\alpha} \quad (1.1)$$

In reality the energy, that particles can reach by acceleration is limited and the energy spectrum naturally cuts off at high energies. In literature mainly three effects are mentioned:

**Finite Age** The time scale at which particles can be accelerated is determined by the number of collisions (or shock crossings) they encounter. The rate of collisions in turn depends on the diffusion coefficient of the medium. Following Hinton and Hofmann (2009) the maximum proton energies in the *Bohm* diffusion limit for shock acceleration in SNRs is approximately given by:

$$E_{Max} = 1 \text{ TeV} \left( \frac{u}{1000 \text{ km s}^{-1}} \right) \left( \frac{t}{1000 \text{ yrs}} \right) \left( \frac{B}{1 \mu\text{G}} \right) \quad (1.2)$$

Where  $t$  is the age of the SNR,  $u$  the shock velocity and  $B$  the magnetic field strength.

**Particle Escape** To keep a particle within the acceleration process for a sufficient amount of time, its radius of gyration must not exceed the size of the acceleration region. This condition sets a natural limit on the maximum energy a particle can reach in an acceleration region of given size  $L$  and magnetic field  $B$ . The condition is also known as the *Hillas condition* for particle escape:

$$E_{Max} = 1000 \text{ TeV} \left( \frac{L}{1 \text{ pc}} \right) \left( \frac{B}{1 \mu\text{G}} \right) Z^\beta \quad (1.3)$$

Where  $Z$  is the charge of the accelerated particle and  $\beta$  the acceleration efficiency.

**Radiation Losses** Charged particles lose energy through the interaction with magnetic fields, radiation fields or matter, where the energy is emitted via synchrotron or IC radiation or Bremsstrahlung. These losses also limit the maximum energy and can be estimated as:

$$E_{Max} = 100 \text{ TeV} \left( \frac{u}{1000 \text{ km s}^{-1}} \right) \left( \frac{B}{1 \mu\text{G}} \right)^{-1/2} \quad (1.4)$$

Where  $u$  is the velocity of the shock and  $B$  the magnetic field strength.

### 1.3.2 Leptonic Emission

One of the dominant production mechanism for VHE gamma-rays is the interaction of relativistic electrons with radiation fields via the *Inverse Compton* (IC) process. Photons from ambient radiation fields such as cosmic microwave background, infrared, or optical are scattered by accelerated electrons and gain energies up to the VHE gamma-ray range.

Figure 1.6 illustrates the spectral energy distribution (SED) that results from a leptonic emission process. A mono-energetic electron of energy  $E_e$  that scatters on a population of photons with a typical energy of  $E_{ph}$  will produce a broad IC gamma-ray spectrum with a peak at an energy of:

$$E_{IC} \approx 5 \times 10^9 \frac{E_{ph}}{10^{-3} \text{ eV}} \left( \frac{E_e}{1 \text{ TeV}} \right)^2 \text{ eV} \quad (1.5)$$

cause a cooling and spectral break of Assuming an underlying electron distribution with index  $\alpha_e = 2$  the gamma-ray SED is characterized by a rising edge, where the index of the primary spectrum is modified to  $\Gamma_{IC} = (\alpha_e + 1)/2$  (Blumenthal and Gould, 1970). Synchrotron losses cool the primary electron distribution which results in a spectral break at high energies. When the cooling time  $\tau_C$  is comparable to the age  $t_{age}$  of the break energy can be estimated as:

$$E_{e,br} = 1.2 \cdot 10^4 \text{ GeV} \left( \frac{B}{10 \mu\text{G}} \right)^{-2} \left( \frac{t_{age}}{10^4 \text{ yrs}} \right)^{-1} \quad (1.6)$$

The spectral break in the primary particle distribution also results in a spectral break of the gamma-ray spectrum. At even higher energies the IC scattering enters the *Klein-Nishina* regime in which the energy losses are almost independent of the electron energy. This results in an even steeper spectral index of  $\Gamma_{IC} = \alpha_e + 1$ .

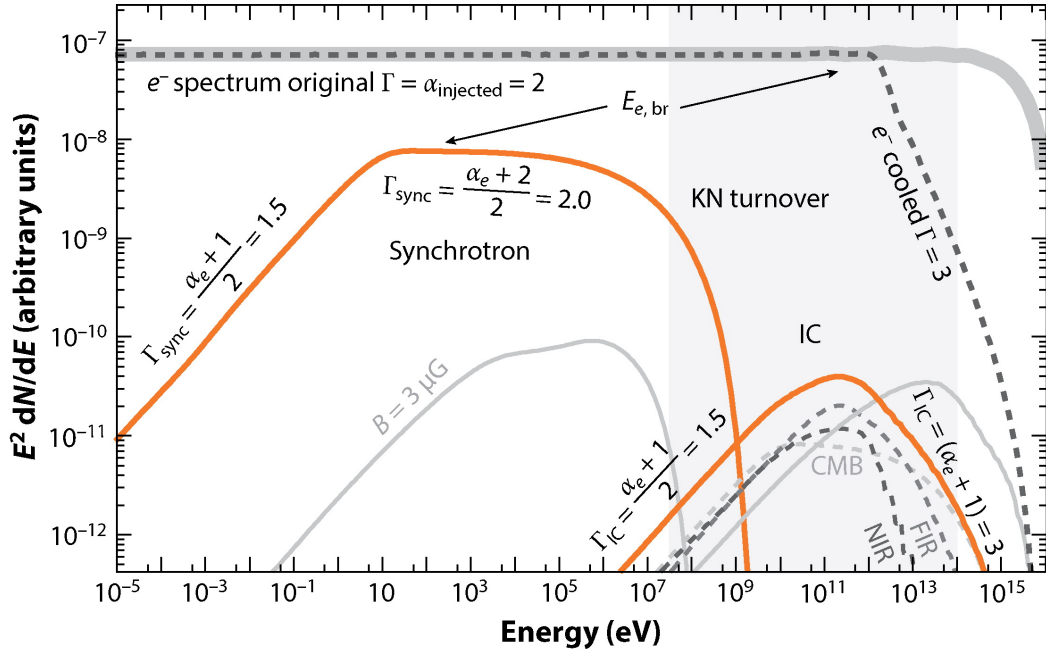


**Fig. 1.6.:** Spectral energy distribution for a leptonic emission model. The bold light gray line shows the primary particle spectrum. The shaded gray band illustrates the sensitivity range of current gamma-ray instruments (*Fermi*-LAT and IACTs). Figure taken from Funk (2015).

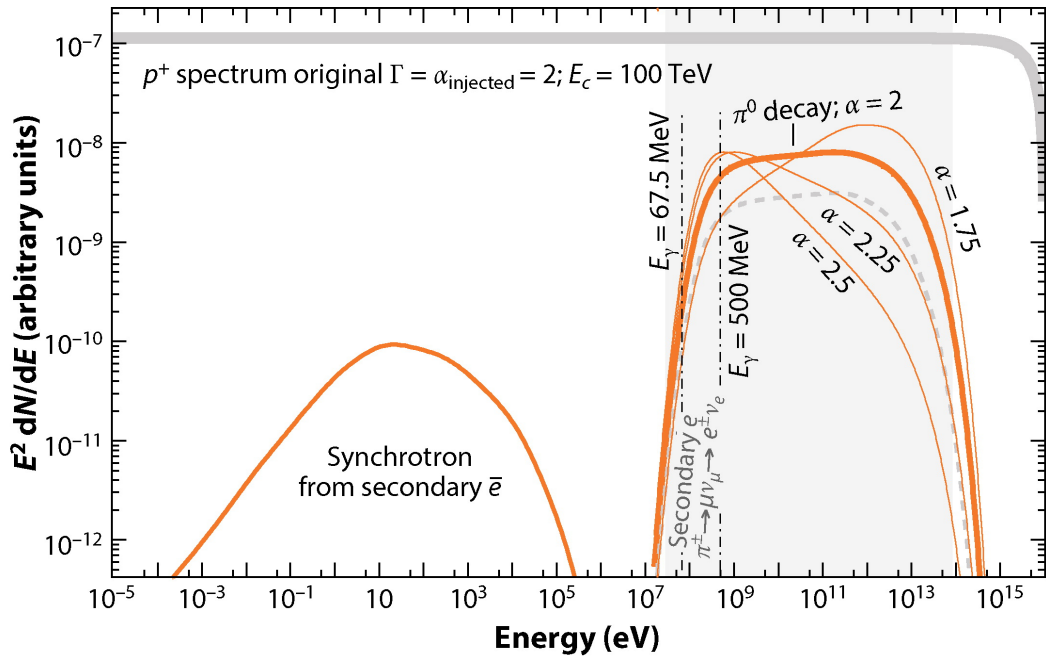


**Fig. 1.7.:** Spectral energy distribution for a hadronic emission model. The solid gray line shows the spectrum of primary protons, assuming a power law with an index of  $\alpha_{\text{injected}} = 2$  and an exponential cut off at  $E_c = 100$  TeV. The resulting spectral energy distribution in gamma-rays is shown for different  $\alpha_{\text{injected}}$ . The shaded gray band illustrates the sensitivity range of current gamma-ray instruments (*Fermi*-LAT and IACTs). Figure taken from Funk (2015).

### 1.3.3 Hadronic Emission

The second important process for the production of VHE gamma-rays is the decay of neutral pions that are created in proton-proton interactions:



Figure 1.7 illustrates the gamma-ray SED that results from this hadronic emission model. The SED is characterized by a broad peak (often called *pion bump*) around half the rest mass of the  $\pi^0$  of 63.5 MeV. The shape of the SED to higher energies is then fully determined by the underlying energy distribution of the accelerated protons. In case of a power law distribution of the primary protons with index  $\alpha_p = 2$  the resulting gamma-ray spectrum will also follow an index of  $\Gamma = 2$ , but shifted to lower energies by a factor of  $\kappa_\pi \approx 0.17$ . In the hadronic emission scenario cooling plays a minor role, because the cooling time for protons for a typical Galactic density ( $n = 1 \text{ cm}^{-3}$ ) is in the order of  $10^7$  yrs (Funk, 2015).

## 1.4 Gamma-ray Data Analysis

### 1.4.1 High Level Data Model and Data Formats

In general the analysis of astronomical gamma-ray data requires specific and detailed knowledge of the instrument it was measured with. Consequently gamma-ray data is either only analyzed internally by the collaborations running the instruments (e.g. all current IACTs and water Cherenkov detectors) or in case of the *Fermi*-LAT, by providing the astronomical community with the software tools required for the analysis.

Though on a higher lever the data can be described with a uniform data model independently of the instrument. It is common to all detectors that they either measure directly or reconstruct the basic properties of the incoming gamma-ray events such as arrival direction, energy and arrival time. This information can be stored in tables named *event lists*. In addition the properties of the detector, such as effective detection area, angular and energy resolution can also be described as quantities dependent on the energy and on instrument specific observation parameters such as zenith angle or offset from the observation position. From this technical information the basic input data for the high level modeling step can be computed. This mainly includes exposure images and cubes and models for the point spread function and energy dispersion. The details of this data preparation step as well as background modeling are dependent on the operation mode and type of the instrument. While for pointed observations (typically IACTs) the data is grouped into single observa-

tion runs, for slewing instruments, such as the *Fermi*-LAT, the data can be treated globally. The details of modeling, exposure computation and background modeling are presented in the dedicated analysis sections in Sects. 2.2.2, 2.2.3 and 2.2.5 for the H.E.S.S. telescopes and Sects. 3.2.2, 3.2.3, and 3.2.5 for the *Fermi*-LAT.

To store the data the flexible image transport system (FITS) data format (Pence et al., 2010) is used, which is very common in other fields of astronomy. The preliminary definition of those data formats is documented online in the *Gamma-Astro-Data-Formats* repository<sup>2</sup>. The general concept and idea of the open data formats is presented in more detail in Deil et al. (2017b).

## 1.4.2 Poisson Maximum Likelihood Fitting

Based on the data model presented in the previous section, the gamma-ray data is typically analyzed using binned *Poisson Maximum Likelihood Fitting*. Assuming Poisson statistics per bin, the likelihood fit then maximizes the *Cash* statistic (Cash, 1979):

$$\mathcal{C} = 2 \sum_i (M_i - D_i \log M_i), \quad (1.8)$$

where  $M_i = S_i + B_i$  represents the sum of the expected number of counts from a given source  $S_i$  and background model  $B_i$ .  $D_i$  (data) is the actual measured counts per bin.

To determine the statistical significance of a best-fit source model compared to the background-only model (i.e. setting  $S_i = 0$ ), we use a likelihood ratio test with test statistic TS. It is defined by the likelihood ratio or equivalently as the difference in TS between both hypotheses:

$$\text{TS} = \mathcal{C}_0 - \mathcal{C}_S, \quad (1.9)$$

where  $\mathcal{C}_S$  corresponds to the value of the *Cash* statistic of the best-fit model and  $\mathcal{C}_0$  to the background-only model.

For a large number of counts, according to Wilks' theorem (Wilks, 1938), TS is asymptotically distributed as  $\chi_N^2$ , where  $N$  is the number of free parameters defining the flux model. In this limit, the statistical significance corresponds to  $\text{sign}(\text{Flux}) \cdot \sqrt{|\text{TS}|}$  where the sign of the best-fit flux is needed to allow for negative significance values in regions where the number of counts is smaller than the background estimate (e.g. due to a statistical downward fluctuation).

<sup>2</sup><https://github.com/open-gamma-ray-astro/gamma-astro-data-formats>

Errors on the best fit parameters can be estimated using mainly two methods. The first method involves the inverse of the *Hesse* matrix at the minimum of the likelihood function to estimate the covariance matrix of the optimized parameters:

$$\sigma_{ij} = \left( \frac{\partial^2 \mathcal{C}_S}{\partial x_i \partial x_j} \right)^{-1} \quad (1.10)$$

The derivatives of the log-likelihood function with respect to the parameters  $x_i$  can be determined numerically.

The second, non-linear method, sometimes called *profile likelihood*, relies on estimating the parameter limits corresponding to a given difference ( $\Delta TS$ ) in the log-likelihood function compared to the minimum value. Both methods and the interpretation of the resulting error estimates are described in detail e.g. in James (1994).

### 1.4.3 Open Source Software *Gammapy*

In the past few years the programming language *Python*<sup>3</sup> has established itself as one of the most important tools for astronomical data analysis (Momcheva and Tollerud, 2015). Reasons for this include free availability, simple syntax, existence of numerous scientific libraries, usability as scripting language to interface other software and programming languages and a supportive and active web community.

In 2012 the astronomical Python community started a project named *Astropy*<sup>4</sup>, which is “A community effort to develop a common core package for Astronomy in Python and foster an ecosystem of interoperable astronomy packages” (Robitaille et al., 2013). Based on *Astropy* as a core dependency we started to develop *Gammapy*<sup>5</sup>, an open-source Python package dedicated to astronomical gamma-ray data analysis. With the open source approach we intend to make the scientific results more transparent and reproducible. The general concept and development approach of *Gammapy* is presented in more detail in Donath et al. (2015). Recently *Gammapy* has also been proposed as a prototype for the CTA science tools (Deil et al., 2017a).

A large fraction of the program code developed for this work has been contributed to the *Gammapy* package. This includes:

- Implementation of a fast computation of TS maps using the algorithm described in Stewart (2009). The method is available in *Gammapy* as *TSImageEstimator* class. This class enabled the computation of TS and residual TS maps for the

---

<sup>3</sup><http://www.python.org>

<sup>4</sup><http://www.astropy.org>

<sup>5</sup><http://www.gammapy.org>

HGPS analysis (e.g. Fig. 2.7) as well as systematic search for shell-like SNRs using the HGPS dataset (H.E.S.S. Collaboration et al., 2018).

- Estimation of image profiles, including error propagation was implemented in the `ImageProfileEstimator` and `ImageProfile` classes. This enabled the comparison between the HGPS and *Fermi*-LAT measurement presented in Sect. 3.3.2.
- Computation of flux points with the `FluxPointEstimator` and `FluxPoints` classes. Those were used to compute spectral points for HGPS sources as described in Sect. 2.3.7 as well as GeV flux points as described in Sect. 3.3.3.
- Handling of source catalogs via the `SourceCatalog` class and its derived classes for the HGPS and *Fermi*-LAT catalogs. Those were used for the computation of flux model images via the `CatalogImageEstimator` class and the association process described in Sect. 2.3.8.
- Computation of *Fermi*-LAT sky images in energy bands. The method is described in more detail in Sect. 3.2.5. It enabled the image based comparison to the HGPS measurement and the computation of *Fermi*-LAT RGB images presented in Sect. 3.3.1. The algorithms are available in *Gammapy* as `FermiLATBasicImageEstimator` class.
- Handling of sky images and spectral cubes with the `SkyImage` and `SkyCube` classes. Those were used as a central data structure for almost all analyses presented in this work.



# The H.E.S.S. Galactic Plane Survey

” *Data has less value than information, which has less value than knowledge. And knowledge has less value than wisdom. What is increasing along this path from data to wisdom at every level, is context.*

— Unknown

## Contents

2.1	Introduction . . . . .	19
2.1.1	Literature Overview . . . . .	20
2.1.2	Survey Region Overview . . . . .	20
2.2	H.E.S.S. Instrument and Dataset . . . . .	22
2.2.1	Instrument . . . . .	22
2.2.2	Observation Selection . . . . .	22
2.2.3	Event Reconstruction and Selection . . . . .	23
2.2.4	Point Spread Function . . . . .	24
2.2.5	Sky Maps . . . . .	25
2.3	Catalog Analysis Method . . . . .	28
2.3.1	Sources not Reanalyzed . . . . .	30
2.3.2	Large-Scale Emission Model . . . . .	31
2.3.3	Regions of Interest . . . . .	32
2.3.4	Multi-Gaussian Source Emission Model . . . . .	34
2.3.5	Component Selection and Classification . . . . .	36
2.3.6	Source Characterization . . . . .	37
2.3.7	Source Spectra . . . . .	39
2.3.8	Source Association . . . . .	43
2.3.9	Statistical False Detection Rate . . . . .	44
2.3.10	Method Discussion . . . . .	46
2.4	Results . . . . .	48
2.4.1	Source Associations and Identifications . . . . .	48
2.4.2	Longitude and Latitude Distribution . . . . .	51

2.4.3	Flux and Size Distribution . . . . .	53
2.4.4	Log N - Log S Distribution . . . . .	55
2.4.5	Distribution in the Milky Way and Survey Horizon . . . . .	57
2.4.6	Comparison with Previous VHE Publications . . . . .	57

---

The content of this chapter is a subset of the work published in *H.E.S.S. Collaboration et al. (2018)*. It presents the work contributed by the author. Work contributed by collaborators is reproduced as far as needed for the understanding of the results. This includes computation of the maps used for the source detection and analysis described in Sect. 2.2.5 (Henning Gast, Francois Brun, Vincent Maradon, Svenja Carrigan), development of the method and creation of the large scale emission model described in Sect. 2.3.2 (Régis Terrier) and fitting of spectral models of sources described in Sect. 2.3.7 (Christoph Deil). Figures were all produced by the author. Supplementary information is provided in Sect. 2.1, Sect. 2.3.9 and Fig. B.2, Fig. B.3 and Fig. B.4.

## 2.1 Introduction

In 2004 the H.E.S.S. telescope array started a systematic observation program of the Galactic plane in TeV gamma-rays: the H.E.S.S. Galactic plane survey (HGPS). With its location on the southern hemisphere, a field of view of  $\sim 5^\circ$  an angular resolution of  $\sim 0.1^\circ$  and a sensitivity of better than 5% Crab per 10 hours, the H.E.S.S. telescope array was better suited for survey operations of the Galactic plane than any previous IACT. Before the H.E.S.S. survey program started only seven Galactic TeV gamma-ray sources were known:

- *Crab Nebula* (PWN) detected by the Whipple telescope (Weekes et al., 1989).
- *Vela X* (PWN) detected by CANGAROO (Yoshikoshi et al., 1997).
- *RX J1713.7-3946* (SNR) detected by CANGAROO (Muraishi et al., 2000).
- *Cassiopeia A* (SNR) detected by HEGRA (Aharonian et al., 2001).
- *TeV J2032+4130* (PWN) detected by HEGRA (Aharonian et al., 2002a).
- *Galactic Center* source detected by CANGAROO (Tsuchiya et al., 2004).
- *Vela Junior* (SNR) detected by CANGAROO (Katagiri et al., 2005).

The HGPS quickly discovered numerous new TeV emitters and revealed the existence of whole populations of TeV gamma-ray sources in the Galactic plane. The data collection for the HGPS program stopped in 2013. The first part of this chapter presents a re-analysis of the complete HGPS dataset with the goal to compile an almost uniform TeV source catalog. Based on this catalog the second part of this chapter studies the distribution of TeV source properties such as flux and extension, as well as the distribution of those sources in the Galaxy.

## 2.1.1 Literature Overview

The first results of the HGPS were presented in (Aharonian et al., 2006f). The analysis was based on the first 230-h of observations and a dataset with inhomogeneous exposure, limited to the inner Galaxy between  $\ell = 30^\circ$  and  $\ell = 330^\circ$ . By locating peaks in Li & Ma significance maps on three different spatial scales ( $0.1^\circ$ ,  $0.22^\circ$  and  $0.4^\circ$ ) in total 14 new objects were detected. Source parameters such as position, size and flux were determined by fitting a two-dimensional symmetric Gaussian model to the data using Poisson maximum likelihood fitting.

With increasing exposure time and survey area many new TeV source were detected and typically announced in individual publications with dedicated analyses. Results on newly detected unidentified sources were published in (Aharonian et al., 2008d), and conference proceedings (Hoppe, 2008a; Chaves et al., 2008; Chaves and for the H.E.S.S. Collaboration, 2009; Gast et al., 2011; Carrigan et al., 2013b; Carrigan et al., 2013a).

A first re-analysis of the complete HGPS dataset with a uniform source detection and characterization procedure was presented by Deil (2012). In his work the author used a Poisson maximum likelihood method to manually model the TeV emission in the Galactic plane using a Gaussian morphology assumption for the sources. From this model he compiled a first version of the HGPS source catalog. In total the author detected 62 sources and measured positions, morphological and spectral parameters for all of them. He also described for the first time the difficulties in modeling complex emission regions, where bright sources tended to decompose into multiple Gaussian emission components and underlying large scale emission could lead to significant extended Gaussian components.

Methods for automatic merging and classification of source components have been studied in detail by Donath (2014). The author showed that any bright source, when modeled with a simple parametric morphology assumption will decompose into multiple components that model morphological details of the source. Based on the experience with this previous study the analysis method presented in Sect. 2.3 was developed.

## 2.1.2 Survey Region Overview

Figure 2.1 illustrates the region observed by the HGPS in context of the dense gas structure of the Galaxy, represented by an all-sky image of *Planck* CO(1-0) data. For comparison the much smaller regions of previous IACT surveys by *HEGRA* (Aharonian et al., 2002b) and *Veritas* (Weinstein, 2009) are shown. The region not

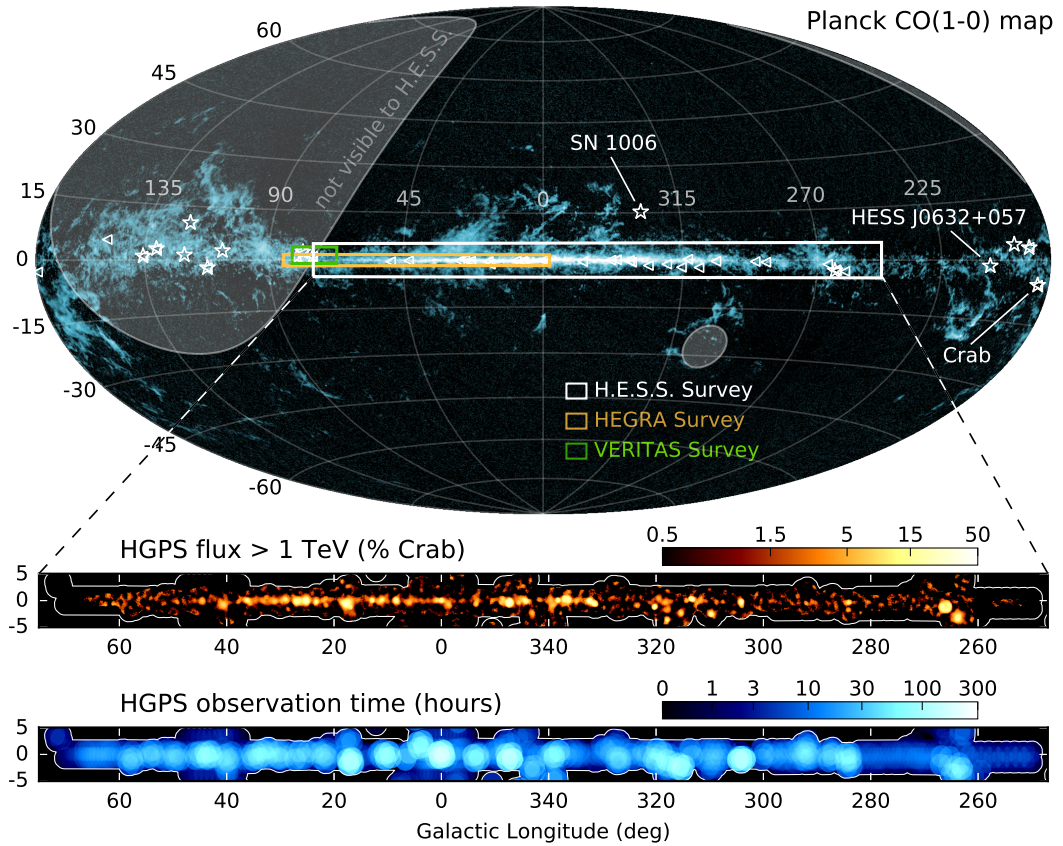


**Fig. 2.1.:** The HGPS region is illustrated in this all-sky image of *Planck* CO(1-0) data (Planck Collaboration et al., 2016) in Galactic coordinates and Hammer-Aitoff projection. For comparison, the HEGRA Galactic plane survey (Aharonian et al., 2002b) and VERITAS Cygnus survey (Weinstein, 2009) footprints are overlaid. The Galactic *Fermi*-LAT 2FHL gamma-ray sources (Ackermann et al., 2016) are shown as triangles. Fifteen Galactic VHE gamma-ray sources outside the HGPS region are shown as stars. Three of these have been detected by H.E.S.S. and are labelled: SN 1006 (Acero et al., 2010a), the Crab Nebula (Abramowski et al., 2014c) and HESS J0632+057 (Aliu et al., 2014). The gray shaded regions mark the part of the sky that cannot be observed from the H.E.S.S. site at reasonable zenith angles (less than  $60^\circ$ ). The lower panels show the HGPS gamma-ray flux above 1 TeV (correlation radius  $R_c = 0.4^\circ$ ) and observation time, both also in Galactic coordinates. The white contours in the bottom panels mark the boundaries of the survey region; the HGPS has little or no exposure beyond Galactic latitudes of  $\pm 3^\circ$  at most locations along the Galactic plane.

visible by the H.E.S.S. instrument is shown in translucent gray. This includes the region around *Cygnus A* and larger parts of the outer Galaxy.

The HGPS covers the region between  $\ell = 250^\circ$  and  $65^\circ$  in longitude and  $b = \pm 3^\circ$  in latitude. It contains only a few percent of the area of the entire sky, but includes the largest part of the dense structure of the Galaxy, where gamma-ray emitters are expected to be found. It also contains the majority of known GeV sources (2FHL, marked by white triangles), whose distribution is not affected by observational selection effects. The three known TeV sources outside the HGPS region are labeled by name.

The middle panel of Fig. 2.1 shows the gamma-ray flux above 1 TeV, measured in % Crab. It illustrates impressively that TeV gamma-ray emission is present almost everywhere in the Galaxy and not a rare phenomenon. The total measured flux above 1 TeV adds up to  $\sim 15$  times the flux of the *Crab Nebula*.

## 2.2 H.E.S.S. Instrument and Dataset

### 2.2.1 Instrument

The *High Energetic Stereoscopic System* (H.E.S.S.) experiment is an array of five imaging atmospheric Cherenkov telescopes (IACT) located in the Khomas highlands of Namibia. It consists of four identical 12 m diameter telescopes arranged in a square with a 120 m sides and a larger 28 m diameter telescope in the center. The four smaller telescopes have been in operation since 2004 and cover an energy range from 200 GeV to 100 TeV. The big telescope was built in a second phase of the experiment to lower the energy threshold of the whole array down to a few tens of GeV. The combined array of smaller telescopes has a FOV  $\sim 5^\circ$  and an angular resolution of better than  $0.1^\circ$ . A more detailed description of the instrument, including technical details can be found in W.Hofmann (2012).

### 2.2.2 Observation Selection

Observations with the H.E.S.S. telescopes are done in single *observation runs*. During one *observation run* the instrument is pointed to a fixed position in the sky for a fixed nominal duration of 28 min. The duration is chosen such, that the instrument response functions such as PSF and energy dispersion can be considered as stable during the observation. In total the HGPS dataset includes 6239 *observation runs* taken between January 2004 and January 2013. Among those are all *observation runs* with zenith angles up to  $65^\circ$  and observation positions centered in the Galactic

coordinate range  $\ell = 244.5^\circ$  to  $77.5^\circ$  and  $|b| < 7.0^\circ$ . Furthermore only those *observation runs* were selected, where the *Cherenkov transparency coefficient*  $T$  (Hahn et al., 2014), which characterizes the atmospheric conditions, fell within the range  $0.8 < T < 1.2$  (for clear skies,  $T = 1$ ).

The lower panel of Fig. 2.1 shows the distribution of observation time across the whole HGPS region. It shows a non-uniform but complete coverage of the Galactic Plane between  $b = \pm 3^\circ$ . The non-uniformity is a result of the HGPS data selection, which includes observations with different purposes:

- Dedicated survey observations, taken with a typical spacing between pointings of  $0.7^\circ$  in longitude and in different latitude bands located between  $b = -1.8^\circ$  and  $b = 1^\circ$ . In addition, for the longitude bands  $\ell = 355^\circ$  to  $5^\circ$  and  $\ell = 38^\circ$  to  $48^\circ$ , we extended the survey observations in latitude, adding observation pointings from  $b = -3.5^\circ$  to  $b = 3.5^\circ$  to explore the possibility of high-latitude emission.
- Deeper follow-up observations of source candidates (“hot spots”) seen in previous survey observations.
- Exploratory and follow-up observations of astrophysical objects located inside the survey region that were promising candidates for emitting VHE gamma-rays.
- Observations to extend the HGPS spatial coverage and “fill-up” observations to achieve a more uniform sensitivity across the Galactic plane.

The total observation time distributed over the whole HGPS region amounts to  $\sim 2700$  hrs. The distribution of the observation time translates into a flux sensitivity of lower than  $\sim 2\%$  Crab for the largest part of the Galactic Plane. A longitude profile and map of the flux sensitivity is shown in Fig. 2.2.

### 2.2.3 Event Reconstruction and Selection

The reconstruction of event directions and energies follows the H.E.S.S. standard methods. First the camera pixel data is converted to pixel amplitudes measured in units of photoelectrons (p.e.) using the calibration procedure described in (Aharonian et al., 2004a). After applying an image cleaning procedure, the Hillas moments of the camera images are determined and from those the direction of the arrival direction of the primary event is reconstructed using stereoscopic imaging. The reconstruction process is described in more detail in (Aharonian et al., 2006e).

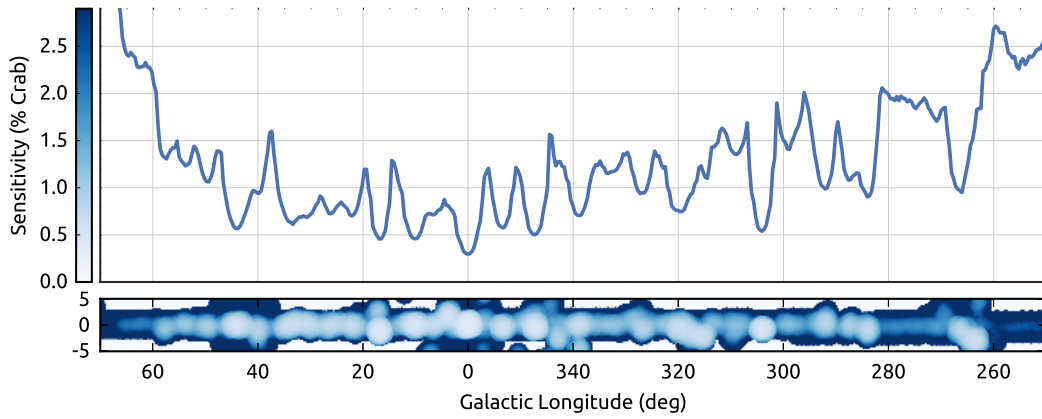


**Fig. 2.2.:** HGPS point-source sensitivity map and profile along the Galactic plane at a Galactic latitude  $b = 0^\circ$ . The sensitivity is given in % Crab, for a correlation radius  $R_c = 0.1^\circ$ , assuming a spectral index  $\Gamma = 2.3$ . The effective sensitivity to source detection is also affected by the catalog construction methodology (cf. Sect. 2.3.10).

To distinguish hadronic background from photon candidate events, a multivariate machine learning method, based on boosted decision trees, is used. Various image shape parameters are combined into a single variable  $\zeta$ , which allows to discriminate hadronic from gamma-like events using a simple cut on its value. In this work *hard*  $\zeta$  cuts were used for the generation of sky maps and *standard*  $\zeta$  cuts for the measurement of spectra. The method and definition of  $\zeta$  cuts is described in detail in (Ohm et al., 2009) (cf. Table 2a).

All results in this work are cross-checked using an alternative calibration, reconstruction, and gamma-hadron separation method based on a semi-analytical description of the shower development. This method is described in detail in (de Naurois and Rolland, 2009).

Event energies are reconstructed by comparing the image amplitudes with the results from MC simulations of the H.E.S.S. instrument (Bernlöhr, 2008). The energy estimate is mainly biased by the degrading and changing optical efficiencies of the telescope mirrors. To take this effect into account four sets of MC simulations were used: at the start of H.E.S.S. operations; at the point when efficiencies had dropped to  $\sim 70\%$ , before the first mirror refurbishment campaign; and after the mirror refurbishment of each telescope. Remaining differences are corrected using the Myon calibration methods described in (Bolz, 2004) and (Leroy, 2004).

## 2.2.4 Point Spread Function

The H.E.S.S. point spread function (PSF) varies with observing parameters, zenith angle, offset, muon efficiency, number of telescopes and energy. Assuming a point-

like source with a PL spectrum of index 2.3, we computed the mean expected PSF for any given position in the survey region using MC shower simulations. Assuming further rotational symmetry of the PSF, we stored the distribution of events in an exposure-weighted  $\theta^2$  histogram for every test position, where  $\theta$  is the reconstructed event offset with respect to the simulated point-source position. Finally, we fit this distribution with a triple-exponential analytical PSF model,

$$\frac{dP}{d\theta^2}(\theta^2) = \sum_{i=1}^3 A_i \exp\left(-\frac{\theta^2}{2\sigma_i^2}\right), \quad (2.1)$$

where  $A_i$  and  $\sigma_i$  are the weights and widths of the corresponding components, respectively. This ad hoc model corresponds to a triple-Gaussian, two-dimensional, PSF model when projected onto a sky map.

The 68% containment radius of the H.E.S.S. PSF is  $\sim 0.08^\circ$  (in  $\theta$ ) and varies by approximately  $\pm 10\%$  across the survey region. Section 2.3.6 discusses systematic uncertainties related to the PSF model, in connection with upper limits on source sizes. Details on the variation of the PSF with position are given e.g. in Donath (2014) (Tab. D.1) or Deil (2012) (Figs. A.10 and A.10).

## 2.2.5 Sky Maps

For the subsequent catalog analysis and modeling procedure we generate sky maps from the event based data. Those sky maps are computed first for each individual *observation run* and later combined (“stacked”) into larger survey maps, by summing the individual observations. Those survey maps cover the region from  $\ell = 70^\circ$  to  $250^\circ$  and  $b = \pm 5^\circ$  and use a Cartesian projection of the sky in Galactic coordinates. The size of the pixels was fixed to  $0.02^\circ \times 0.02^\circ$ , which corresponds to  $\sim 1/5$  of the  $R_{68}$  of the PSF.

### Counts

The counts map contains the number of detected events per solid angle or pixel of the map. For every *observation run* all events within a radius of  $2^\circ$  around the observation position are selected. This selection is applied to avoid systematic effects at the edge of the FOV. To also avoid systematic effects related to the reconstructed energy of the events, only events above the *safe energy threshold* are selected. This threshold is defined as the energy where the reconstructed energy is not biased more than 10% across the entire FOV, where the energy bias is determined using MC simulations.

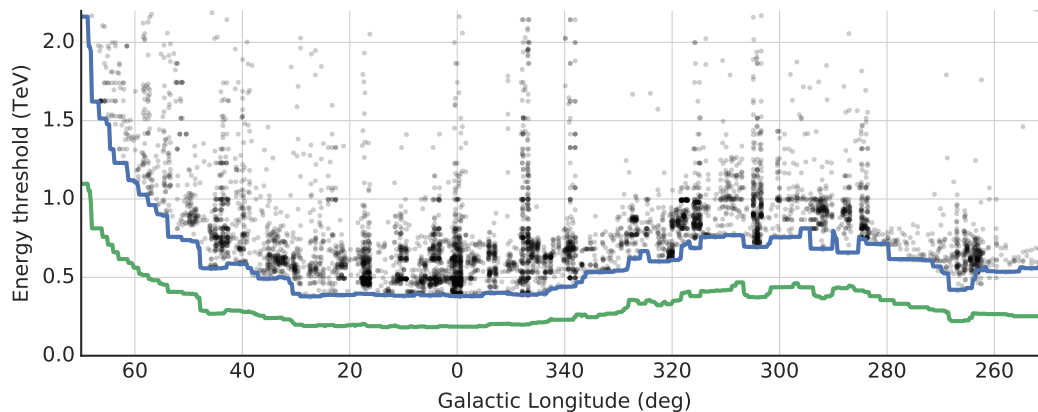


**Fig. 2.3.:** HGPS minimum safe energy threshold as a function of the Galactic longitude for a latitude of  $b = 0^\circ$ . The blue curve is the minimum threshold for *hard* cuts (used for maps) and the green curve is for *standard* cuts (used for spectra). The black dots represent the safe threshold for each observation run, obtained for the *hard* cuts configuration. (The few black dots below the blue line correspond to runs at Galactic latitude  $|b| > 2^\circ$ .)

The distribution of safe energy thresholds of the individual *observation runs* and the resulting minimal safe energy threshold longitude profiles for two different quality cuts are shown in Fig. 2.3. The minimal threshold varies between 400 GeV and 800 GeV for *hard*  $\zeta$  cuts and between 200 GeV and 400 GeV for *standard*  $\zeta$ . The global shape of the profiles reflects the dependency of the lower energy threshold on the zenith angle of the observation.

## Background

A large fraction of the events passing the gamma-hadron selection cuts described in the previous section are false classified hadronic, electron or positron events. Those events appear as a uniform source of background emission in the *counts* sky map. A standard method to estimate this background component is the *ring background* method described in (Berge et al., 2007). For the analysis of the HGPS data this method has been refined by adaptively changing the ring size to the local size of the exclusion regions. The method is illustrated in Fig. 2.4. For every position (pixel center) in the FOV the background is estimated by summing all counts within a ring around the center position. Regions outside the FOV and inside exclusion regions are ignored. In case the available ring area exceeds a lower threshold, the size of the ring is adaptively enlarged.

The background map is improved iteratively by updating the exclusion region mask in every step and recomputing the background estimate with the adaptive ring method. This procedure typically converges after  $< 5$  iterations. The final exclusion region mask is illustrated in Fig. B.9.

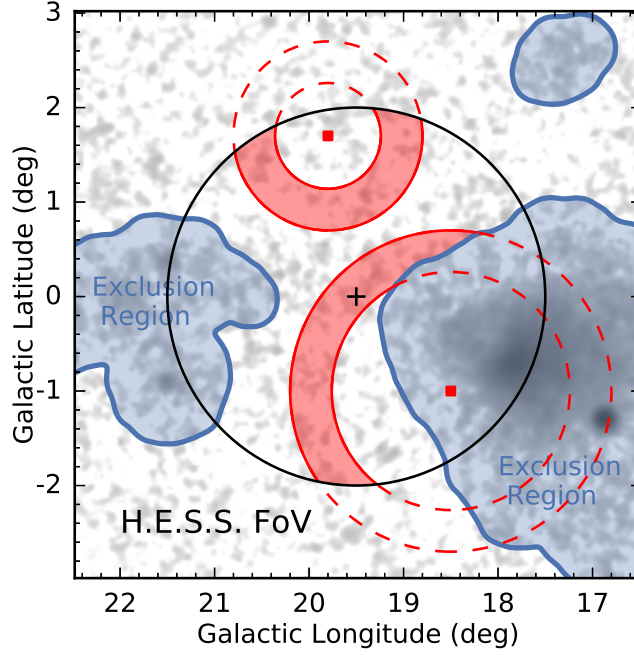


**Fig. 2.4.:** Illustration of the adaptive ring method for background estimation for a single observation (cf. Sect. 2.2.5). The HGPS significance image is shown in inverse gray-scale and exclusion regions as blue contours. The analysis FoV for one observation is shown as a black circle with  $2^\circ$  radius and a black cross at the observation pointing position. The red rings illustrate the regions where the background is estimated for two positions in the FoV (illustrated as red squares). Only regions in the ring inside the FoV and outside exclusion regions are used for background estimation. For the position in the lower right, the ring was adaptively enlarged to ensure an adequate background estimate.

## Exposure

To estimate astrophysical fluxes of gamma-ray sources from counted events, the detector response and observation time are combined into a quantity named *exposure*. In this definition the *exposure* is equivalent to the number of expected gamma-ray events per unit time and area from a source with an assumed reference spectrum  $w_{ref}$ . The exposure of a single *observation run* is then given by:

$$\mathcal{E}_R = T_R \int_{E_{min,R}}^{\infty} w_{ref}(E_r) \cdot A_{eff}(E_r, q_R) dE_r \quad (2.2)$$

Where  $E_r$  is the reconstructed energy,  $T_R$  is the observation time and  $q_R$  a vector of additional observation parameters such as zenith and azimuth angle, optical efficiency and telescope multiplicity.  $A_{eff}$  is the effective area determined with MC simulations.  $E_{min}$  is the safe energy threshold for the *observation run* as defined above. For the reference spectrum we assume a power law, that is normalized to unity in a given energy band ( $E_{min}, E_{max}$ ):

$$w_{ref}(E) = \frac{1 - \Gamma}{E_{max}^{1-\Gamma} - E_{min}^{1-\Gamma}} \cdot E^{-\Gamma} \quad (2.3)$$

The spectral index is chosen  $\Gamma = 2.3$ , which corresponds to the expected average spectral index of Galactic source above 1 TeV. Using the definition of exposure above the flux in the energy band  $(E_{min}, E_{max})$  can now be computed from:

$$F = \frac{C - B}{\mathcal{E}} \quad (2.4)$$

## Test Statistic

The test statistic (TS) value denotes the likelihood ratio of the assumed source hypothesis versus the null hypothesis (i.e. background only) for every position (pixel) in the map. These maps are computed assuming different spatial templates  $S_0$ : a point-like source morphology (i.e. PSF only), and PSF-convolved Gaussian morphologies with widths  $0.05^\circ$ ,  $0.10^\circ$  and  $0.20^\circ$ . During the computation of each map, at the center of each map pixel, a single-parameter likelihood fit of the amplitude  $F_0$  of the template is performed, according to the following model:

$$N_{Pred} = N_{Bkg} + PSF * (\mathcal{E} \cdot F_0 \cdot S_0) \quad (2.5)$$

Where  $N_{Bkg}$  is the predicted number of counts from the background model. Then the map is filled with the TS value defined in Eq. 1.9.

In this work TS maps are primarily used to compute residual maps and distributions. The main advantage over standard Li & Ma significance maps is that source morphology and PSF information can be taken into account. Technically, it is very similar to the full free-parameter likelihood fit that was applied during the subsequent modeling procedure. Additionally, this work uses TS maps when presenting sky maps, because they contain uniform statistical noise everywhere in the map. In contrast, flux or excess maps that are smoothed with the same spatial templates still show increased noise in regions of low exposure. The TS map algorithm is available in *Gammapy*; see also Stewart (2009) for a more detailed description of TS maps.

## 2.3 Catalog Analysis Method

Since the first HGPS publication in 2006, H.E.S.S. has increased its exposure tenfold and enlarged the survey region more than twofold, while also improving the homogeneity of the exposure. As illustrated in the upper panel of Fig. 2.5, the data now show many regions of complex emission, e.g. overlapping emission of varying sizes and multiple sources with clearly non-Gaussian morphologies. Apart from discrete emission, the Galactic plane also exhibits significant emission on large spatial scales (Abramowski et al., 2014a). For these reasons, we needed to develop a more complex

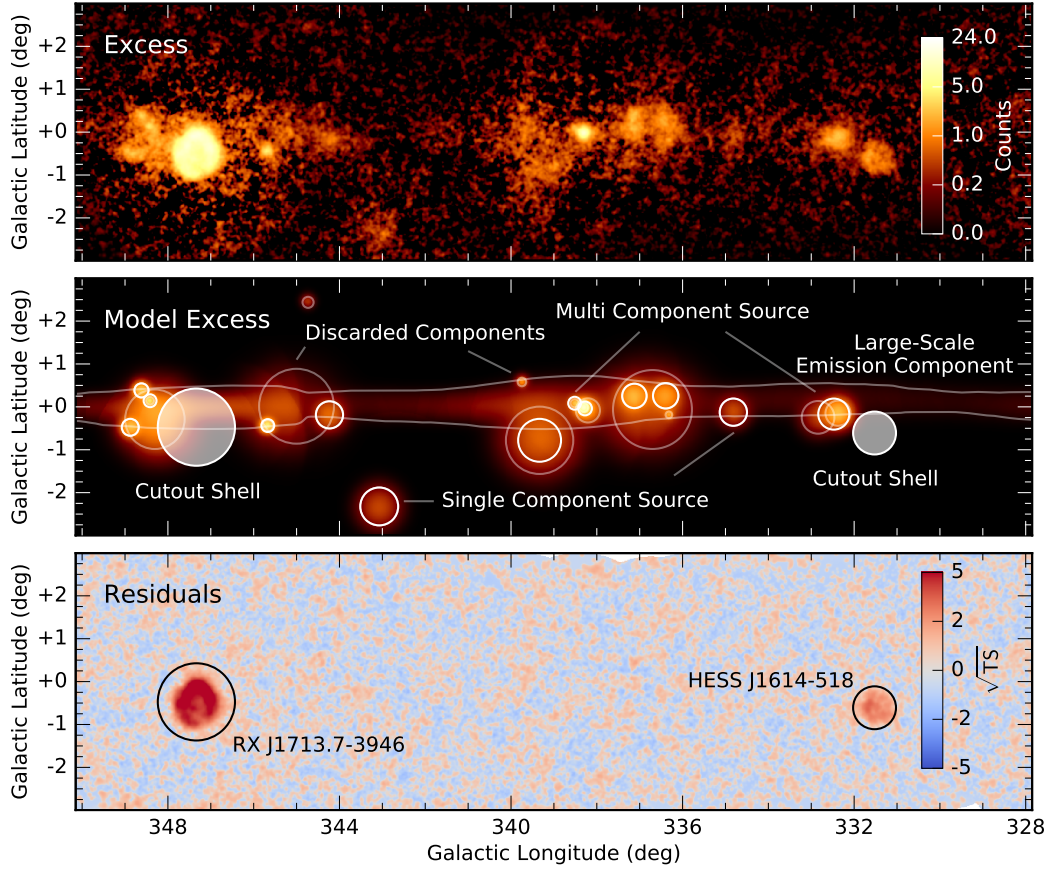


**Fig. 2.5.:** Illustration of the catalog model construction in the region of  $350^\circ$  to  $328^\circ$  in Galactic longitude. The top panel shows the gamma-ray excess counts, the middle panel the PSF-convolved excess model and the lower panel the residual  $\sqrt{TS}$  map. We did not re-analyze the SNR RX J1713.7–3946 and SNR candidate HESS J1614–518 because of their more complex shell morphologies. We discarded two components of the emission model, because they were not significant in the cross-check analysis. For details on the catalog construction procedure, cf. Sect. 2.3. For a complete overview of all analysis regions (ROIs) and excluded sources, see Fig. B.9.

analysis procedure to construct a more realistic model of the gamma-ray emission in the entire survey region. The procedure is as follows:

1. Cut out the Galactic center (GC) region and shell-type supernova remnants from the dataset because of their complex morphologies (Sect. 2.3.1).
2. Model the large-scale emission in the Galactic plane globally (Sect. 2.3.2).
3. Split the HGPS region into manageable regions of interest (ROIs) (Sect. 2.3.3).
4. Model the emission in each ROI as a superposition of components with Gaussian morphologies (Sect. 2.3.4).
5. Merge Gaussian components into astrophysical VHE gamma-ray sources (Sect. 2.3.5).
6. Determine the total flux, position and size of each gamma-ray source (Sect. 2.3.6).
7. Determine the spectrum of each source (Sect. 2.3.7).
8. Associate the HGPS sources with previously-published H.E.S.S. sources and MWL catalogs of possible counterparts (Sect. 2.3.8).

### 2.3.1 Sources not Reanalyzed

H.E.S.S. observations have revealed many sources with complex morphology, e.g. RX J0852.0–4622 (Vela Junior), with a very pronounced shell-like structure (H.E.S.S. Collaboration et al., 2016b), or the Galactic center region, with multiple point-sources embedded in a very elongated ridge-like emission (H.E.S.S. Collaboration et al., 2017b). Dedicated studies model such regions of emission using complex parametric models, e.g. model templates based on molecular data, shell-like models, asymmetric Gaussian models and even combinations thereof. It is challenging to systematically model the emission across the entire Galactic plane using these more complex models, which tend to yield unstable or non-converging fit results because of the large number of free and often poorly-constrained parameters. This can be especially problematic in ROIs with multiple, complex, overlapping sources.

Given the difficulties with modeling complex source morphologies, we decided to restrict the HGPS analyses to a symmetrical Gaussian model assumption and exclude all firmly-identified shell-like sources and the very complex GC region from re-analysis. Table 2.1 provides a complete list of the excluded (or “cut-out”), sources in the HGPS region, with references to the latest H.E.S.S. publications which do treat these sources in detail. The table also contains a handful of sources that were not significant in the current HGPS analysis but were found to be significant in other

**Tab. 2.1.:** VHE sources in the HGPS catalog with source parameters taken from other publications. We list briefly the reasons for not re-analyzing these sources in the HGPS (further explanation in main text, Sect. 2.3.1), with references to the respective publications.

Source name	Common name	Reason for not re-analyzing	Reference
HESS J0852–463	Vela Junior	Shell morphology	2016b <sup>a</sup>
HESS J1442–624	RCW 86	Shell morphology	2016c <sup>a</sup>
HESS J1534–571	G323.7–1.0	Shell morphology	2017a <sup>a</sup>
HESS J1614–518	—	Shell morphology	2017a <sup>a</sup>
HESS J1713–397	RX J1713.7–3946	Shell morphology	2016e <sup>a</sup>
HESS J1731–347	G353.6–0.7	Shell morphology	2011a <sup>a</sup>
HESS J1912+101	—	Shell morphology	2017a <sup>a</sup>
HESS J1745–290	Galactic center	Galactic center region	2016a <sup>a</sup>
HESS J1746–285	Arc source	Galactic center region	2017b <sup>a</sup>
HESS J1747–281	G0.9+0.1	Galactic center region	2005e <sup>b</sup>
HESS J1718–374	G349.7+0.2	Not significant in HGPS	2015b <sup>a</sup>
HESS J1741–302	—	Not significant in HGPS	2017c <sup>a</sup>
HESS J1801–233	W28	Not significant in HGPS	2008b <sup>b</sup>
HESS J1911+090	W49B	Not significant in HGPS	2016f <sup>a</sup>

<sup>a</sup> H.E.S.S. Collaboration et al.

<sup>b</sup> Aharonian et al.

dedicated, published analyses. We have added all of the sources not re-analyzed to the final HGPS catalog for completeness; they are therefore included in the various distributions, histograms and other plots exploring the global properties of the HGPS sources in Sec. 2.4.2.

### 2.3.2 Large-Scale Emission Model

H.E.S.S. previously showed the existence of large-scale, diffuse, VHE gamma-ray emission along the Galactic plane (Abramowski et al., 2014a). In this study The authors constructed a mask to exclude the regions of the plane where significant emission was detected. The latitude profile of excess gamma-rays outside this mask clearly showed the presence of significant large-scale gamma-ray emission. Whether this emission originates from interactions of diffuse cosmic rays in the interstellar medium or from faint, unresolved gamma-ray sources (or a combination thereof) is not investigated further here.

The presence of a large-scale component of gamma-ray emission along the Galactic plane complicates the extraction of the Gaussian gamma-ray source components. The large-scale emission can mimic the presence of spurious degree-scale sources in some regions of the plane and also tends to broaden the Gaussian components that describe otherwise well-defined sources. It is therefore necessary to model the large-scale gamma-ray emission in order to measure the HGPS sources' flux and morphology more accurately.

To do so, we built an empirical model of the large-scale emission, where the latitude profile is Gaussian and defined by three parameters: the peak position in latitude, the width and the amplitude of the Gaussian. We estimated the parameters using a maximum likelihood fit in regions where no significant emission is measurable on small scales, i.e. outside the exclusion regions defined for the ring background model. Regardless of the physical origin of the large-scale emission, it is likely to be structured along the plane and not constant.

To estimate the variable parameters of the model, we fit the Gaussian parameters in rectangular regions of width  $20^\circ$  in longitude and height  $6^\circ$  in latitude. We excluded all pixels inside the standard exclusion regions used to produce the background maps (see Sect. 2.2.5). The Gaussian parameters were dependent on the size of both the exclusion regions and rectangular regions. We found that the typical variations were  $\sim 25\%$ . To obtain a good, smooth sampling of the variations, we followed a sliding-window approach, distributing the centers of the rectangular regions every  $2.5^\circ$  in longitude and interpolating between these points.

The maximum likelihood fit compares the description of the data between the cosmic-ray (CR) background only and the CR background plus the model. We used the likelihood ratio test to estimate the significance of adding the large-scale component in each 20-deg-wide window, finding it to be larger than  $3\sigma$  (TS difference of 9) over most of the HGPS region. Figure 2.6 shows the resulting best-fit Gaussian parameters together with the associated uncertainty intervals estimated from the likelihood error function. After this fit, we froze the parameters of the model for use in the gamma-ray source detection and morphology fitting procedure.

While the approach presented here provides an estimate of the large-scale emission present in the HGPS maps, it does not comprise a measurement of the total Galactic diffuse emission. An illustration of the large scale emission model for the whole survey region is shown in Fig. B.3.

### 2.3.3 Regions of Interest

To search for sources, we divided the whole HGPS region into smaller ROIs. This was necessary to limit both the number of simultaneously fitted parameters and the number of pixels involved in the fit. Given the Gaussian morphology assumption – with four parameters  $F$ ,  $\sigma$ ,  $l$  and  $b$  – and an expected number of sources of  $\mathcal{O}(100)$ , the total number of parameters in a global fit would be  $\approx 400$ . Since this large number of free parameters would not yield any stable and reliable fit results in a reasonable time and since it is also not necessary to fit all sources simultaneously (because sources e.g. in the Vela region are completely independent of the sources in the GC region), we used more manageable ROIs.

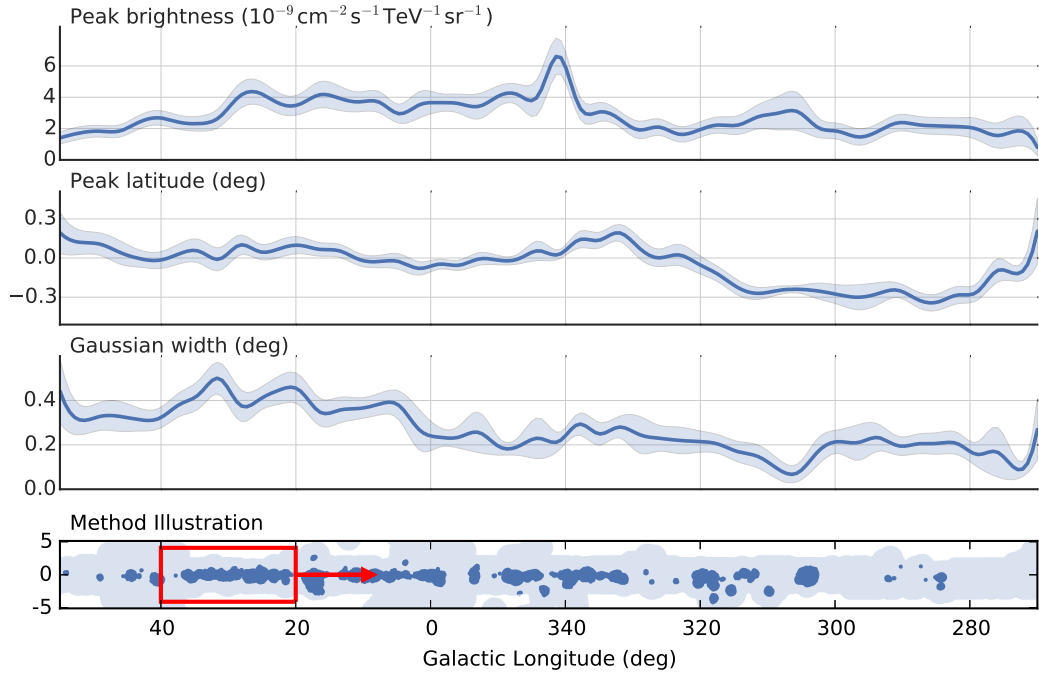


**Fig. 2.6.:** Distribution of the fitted large-scale emission model parameters with Galactic longitude. The first panel gives the peak brightness of the large-scale emission model in units of  $10^{-9} \text{ cm}^{-2} \text{ s}^{-1} \text{ TeV}^{-1} \text{ sr}^{-1}$ . The second panel shows the peak position of the Gaussian along the Galactic latitude axis in degrees and the third panel shows the width ( $\sigma$ ) of the Gaussian in degrees. The solid lines are the result of fitting each set of parameters every  $2.5^\circ$  in longitude and interpolating. The light blue bands show the  $1\text{-}\sigma$  error region obtained from the covariance matrix of the likelihood function. The lower panel illustrates the  $20^\circ$ -wide sliding-window method (red rectangle) that was used to determine the large-scale emission model in areas (shown in light blue) where the HGPS sensitivity is better than 2.5% Crab but outside exclusion regions (shown in dark blue), explained in further detail in the main text.

We manually applied the following criteria to define the ROIs:

- (a) All significant emission (above  $5\sigma$ ) in the HGPS region should be contained in at least one ROI.
- (b) No significant emission should be present close to the edges of an ROI.
- (c) The width of each ROI should not exceed  $\sim 10^\circ$  in longitude to limit the number of pixels involved in the fit.
- (d) ROIs should cover the full HGPS latitude range from  $-5^\circ$  to  $5^\circ$ .

Criterion (a) ensures that every source or source candidate is contained in at least one ROI. Criterion (b) ensures that all the significant emission is fully enclosed in an ROI to avoid boundary effects. In cases where this criterion was not fulfilled, we excluded the corresponding emission from the ROI and assigned it to a different, overlapping ROI. Criterion (c) limits the total number of pixels and number of fitted parameters to reduce the computational time required for the likelihood fit. Criterion (d) ensures the full latitude range available is used. Figure B.9 illustrates the boundaries of the 18 ROIs defined with these criteria. Some of the ROIs show regions without any exposure; these regions were masked out and ignored in the subsequent likelihood fit.

### 2.3.4 Multi-Gaussian Source Emission Model

After excluding shell-type SNRs and the GC region from re-analysis and adding a model for large-scale emission to the background, we modeled all remaining emission as a superposition of Gaussian components. We took the following model as a basis:

$$N_{\text{Pred}} = N_{\text{B}} + \text{PSF} * \left( \mathcal{E} \cdot \sum_i S_{\text{Gauss},i} \right) + \mathcal{E} \cdot S_{\text{LS}}, \quad (2.6)$$

where  $N_{\text{Pred}}$  corresponds to the predicted number of counts,  $N_{\text{B}}$  to the number of counts from the background model,  $S_{\text{LS}}$  the contribution of the large-scale emission model,  $\sum_i S_{\text{Gauss},i}$  the sum of the Gaussian components and  $\mathcal{E}$  the exposure as defined in Eq. 2.2.

For a given set of model parameters, we integrated the surface brightness distribution  $S$  over each spatial bin, multiplied it by the exposure  $\mathcal{E}$  and convolved it with the PSF to obtain the predicted number of counts per pixel. For every ROI, we took the PSF at the position of the brightest emission and assumed it to be constant within the ROI.

For the Gaussian components, we chose the following parametrization:

$$S_{\text{Gauss}}(r|\phi, \sigma) = \phi \frac{1}{2\pi\sigma^2} \exp\left(-\frac{r^2}{2\sigma^2}\right), \quad (2.7)$$

where  $S_{\text{Gauss}}$  corresponds to the surface brightness and  $\phi$  to the total spatially-integrated flux of the component. The offset  $r = \sqrt{(\ell - \ell_0)^2 + (b - b_0)^2}$  is defined with respect to the position  $(\ell_0, b_0)$  of the component, measured in Galactic coordinates.

We conducted the fitting process following a step-by-step procedure. Starting with one Gaussian component per ROI, we added Gaussian components and re-fit parameters successively until no significant residuals were left. In each step, we varied the starting parameters of the fit to avoid convergence towards a local minimum. The significance of the tested component was estimated from:

$$TS = \mathcal{C}(\text{with component}) - \mathcal{C}(\text{best solution without component}) \quad (2.8)$$

We considered the component to be significant and kept it in the model when the TS value exceeded a threshold of  $TS = 30$ .

The definition of TS above differs slightly from the definition given in Eq. 1.9. For a single, isolated component, both values are identical. However, if a second, overlapping component exists, some of the emission of the first source is modeled by the second one, reducing the significance of the first. We therefore estimated the significance of a component from the TS difference in the total model of the ROI and not from the the TS difference compared to the background-only model.

We performed the modeling and fitting described above in Eqs. 2.6, 1.8 and 1.9 in pixel coordinates using the HGPS maps in Cartesian projection. Spatial distortion of flux models because of the projection from the celestial sphere are negligible, because the HGPS data only covers a latitude range of  $|b| \leq 3^\circ$ . We implemented the analysis in Python using Astropy version 1.3 (Astropy Collaboration et al., 2013), Sherpa version 4.8 (Freeman et al., 2001) and Gammapy version 0.6 (Donath et al., 2015; Deil et al., 2017a).

Figure 2.7 depicts the residual  $\sqrt{TS}$  distributions over the entire HGPS region. They demonstrate that there is good agreement with a normal Gaussian distribution; in particular, we find no features above the  $\sqrt{TS} = \sqrt{30}$  detection threshold. Inherent imperfections in the background, large-scale emission models and source emission models lead to a slight broadening of the distributions with respect to a normal distribution, as expected. A residual  $\sqrt{TS}$  map for the whole survey regions is shown in Fig. B.4.

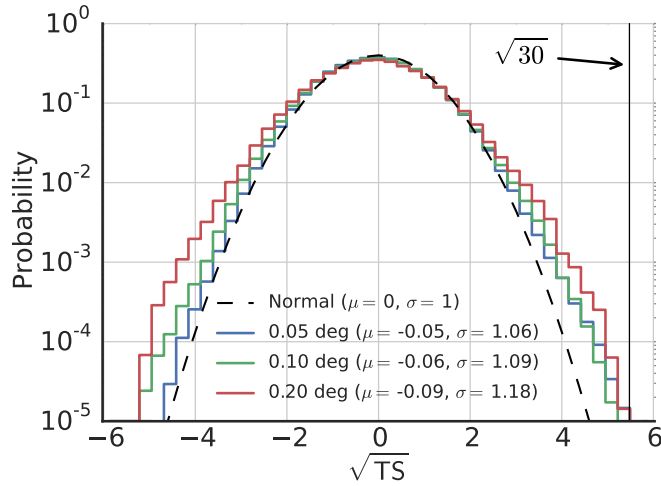


**Fig. 2.7.:** Residual significance distribution after taking the HGPS emission model into account (cf. Fig. 2.5, middle panel). The significance was computed using Eq. 1.9, assuming source sizes of  $R_c = 0.05^\circ$ ,  $0.10^\circ$  and  $0.20^\circ$ . A vertical line at  $\sqrt{TS} = \sqrt{30}$  is shown, corresponding to the detection threshold for the HGPS multi-Gauss modeling. The sky region corresponding to this distribution includes pixels inside exclusion regions, but not the Galactic center and shell-type SNRs that were not modeled for HGPS (cf. Table 2.1, bottom panel of Fig. 2.5 and Fig. B.9).

For reference, the 98 Gaussian components have been assigned identifiers in the format HGPSC NN, where NN is a two-digit number, sorted by right ascension (which is right to left in the survey maps). The complete list of components is provided in the electronic catalog table.

### 2.3.5 Component Selection and Classification

We repeated the entire modeling procedure described in the previous section with a second set of maps produced with an independent event reconstruction method (cf. Sect. 2.2.3). Five of the 98 HGPS components were not significant in the cross-check analysis and were therefore discarded (cf. Fig. 2.5).

We observed two other side-effects of the modeling procedure. The first was where very bright VHE sources, even some with center-filled morphologies, decomposed into several Gaussian components, modeling different morphological details of the source. Figure 2.5 illustrates this effect, where we found two *multi-component sources* in a region. Since these modeling components were clearly part of the same astrophysical object, we merged them into a single source in the final HGPS source catalog. In total, we found 15 multi-component sources: ten consisting of two Gaussian components and five consisting of three Gaussian components. More detailed analyses of the complex morphology of these multi-component sources is intriguing but beyond the scope of this survey paper.

The second side-effect was that some of the Gaussian components appeared to have very large sizes coupled with very low surface brightness. This seems very likely due to the modeling procedure accounting for additional large-scale emission not already covered by the simple large-scale emission model (Sect. 2.3.2). For example, as shown in Fig. 2.5, the emission around  $\ell \sim 345^\circ$  initially comprised three model components: two components that clearly converged on the two discrete emission peaks visible in the excess map; and one very large and faint component that appeared to be modeling large-scale emission along the Galactic plane in between the two and not clearly related to either of the two peaks. In total, we found nine such large-scale components which we discarded and did not include in the final HGPS source catalog. All discarded components are visible in Fig. B.3.

## 2.3.6 Source Characterization

### Merged Sources Parameters

For HGPS sources that consist of several components, we determined the parameters of the final merged sources as follows:

The total flux is the sum of the fluxes of the individual components:

$$F_{\text{Source}} = \sum_i^N F_i \quad (2.9)$$

We calculated the position by weighting the individual component positions with the respective fluxes. The final  $\ell_{\text{Source}}$  and  $b_{\text{Source}}$  coordinates of the source are then:

$$\ell_{\text{Source}} = \frac{1}{F_{\text{Source}}} \sum_i^N \ell_i F_i \quad \text{and} \quad b_{\text{Source}} = \frac{1}{F_{\text{Source}}} \sum_i^N b_i F_i \quad (2.10)$$

We obtained the extension in  $\ell$  and  $b$  directions from the second moment of the sum of the components:

$$\sigma_{\ell, \text{Source}}^2 = \frac{1}{F_{\text{Source}}} \sum_i^N F_i \cdot (\sigma_i^2 + \ell_i^2) - \ell_{\text{Source}}^2 \quad (2.11)$$

$$\sigma_{b, \text{Source}}^2 = \frac{1}{F_{\text{Source}}} \sum_i^N F_i \cdot (\sigma_i^2 + b_i^2) - b_{\text{Source}}^2 \quad (2.12)$$

where additionally we defined the average circular extension as:

$$\sigma_{\text{Source}} = \sqrt{\sigma_{\ell, \text{Source}} \sigma_{b, \text{Source}}} \quad (2.13)$$

We computed the uncertainties of the parameters using Gaussian error propagation, taking the full covariance matrix estimate from the fit into account.

### Extension Upper Limits

During the morphology fit, we did not take into account uncertainties in the PSF model. However, H.E.S.S.-related studies (e.g. Stycz, 2016) have revealed a systematic bias on the extension of point-like extragalactic sources on the order of  $\sigma_{\text{syst}} = 0.03^\circ$ , and we adopted this number as the systematic uncertainty of the PSF. To claim a significant extension beyond the PSF, we used the following criterion:

$$\sigma_{\text{syst}} < \sigma_{\text{Source}} - 2\Delta\sigma_{\text{Source}}, \quad (2.14)$$

i.e. the extension of a source should be  $2\Delta\sigma_{\text{Source}}$  beyond the systematic minimum  $\sigma_{\text{syst}}$ . If this criterion is not met, we consider the source to be point-like and define an upper limit on the source extension as follows:

$$\sigma_{\text{UL}} = \max(\sigma_{\text{syst}}, \sigma_{\text{Source}} + 2\Delta\sigma_{\text{Source}}). \quad (2.15)$$

### Localization

The HGPS source location error is characterized by error circles  $R_\alpha$  at confidence levels  $\alpha = 0.68$  and  $\alpha = 0.95$ , computed as

$$R_\alpha = f_\alpha \times \sqrt{\Delta\ell_{\text{stat}}^2 + \Delta\ell_{\text{syst}}^2 + \Delta b_{\text{stat}}^2 + \Delta b_{\text{syst}}^2}. \quad (2.16)$$

$\Delta\ell_{\text{stat}}$  and  $\Delta b_{\text{stat}}$  are the statistical errors on Galactic longitude  $\ell$  and latitude  $b$ , respectively, from the morphology fit. For the H.E.S.S. systematic position error, a value of  $\Delta\ell_{\text{syst}} = \Delta b_{\text{syst}} = 20'' = 0.0056^\circ$  per axis was assumed, following the method and value in (Acero et al., 2010b).

Assuming a Gaussian probability distribution, the pre-factor is given by  $f_\alpha = \sqrt{-2\log(1-\alpha)}$  for a given confidence level  $\alpha$  (cf. Eq. 1 in Abdo et al., 2009).

### Identifier

The 78 HGPS catalog sources have been assigned source names in the format HESS JHHMM+DDd. For new sources, the source name was based on the source location reported in this paper. For sources that had been assigned names in previous H.E.S.S. publications or conference presentations, the existing name was kept for the HGPS catalog, even if the position in the HGPS analysis would have led to a different name in the last digit.

### 2.3.7 Source Spectra

After detection and subsequent morphological analysis of the sources, we measured a spectrum for each of the sources using an aperture photometry method. In this method, which is the standard one used in H.E.S.S., we sum the ON counts within an aperture defined as a circular region centered on the best-fit position of each source. We fit a spectral model within that aperture using an ON-OFF likelihood method (Piron et al., 2001) where the OFF background is estimated using reflected regions defined on a run-by-run basis (Berge et al., 2007). Based on the morphology model, we then corrected the measured flux for containment and contamination from other nearby sources. For the spectral analysis, we applied *standard* cuts, resulting in energy thresholds in the range 0.2–0.5 TeV, lower than the thresholds achieved using *hard* cuts in the detection and morphology steps. Figure 2.3 shows the variation of the threshold with longitude. In the following sections, we describe the spectral analysis process in more detail.

#### Circular Apertures and Reflected Region Background Estimate

The *optimal* choice for the size for the spectral extraction region is a balance between including a large fraction of flux from the source and limiting the contamination of the measurement by hadronic background events, large-scale emission and other nearby sources. Following these requirements, we chose the aperture radius  $R_{\text{spec}}$  as follows:

- a default of 70% containment radius, measured on the PSF-convolved excess model image (R70 in the catalog) for medium-size sources (34 sources),
- a minimum of  $0.15^\circ$  for small sources that have a size smaller than  $0.15^\circ$  (21 sources),
- a maximum of  $0.50^\circ$  for very large sources that have a size larger than  $0.5^\circ$  (9 sources).

A minimal aperture radius of  $0.15^\circ$  was imposed to make the measurement of the source spectrum more robust against systematic uncertainties of the PSF and the source morphology assumption.

The aperture radius was limited to a maximum radius of  $R_{\text{spec}} = 0.50^\circ$  to limit the fraction of observations that cannot be used for the spectrum measurement, because no background estimate could be obtained. This will become clear later when the background method is explained in more detail.

As illustrated in Fig. 2.8, the background is estimated using the reflected region method, described in Berge et al. (2007). For every spectral extraction region (ON region), corresponding OFF regions with the same shape and offset to the pointing position are chosen outside exclusion regions.

The method works well for small, isolated gamma-ray sources such as active galactic nuclei (AGNs) or the Crab nebula, where typically  $\sim 10$  OFF regions are found in every observation. This results in a well-constrained background, and all the exposure can be used for the spectral measurement. Because of the high density of sources in the Galactic plane, large areas of emission are excluded as background regions and only few reflected regions can be found. This effectively results in a loss of exposure for the spectrum measurement compared to the map measurement. In cases where the loss of exposure is very high, the background cannot be well constrained, which consequently results in spectral parameters that are not well constrained. The following sources are affected by this issue:

- Sources located in or near large exclusion regions (see Fig. B.9). An area of width  $\sim 2^\circ$  is often excluded along the Galactic plane, and this covers a significant fraction of the analysis FoV (which has a diameter of  $4^\circ$ ).
- Sources with large ON regions.
- Sources observed with too small or too large offsets, because they are located close to other sources that were covered with dedicated observations.

## Flux Containment and Contamination Correction

By construction and because of additional effects such as PSF leakage or source morphologies featuring tails, the spectral extraction region does not contain the full flux of the source. Additionally, the large-scale emission model and other nearby Gaussian components bias the flux measurement within the spectral region. Based on this emission model, we separate the contributions from the different components and derive a correction factor for the spectral flux measurement.

The total flux in the spectral measurement region is

$$F_{\text{Total}}^{\text{ON}} = F_{\text{Source}}^{\text{ON}} + F_{\text{LS}}^{\text{ON}} + F_{\text{Other}}^{\text{ON}}, \quad (2.17)$$

where  $F_{\text{Source}}^{\text{ON}}$  is the contribution from the source itself,  $F_{\text{LS}}^{\text{ON}}$  is the contribution from the large-scale emission model and  $F_{\text{Other}}^{\text{ON}}$  is the contribution from nearby sources and other, discarded Gaussian emission components.

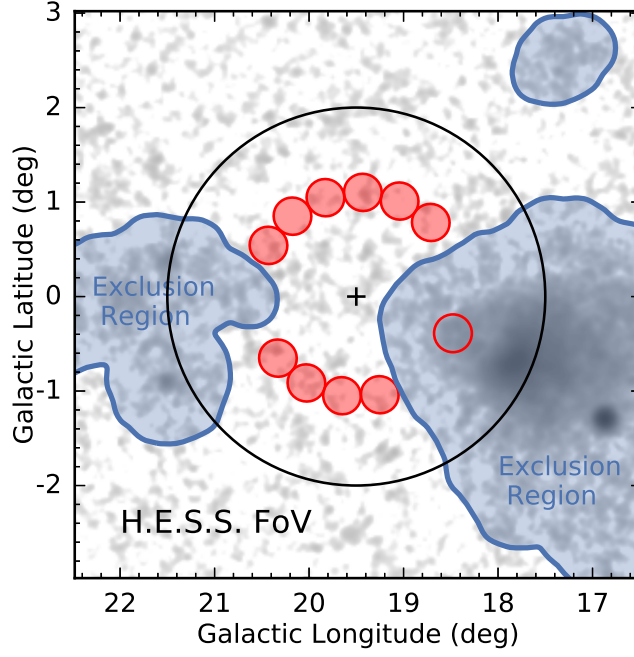


**Fig. 2.8.:** Illustration of reflected region background estimation for spectra (Sect. 2.3.7). The HGPS significance image is shown in inverse grayscale and exclusion regions as blue contours. The analysis FoV for one observation is shown as a black circle with  $2^\circ$  radius and a black cross at the observation pointing position. The non-filled red circle illustrates the ON region for spectral analysis, the filled red circles the OFF regions.

Assuming  $F_{\text{Source}}$  is the flux measurement from the morphology fit, we define the *correction factor* as

$$C_{\text{Correction}} = F_{\text{Source}}/F_{\text{Total}}^{\text{ON}}. \quad (2.18)$$

To summarize the contributions from the large-scale emission model and other sources in close (angular) proximity, we define a quantity called *contamination*. This quantity measures the fraction of flux within the spectral region that does not originate from the source itself:

$$C_{\text{Contamination}} = \frac{F_{\text{LS}}^{\text{ON}} + F_{\text{Other}}^{\text{ON}}}{F_{\text{Total}}^{\text{ON}}} \quad (2.19)$$

Additionally, we define the *containment* of a source as the ratio between the flux of the source within the spectral measurement region  $F_{\text{Source}}^{\text{ON}}$  (taking the morphology model into account) and the total flux obtained from the morphology fit  $F_{\text{Source}}$ :

$$C_{\text{Containment}} = F_{\text{Source}}^{\text{ON}}/F_{\text{Source}} \quad (2.20)$$

The catalog provides all of these quantities, which have been computed numerically from the morphology model. Spectral parameters of sources with significant contamination or modest containment are to be treated with caution.

## Spectral Model Fit

We performed the spectral fits on the *stacked*<sup>1</sup> observations, using the ON-OFF Poisson likelihood function, referred to as the  $W$  statistic (WSTAT) in XSPEC<sup>2</sup>. For each observation, we applied a *safe energy threshold* (see Sec. 2.2.5) cut at low energies, and the maximum energy was chosen at the highest event energy in the stacked counts spectrum for the on region (resulting in a maximum energy of 30 TeV to 90 TeV). Energy dispersion was taken into account not via a matrix, but in an approximate way where effective area is computed in such a way that it results in fully spectral results for power-law spectra with spectral index 2, and, given the good energy resolution of H.E.S.S., only small errors are made for other spectral shapes Hoppe (2008b).

To describe the spectral shape of the VHE gamma-ray emission, we fit a PL model to the data,

$$\phi(E) = \frac{dN}{dE} = \phi_0 \left( \frac{E}{E_0} \right)^{-\Gamma}, \quad (2.21)$$

where  $\phi_0$  is the differential flux at a reference (pivot) energy  $E_0$  and  $\Gamma$  is the spectral index. In addition, we also fit an exponential cut-off power-law (ECPL) model,

$$\phi(E) = \phi_0 \left( \frac{E}{E_0} \right)^{-\Gamma} \exp(-\lambda E) \quad (2.22)$$

which additionally contains the inverse cut-off energy  $\lambda = 1/E_{\text{cutoff}}$  as a third, free parameter. The reference (pivot) energy  $E_0$  is not a free parameter in both models; we compute it on a source-by-source basis to minimize the correlation between the other fit parameters. The source catalog provides the PL fit results for every source and the ECPL parameters where the ECPL model is more likely ( $TS = W_{\text{PL}} - W_{\text{ECPL}} > 9$ ).

We computed integral fluxes as

$$F(E_1, E_2) = \int_{E_1}^{E_2} \phi(E) dE, \quad (2.23)$$

usually for the energy band above 1 TeV, with integral flux errors computed using Gaussian error propagation. We computed energy fluxes for a given energy band as

$$G(E_1, E_2) = \int_{E_1}^{E_2} E \phi(E) dE. \quad (2.24)$$

---

<sup>1</sup>Observation stacking was performed as described here: <http://cxc.harvard.edu/ciao/download/doc/combine.pdf>

<sup>2</sup>See <https://heasarc.gsfc.nasa.gov/xanadu/xspec/manual/XSappendixStatistics.html> or Appendix A of Piron et al. (2001).

## Flux Points

Flux points are estimates of the differential flux  $\phi$  at given set of reference energies  $E_{ref}$ . To compute flux points for the HGPS catalog, we chose a method similar to the one used for the *Fermi*-LAT catalogs (see e.g. Sect. 5.3 in Acero et al., 2015). For every source we selected a total number of 6 bins  $(E_1, E_2)$  in reconstructed energy, logarithmically spaced between the *safe energy threshold* and a maximum energy of 50 TeV. The reference energy for the flux point estimation was set to the logarithmic bin center:  $E_{ref} = \sqrt{E_1 E_2}$ . The differential flux  $\phi$  was computed via a one-parameter likelihood fit (same method as described in Sect. 2.3.7), under the assumption of the global best-fit power-law and using only the data within the reconstructed energy bin  $(E_1, E_2)$ . An 1-sigma asymmetric error on  $\phi$  was computed from the likelihood profile, and for spectral points of small significance ( $TS < 1$ ), in addition an upper limit on  $\phi$  was computed at 95% confidence level. Finally, all fluxes were corrected for *containment* and *contamination* as described in Sect. 2.3.7.

## 2.3.8 Source Association

It is expected that most sources of Galactic gamma-ray emission are associated to stellar objects in late stages of their evolution, such as PSRs, PWNe and SNRs. To help identifying the physical origin of the gamma-ray emission we systematically associate the HGPS sources using catalogs of possible counterpart objects. For the association procedure we choose the following catalogs:

### Energetic Pulsars

For the association with highly energetic pulsars we used a subset of the ATNF (v1.54) pulsar catalog (Manchester et al., 2005). As millisecond pulsars are not expected to power VHE PWNe, we excluded those from the association process. To reduce the number of unlikely pulsar associations we selected only those with a spin-down energy flux of  $\dot{E}/d^2 > 10^{33} \text{ erg s}^{-1} \text{ kpc}^{-2}$  and to account for energetic pulsar with unknown distance we also selected pulsars a spin-down luminosity  $\dot{E} > 10^{34} \text{ erg s}^{-1}$ . After applying those selection cuts we were left with 352 objects within the HGPS region.

### Supernova Remnants and Pulsar Wind Nebulae

For the association with SNRs and PWNe we used the *SNRCat*<sup>3</sup> catalog (Ferrand and Safi-Harb, 2012). *SNRCat* is a database of Galactic supernova remnants observed at high energies. It is based on *Green's* catalog of Galactic radio SNRs (Green,

<sup>3</sup><http://www.physics.umanitoba.ca/snr/SNRCat>

2014) but also includes PWNe and composite (combined PWN and SNR) objects. For the association with HGPS sources we exclude the objects classified as PWNe solely based on observed VHE emission to avoid a *self association* with previous H.E.S.S. detections. For the association with HGPS sources we distinguished between three types of objects. The first type does not show evidence of nebular emission and belongs to the category of shell or filled-center sources in SNRCat (SNR). The second type is classified as PWNe or PWN candidate in SNRCat, because they do not show evidence for shell-like emission (PWN). The third type shows evidence for shell as well as nebular emission and we classify it as composite.

## High Energy Gamma-ray Sources

For the association with high energy GeV sources we used the second catalog of hard *Fermi*-LAT sources (2FHL, (Ackermann et al., 2016)). The catalog contains *Fermi*-LAT sources detected between 50 GeV and 2 TeV, an energy range partly overlapping with the HGPS analysis. In addition we also use the third catalog of *Fermi*-LAT point sources (3FGL, (Acero et al., 2015)). With its lower energy range of 0.1 GeV to 300 GeV it contains numerous high energetic pulsars, which might not be listed in the ATNF catalog.

For the automatic association with the counterpart catalog we choose a simple proximity criterion. We consider an object as associated if it is located within the spectral extraction region of the HGPS source (defined by a circle of radius  $R_{spec}$ , cf. Sect. 2.3.7) around the source position. The choice of this criterion is a trade off between reducing the number of spurious associations and accounting for the extension of the TeV source and the possibility that the VHE emission is offset from the e.g pulsar position.

### 2.3.9 Statistical False Detection Rate

To estimate the statistical false detection rate for a given TS threshold and understand its dependency on source size, we simulated survey counts maps and applied a simplified detection procedure to it. In total we created  $N = 100$  count maps by randomizing the HGPS background model map using Poisson statistics. Next we computed TS maps as described in Sect. 2.2.5 assuming a Gaussian source morphology and source sizes (Gaussian width) of  $\sigma = 0^\circ, 0.05^\circ, 0.1^\circ, 0.2^\circ$  and  $0.4^\circ$ . Sources were detected using a standard local peak detection algorithm<sup>4</sup> with a detection threshold of  $TS = 10$  and excluding nearby peaks within a radius of  $1 \sigma$  (Gaussian width) around the most significant pixel.

<sup>4</sup>[https://photutils.readthedocs.io/en/stable/api/photutils.detection.find\\_peaks.html](https://photutils.readthedocs.io/en/stable/api/photutils.detection.find_peaks.html)

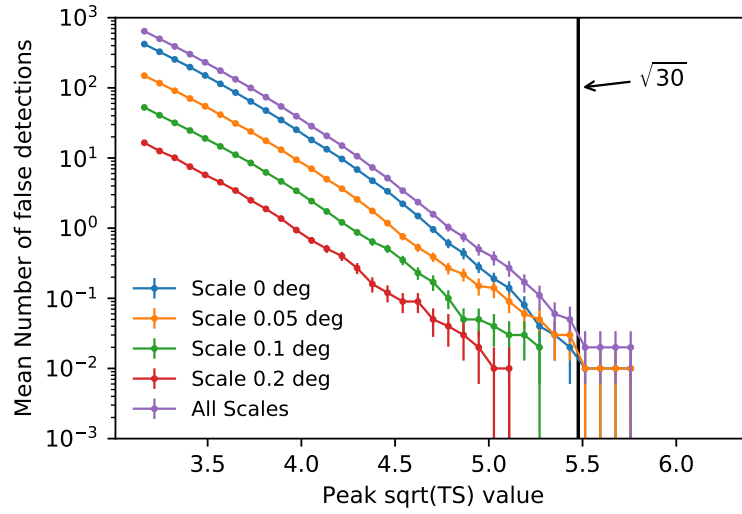


**Fig. 2.9.:** Mean number of false detections for different source sizes. The numbers are averaged over  $N = 100$  surveys, with the error bars representing the uncertainty of the mean, estimated from  $\bar{\sigma} = \sigma/\sqrt{N}$ . The detection threshold of  $\sqrt{TS} = \sqrt{30}$  used for the HGPS is marked with a black vertical line.

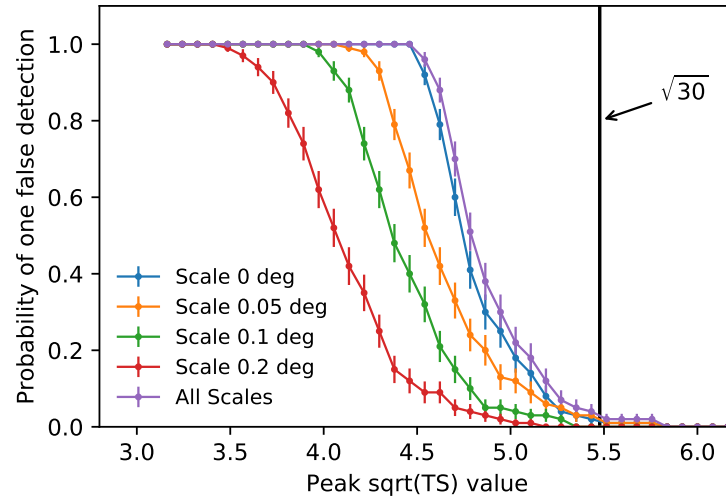


**Fig. 2.10.:** Probability of one false detection for different source sizes. The numbers are averaged over  $N = 100$  surveys, with the error bars representing the uncertainty of the mean, estimated from  $\bar{\sigma} = \sigma/\sqrt{N}$ . The detection threshold of  $\sqrt{TS} = \sqrt{30}$  used for the HGPS is marked with a black vertical line.

Figure 2.9 shows the mean number of expected false detections per survey for the different source sizes as well as for all sizes combined. For a threshold of  $\sqrt{TS} = \sqrt{30}$  we expect  $\sim 0.03$  false detections per survey (across all source sizes) just from statistical fluctuations of the background model. Going to lower detection thresholds this number rapidly increases with approximately ten times more false detections per  $\sqrt{TS} = 0.5$ . The total number of false detections is dominated by the false detection of point sources. This is expected because the correlation of pixels by using templates with larger source sizes effectively reduces the number of trials.

Figure 2.10 shows the probability of at least one false detection per survey for the different source sizes as well as for all sizes combined. For a threshold of  $\sqrt{TS} = \sqrt{30} \approx 5.5$  the probability of one false detection is  $\sim 0.03$ . With decreasing detection threshold it rapidly rises and reaches a probability of  $\sim 1$  for  $\sqrt{TS} < 4.5$ .

### 2.3.10 Method Discussion

The sensitivity profile and map shown in Fig. 2.2 were computed assuming a point-like source morphology and using the Li & Ma significance estimation. The likelihood fit method including the large-scale emission model component used for the catalog production fundamentally differs from that. The most important differences and their influence on the effective sensitivity, with which the catalog was produced, are qualitatively discussed below.

Sensitivity is defined as the minimum required flux for a source to be detected with a certain level of confidence. Assuming the source is extended, which applies to most of the Galactic sources found by H.E.S.S., the total flux of the source is distributed over a larger area on the sky. Given a fixed background level, the signal-to-noise ratio is decreased and the sensitivity scales with the size of the source as

$$F_{\min}(\sigma_{\text{source}}) \sim \sqrt{\sigma_{\text{source}}^2 + \sigma_{\text{PSF}}^2}, \quad (2.25)$$

where  $\sigma_{\text{source}}$  is the size of the source and  $\sigma_{\text{PSF}}$  the size of the PSF (Hinton and Hofmann, 2009). It is constant for sources smaller than the PSF and increases linearly with source size for sources larger than the PSF.

For small sources ( $< 0.3^\circ$ ) close to the Galactic plane, high levels of contamination (defined as in Eq. 2.19) from the large-scale emission model were observed. This effectively reduces the sensitivity close to the Galactic plane and even caused a few previously-detected H.E.S.S. sources to fall below the detection threshold chosen for the HGPS analysis. For sources far from the Galactic plane, however, the influence of the large-scale emission can be neglected.

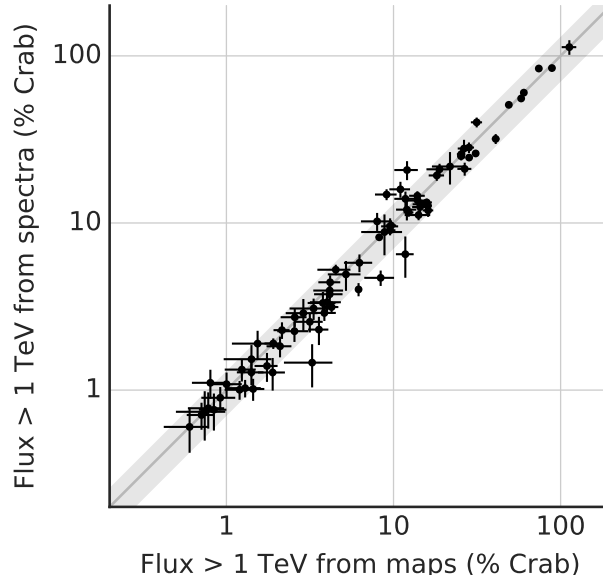


**Fig. 2.11.:** Comparison of integral source flux measurements above 1 TeV as calculated with two different methods. The flux estimate from maps is the total source flux according to the fitted morphology model, assuming a spectral index of  $\Gamma = 2.3$  (the `Flux_Map` column in the catalog). The flux estimate from spectra is the result of the spectrum extracted using aperture photometry and aperture correction (the `Flux_Spec_Int_1TeV` column in the catalog). The gray band in the background illustrates a systematic uncertainty of 30% on the flux values.

Systematic and statistical background uncertainties, neglected in this analysis, bias the sensitivity for large sources. Neglecting background fluctuations in the likelihood fit can lead to an overestimation of the significance of large sources. While technically this improves the sensitivity, it can lead to unreliable detections of large emission components. In addition, the adaptive ring method (Sect. 2.2.5), with a minimal inner ring radius of  $0.7^\circ$ , does not provide a reliable background estimate for very large structures in the data.

Systematic uncertainties of various origins affect the sources' spectral parameters. In addition to the transparency of the atmosphere, the calibration, and the event reconstruction (see Sect. 2.2.3), the analysis method itself can introduce uncertainties. In particular, the way the PSF is handled, the background model or the large-scale emission, and the assumed source morphology can all influence the flux and spectral index measurement. We estimate the systematic uncertainties of the flux extracted from the maps (Sect. 2.2.5) and from the spectrum (Sect. 2.3.7) to be 30%, for the spectral index (Sect. 2.3.7) we estimate an uncertainty of 0.2. These values are those from the previous HGPS publication (Aharonian et al., 2006f) and they are compatible with the scatter we find when comparing the main and the cross-check analysis. As expected for a population of extended sources in the Galactic plane, these values are slightly larger than the systematic uncertainties previously estimated for isolated point-like sources like the Crab Nebula (Aharonian et al., 2006e).

**Tab. 2.2.:** Results of the automatic association procedure for each catalog used (see main text for details and selections applied). The second column lists the numbers of objects in the HGPS survey region for each catalog. The third column gives the total number of associations found. The last column gives the number of HGPS sources having at least one associated object of a given category. The difference between the two last columns is only large for 3FGL because 3FGL is the only counterpart catalog for which the source density is so high that many HGPS sources are associated with multiple 3FGL sources. Out of the 78 HGPS sources, only 11 are left without any association.

Type	Number of objects in HGPS region	Number of associations	Number of HGPS sources with at least 1 association
2FHL sources	44	31	29
3FGL sources	352	64	40
Supernova remnants	211	24	21
Pulsar wind nebulae	29	16	16
Composite remnants	42	21	20
Energetic pulsars	222	47	42
Extra associations	–	20	–

A comparison of the two methods presented in this paper for calculating HGPS source integral flux ( $E > 1$  TeV) was performed as a diagnostic test. The resulting scatter plot (Fig. 2.11) compares the flux measurements obtained from the flux maps (Sect. 2.2.5), assuming  $\Gamma = 2.3$ , with those obtained from individual source spectral analyses (Sect. 2.3.7). The former is an aperture photometry method that is corrected for containment and contamination. The latter is calculated by fitting a power-law model to the gamma-ray excess in the spectral extraction region, then correcting for containment and contamination factors according to Eq. 2.18. When comparing fluxes for a given source, there may be minor deviations, often explained simply by spectral indices that differ from  $\Gamma = 2.3$ . However, one can see that these two methods agree very well with each other for the HGPS source population as a whole, well within the 30% systematic uncertainties.

## 2.4 Results

### 2.4.1 Source Associations and Identifications

Table 2.2 summarizes the results from the semi automatic association procedure. In total we find 352 3FGL sources in the HGPS region of which 64 are associated to a HGPS source. Of the 44 2FHL sources in the HGPS region we find 31 to be associated with an HGPS object. The high agreement is expected, because of the partly overlapping energy range of the 2FHL and HGPS catalogs. In total 13 2FHL source are not associated to a HGPS source, of which we find most to be located in HGPS regions of few exposure. Out of the 211 SNRs in the HGPS region, we find 24

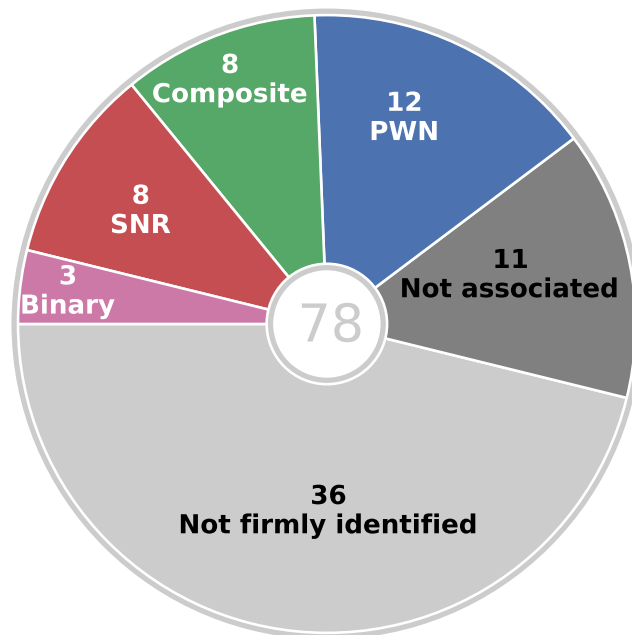


**Fig. 2.12.:** Source identification summary pie chart. The category *Not firmly identified* includes all sources with multiple associations, where no clear identification is possible. *Not associated* includes all sources without any associated MWL counterpart. Among those are 7 *dark* sources without any association at all and 4 sources with associations to GeV gamma-ray sources.

to be associated with 21 different HGPS sources. Among the 29 PWNe in the survey region 16 are associated with 16 HGPS objects. In addition half of the 42 composite objects are associated to an HGPS source. A sky map with all the HGPS sources and their associations labeled is shown in Figs. B.5 to B.8.

The firm identification of sources is based on additional information, such as morphology and variability of sources. The list of firmly identified HGPS sources is shown in Tab. 2.3. For every source the H.E.S.S. name, the identified object, the source class, the evidence of the identification and a reference is given. In total 31 of 78 sources can be identified.

Figure 2.12 shows the relative distribution of the identified as well as not firmly identified and not associated sources. With a percentage of 39% PWNe represent the largest fraction of identified sources, followed by SNRs (26%) and composite SNRs (26%). In addition there are also three (10%) identified gamma-ray binary systems. More than half (47 of 78) of the HGPS sources cannot be firmly identified yet or are not associated at all. However 36 of those 47 sources have potential spatial counterparts and can be identified in future with detailed studies. In total we find 11 HGPS sources neither associated to a PWN or SNR nor a high energetic pulsar. For 4 of those we still found a *Fermi-LAT* counterpart, but 7 sources remain *dark* without any association in other wavelengths at all.

**Tab. 2.3.:** Table of 31 firmly-identified objects among the HGPS sources. The object classes are gamma-ray binary, shell-type supernova remnant (SNR), pulsar wind nebula (PWN), and composite SNR (in cases where it is not possible to distinguish between the shell and interior nebula). The evidence used to identify the VHE gamma-ray emission include position, morphology, variability, and energy-dependent morphology (ED Morph.).

Source name	Identified object	Class	Evidence	Reference
HESS J1018–589 A	1FGL J1018.6–5856	Binary	Variability	2015a <sup>a</sup>
HESS J1302–638	PSR B1259–63	Binary	Variability	2005c <sup>b</sup>
HESS J1826–148	LS 5039	Binary	Variability	2006a <sup>b</sup>
HESS J0852–463	Vela Junior	SNR	Morphology	2005a <sup>b</sup>
HESS J1442–624	RCW 86	SNR	Morphology	2016c <sup>a</sup>
HESS J1534–571	G323.7–1.0	SNR	Morphology	2017a <sup>a</sup>
HESS J1713–397	RX J1713.7–3946	SNR	Morphology	2004c <sup>b</sup>
HESS J1718–374	G349.7+0.2	SNR	Position	2015b <sup>a</sup>
HESS J1731–347	G353.6–0.7	SNR	Morphology	2011a <sup>a</sup>
HESS J1801–233	W 28	SNR	Position	2008b <sup>b</sup>
HESS J1911+090	W 49B	SNR	Position	2016f <sup>a</sup>
HESS J0835–455	Vela X	PWN	Morphology	2006d <sup>b</sup>
HESS J1303–631	G304.10–0.24	PWN	ED Morph.	2012 <sup>a</sup>
HESS J1356–645	G309.92-2.51	PWN	Position	2011b <sup>a</sup>
HESS J1418–609	G313.32+0.13	PWN	Position	2006b <sup>b</sup>
HESS J1420–607	G313.54+0.23	PWN	Position	2006b <sup>b</sup>
HESS J1514–591	MSH 15–52	PWN	Morphology	2005b <sup>b</sup>
HESS J1554–550	G327.15–1.04	PWN	Morphology	
HESS J1747–281	G0.87+0.08	PWN	Morphology	2005e <sup>b</sup>
HESS J1818–154	G15.4+0.1	PWN	Morphology	2014 <sup>a</sup>
HESS J1825–137	G18.00–0.69	PWN	ED Morph.	2006c <sup>b</sup>
HESS J1837–069	G25.24-0.19	PWN	Morphology	2008 <sup>c</sup>
HESS J1849–000	G32.64+0.53	PWN	Position	
HESS J1119–614	G292.2–0.5	Composite	Position	
HESS J1640–465	G338.3–0.0	Composite	Position	2014b <sup>d</sup>
HESS J1714–385	CTB 37A	Composite	Position	2008a <sup>b</sup>
HESS J1813–178	G12.8–0.0	Composite	Position	2007 <sup>e</sup>
HESS J1833–105	G21.5–0.9	Composite	Position	
HESS J1834–087	W41	Composite	Morphology	2015d <sup>a</sup>
HESS J1846–029	G29.7–0.3	Composite	Position	
HESS J1930+186	G54.1+0.3	Composite	Position	2010 <sup>f</sup>

<sup>a</sup> H.E.S.S. Collaboration et al.    <sup>b</sup> Aharonian et al.    <sup>c</sup> Marandon et al.

<sup>d</sup> Abramowski et al.    <sup>e</sup> Funk et al.    <sup>f</sup> Acciari et al.

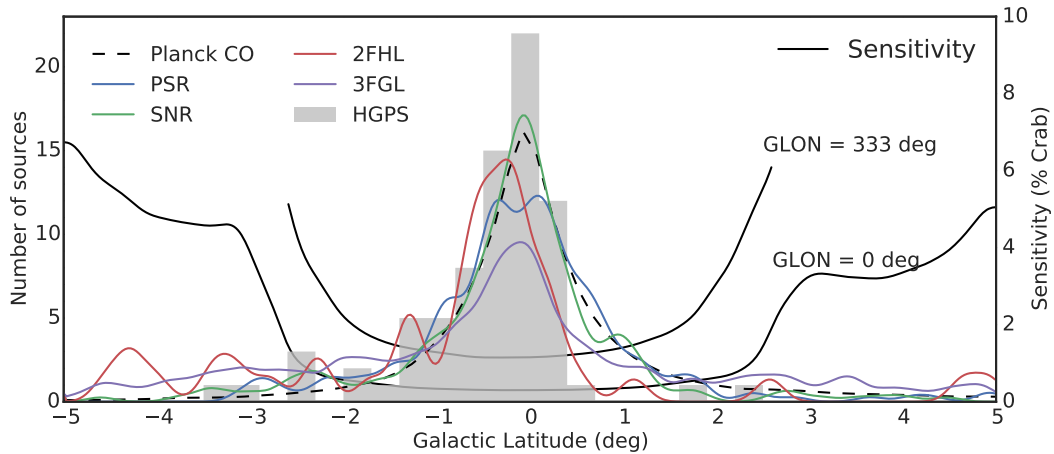


**Fig. 2.13.:** Galactic latitude distribution of the HGPS sources (gray histogram). The bin size of this histogram is  $0.3^\circ$ . The HGPS point source sensitivity is shown (in units of % Crab) at two different longitudes of  $0^\circ$  and  $333^\circ$ . For comparison, the pulsar (PSR), supernova remnant (SNR), 3FGL and 2FHL source distributions in the HGPS map region (including areas without HGPS exposure) are shown as overlaid curves, smoothed with Gaussians of width  $0.15^\circ$ . The dashed line shows *Planck* measurements of CO(1-0) line emission as an estimate for matter density in the Galaxy and similarly smoothed. All curves are normalized to the area of the histogram.

## 2.4.2 Longitude and Latitude Distribution

We can now investigate the global properties of the VHE gamma-ray sources in the HGPS catalog. We do this by producing distributions of various source parameters and also by comparing certain key source parameters against each other. We then briefly discuss the implications in the context of the Galactic VHE source population, survey sensitivity, and firmly-identified MWL source classes.

The latitude distribution of the 78 HGPS sources is shown in Fig. 2.13. The source distribution has a mean of  $b = -0.41^\circ$  and a standard deviation of  $0.87^\circ$ . The median value may be more representative of the center of the distribution since it is more robust to outliers; it is found at  $b = -0.20^\circ$  with a median absolute deviation of  $0.51^\circ$ . For visual comparison, the latitude distributions of the main classes of associated counterparts (Sect. 2.4.1) — SNRs, energetic pulsars, 3FGL sources and 2FHL sources — are shown on this figure. Also shown for reference is an estimate of the matter density profile as traced by *Planck* measurements of CO(1-0) line emission (Planck Collaboration et al., 2016). It should be kept in mind throughout this section that the HGPS sensitivity is not completely uniform as a function of longitude or latitude.

The HGPS latitude distribution of sources correlates well with both the tracers of matter density and potential counterparts. The distribution is somewhat skewed toward negative latitudes even though the HGPS sensitivity has a relatively wide and

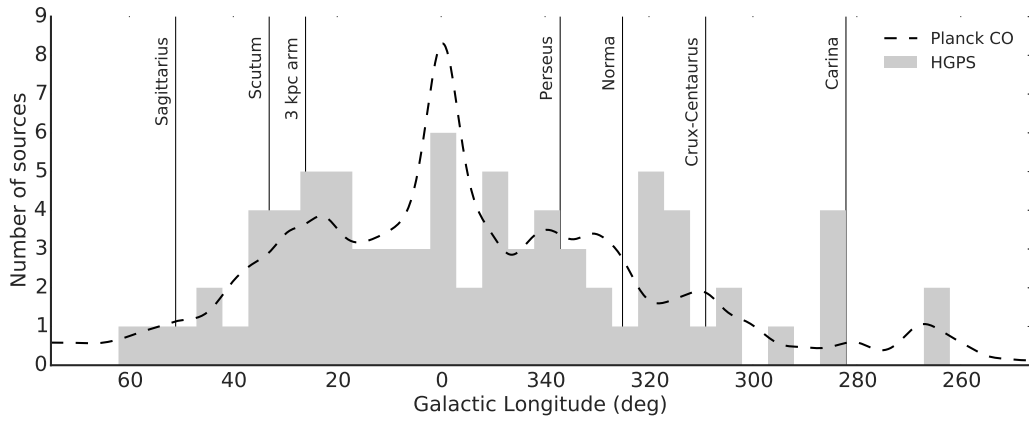


**Fig. 2.14.:** Galactic longitude distribution of the HGPS sources (gray histogram), together with the CO gas distribution. The bin size of this histogram is  $5^\circ$ . The dashed line shows the matter density as traced by *Planck* measurements of CO(1-0) line emission smoothed with a Gaussian of width  $1.5^\circ$ . The curve is normalized to the area of the histogram. Spiral arm tangent locations from Vallée, 2014 are shown.

flat coverage in latitude. In Fig. 2.13, the sensitivity is represented by two curves showing relatively good sensitivity (e.g. at  $\ell = 0^\circ$ ) and relatively poor sensitivity (e.g. at  $\ell = 333^\circ$ ). These curves demonstrate how the HGPS sensitivity coverage in latitude is, in general, much wider than the HGPS source distribution. Although there are local exceptions at some longitudes, the latitude coverage is generally complete in the range  $-2.0^\circ < b < 1.5^\circ$  and as good as  $-2.5^\circ < b < 2.5^\circ$  at various locations. However, the counterpart catalogs are known to suffer from various selection biases (especially SNRs and pulsars), and the Galactic disk itself is known to not be perfectly symmetric as observed across the spectrum.

In addition, one might still argue that, given the narrow range of latitudes observed with respect to surveys at other wavelengths, the HGPS sources may not be representative of the underlying distribution of VHE gamma-ray sources. However, in light of the counterpart distributions, in particular the 2FHL sources, it can be reasonably assumed that the non-uniform and relatively narrow sensitivity in latitude only has a weak effect on the observed source population distribution. Furthermore, the sensitivity of Cherenkov telescopes is known to decrease as the source size increases (see Eq. 2.25). Therefore, the HGPS is somewhat less sensitive to larger – and possibly closer — sources, resulting in a narrower observed Galactic latitude distribution than those of the parent populations (traced roughly by the chosen counterparts).

The longitude distribution of the 78 HGPS sources is shown in Fig. 2.14, together with the matter density profile as traced by CO(1-0) line emission (same as in the previous figure). The latter, measured by *Planck* (Planck Collaboration et al., 2016), has a uniform exposure (sensitivity) over the sky, unlike the HGPS, limiting what one could conclude based on potential correlations seen on this figure. Nonetheless, from

this figure, one can see that there is a very general correlation in longitude between the number of HGPS sources and the matter density and that the HGPS sources are mostly found in the inner  $\sim 60^\circ$  of the Galaxy. Additionally, the spiral arm tangents from CO tracers are shown (Vallée, 2014) in Fig. 2.14. Compared with Fig. 2.18, an increased number of sources could be expected in the directions of the near spiral arm tangents. In the longitude distribution, a slight excess of sources in the direction of *Scutum* and between *Norma* and *Crux-Centaurus* can be observed. However, due to the limited sample size of 1-6 sources per bin, no strong conclusion can be drawn.

The counterpart catalogs shown in the latitude distribution suffer from various, significant biases in longitude coverage (e.g. Green, 1991) and are not very meaningful to over-plot on the HGPS longitude distribution.

### 2.4.3 Flux and Size Distribution

We compare the HGPS source integral fluxes ( $E > 1$  TeV) to source sizes in panel A of Fig. 2.15 and show the distributions of fluxes and sizes separately in panel B and panel C, respectively. In the flux–size figure, we plot the approximate flux sensitivity limit of the HGPS as a function of source size. This sensitivity decreases as the source size increases, as expressed by Eq. 2.25. The HGPS sources indeed generally follow this trend; in particular, one can see that there are no sources in the upper left corner of Fig. 2.15. This demonstrates that the HGPS is complete with respect to relatively small and bright sources in the surveyed region.

The distribution of HGPS source integral fluxes ( $E > 1$  TeV), calculated assuming a spectral index of  $\Gamma = 2.3$ , is shown in panel B of Fig. 2.15. It is naturally expected that, at higher fluxes, the number of sources decreases. At the lowest fluxes, the number is small because the sensitivity limit of the HGPS has been reached.

As can be seen in panel C of Fig. 2.15 and despite the modest H.E.S.S. PSF ( $\sim 5'$ ), the majority of sources are not point-like but rather found to be significantly extended and as large as  $1^\circ$ . Due to the methods used for background subtraction (see Sect. 2.2.5), the HGPS is not sensitive to sources with larger sizes.

The firmly-identified HGPS sources (Sect. 2.4.1) are highlighted in Fig. 2.15. It can be seen that all identified binary systems are point-like sources in the HGPS, as expected. Identified PWNe are detected at all size scales, in agreement with the diversity observed in the VHE PWN population (H.E.S.S. Collaboration et al., 2017d). Identified SNRs all have sizes above  $\sim 0.17^\circ$ , likely because smaller SNRs are difficult to identify (e.g. based on shell-like morphology) due to the H.E.S.S. PSF. The identified composite SNRs, on the other hand, are typically smaller, owing to the difficulty in distinguishing VHE emission from the SNR shell or interior PWN,

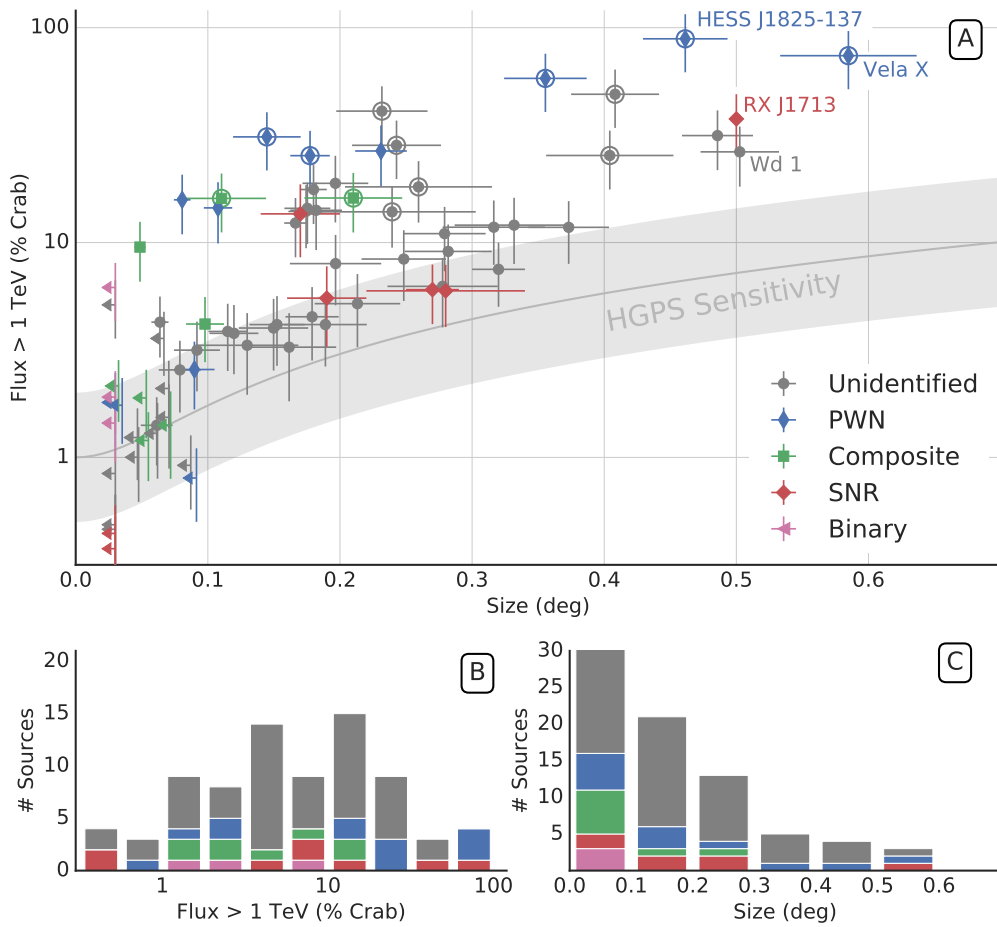


**Fig. 2.15.:** **Panel A:** Integral source flux ( $E > 1$  TeV) versus source size scatter plot, with colors representing the different classes of firmly-identified sources. For HGPS sources modeled as single Gaussians, the size is its width ( $\sigma$ ). For sources modeled as multiple Gaussians (indicated with a circle around the marker), the size is the RMS of the 2-dimensional intensity distribution. For sources with shell-like morphology (SNRs), the size is the outer shell radius. The SNR Vela Jr (HESS J0852–463) is not shown at size  $1^\circ$  and flux 103% Crab to improve visibility of the rest of the plot. The approximate sensitivity limit of the HGPS given in Eq. 2.25 is shown (see caveats in main text), with an assumed point-source sensitivity of 1% Crab and an uncertainty band with a factor  $\pm 2$  to represent the sensitivity variations in the survey region.

**Panel B:** Distribution of the HGPS sources' integral fluxes ( $E > 1$  TeV), with colors as in Panel A.

**Panel C:** Distribution of the HGPS source sizes, with colors as in Panel A. The first bin contains 30 sources, of which 17 are compatible with point-like sources according to Eq. 2.15.

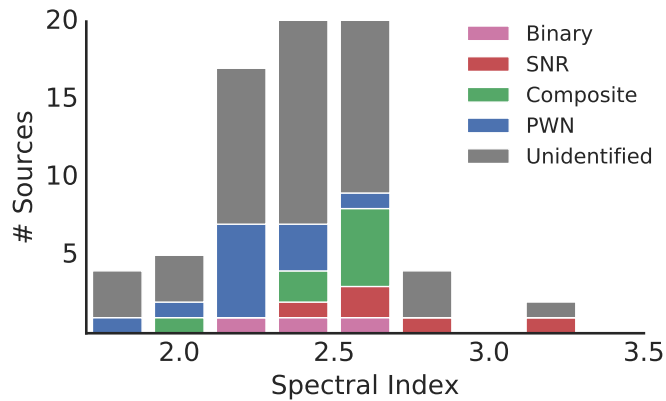


**Fig. 2.16.:** Distribution of the HGPS source spectral indices over the available energy ranges. The indices plotted are those from the PL model fits, also for sources best-fit by ECPL models, for consistency. Taking statistical and systematic uncertainties into account, all indices are compatible within  $2\sigma$  with the mean  $\Gamma = 2.4 \pm 0.3$  of the distribution.

similarly related to the H.E.S.S. PSF. In any case, it does not seem possible to identify the nature of the many unidentified sources on the sole basis of a source flux-size comparison.

Figure 2.16 shows the distribution of the HGPS source spectral indices  $\Gamma$ . The indices plotted are those that are a result of fitting a PL spectral model during individual HGPS spectral analyses (Sect. 2.3.7) and, for EXTERN sources (Sect. 2.3.1, the PL fit from the corresponding publication). For consistency, we plot the PL index also for sources whose spectra are best fit by ECPL models. The index distribution has a mean  $\Gamma = 2.4 \pm 0.3$ , not particularly hard (flat) or soft (steep). This is compatible with the index ( $\Gamma = 2.3$ ) adopted in the production of the HGPS flux maps (Sect. 2.2.5). Note that individual source indices have typical statistical uncertainties of order  $\pm 0.2$  and a similar systematic uncertainty; HGPS data are often not sufficient to precisely constrain the index because the energy range is only about one decade ( $1 < E < 10$  TeV). Finally, the figure also shows how the firmly-identified HGPS sources are distributed in index, showing no strong tendency with respect to source class.

#### 2.4.4 Log N - Log S Distribution

The cumulative  $\log N(> S) - \log S$  distribution of HGPS source integral fluxes ( $E > 1$  TeV, obtained from the maps) is shown in Fig. 2.17. The 78 HGPS sources span a range in flux from 0.6% Crab to 103% Crab, with 32 sources above 10% Crab. We performed an unbinned likelihood fit of a PL model to the  $\log N - \log S$  distribution (also shown in Fig. 2.17), using only the range  $S > 10\%$  Crab where we consider the HGPS survey mostly complete. The best fit value of the PL slope is  $-1.3 \pm 0.2$  (for the cumulative distribution) and the amplitude corresponds to

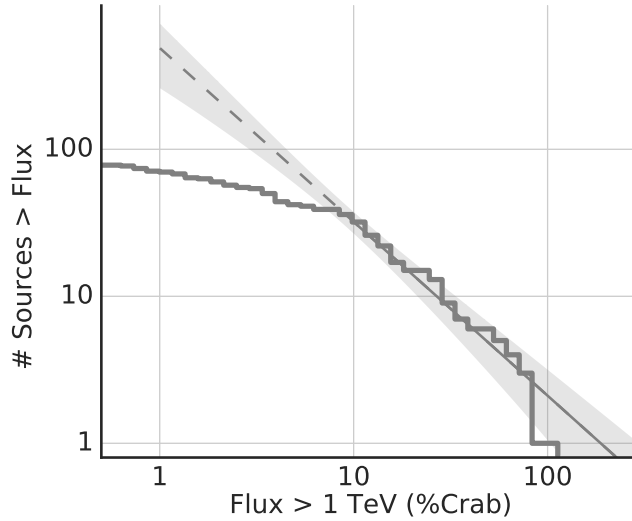


**Fig. 2.17.:** Number of HGPS sources  $N$  above a given flux threshold,  $\log N(> S)$ , as a function of flux threshold  $\log S$ , where  $S$  is the integral flux above 1 TeV in % Crab. A PL model fit (above 10% Crab flux threshold) is overlaid with shaded envelopes representing the statistical uncertainties of the best fit.

$32 \pm 5$  sources above 10% Crab. This slope is consistent with Galactic models where equal-luminosity sources are homogeneously distributed in a thin disk, which predict a slope of  $-1.0$ .<sup>5</sup>

The only robust statement that can be inferred from the  $\log N - \log S$  distribution of HGPS sources is that it provides a lower limit on the true  $\log N - \log S$  distribution, i.e. there are e.g. at least 70 sources above 1% Crab. If one assumes that  $\log N - \log S$  distributions are always concave (most “reasonable” spatial distributions and source luminosity functions encountered in the literature are), then the extrapolation of the PL fit shown in Fig. 2.17 sets an upper limit of  $\sim 600$  sources above 1% Crab, with a statistical error of a factor of 2.

More detailed analyses of the  $\log N - \log S$  distribution or of the flux-size distribution are possible in principle but in practice do not yield robust results because of the limited number of sources and the large uncertainties concerning the effective sensitivity achieved. The catalog creation procedure is complex (special treatment of known shell-type sources, large-scale emission model component, 15 discarded and several merged components; see Sect. 2.3.5), with the net effect that the sensitivity shown in Fig. 2.2 and also panel A of Fig. 2.15 is not reliably achieved, because those sensitivity estimates assume isolated sources, with no underlying large-scale emission or source confusion, and a detection threshold of  $5\sigma$ , whereas the component detection threshold of  $TS = 30$  corresponds to  $\sim 5.5\sigma$ .

<sup>5</sup>The flux  $S$  of a source scales with the distance  $d$  like  $S \propto L/d^2$ , where  $L$  is the intrinsic luminosity of the source. For a thin disc, we have  $N(> S) \propto d^2 \propto L/S$ , which corresponds to an slope of  $-1.0$  in the cumulative  $\log N - \log S$  distribution.

## 2.4.5 Distribution in the Milky Way and Survey Horizon

A representation of the Galaxy seen face-on is depicted in Fig. 2.18, in order to visualize how much of the Galaxy the HGPS has been able to probe at different sensitivity levels. Two limits are shown, illustrating the sensitivity detection limit (horizon) of the HGPS for potential point-like sources with presumed luminosity of  $10^{33}$  and  $10^{34}$  erg/s. Given the achieved sensitivity in the Galactic plane, it is clear that H.E.S.S. has only probed a small fraction of the Galaxy – just up to a median distance of 7.3 kpc for bright ( $10^{34}$  erg/s) sources. The horizon shown is for point-like sources; considering that sensitivity decreases with source size, this conclusion is even more true for extended sources. An instrument with an increased sensitivity like CTA will allow a more complete census of the Galaxy. Furthermore, this illustrative look at survey completeness strengthens the hypothesis that the large-scale emission described in Sect. 2.3.2 could be partly explained by a population of unresolved sources, presumed to be distant.

## 2.4.6 Comparison with Previous VHE Publications

In total, we re-analyzed 48 VHE gamma-ray sources that have been the subject of past H.E.S.S. publications. In this section we present a systematic comparison of the present HGPS results, with the latest published results, as summarized in *gamma-cat*<sup>6</sup>, the open TeV source catalog.

We associated HGPS sources with previous analyses simply by the name of the source, which was unique except for three cases: HESS J1800-240, HESS J1746-308 and HESS J1930+188. We excluded these sources from the systematic comparison in the first place.

To further identify the cases where we obtained significantly different results from previously published analyses, we compared the position, size, spectral index and flux of the remaining uniquely associated sources, taking statistical and systematic errors of the measurements into account. For each of these parameters, we estimated the total uncertainty  $\sigma_{\text{tot}}$  as the 1- $\sigma$  statistical and systematic uncertainties added in quadrature. We estimated this quantity for both the HGPS-derived source parameters as well as previously published H.E.S.S. values.

The systematic uncertainties on position and size are given in Sect. 2.3.6 and Sect. 2.3.6, respectively. Additionally, we assumed a systematic uncertainty  $\Delta\Gamma_{\text{syst}} = 0.2$  on the spectral index and 30% on the flux of the source, in agreement with

---

<sup>6</sup><https://github.com/gammapy/gamma-cat>, accessed July 24, 2017

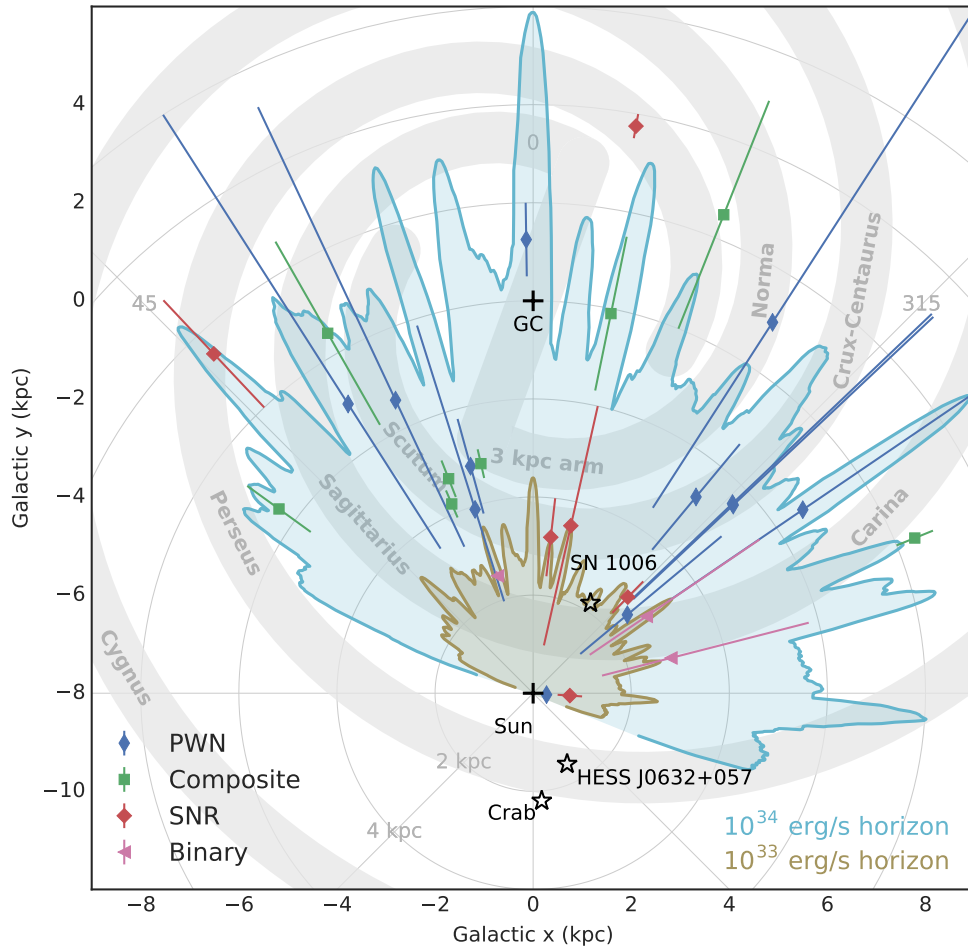


**Fig. 2.18.:** Illustration of the location of identified H.E.S.S. sources in the Galaxy with respect to HGPS completeness (sensitivity limits). This is a face-on view, with the spiral arms (Vallée, 2014) schematically drawn as gray bars. The HGPS horizons for source luminosities of  $10^{33}$  and  $10^{34}$  erg/s (for a putative  $5\text{-}\sigma$  detection of a point-like source, same as Fig. 2.2) are depicted by the light blue and light brown lines (and shaded regions therein), respectively. The source distances are from SNRcat (Ferrand and Safi-Harb, 2012) and ATNF pulsar catalog (Manchester et al., 2005). When no distance uncertainties were available, we applied a generic uncertainty of factor two on the distance. The three labeled sources are the Galactic gamma-ray sources outside the HGPS region detected by H.E.S.S.

previous estimates (Aharonian et al., 2006e). We then defined the criterion for significant outliers as

$$\Delta_{\text{HGPS-H.E.S.S.}} > 2\sqrt{\sigma_{\text{tot,HGPS}}^2 + \sigma_{\text{tot,H.E.S.S.}}^2} \quad (2.26)$$

where  $\Delta_{\text{HGPS-H.E.S.S.}}$  is the difference between the corresponding parameter values. When comparing the position we chose the angular separation as comparison parameter. We note that for many sources, the data sample used here is significantly different from the one used in the publication, hence the correlation of statistical errors is usually not too large.

For the vast majority of sources, we find that there is good agreement between the HGPS-derived position, morphology, and spectrum within the statistical and systematic uncertainties.

**Position** We found the position of 43 (out of 45) sources to be compatible with the previously published value, according to Eq. 2.26. For point-like sources we found an average shift of  $0.02 \pm 0.01$  deg, while for extended sources the value was  $0.06 \pm 0.05$  deg. Both values agree well with the expected scatter considering the statistical and systematic uncertainties on the measurements. As an additional check, we also verified that the positions of the identified gamma-ray binaries (known point sources) HESS J1826–148 and HESS J1302–638 are in good agreement (within  $40''$ ) with the reference positions of the corresponding objects LS 5039 and PSR B1259–63 as listed in SIMBAD<sup>7</sup>.

**Size** Comparing the sizes of the extended sources we found 30 (out of 35) sources to be compatible with the previously published value. The average size difference for the extended sources was in the order of  $\sim 18\%$ , the distribution of values having a width of  $\sim 40\%$ . This indicates that with the current analysis we measured slightly larger sizes of the sources on average, but the distribution is dominated by a large scatter. We expect the scatter to result mainly from differences in the analysis procedure. Previous analyses mainly fitted single Gaussian morphologies, while in this analysis we allowed for multiple Gaussian components. Further differences are the addition of the large scale emission model and the systematic modeling of emission from neighboring sources.

Previous publications found 7 sources to be compatible with a point-like source. In the current analysis we found all these sources to be compatible with a point-like source again. Additionally, we identified three cases that are compatible with a point-like source according to Eq. 2.15, which were previously found to be extended:

<sup>7</sup><http://simbad.u-strasbg.fr/simbad>

1. For HESS J1427–608 we measured a size of  $0.048 \pm 0.009^\circ$ , compared to  $0.063 \pm 0.010^\circ$  in Aharonian et al. (2008d). This source is an edge case which just meets our criterion for a point-like source.
2. For HESS J1714–385 we found a size of  $0.034 \pm 0.011^\circ$  compared to  $0.067 \pm 0.017^\circ$  in Aharonian et al. (2008a). With the current analysis, a smaller size was found because underlying emission was modeled by separate emission components (see Fig. 2.5).
3. We now measure the size of HESS J1808–204 to be  $0.058 \pm 0.014^\circ$  (consistent with point-like, in the definition of Eq. 2.15), compared to the previously measured size  $0.095 \pm 0.015^\circ$  (extended) (H.E.S.S. Collaboration et al., 2016d). This discrepancy is due to the HGPS’s inclusion of a large-scale emission component that now models gamma-ray excess previously accounted for in the source component itself.

**Flux** We found the flux of 42 (out of 45) sources to be compatible with the previous published value, according to Eq. 2.26.

The average difference in flux for extended sources was 3 % with a width of 43 % for the distribution of values. While the average value is compatible with previous analyses, we still found a large scatter (albeit compatible to the systematic and statistical errors) of the distribution.

A fair comparison between flux values obtained with the current method and earlier analyses proved to be difficult again because of fundamental differences between the methods used. In previous publications, aperture photometry was mostly used, while in this analysis the main flux measurement was based on a model fit, taking the PSF and morphology of the source and large-scale emission into account. Flux estimate differences with these two methods are shown in Fig. 2.11 (both measures from the HGPS analysis, not with respect to previous publications). Many of the differences in spectra and fluxes measured in the HGPS analysis and previous publications are the result of changes in the spectral extraction region (position and size).

**Spectral index** For all sources we found the spectral power law indices to be compatible with the previously published values. The mean difference in spectral index was 0.04 with a width of 0.23 for the distribution. This is well compatible with the expected scatter taking statistical and systematic uncertainties of the measured spectral indices into account.

# The H.E.S.S. Galactic Plane Survey compared to *Fermi*-LAT Observations

” *There are two possible outcomes: if the result confirms the hypothesis, then you’ve made a measurement. If the result is contrary to the hypothesis, then you’ve made a discovery.*

— Enrico Fermi

## Contents

---

3.1	Introduction . . . . .	62
3.1.1	Literature Overview . . . . .	62
3.1.2	GeV Milky Way and HGPS Region . . . . .	63
3.2	<i>Fermi</i> -LAT Instrument and Datasets . . . . .	64
3.2.1	Instrument . . . . .	64
3.2.2	Event Selection and PSF . . . . .	64
3.2.3	Diffuse Emission Model . . . . .	67
3.2.4	3FHL Catalog . . . . .	68
3.2.5	Sky Maps . . . . .	70
3.3	Analysis Methods . . . . .	72
3.3.1	RGB Flux Images . . . . .	72
3.3.2	Longitude and Latitude Flux Profiles . . . . .	74
3.3.3	Spectral Flux Points . . . . .	75
3.4	Results . . . . .	76
3.4.1	Survey RGB Images . . . . .	76
3.4.2	Survey Longitude Flux Profiles . . . . .	79
3.4.3	Survey Latitude Flux Profiles . . . . .	81
3.4.4	Source Associations . . . . .	82
3.4.5	GeV Source Candidates . . . . .	83
3.4.6	Shell-Type SNR Candidates . . . . .	86
3.4.7	Examples of Typical Source Classes . . . . .	88

---

## 3.1 Introduction

The energy range of HGPS dataset is not wide enough to measure and constrain the broadband features of typical SEDs of gamma-ray-sources. In individual cases it is possible to measure a spectral cut-off at high energies, but to determine e.g. the emission peak in IC spectra or to distinguish leptonic from hadronic origin of the gamma-rays, the TeV data must be extended by measurements of the *Fermi-LAT* instrument at lower GeV energies. The almost homogeneous HGPS dataset and the availability of >6 years of high-energy *Fermi-LAT* data now allow for a systematic study of the Galactic gamma-ray source population as a whole and further explore the connection between their GeV and TeV gamma-ray emission.

This chapter compares the results from the HGPS analysis presented in Chapter 2 with observations from the *Fermi-LAT* instrument in the high-energy GeV regime between 10 GeV and 2 TeV. The goal is to systematically study the physical and observational connection or non-connection between the sources detected in the GeV and TeV energy range.

### 3.1.1 Literature Overview

*The GeV-TeV connection in Galactic gamma-ray sources* has already been studied systematically by Funk et al. (2008). Based on the 3rd EGRET source catalog (between 100 MeV and 10 GeV) and the 22 sources detected by the H.E.S.S. Galactic plane survey up to this time, the authors investigated the spatial and spectral compatibility of those sources. Within the 99% positional confidence region of the EGRET sources they only found few (<10) TeV objects and argued that the correspondences they found, likely happened by chance. They also found that a simple power-law extrapolation of the spectra of EGRET sources was incompatible with flux ULs measured by H.E.S.S.. Based on those findings the authors concluded that most EGRET spectra likely cut off in the unexplored region below 100 GeV, indicating different source populations in the GeV and TeV regime.

*A systematic search for VHE counterparts of Galactic Fermi-LAT bright sources and MeV to TeV spectral characterization* has been carried out by Tam et al. (2010). Based on the first *Fermi-LAT* bright source list and  $\sim 50$  VHE gamma-ray sources known up to this time, they studied the spatial and spectral compatibility of those sources. In contrast to Funk et al. (2008) they found much more spatially coincident objects, but again concluded that a single spectral component could not describe the global MeV to TeV spectrum. They suggested that a gamma-ray pulsar, with a spectrum that cuts off at a few tens GeV, accompanied by a VHE gamma-ray emitting nebula could be a common scenario to explain this discrepancy.

*Constraints on the Galactic Population of TeV Pulsar Wind Nebulae Using Fermi-LAT Observations* were presented by Acero et al. (2013). The authors used 45 months of *Fermi*-LAT data above 10 GeV to systematically analyze the regions around the position of 58 TeV sources. In total they detected 30 of those sources and derived flux upper limits for the remaining 28. Of the 30 detected sources they concluded 9 may be due to pulsar emission above 10 GeV, 11 are PWN candidates, 7 cannot be clearly associated to a PWN and 3 are clearly identified PWNe. They found 8 of the sources to be extended.

*A search for extended GeV sources in the Galactic plane* was presented in Ackermann et al. (2017). The authors detected 46 extended GeV gamma-ray sources using 6 years of *Fermi*-LAT data above 10 GeV. On average those sources showed hard spectra, with 70% of the sources having an index harder than 2.2 and even 40% harder than 2.0. The authors concluded this implies high-energy SED peaks in the TeV band. They also found 7 SNRs and one star forming region detected with the *Fermi*-LAT were undetected at TeV energies.

### 3.1.2 GeV Milky Way and HGPS Region

Figure 3.1 illustrates the HGPS region in the context of a *Fermi*-LAT all-sky counts image above 10 GeV. The Milky Way is the most prominent feature on the GeV gamma-ray sky and primarily appears as a narrow strip of bright GeV gamma-ray emission concentrated along the Galactic equator. The emission is more compact in the inner part and widens towards the outer part of the Galaxy. The giant, but weaker structure of the *Fermi Bubbles* (Su et al., 2010) originates from the Galactic center and extends over large parts of the sky above and below the Galactic plane. Their spectrum shows a hard spectral index of  $\sim 1.9$  and seems to cut off at  $\sim 110$  GeV (Ackermann et al., 2014).

The emission in the Galactic plane is composed of a population of distinct gamma-ray sources and interstellar diffuse emission. The diffuse emission above 10 GeV results from the decay of pions, that are produced in collisions of cosmic rays with the interstellar medium, IC interactions of cosmic ray electrons with interstellar radiation fields and a population of unresolved gamma-ray sources. The population of distinct gamma-ray sources dominates at higher (TeV) energies, while the diffuse emission is more prominent at lower energies.

The markers show the positions of galactic identified GeV sources, distinguished by source class. As the *Fermi*-LAT is an all-sky survey instrument, the spatial distribution of those sources is not as much affected by observational selection effects as HGPS observations (cf. Fig. 2.1). The vast majority of the sources can

be found within the region covered by the HGPS. The sources outside are mainly pulsars, including only a few SNR and PWN objects.

The middle panel of Fig. 3.1 shows the flux measured by the *Fermi*-LAT between 10 GeV and 2 TeV in the region covered by the HGPS. The contribution from the Galactic diffuse emission is subtracted. For comparison the lower panel shows the flux measured by the HGPS above 1 TeV. The global structure of the emission in both measurements is very similar and mostly reflects the distribution of bright gamma-ray sources in the Galaxy. In the HGPS as well as the 3FHL catalog the upper 20% of the brightest sources contribute more than 70% of the total source flux (not including diffuse emission) in the HGPS region.

## 3.2 *Fermi*-LAT Instrument and Datasets

### 3.2.1 Instrument

The Large Area Telescope (LAT) is the main instrument on board of the *Fermi* Gamma-Ray Space Telescope satellite. It is an imaging, wide field-of-view high energy gamma-ray telescope, which covers an energy range of 20 MeV to more than 300 GeV. The *Fermi*-LAT is a pair-conversion telescope, composed of a precision tracker module to detect and reconstruct the direction of incoming gamma-rays and a calorimeter module to measure their energy. The tracker as well calorimeter are surrounded by an anticoincidence shield to veto events not caused by gamma-rays. A more detailed description of the instrument can be found in Atwood et al. (2009). The in-flight performance of the telescope is evaluated in Ackermann et al. (2012).

### 3.2.2 Event Selection and PSF

In addition to the information given in the 3FHL catalog we use the same 84 months (August 4th 2008 - August 2nd 2015) *Fermi*-LAT dataset to produce high energy images and measure GeV flux points and ULs for all HGPS sources. Identically to the 3FHL analysis we choose P8\_PHOTON\_V6 photons in the energy range between 10 GeV and 2 TeV. To limit the contamination by earth limb photons we apply a zenith angle cut of  $\theta = 105$  deg and also use the recommended data quality cuts (DATA\_QUAL) == 1 && (LAT\_CONFIG) == 1. The dataset was prepared using the *Fermi*-LAT science tools<sup>1</sup> version *v10r0p5* and P8R2\_SOURCE\_V6 instrument response functions. The full dataset including a detailed description of the data selection

---

<sup>1</sup><https://fermi.gsfc.nasa.gov/ssc/data/analysis/documentation/>

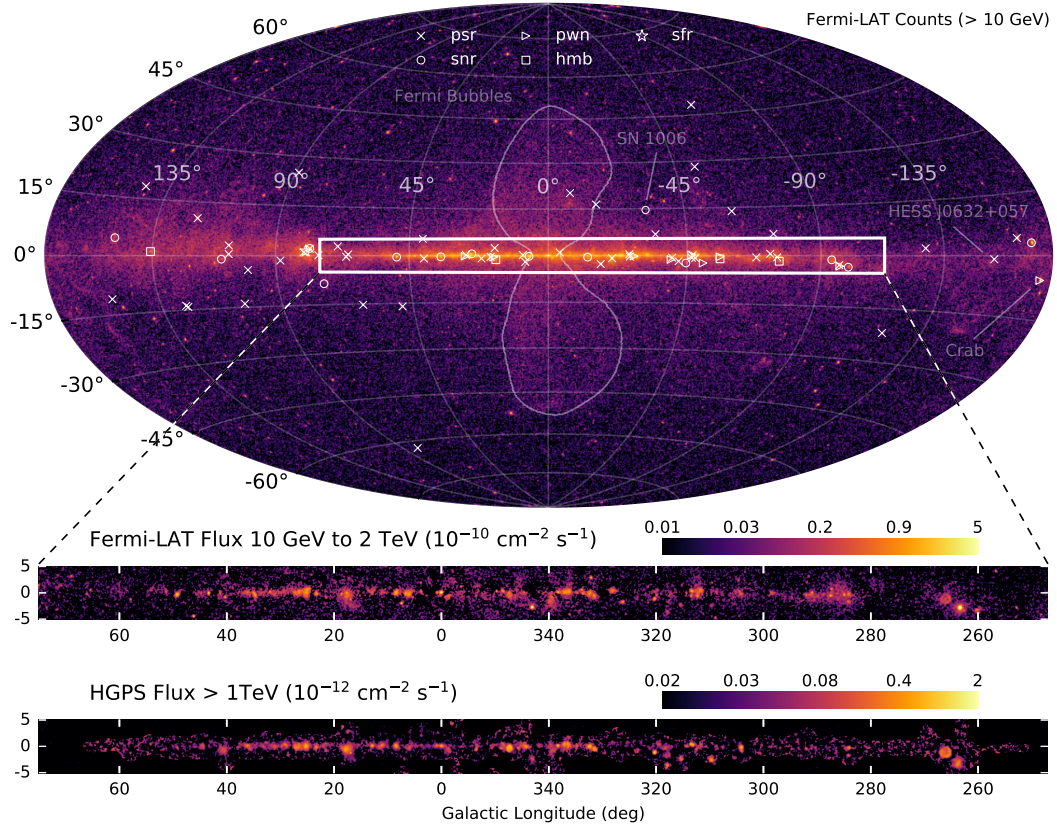


**Fig. 3.1.:** The HGPS region (white box) illustrated on top of an all-sky image of *Fermi*-LAT counts data above 10 GeV. The image is shown in Galactic coordinates, using Hammer-Aitoff projection. The white markers illustrate the positions of identified, Galactic 3FHL catalog sources (Ajello et al., 2017), distinguished by source class. The source classes are: pulsars (psr), pulsar wind nebulae (pwn), supernova remnants (snr), high mass binaries (hmb) and star forming regions (sfr). Three sources detected by H.E.S.S. are outside the HGPS region. Two of them are not listed in the 3FHL catalog, but have been recently detected in the GeV range: *SN 1006* (Condon et al., 2017) and HESS J0632+057 (Li et al., 2017). The middle panel shows the background subtracted gamma-ray flux image between 10 GeV and 2 TeV measured by the *Fermi*-LAT in Galactic coordinates. The lower panel shows the background subtracted gamma-ray flux image above 1 TeV measured by the HGPS also in Galactic coordinates. The image is only filled where the point-source sensitivity for a  $5\sigma$  detection (cf. Fig. 2.2) is better (lower) than 2.5% Crab. All images are smoothed with a Gaussian of width  $0.2^\circ$ .

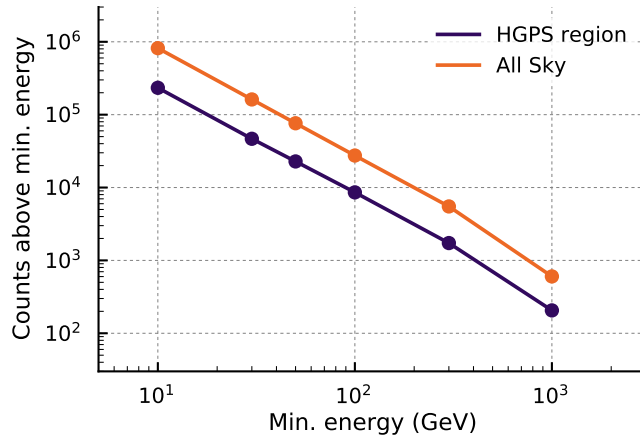


**Fig. 3.2.:** Number of counts measured by *Fermi*-LAT above given energy thresholds. The orange line shows the number of counts for the total sky and the blue line the number of counts within the HGPS region.

parameters and configuration files is available online in the public *Gammapy Fermi-LAT Data Repository*<sup>2</sup>.

Figure 3.2 shows the resulting number of gamma-ray events measured above various minimum energies for the whole sky as well as the subset of events in the HGPS region. While the HGPS region only covers 4% of the area of the whole sky it still contains  $\sim 30\%$  of all measured gamma-ray events. This again identifies the galactic plane as the brightest feature on the GeV gamma-ray sky. On close inspection we can see that this fraction even slightly increases towards higher energies, indicating that the emission from the galactic plane is harder on average compared to the extragalactic sky. The total number of events above 10 GeV in the region surveyed by the HGPS is  $\sim 200,000$ , which corresponds to  $\sim 100$  events/deg<sup>2</sup>. With increasing energy threshold the number of events drops with a PL behavior with an index of  $\Gamma \sim 1.5$ . Above 1 TeV the total number of events in the HGPS region is only  $\sim 2000$ , which corresponds to  $\sim 1$  event/deg<sup>2</sup>.

Figure 3.3 shows the variation of the width of the *Fermi*-LAT PSF with energy, where the width is measured by the 68%, 90% and 95% containment radii ( $R_{68}$ ,  $R_{90}$  and  $R_{95}$ ). The best angular resolution is achieved at the highest energies above 1 TeV, slowly worsens towards 100 GeV and rapidly worsens below 30 GeV. For all containment fractions the width of the PSF at 10 GeV is a factor of  $\sim 2 - 3$  higher compared to the width at 1 TeV. The ratio between  $R_{68}$  and  $R_{95}$  is in the order of  $\sim 4$ , which shows that the shape of the *Fermi*-LAT PSF features strong tails. The ratio between  $R_{68}$ ,  $R_{90}$  and  $R_{95}$  is approximately constant across the whole energy range. This indicates the shape of the PSF does not vary significantly with energy.

<sup>2</sup><https://github.com/gammapy/gammapy-fermi-lat-data>

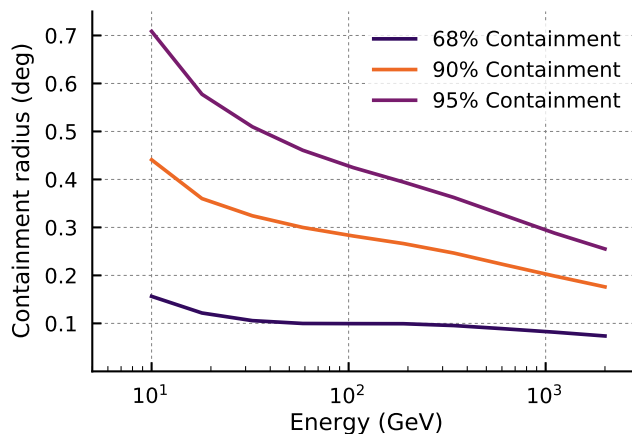


**Fig. 3.3.:** Variation of the containment radius of the *Fermi*-LAT PSF with energy for three different containment fractions.

For the energy range between 10 GeV and 2 TeV the energy resolution of the *Fermi*-LAT instrument varies between  $\Delta E/E \approx 0.05$  and  $\Delta E/E \approx 0.3$ <sup>3</sup>. The energy bins used for the spectral measurements in this analysis are typically much wider with  $\Delta E/E > 1$ . For this reason the effect of the energy resolution on all measurements in this work is neglected.

The lower energy threshold of 10 GeV represents a good compromise between sufficient signal statistics and obtaining good angular resolution to limit the problem of source confusion.

### 3.2.3 Diffuse Emission Model

For the *Fermi*-LAT instrument the dominating source of background for source analyses is true interstellar Galactic diffuse emission and an isotropic component from unresolved extragalactic sources as well as a small fraction of false classified cosmic ray events. For the analysis of small ( $< 2^\circ$ ) sources the *Fermi*-LAT collaboration provides a three dimensional  $(\ell, b, E)$  background model. The model predicts the expected Galactic diffuse gamma-ray emission from  $\pi^0$ -decay, based on templates derived from gas maps of the Galaxy. It includes contributions from atomic, molecular and ionized hydrogen and a dark neutral medium. The contribution from diffuse IC emission is modeled with the cosmic ray propagation code GALPROP<sup>4</sup>. The development of the model is described in detail in (Acero et al., 2016).

<sup>3</sup>[http://www.slac.stanford.edu/exp/glast/groups/canda/lat\\_Performance.htm](http://www.slac.stanford.edu/exp/glast/groups/canda/lat_Performance.htm)

<sup>4</sup><https://galprop.stanford.edu/>

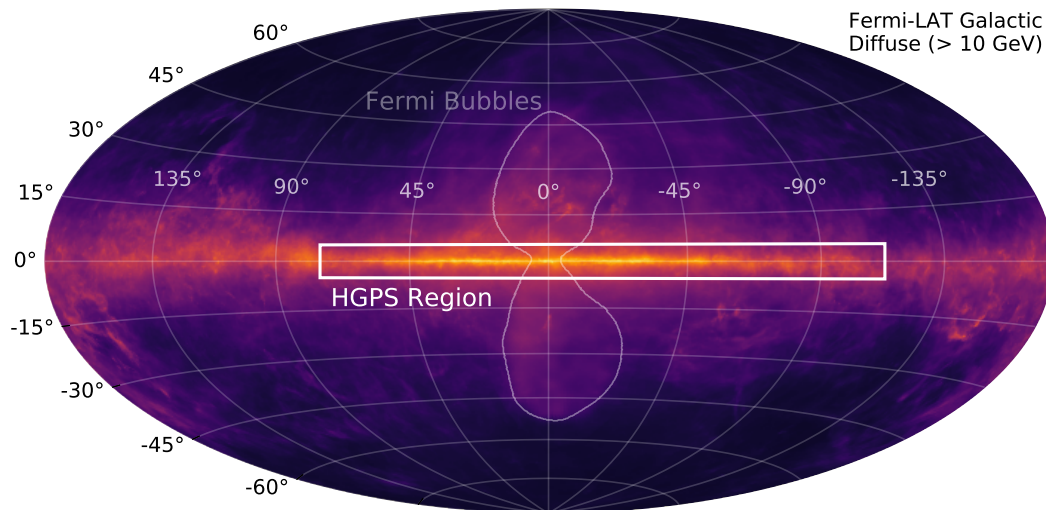


**Fig. 3.4.:** All-sky image of *Fermi*-LAT Galactic diffuse model above 10 GeV. The HGPS region is illustrated on top as a white box. The contour of the *Fermi Bubbles* is outlined with the transparent white line.

For the present analysis use the Galactic diffuse model version `gll_iem_v06.fits` as well as the isotropic extragalactic background model `iso_P8R2_SOURCE_V6_v06.txt`, both provided by the *Fermi*-LAT collaboration<sup>5</sup>.

Figure 3.4 illustrates the HGPS analysis region on top of the *Fermi*-LAT Galactic diffuse emission model above 10 GeV. The model shows enhanced emission in the central part of the Galaxy, which is covered by the HGPS. This reduces the sensitivity of any *Fermi*-LAT analysis in this region. We consider the uncertainties associated with the background model as the main source of systematic errors in the following analysis. The distribution of background flux normalization parameters in the 3FHL analysis (cf. Fig. 19 in Ajello et al. (2017)) suggests the model is underestimated by 10%-20% for most part of the Galactic Plane. The largest corrections are observed in the region between  $\ell = 310^\circ$  and  $\ell = 270^\circ$  where the norm of the background model is underestimated by 50%.

### 3.2.4 3FHL Catalog

The *Fermi*-LAT collaboration releases catalogs on a regular basis. Starting with a first list of the 205 brightest sources, presented in Abdo et al. (2009), the collaboration successively improved the reconstruction and high-level analysis methods and released updated catalogs with increasing observation time. The current source detection and classification procedure is described in detail in Acero et al. (2015) and will be shortly summarized in the following section.

<sup>5</sup><https://fermi.gsfc.nasa.gov/ssc/data/access/lat/>

The whole sky is divided into circular regions of interests (ROI) with varying radius between  $2.5^\circ$  to  $8.9^\circ$  and the gamma-ray emission in every ROI is modeled with a combined spatial and spectral model using a Poisson maximum likelihood fit. Morphology of extended sources is modeled by either generic templates, such as disk or Gaussian shapes, or using spatial templates derived from measurements in other wavebands, e.g. from X-ray or TeV observations. Spectra are modeled with parametric models such as PL, exponential cut-off PL and log parabola.

To test for new detections the best fit model for each ROI is extended by sources from seed catalogs, created with a wavelet detection algorithm and sources from previous *Fermi*-LAT catalogs. If a tested source reaches a threshold of  $TS = 25$ , the source is kept in the model. Except for the lower detection threshold this is equivalent to the HGPS detection criterion defined in Eq. 2.8.

For every source a set of flux points is estimated. Therefore the source spectrum is approximated by a local PL in a selected energy range and the amplitude of the model is varied to fit the observed counts in this energy range. The best fit model is evaluated at the log-center energy as an estimate of the mean flux in this energy band. Flux error and ULs are estimated from the likelihood profile as described in Sec. 1.4.2.

An automatic association of sources with objects from MWL catalogs is done with a Bayesian likelihood method. Trading the positional coincidence of possible counterparts against the expected number of chance coincidences a total association likelihood is estimated. Objects are considered as associated if this likelihood exceeds 80%. For association with pulsars the ATNF catalog is used, for SNRs the Greens catalog, for TeV sources TeVCat and for PWN a *Fermi*-LAT collaboration internal catalog.

Firm identifications of sources are based on additional information such as periodic variability for PSRs, spatial morphology for PWNe and SNRs or correlated variability of sources for binary objects.

The third catalog of hard *Fermi*-LAT sources (3FHL) is based on 84 month of *Pass 8 Fermi*-LAT data and contains spectral and morphological parameters for 1558 sources in the energy range between 10 GeV and 2 TeV (Ajello et al., 2017). The spatial models for extended sources are adopted from a dedicated study of *Fermi*-LAT Galactic extended sources, presented in Ackermann et al. (2017). The spectrum of the sources is modeled by a PL or, if significantly curved, by a log-parabola.

Of the total 1558 sources, 146 fall in the region surveyed by the H.E.S.S. telescopes. A more detailed classification of those sources is summarized in Tab. 3.1. Within the HGPS region there are 27 identified pulsars, 8 supernova remnants, 8 pulsar

**Tab. 3.1.:** Summary table of identified and associated galactic *Fermi*-LAT 3FHL sources. The numbers are given for all sources and the subset of sources, that lie in the region covered by the HGPS. Pulsars are identified (PSR) by pulsations, associations (*psr*) are concluded from spatial coincidence with objects from the ATNF pulsar catalog. The class *spp* indicates potential association with SNR or PWN. The class *unknown* denotes objects with associated ROSAT X-ray counterparts, but unknown origin of the gamma-ray emission.

Description	Identified			Associated		
	Class	$N_{\text{HGPS}}$	$N$	Class	$N_{\text{HGPS}}$	$N$
Total		46	138		52	1218
Extragalactic		–	54		18	1173
Galactic		46	84		34	45
Pulsar	PSR	27	58	psr	5	7
Pulsar Wind Nebula	PWN	8	8	pwn	5	6
Supernova Remnant	SNR	8	13	snr	14	19
SNR / PWN		–	–	spp	8	9
High-mass Binary	HMB	2	3	hmb	–	1
Binary	BIN	1	1		–	–
Globular Cluster		–	–	glc	1	2
Star-forming Region	SFR	–	1	sfr	1	1
Unclassified		–	–	unknown	2	24
Unassociated		–	–		46	178

wind nebulae, two high mass binary and one binary object. Most of the remaining sources are potentially associated to SNRs, PWN or pulsars. Two objects have only a X-ray counterpart, but the origin of the X-ray as well as gamma-ray emission is *unknown*. Approximately one third of the sources in the HGPS region remains *unassociated* to known objects. Some fraction of those sources might be false detections or *dark* sources, but another fraction is potentially associated to new objects in the HGPS catalog.

The 3FHL catalog is a complete superset of the previous catalogs 1FHL and 2FHL, with one exception in the HGPS region: the source 2FHL J1505.1-5808 is not listed in the 3FHL catalog any more.

### 3.2.5 Sky Maps

To systematically compare the observations of the Galactic plane by both instruments, we generate sky maps from the high energy *Fermi*-LAT data for the same region as surveyed by the H.E.S.S. telescope array (see Fig. 3.1). Starting from the basic dataset prepared with the *Fermi*-LAT science tools described in the previous section, we define an energy band by choosing  $E_{\min}$  and  $E_{\max}$ .

**Tab. 3.2.:** Energy ranges and number statistics of the event based *Fermi*-LAT images used in this work. *Counts* is the number of observed events, *Bkg.* the expected number of events from the galactic and isotropic diffuse background model (cf. Eq. 3.1) and *Excess* the difference between *Bkg.* and *Counts*. The first column indicates the mapping of the energy ranges to the *Red* (R), *Green* (G) and *Blue* (B) color channels of the RGB images described in Sect. 3.3.1.

Color	$E_{Min}$ GeV	$E_{Max}$ GeV	Counts ph	Counts Mean ph / deg <sup>2</sup>	Bkg. Total ph	Bkg. Mean ph / deg <sup>2</sup>	Excess ph
R	10	30	159,706	85.0	129,258	68.8	30,447
G	30	100	32,502	17.3	24,204	12.9	8,297
B	100	2000	7,386	3.9	5,854	3.1	1,531
	10	20	128,815	68.5	105,368	56.0	23,446
	20	50	51,245	27.3	39,953	21.3	11,291
	50	150	15,456	8.2	11,246	6.0	4,209
	150	500	3,387	1.8	2,787	1.5	599
	500	2000	691	0.4	708	0.4	-17

The counts map  $C_C$  is computed by selecting the subset of events from the total event list within the given energy range and by histogramming the events in a map with a WCS geometry identical to the HGPS maps (cf. 2.2.5).

To compute the expected counts from the galactic diffuse and isotropic background model  $B_C$ , we integrate the predicted flux from both models weighted with the differential exposure  $\mathcal{E}$  in the selected energy band and convolve the resulting image with the mean PSF:

$$B(\ell, b) = PSF * \int_{E_{min}}^{E_{max}} [B_{Gal}(\ell, b, E) + B_{Iso}(E)] \cdot \mathcal{E}(\ell, b, E) dE \quad (3.1)$$

As the Galactic and isotropic diffuse background model provided by the *Fermi*-LAT collaboration is only given up to an energy of  $\sim 500$  GeV, we extrapolate both models up to 2 TeV using a PL approximation. This is equivalent to the approach used in the 3FHL analysis (Ajello et al., 2017).

To compute a mean integral exposure image in the given energy range  $\mathcal{E}$  we weight the differential, energy-dependent exposure by a reference spectrum  $w_{ref}$  and integrate:

$$\mathcal{E}(\ell, b) = \int_{E_{min}}^{E_{max}} w_{ref}(E) \mathcal{E}(\ell, b, E) dE. \quad (3.2)$$

For the reference spectrum we assume a power law, that is normalized to unity in the given energy band ( $E_{min}, E_{max}$ ):

$$w_{ref}(E) = \frac{1 - \Gamma}{E_{max}^{1-\Gamma} - E_{min}^{1-\Gamma}} \cdot E^{-\Gamma} \quad (3.3)$$

**Tab. 3.3.:** Energy ranges and number statistics of the derived *Fermi*-LAT images used in this work. *Exposure* is the mean integral exposure as described by Eq. 3.2, *Flux* the background subtracted integral flux described by Eq. 3.4. The mean weighted PSF widths are given by means of the 68% and 95% containment radii  $R_{68}$  and  $R_{95}$ . The first column indicates the mapping of the energy ranges to the *Red* (R), *Green* (G) and *Blue* (B) color channels of the RGB images described in Sect. 3.3.1.

Color	$E_{Min}$	$E_{Max}$	Exposure		Flux	PSF $R_{68}$	PSF $R_{95}$
	GeV	GeV	$10^{12} \text{ cm}^2 \text{ s}$	$10^{-12} \text{ cm}^{-2} \text{ s}^{-1}$		deg	deg
R	10	30	32.2		947.4	0.14	0.56
G	30	100	33.1		249.1	0.10	0.46
B	100	2000	32.4		47.1	0.10	0.39
	10	20	32.1		731.5	0.13	0.38
	20	50	32.6		344.0	0.10	0.35
	50	150	33.0		126.7	0.10	0.34
	150	500	32.6		18.1	0.10	0.32
	500	2000	31.2		-0.5	0.10	0.29

For the spectral index we choose a value of  $\Gamma = 2.3$ . The integrated flux  $F$  in the given energy band is then computed from:

$$F = \frac{C - B}{\mathcal{E}} \quad (3.4)$$

A mean PSF in the given energy range was likewise computed by weighting the energy-dependent PSF model provided by the *Fermi*-LAT collaboration with the exposure  $\mathcal{E}$  and the same reference PL as defined in Eq. 3.3.

Table 3.2 gives an overview of the resulting total number of events in the count, background and excess images for all energy bands used in this work. The negative excess in the energy band  $> 500$  GeV indicates that the simple PL extrapolation of the Galactic and isotropic diffuse background model globally overestimates the real background. For local analyses the high energy GeV range is limited by low statistics (typically  $< 5$  counts even for bright sources) and the influence of the background model and its uncertainty can be neglected. Table 3.3 likewise summarizes the mean exposure, flux and exposure weighted PSF sizes per energy band. While the flux varies about 3 orders of magnitude, the exposure is almost independent of energy.

## 3.3 Analysis Methods

### 3.3.1 RGB Flux Images

In other fields of astronomy, inspired from optical observations, it is common to work with colored sky images. Beside the more aesthetic appeal of those images, they represent an intuitive approach to show basic spectral information along with

the spatial information contained in single band gray-scale images. To generate colored images from astronomical data, the data taken in three different energy bands is mapped to the corresponding color channels (Red, Green and Blue) of the RGB image. A standard method for this is described in Lupton et al. (2004). As mentioned by the authors, the data should be background-subtracted, if necessary linearized, flat-fielded, and scaled appropriately to achieve optimal results.

The prepared *Fermi*-LAT flux images are already background subtracted and exposure corrected (see Eq. 3.4). As gamma-ray spectra typically show a PL behavior, we re-normalize the data by weighting the flux contained in each energy band  $F$  with the integrated flux of the reference PL spectrum (Eq. 3.3) in the same energy band:

$$\tilde{F} = \frac{F}{F_0 \int_{E_{min}}^{E_{max}} w_{ref}(E) dE} \quad (3.5)$$

Where the index  $C$  corresponds to the different energy bands R, G and B as defined in Tab. 3.2. The reference spectrum  $w_{ref}$  is chosen such that it integrates to unity for the full energy range of 10 GeV to 2 TeV. We also assume a spectral index of  $\Gamma = 2.3$  and a flux scale factor of  $F_0 = 10^{-10} \text{ cm}^{-2} \text{ s}^{-1}$ . After the normalization we clip the data at  $\tilde{F}_{min} = 0$  and  $\tilde{F}_{max} = 1$ .

To enhance faint structures in the image, we follow again Lupton et al. (2004) and stretch the data in all energy bands using an asinh function:

$$\tilde{F}_S(\tilde{F}) = \frac{\text{asinh}(\tilde{F}/a)}{\text{asinh}(1/a)}. \quad (3.6)$$

The parameter  $a$  allows us to set a smooth transition between a linear and logarithmic stretching. For our data we find a value of  $a = 0.2$  to sufficiently enhance faint structures in the image while not saturating the brightest features. Strong saturation would bias the mapped color to *white* for the brightest sources.

Finally, to reduce the noise contained in the image and to partly compensate for the energy dependent size of the *Fermi*-LAT PSF, we smooth every color channel with a Gaussian filter of width  $\sigma = 0.1^\circ$ , a width comparable to the  $R_{68}$  of the PSF in the middle energy band.

Figure 3.5 shows the method applied to an example point source with different assumptions for the spectral shape. For comparison the representation of the *Crab Nebula* model by Meyer et al. (2010) is also shown in the lower right. The upper row illustrates the result of the method for a source with an assumed PL spectrum and different spectral indices  $\Gamma$ . In the case of  $\Gamma = 2.3$  the source appears white by construction. The cases of softer ( $\Gamma = 2.6$ ) and harder ( $\Gamma = 2$ ) indices show the expected shift to reddish and blueish colors. A typical pulsar spectrum, modeled by

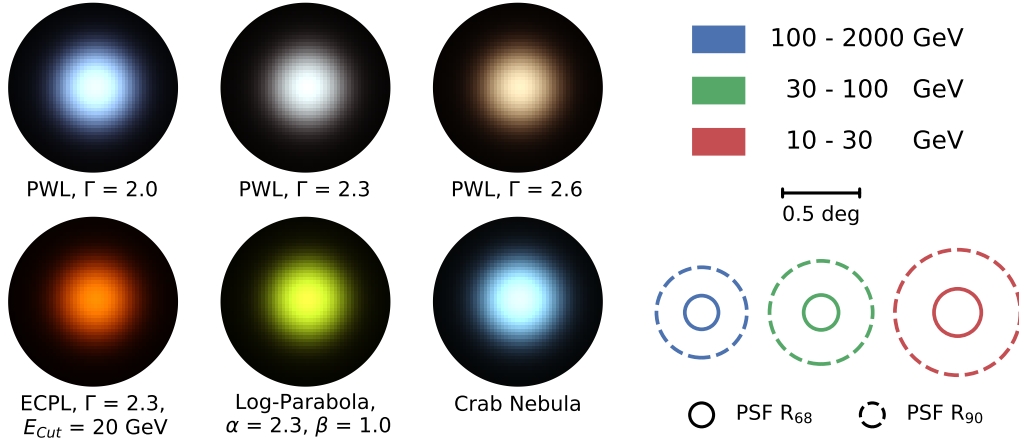


**Fig. 3.5.:** The RGB image method applied to a *Fermi*-LAT example point source assuming different spectral shapes. The upper row illustrates the result for a PL spectrum with index  $\Gamma = 2$ ,  $\Gamma = 2.3$  and  $\Gamma = 2.6$  (left to right). The lower row shows the result of the method applied to an exponential cut-off PL with  $E_{Cut} = 20$  GeV and  $\Gamma = 2.3$  (left), to a log parabola model with  $\alpha = 2.3$  and  $\beta = 1$  (mid) and the Crab nebula model by Meyer et al. (2010) (right). The red, green and blue circles illustrate the size of the PSF in the corresponding energy band. The dashed and solid circles represent the 68% and 90% containment radii of the PSF respectively.

an exponential cut-off PL with a cut-off energy at a few GeV, is shown in the lower left. The spectrum is represented with a deep red color, indicating that the source predominantly emits in the 10 GeV to 30 GeV energy band. The core appears slightly yellow, which is the effect of the smaller PSF at higher energies. A peaked spectrum, modeled by a log-parabola with a maximum energy of  $\sim 40$  GeV is shown in the mid panel. The emission is represented by a green-yellow color, which indicates the peak of the emission in the lower range of the middle energy band.

### 3.3.2 Longitude and Latitude Flux Profiles

For a quantitative comparison of the global emission structure we measure longitude and latitude flux profiles on the HGPS and *Fermi*-LAT sky maps. For this we choose the *Fermi*-LAT-data above 100 GeV, which limits the influence of the PSF and pulsar emission on the measurement. With  $\sim 10.000$  counts (cf. Fig. 3.2) above 100 GeV the measurement is still dominated by systematic and not statistical uncertainties. To reduce the effect of low exposure regions with large uncertainties in the HGPS map we limit the measurement to the region between  $b = \pm 2.5^\circ$  (cf. Fig. 2.1, lower panel).

We measure the flux profiles on the publicly available  $0.2^\circ$  correlated HGPS flux maps. For better comparability we also correlate the *Fermi*-LAT flux maps with a top-hat filter of the same radius. The flux and flux error maps have an initial pixel size of  $0.02^\circ \times 0.02^\circ$ . After correlation with a top-hat filter of radius  $0.2^\circ$ , the new

effective pixel size is  $\sim 0.4^\circ \times 0.4^\circ$ , which results in a downsampling factor of 20 per axis to avoid correlated error estimates. For both datasets the profiles are then measured on the downsampled map by summing the emission pixel-wise along the independent axis. The error on the summed flux is estimated using Gaussian error propagation of the pixel-wise flux errors. The method is available in *Gammapy* as `ImageProfileEstimator` class.

### 3.3.3 Spectral Flux Points

The 3FHL catalog provides flux point measurements for the energy ranges 10–20 GeV, 20 – 50 GeV, 50 – 150 GeV, 150 – 500 GeV and 500 – 2000 GeV. Those are measured with a certain assumption on the morphology and using the best fit position of the 3FHL source. Both are not necessarily compatible with the position and morphology of an associated HGPS source and in some cases there is no association at all. For this reason we determine a new set of GeV flux points using the morphology and position found in the HGPS. In addition we derive a single flux measure and ULs for the full energy range of 10 – 2000 GeV.

To measure the flux points and corresponding ULs, we use a simplified method, based on a single parameter Poisson maximum likelihood fit. While the 3FHL analysis varies the background model during the fit and uses a local approximation of the spectral index within the energy band, our method uses a fixed background model and a fixed spectral index of  $\Gamma = 2.3$  for all energy bands. For this we first compute sky maps as described in Sec. 3.2.5 for the same five energy bands as given in the 3FHL catalog. In a second step we use the HGPS morphology model as a spatial template, convolve it with the mean *Fermi*-LAT PSF in this energy band and fit the amplitude  $F$  of the resulting spatial template to the map, according to the following model:

$$N_{Pred} = B + PSF * (\mathcal{E}_C \cdot F_0 \cdot S_{HGPS}) \quad (3.7)$$

Where  $\mathcal{E}_C$  is the exposure map as defined by Eq. 3.2,  $S_{HGPS}$  the morphology template of the HGPS source,  $F_0$  the amplitude parameter,  $PSF$  the mean *Fermi*-LAT PSF in the given energy range and  $B$  the map with the predicted number of events from the Galactic diffuse and isotropic background model, as computed from Eq. 3.1. The background map  $B$  is already PSF convolved and is assumed to be fixed during the fit. Error and upper limits on the best fit amplitude  $F_0$  are estimated from the likelihood profile as described in Sec. 1.4.2.

To validate this simplified approach we apply the method to the 3FHL dataset and reproduce the flux points of the sources listed in the 3FHL catalog. For this we use the morphology model provided in the 3FHL catalog as spatial template and added surrounding sources to the background model. Figure 3.6 shows the result for the

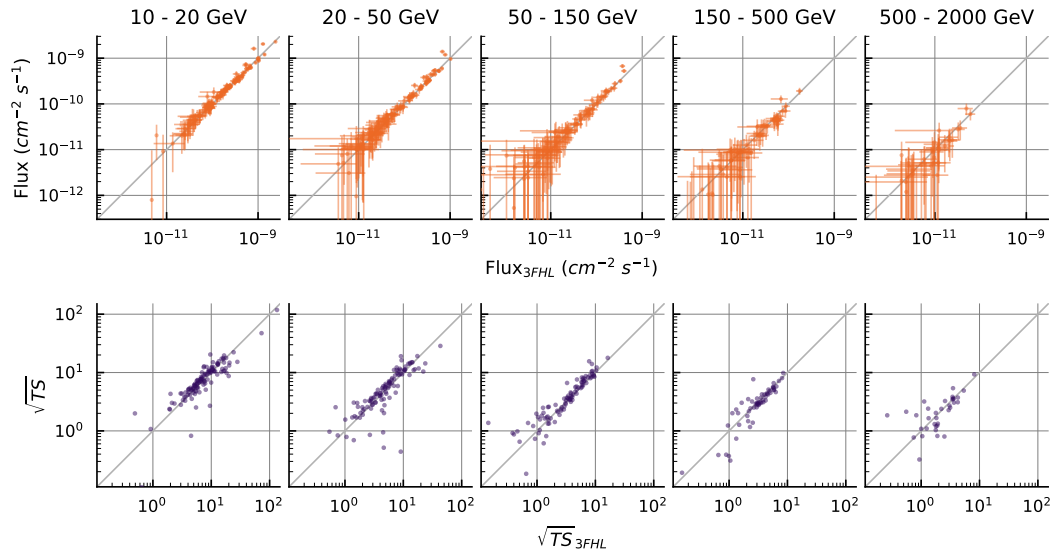


**Fig. 3.6.:** Comparison of the simplified flux point measurement method against results from the *Fermi*-LAT 3FHL catalog for five energy bands. The upper row shows the comparison of the flux values, the lower row the comparison of  $\sqrt{TS}$ . The flux point measurement is based on an amplitude fit of the 3FHL morphology template in the given energy range. The background model was not varied during the fit and the spectral index in all energy bands was fixed to  $\Gamma = 2.3$ . The total number of measured points decreases for the higher energy ranges because of decreasing statistics.

five energy ranges. The upper row show the flux values measured by the simplified method agree within errors with the reference points from the 3FHL catalog. The notable scattering can be explained by differences in the methods.

## 3.4 Results

### 3.4.1 Survey RGB Images

#### Flux Image

The RGB image of *Fermi*-LAT measured flux in the HGPS region produced with the method described in Sec. 3.3.1 is shown in Fig. B.10 (page 127). Regions with extended *white* emission are associated with the known bright sources along the Galactic plane with PL shaped spectra. All those regions are encircled by TeV emission contour lines and are therefore also detected at higher energies. The color of the bright TeV sources such as *Vela Junior* and *HESS J1825-137* is shifted to blue indicating harder spectra with an index closer to  $\Gamma = 2$ .

A few compact, very bright emission regions without TeV counterpart can be noticed:

- At  $\ell \approx 260^\circ$ , located off plane, there is an emission spot corresponding to the SNR *Puppis A* (3FHL J0822.1-4253e). The *lack of TeV emission* from this source has been studied in detail by H.E.S.S. Collaboration et al. (2015c). The authors measured an exponential cut off of the spectrum below 450 GeV with 99% CL. They found none of the standard limitations such as age, size and radiative losses could explain the lack of the TeV signal. As alternative explanation they suggest the particle acceleration ceased in this object some time ago.
- The extended emission region near the Galactic plane at  $\ell \approx 328^\circ$  corresponds to the source 3FHL J1553.8-5325e. The source has been newly detected by Ackermann et al. (2017), but marked as confused or contaminated by the diffuse background model. No plausible counterpart was found. The source has not been subject of any dedicated analyses so far.
- The extended emission below the Galactic plane at  $\ell \approx 326^\circ$  corresponds to the source 3FHL J1552.7-5611e, which is likely associated to the composite supernova remnant *MSH 15-56*. The source was studied in detail by Temim et al. (2013). The authors struggled to explain the origin of the gamma-ray emission, but considered either an evolved PWN or a SNR with high magnetic field, possibly expanding into a clumpy ISM as the most likely scenarios.
- The bright emission spot at  $\ell \approx 278^\circ$  and  $b \approx -1^\circ$  is associated to *Eta Carinae* (3FHL J1045.1-5941). The analysis of *Fermi*-LAT data by Reimer et al. (2015) showed a strong variability in the high energy component above 10 GeV. With an energy threshold of  $\sim 500$  GeV and non-continuous exposure the source was not detectable by the HGPS analysis (cf. 2.3). A more recent study by Leser et al. (2017) using data from the H.E.S.S. II instrument with a lower energy threshold  $\sim 200$  GeV resulted in a  $13.6\sigma$  detection of the source.
- The bright point-like source at  $\ell \sim 332.5^\circ$  and  $b \sim 2.5^\circ$  (3FHL J1603.8-4903) is likely associated to a BL-Lac object and will not be considered further.

However those regions have in common that the emission is represented with a faint green color, which is a hint for a peak of the emission in the energy band between 30 GeV and 100 GeV. This implies the spectra fall off towards higher energies and the non-detection at TeV energies seems plausible. Those emission regions are obvious candidates for follow-up observations with the H.E.S.S. II telescope array.

A special case are the large, few degree size emission regions located at  $\ell = 285^\circ$  and  $\ell = 312^\circ$ . Both regions are modeled in the 3FHL analysis and are listed in the 3FHL catalog with identifiers *3FHL J1036.3-5833e* and *3FHL J1409.1-6121e* respectively. In Ackermann et al., 2017 the sources were marked as confused or contaminated by diffuse background emission and no suitable physical counterpart was found. With a radius of  $2.5^\circ$  and  $0.7^\circ$  respectively both emission regions are probably too large to be detected by H.E.S.S. observations. Comparing to Fig. 2.14 it is worth noting that *3FHL J1036.3-5833e* is close to the position of the spiral arm tangent of *Carina* and *3FHL J1409.1-6121e* is close to the tangent of the *Crux Centaurus* arm.

Point-like, *red* emission in the image is typically associated to gamma-ray pulsars which are not detectable in TeV range, because their spectra cut off in the few GeV regime. Those will not be considered further.

An exceptional case is the emission detected by the HGPS (Gaussian component *HGPSC 71*) in the region south-east of HESS J1825-137, which is also present in the *Fermi*-LAT maps. By eye there is a slight excess in the highest energy band between 100 GeV and 2 TeV, which is an additional hint that the TeV emission is real and not an artifact of HGPS catalog analysis. However the origin of this emission is currently unknown, but seems likely associated to HESS J1825-137 because of its proximity.

## Model Flux and Residual Image

A colored image of the 3FHL catalog model is represented in Fig. B.11 (page 128). It first illustrates the variety of spectral and morphological shapes of GeV gamma-ray sources. The visual impression is again dominated by extended sources represented with a *blueish-white* color clustered along the Galactic plane.

There is a small population of GeV point sources with a hard spectrum (represented in *blue*) without TeV counterpart (only exception is the source *HESS J1943+213*, which is also detected in TeV). Those are typically associated to extra-galactic objects and are not considered further.

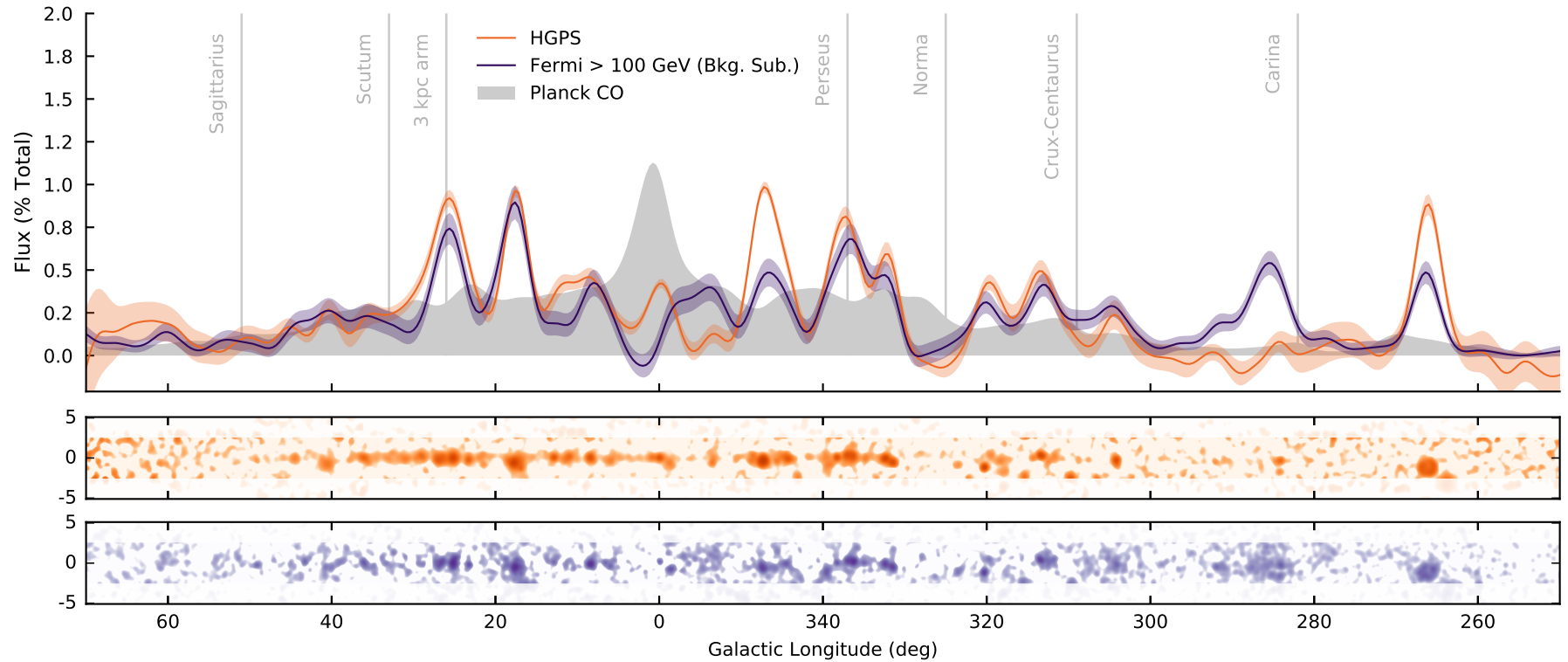
The existence of the extended underlying emission components at  $\ell \sim 286^\circ$ ,  $\ell \sim 291^\circ$  and  $\ell \sim 312^\circ$  indicate similar difficulties with separating distinct gamma-ray source from large scale emission as observed during the HGPS analysis described in Sec. 2.3.5. Instead of selecting and rejecting the emission components by hand, Ajello et al. (2017) decided to list the components in the 3FHL catalog and mark those with a classification flag *confused or contaminated by diffuse background emission*.

The corresponding model residual image is shown in Fig. B.12 (page 129). While most of the emission seems well covered by the 3FHL catalog model, there are still regions with large scale residual emission offset from the Galactic plane, at low latitudes. Those are likely compatible with systematic background uncertainties, but at least indicate the difficulties of modeling the gamma-ray emission in the Galactic plane, where problem such as source confusion, a population of unresolved background sources and separating distinct gamma-ray sources from large scale emission arise. In general it can be noticed that morphologies of large source are not modeled in detail. *HESS J1825-137* shows residuals close to the core of the TeV emission. The shell like SNRs *Vela Junior* and *RX J1713.7-3946* have negative residuals in their central regions, because their morphology was modeled with a disk shaped template.

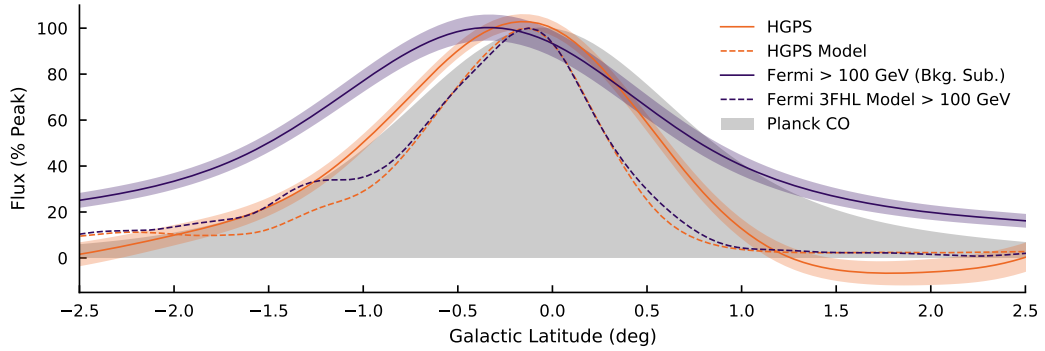
### 3.4.2 Survey Longitude Flux Profiles

Figure 3.7 compares the measured HGPS and *Fermi*-LAT longitude flux profiles. In both measurements large scale background emission was subtracted. For this reason the shape of the profile is mostly determined by the population of distinct gamma-ray sources. In general there is good agreement between the positions of the peaks in both profiles. Sources emitting prominently in the TeV band are typically also present in the  $>100$  GeV band and vice versa. The bright emission peaks at  $\ell = 347^\circ$  and  $\ell = 265^\circ$  in the HGPS profile are associated to the young shell-like SNRs *RX J1713.7-3946* and *Vela Junior*. Both show hard spectra ( $\Gamma = 1.5$ ) in the GeV band with an emission peak in the TeV band (compare Fig. 7 in Funk (2015)), which explains the significantly higher fraction they contribute to the total emission in the TeV range.

Two regions show larger differences between the HGPS and *Fermi*-LAT flux profile: the region around the Galactic Center and the region between  $\ell = 310^\circ$  and  $\ell = 270^\circ$ . The region around the Galactic Center is known to be complicated to analyze for both instruments and dominated by systematic uncertainties in both cases. The region between  $\ell = 310^\circ$  and  $\ell = 270^\circ$  shows increased gamma-ray emission in the *Fermi*-LAT profile. This part of the Galaxy is observed by the H.E.S.S. instrument with only few observation time (compare to 2.1, lower panel). This is reflected in the HGPS flux profile by a larger statistical uncertainty of the measurement. In addition this region can only be observed at high zenith angles by the H.E.S.S. telescopes which also leads to larger expected systematic uncertainties (not included in the figure). The distinct peak at  $\ell = 285^\circ$  is not present in the TeV profile. It is associated to an extended emission region listed in the 3FHL catalog as *3FHL J1036.3-5833e*. With a measured radius of  $\sim 2.5^\circ$  it is not detectable by the H.E.S.S. instrument. No plausible counterpart is known for this emission and in Ackermann et al., 2017



**Fig. 3.7.:** **Top:** Longitude profile of the HGPS measured flux above 1 TeV and the *Fermi*-LAT measured flux above 100 GeV with the emission from the diffuse and isotropic background model subtracted. The error bands represent the  $1\sigma$  statistical error on the measurement. The gray background shows the matter density as traced by *Planck* measurements of CO(1-0) line emission. All profiles are normalized such that the area under the curve integrates to unity. All profiles are smoothed with a Gaussian of width  $0.5^\circ$ . Spiral arm tangent locations are taken from Vallée (2014). **Middle and Bottom:** HGPS flux image above 1 TeV and *Fermi*-LAT flux image in arbitrary units. Both images are smoothed with a Gaussian of width  $0.5^\circ$  to match the size of the features to the scale of the longitude profiles.



**Fig. 3.8.:** Latitude profile of the HGPS measured flux and flux model above 1 TeV as well as the *Fermi*-LAT measured flux >100 GeV and the *Fermi*-LAT 3FHL model. Both model profiles only include the contributions from sources. The contribution from the HGPS large scale emission model was subtracted from the data as well as the model. The error bands represent the  $1\sigma$  statistical error on the measurement. The gray background shows the matter density as traced by *Planck* measurements of CO(1-0) line emission. All profiles are normalized to their peak value. All profiles are smoothed with a Gaussian of width  $0.05^\circ$ .

the source was marked as confused and likely contaminated by diffuse background emission.

For comparison the figure also shows the profile of the matter density in the Galaxy, traced by *Planck* measurements of CO(1-0) line emission (Planck Collaboration et al., 2016) as well as the position of spiral-arm tangents measured by Vallée (2014). While there is a very general correlation between the number of HGPS sources and the matter density in the Galaxy (cf. 2.14), this observation does not hold for the distribution of the gamma-ray flux. There is no general correlation between the position of spiral arm tangents and enhanced gamma-ray flux from the corresponding region either. However both profiles show an emission peak corresponding to the position of the tangents of the 3 kpc arm and the *Perseus* spiral arm.

### 3.4.3 Survey Latitude Flux Profiles

Figure 3.8 compares the latitude flux profiles of the HGPS measurement and HGPS source flux model to the *Fermi*-LAT measurement >100 GeV and the *Fermi*-LAT 3FHL source model >100 GeV. The reference profile of the matter density in the Galaxy, traced by *Planck* measurements of CO(1-0) line emission is also shown in the background. All profiles feature a distinct peak close to latitude zero, which indicates that the bulk of TeV as well as GeV gamma-ray emission originates from the Galactic plane.

Comparing both data profiles, the *Fermi*-LAT data profile shows a wider shape, which indicates the HGPS emission concentrates more along the Galactic plane. This can

be partly explained by the effect of the ring background method, which subtracts large scale emission from the data (cf. Fig. B.14 and Fig. B.15). This in turn leads to a smaller width of the measured HGPS emission profile.

The source model profiles are almost perfectly aligned, confirming the general agreement in the distribution of distinct high energy GeV and TeV gamma-ray sources (cf. Fig. 2.13). Compared to both data profiles the model profiles are notably less wide. This indicates the existence of un-modeled residual emission in both cases, which accumulates along the Galactic plane. In case of the *Fermi*-LAT profiles, the emission is typically absorbed by the background normalization factor from the 3FHL analysis (cf. Fig. 19 in Ajello et al. (2017), the normalization factor is  $>1$  over the largest part of the Galactic plane). In case of the HGPS profiles the emission is partly absorbed by extended underlying Gaussian components, that were excluded from the catalog model (cf. Sec. 2.3.5). In both cases the residual emission includes contributions from unresolved sources, true interstellar emission and background systematics.

#### 3.4.4 Source Associations

In the previous chapter we used a simple proximity criterion to find candidates for counterparts of HGPS sources (cf. 2.3.8) in the *2FHL*, *ATNF* and *SNRCat* catalogs. Now we extend the association procedure to the 3FHL catalog, which was not available at the time of the first study. Again we consider a 3FHL source as associated, if its center is located within the spectral extraction region (defined by a circle with radius  $R_{\text{SPEC}}$  around the best-fit source position) of the HGPS source.

Table A.3 (page 108) lists the resulting 3FHL associations for all HGPS sources, according to the criterion defined above. In addition it lists the corresponding HGPS and 3FHL source classification and, if available, the identified object. The total number of 3FHL sources within the HGPS region amounts to 145. We find 56 of these sources to be associated with 49 HGPS sources in total. In 42 cases the association is unique, in 6 cases there is more than one 3FHL source associated to a HGPS object. Among the 31 identified HGPS sources are 22 objects that have a 3FHL counterpart. The association with the 3FHL catalog did not yield any new counterpart objects for the 7 *dark* (i.e. sources without any known association) HGPS sources.

There are three HGPS sources that have a new 3FHL association and did not have any previous associations to a 2FHL or 3FGL source:

- HESS J1302-638 is an identified high mass binary object associated to the pulsar PSR B1259-63 (Aharonian et al., 2005d). The 3FHL catalog now lists an

individual object 3FHL J1303.0-6350. The proximity to the extended source 3FHL J1303.0-6312e probably prevented an earlier detection because of source confusion.

- HESS J1427-608 is an unidentified gamma-ray source detected by Aharonian et al. (2008d). It has a known X-ray counterpart named Suzaku J1427-6051 (Fujinaga et al., 2013). The associated GeV source is the object 3FHL J1427.9-6054.
- HESS J1713-381 is an identified SNR associated to the object CTB 37B. There is now a GeV counterpart named 3FHL J1714.0-3811. The proximity to the source 3FHL J1714.4-3829 probably prevented an earlier detection because of source confusion.

Table A.3 also shows that there are multiple cases, where the identifications and source classifications disagree between the HGPS and 3FHL analysis. This is mainly because of different association methods and applied identification criteria. In both cases the firm identifications were decided manually. For this reason those discrepancies can only be resolved manually, which was not done in this work.

### 3.4.5 GeV Source Candidates

The GeV flux points and ULs for all HGPS sources, determined using the method described in Sec. 3.3.3, are listed in Tab. A.4 (page 112). Flux UL values are given where the significance in the corresponding energy band dropped below  $\sqrt{TS} = 1$ , which is equivalent to the criterion used for the 3FHL analysis. In total we find 55 HGPS sources with significant GeV emission  $\sqrt{TS} > 5$  in the energy band between 10 GeV and 2000 GeV. Among these are 9 sources, that do not have an associated 3FHL object. Because of the caveats associated with the analysis method (cf. Fig. 3.6) we classify those objects as *GeV source candidates*.

#### **HESS J1026-582**

*HESS J1026-582* is a PWN candidate close to the PSR object 3FHL J1028.5-5818, but outside the association circle. Significant GeV emission is mostly found in the lower two energy bands and likely originates from the PSR. Higher energetic GeV is not detected, which is in line with the results from Acero et al. (2013). However the estimated ULs in the overlapping energy range are compatible with the HGPS flux points. A future detection is not excluded. The spectral points and corresponding RGB image are shown in Fig. C.1.

## **HESS J1632-478 and HESS J1634-472**

*HESS J1634-472* is an unidentified TeV source first discovered by Aharonian et al. (2006f). The GeV detection was announced by Acero et al. (2013), with a significance of  $TS = 33$  and a measured flux of  $(5.6 \pm 1.3) \cdot 10^{-10} \text{ cm}^{-2} \text{ s}^{-1}$  above 10 GeV. An RGB image and combined GeV and TeV spectrum is shown in Fig. C.2. The region of *HESS J1634-472* and *HESS J1632-478* is a region of complex GeV emission, that was modeled with three extended 3FHL sources: 3FHL J1633.0-4746e, 3FHL J1631.6-4756e and 3FHL J1636.3-4731e. While there is a clear correspondence between the distinct emission spot 3FHL J1631.6-4756e and the HGPS source *HESS J1632-478*, this does not hold for *HESS J1634-472*. Most of its emission is modeled by the larger underlying component 3FHL J1633.0-4746e and close by emission peak to the south. In this case no clear association between the HGPS and 3FHL source can be made, because of the fundamental differences in modeling. However the GeV flux points for *HESS J1632-478* show good agreement with the TeV flux points and a smooth continuation of TeV spectrum to lower energies. Our measured flux value of  $(9.4 \pm 0.8) \cdot 10^{-10} \text{ cm}^{-2} \text{ s}^{-1}$  does not agree with Acero et al. (2013), which can be explained again by fundamental differences in modeling.

## **HESS J1702-420**

The object *HESS J1702-420* is one of the 7 *dark* sources in the HGPS catalog without any known MWL counterpart. It was already detected during the H.E.S.S. survey of the inner Galactic plane (Aharonian et al., 2006f) and later analyzed in more detail by Aharonian et al. (2008d). The nearest 3FHL catalog source is the object 3FHL J1703.4-4145, which is associated to the SNR G344.7-00.1. Acero et al. (2013) measured an UL of  $4.7 \cdot 10^{-10} \text{ cm}^{-2} \text{ s}^{-1}$  above 10 GeV for this source. Figure C.3 shows an RGB image of the region and a combined spectrum. The image shows bright GeV emission, which is notably offset from the HGPS source region. Better agreement with the GeV emission is found in the TeV significance contours, which reveal a bright emission center at the position of *HESS J1702-420* and an emission tail to the *north west*, which is in agreement with the GeV source. The flux point measurement using the HGPS morphology yielded significant emission ( $\sqrt{TS} = 5.4$ ) in the GeV band between 10 GeV and 2 TeV. The flux points in the overlapping energy range are compatible with the HGPS for the 3FHL as well as our measurement. The measured flux of  $(2.9 \pm 0.6) \cdot 10^{-10} \text{ cm}^{-2} \text{ s}^{-1}$  is compatible with the UL derived by Acero et al. (2013).

## **HESS J1746-308**

*HESS J1746-308* is an unidentified source located in a complex region to the south east of the Galactic center. While in the HGPS analysis the emission was modeled

as two distinct sources, in 3FHL there is only a single very extended source 3FHL J1745.8-3028e. In this case the association is not unique. The flux points in the high energy GeV range are not very constraining, but still compatible with the HGPS measurement. The spectral points and corresponding RGB image are both shown in Fig. C.4.

### ***HESS J1813-178***

The object *HESS J1813-178* was already discovered during the first H.E.S.S. survey of the inner Galactic plane (Aharonian et al., 2006f). Its detection was later confirmed by MAGIC observations (Albert et al., 2006). The source is classified as a composite SNR / PWN with the counterparts in the radio and X-ray domain. A possible VHE association named *2HWC J1814-173* was reported in Abeysekara et al. (2017). ULs on the flux in the GeV band were reported by Acero et al. (2013). With a TS value of 2.5 they found an UL on the integrated flux above 10 GeV of  $2.4 \cdot 10^{-10} \text{ cm}^{-2} \text{ s}^{-1}$ . The UL was also derived assuming the H.E.S.S. morphology as spatial shape. In the present analysis we measured a significance of the source of  $\sqrt{TS} = 5.9$  between 10 GeV and 2000 GeV. Figure C.5 shows the *Fermi*-LAT RGB image of the region and a combined spectrum with the HGPS measured flux points and the best fit PL spectrum. The image shows a *white-blueish* GeV emission peak, coincident with the position of *HESS J1813-178*. It is embedded in a complex region with lower energetic *greenish* emission. Source confusion or an increased background level can explain the non-detection in the 3FHL analysis, keeping in mind that our method probably overestimates the detection significance. The flux points in the overlapping energy range are compatible. We measured an integrated flux between of  $(1.7 \pm 0.4) \cdot 10^{-10} \text{ cm}^{-2} \text{ s}^{-1}$ , which is compatible with the UL stated above.

### ***HESS J1843-033***

*HESS J1843-033* is unidentified source located in very complex emission region in between the spiral arm tangents of *Scutum* and the 3 kpc arm. The *Fermi*-LAT data shows a lot of surrounding emission, which likely leads to an increased background level and may have prevented the detection of the source. The flux points are compatible with the HGPS measurement in the overlapping energy range. The spectral points and corresponding RGB image are shown in Fig. C.6.

### ***HESS J1848-018***

*HESS J1848-018* is located in the same complex emission region in between the spiral arm tangents of *Scutum* and the 3 kpc arm. It is possibly associated with the star forming region W43. Again the *Fermi*-LAT data shows a lot of surrounding emission, which confuses the localized emission from the source. The flux points in

the two highest energy bands are not significant, but the ULs are compatible with the flux points measured by the HGPS. The spectral points and corresponding RGB image are shown in Fig. C.7.

### **HESS J1852-000**

*HESS J1852-000* is an unidentified source possibly associated with the SNR *Kes 78*. It also located in a complex emission region and no distinct 3FHL source was detected. While the high energy flux points ( $> 150$  GeV) are not significant and do not meaningfully constrain the spectrum, the lower flux points ( $< 150$  GeV) seem compatible with a PL extrapolation of the HGPS flux points. The spectral points and corresponding RGB image are shown in Fig. C.8.

### **HESS J1858+020**

*HESS J1858+020* is an unidentified TeV source possibly associated to the SNR G35.6-0.4. It is embedded in a complex region of GeV emission. It is close to the source 3FGL J1857.9+0210, which shows a typical pulsar spectrum, but is no identified PSR. At the low energy end ( $< 50$  GeV) we found the flux points to be compatible with the spectrum of 3FGL J1857.9+0210. The flux measurement between 50 GeV and 150 GeV is an UL, while the highest flux points are significant again and compatible with the HGPS measurement. The spectral points and corresponding RGB image are shown in Fig. C.9.

## 3.4.6 Shell-Type SNR Candidates

The HGPS source catalog currently includes 6 known TeV shell-type SNRs, of which three have also been detected in the 3FHL analysis: *Vela Junior*, *RX J1713.7-3946* and *RCW 86*. In the following we shortly discuss the remaining objects *HESS J1534-571*, *HESS J1731-347* and *HESS J1912+101*.

### **HESS J1534-571**

The object *HESS J1534-571* is a TeV source detected in the HGPS analysis and recently identified as a shell-like SNR by H.E.S.S. Collaboration et al. (2018). It has a radio SNR candidate counterpart *G323.7-1.0*, which is in very good positional and morphological agreement. The GeV detection was recently reported in Araya (2017) with a significance of  $\sqrt{TS} = 7.5$ , using an updated dataset with  $\sim 40\%$  more observation time and a lower energy threshold of 5 GeV compared to the 3FHL analysis. The author found a source with disk shaped morphology with a radius of  $0.4 \pm 0.1^\circ$  at a position of R.A. =  $233.5^\circ$ , Dec. =  $-57.2^\circ$ . The spectrum of the source

was found with a PL shape of index  $2.2 \pm 0.6$  and an integral flux between 10 GeV and 2 TeV of  $(1.5 \pm 0.4) \cdot 10^{-10} \text{ cm}^{-2} \text{ s}^{-1}$ .

In this analysis the source is found with  $\sqrt{TS} = 3.8$  for the total energy band between 10 GeV and 2 TeV and a maximum  $\sqrt{TS} = 4.5$  in the energy band from 150 GeV to 500 GeV. Figure C.10 shows the corresponding *Fermi*-LAT RGB image of the region and a combined spectrum including the flux points and spectrum measured by the HGPS. The image shows enhanced emission in the  $>100$  GeV energy band (*blue*), which coincides with the most significant emission spot in the HGPS map. The flux points indicate a hard GeV spectrum and a peak around 1 TeV. In the overlapping energy range the measurement is compatible with the HGPS analysis. With an integral flux of  $(0.9 \pm 0.3) \cdot 10^{-10} \text{ cm}^{-2} \text{ s}^{-1}$  between 10 GeV and 2 TeV, the measurement is compatible within errors with the values reported by Araya (2017). The differences can be explained by different assumptions on morphology spectral index of the source.

### **HESS J1731-347**

The object *HESS J1731-347* is a TeV shell-type SNR detected by Aharonian et al. (2006f) and analyzed in detail by H.E.S.S. Collaboration et al. (2011a). It belongs to the class of young TeV and X-ray bright SNRs such as *RX J1713.7-347*, *Vela Junior* or *RCW 86*. The source also has a radio counterpart named *G353.6-0.7*. The GeV detection of the source was recently reported in Condon et al. (2017) with a significance of  $\sqrt{TS} = 7.5$ , measured between 1 GeV and 2 TeV. The authors reported a point source at position R.A. =  $262.92^\circ$ , Dec. =  $-34.77^\circ$  and a hard spectral PL index of  $\Gamma \sim 1.66$ . The integral flux measured between 10 GeV and 2 TeV was  $(1.1 \pm 0.4) \cdot 10^{-10} \text{ cm}^{-2} \text{ s}^{-1}$ . They also tested a disk and TeV morphology template, but could not find a significant extension, likely because of limited statistics. They also considered alternative scenarios of the origin of the GeV emission such as molecular clouds or an extragalactic source, but concluded the association to *HESS J1731-347* was the most likely scenario.

Figure C.11 shows the *Fermi*-LAT RGB image of the region and combined SED including GeV flux points and the flux points and spectral model measured by the HGPS analysis. The image shows a complex emission region with a distinct greenish-white emission peak coincident with the H.E.S.S. source. The spectrum shows good agreement with the H.E.S.S. spectrum for the highest flux point, albeit with a large error on the GeV measurement. The UL derived in the range 150 GeV to 500 GeV is not compatible with the H.E.S.S. data points and is not confirmed by Condon et al. (2017), which found good agreement with the H.E.S.S. analysis. The total flux value of  $(1.3 \pm 0.4) \cdot 10^{-10} \text{ cm}^{-2} \text{ s}^{-1}$  in the range between 10 GeV

and 2000 GeV agrees again very well with the value measured by Condon et al. (2017).

### **HESS J1912+101**

The TeV source *HESS J1912+101* was discovered by Aharonian et al. (2008c) and recently classified as shell-type candidate SNR by H.E.S.S. Collaboration et al. (2018). The authors found a clear shell-type morphology in the TeV range, with an inner radius of  $0.32^\circ$ , outer radius of  $0.49^\circ$  and center location of  $\ell = 44.46^\circ$  and  $b - 0.13^\circ =$ . No suitable radio, X-ray or GeV counterpart could be identified. Because of the lack of any MWL association the object *HESS J1912+101* was given the status of a *candidate SNR*. For this object Acero et al. (2013) derived an UL on the GeV flux of  $4.6 \cdot 10^{-10} \text{ cm}^{-2} \text{ s}^{-1}$  above 10 GeV.

Using the TeV morphology as a template we find a best-fit GeV excess with  $\sqrt{TS} = 4.4$  and a flux of  $(1.7 \pm 0.4) \cdot 10^{-10} \text{ cm}^{-2} \text{ s}^{-1}$  between 10 GeV and 2000 GeV, which is compatible with the ULs derived by Acero et al. (2013). Figure C.12 shows an RGB image of the region and a spectrum of the GeV and TeV flux points as well as the best fit TeV PL spectral model. The image reveals a complex region in the GeV band with slightly enhanced emission in the *north-western* part of the TeV shell. The combined spectrum shows a curved shape, with an emission peak in the lower TeV range. The high energy GeV range is not well constraint, because of missing statistics. At the lower GeV end the spectrum turns up, likely because of contamination by the nearby pulsar 3FGL J1915.2+0954.

## 3.4.7 Examples of Typical Source Classes

The representation of GeV gamma-ray data with RGB images and comparison with TeV contours allows for a visual classification of gamma-ray sources. The following section revisits qualitatively a few examples of the source classes introduced in Sect. 1.2.2.

### **HESS J1708-443 (PSR and PWN)**

An example for a PSR with its associated PWN is depicted in Fig. 3.9. The RGB image shows a region of point-like *red-yellowish* GeV emission, associated to the PSR 3FHL J1709.7-4429. Offset from the PSR to the north, the TeV contours show an extended object with center-filled morphology. This is the corresponding PWN, detected by the H.E.S.S. instrument at higher energies as *HESS J1708-443*.

The combined SED clearly shows two components. The first, lower energetic component is associated to the PSR and cuts off at a few GeV. At higher energies  $> 100$  GeV

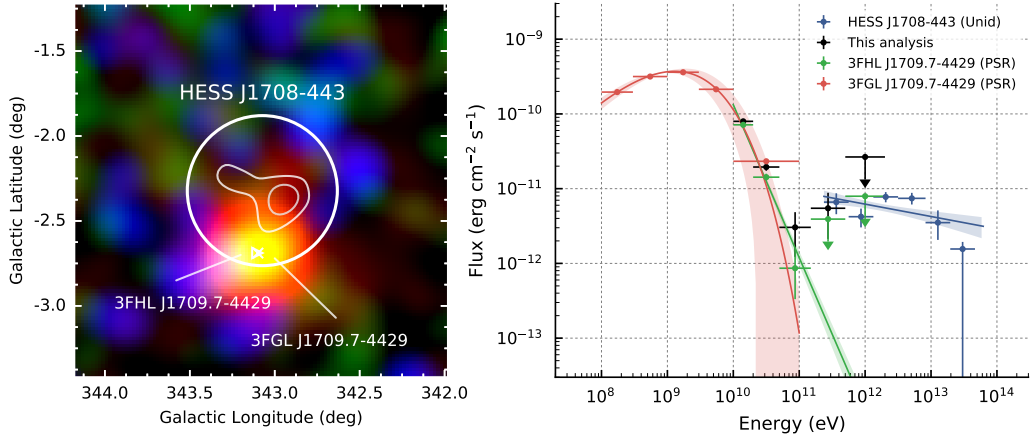


**Fig. 3.9.:** *Fermi*-LAT RGB image and spectrum of *HESS J1708-443*. The white circle marks the  $R_{Spec}$  of the H.E.S.S. source.

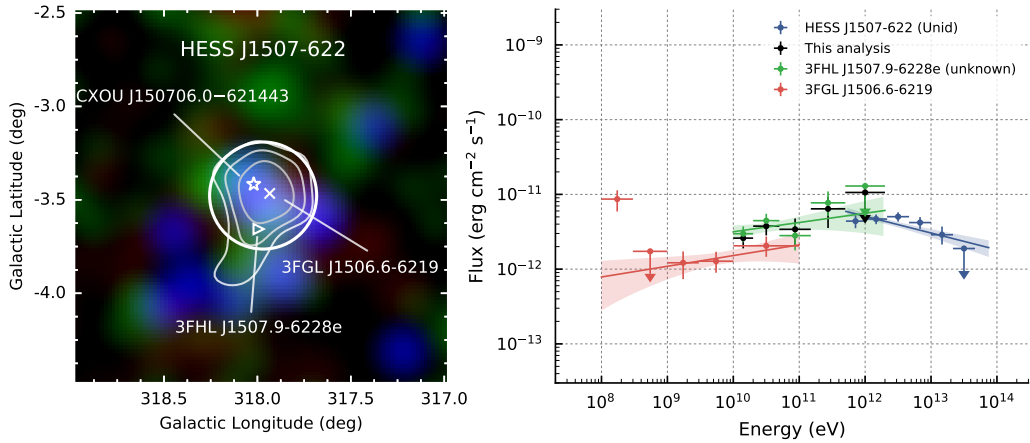


**Fig. 3.10.:** *Fermi*-LAT RGB image and spectrum of *HESS J1507-622*. The white circle marks the  $R_{Spec}$  of the H.E.S.S. source.

the second component takes over, which is associated to the PWN. The high energy component features a curved shape, with an emission peak in the region around  $\sim 1$  TeV. The spectrum also shows that there is high energy GeV emission at the position of the PWN, which is not visible in the image, because it is outshone by the bright PSR. In the overlapping energy range the *Fermi*-LAT and HGPS measurement agree well.

### ***HESS J1507-622* (Unid, PWN candidate)**

An example for an unidentified source in the HGPS as well as 3FHL analysis is shown in Fig. 3.9. The source is special because its located far off the Galactic plane at  $b = 3.5^\circ$ . The RGB image shows a region of extended *blueish-white* GeV emission associated to the source 3FHL J1507.9-6228e. The contours outline an extended TeV source, detected as *HESS J1507-622*. The contours are approximately compatible in

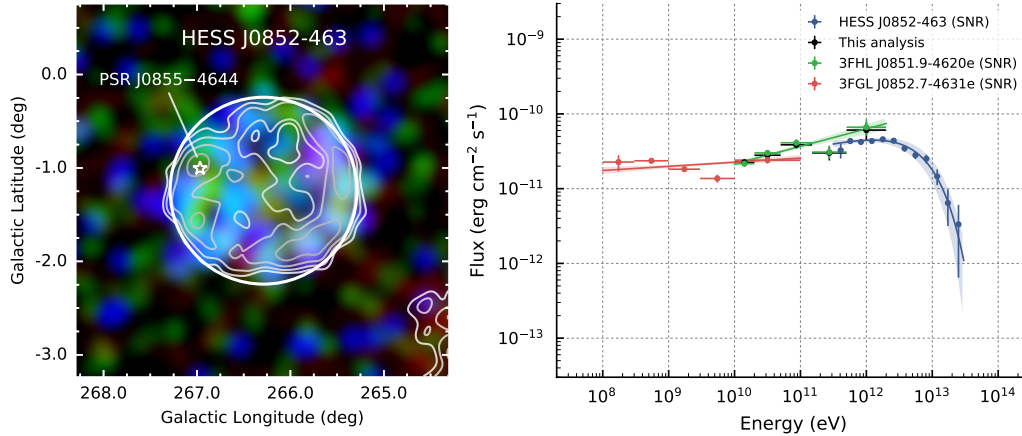


**Fig. 3.11.:** *Fermi*-LAT RGB image and spectrum of *HESS J0852-463*. The white circle marks the outer radius of the H.E.S.S. source as measured by H.E.S.S. Collaboration et al. (2018).

shape with the GeV emission. Close to the position of *HESS J1507-622*, there is an X-ray-source CXOU J150706.0-621443 discovered by Tibolla et al. (2014).

The combined SED shows a single, curved component above  $>1$  GeV and enhanced emission in the lowest 3FGL flux point. The *Fermi*-LAT flux UL derived  $>500$  GeV is compatible with the HGPS measurement. Because of the X-ray counterpart an interpretation as an old PWN scenario seems plausible.

### ***HESS J0852-463* (SNR)**

The object *HESS J0852-463* is a TeV shell type SNR, associated to *RX J0852.0-4622*, also named *Vela Junior*. Figure 3.11 shows the corresponding *Fermi*-LAT RGB image of the region and a combined GeV-TeV spectrum. The RGB image shows a very extended ( $\sim 2^\circ$  in diameter) region of GeV gamma-ray emission, represented with a *blueish-white* color, which indicates a hard GeV spectrum. The TeV emission contours, measured with better angular resolution, agree well in size with the GeV emission and clearly reveals the shell-type morphology.

The combined SED indicates a single emission component in the energy range above 10 GeV. The GeV emission has a hard spectral index and smoothly connects to TeV SED. In the TeV range the SED reaches a peak at  $\sim 2$  TeV and cuts off at 10 TeV. The GeV measurement indicates a larger flux in the overlapping energy range  $> 500$  GeV, but still compatible within errors with the TeV measurement.

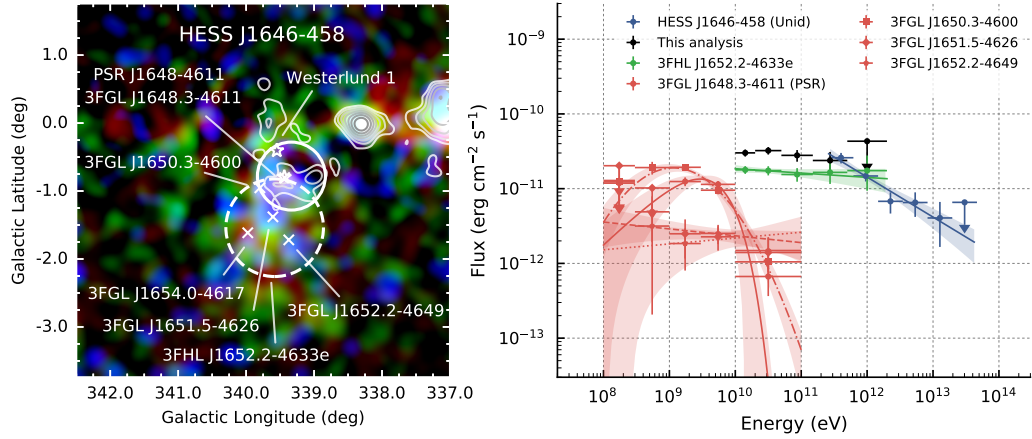


**Fig. 3.12.:** *Fermi*-LAT RGB image and spectrum of *HESS J1646-458*. The solid white circle marks the  $R_{Spec}$  of the H.E.S.S. source. The dashed white circle marks the extension of the 3FHL source.

### ***HESS J1646-458* (Complex Unid)**

The object *HESS J1646-458* is associated to the star forming region *Westerlund 1*. Figure 3.12 shows the detail *Fermi*-LAT RGB image of the region and a combined GeV-TeV spectrum. The image reveals a very extended, fragmented GeV emission region with a size of  $\sim 2^\circ$  in diameter. The emission is associated to the extended source 3FHL J1652.2-4633e. In the previous 3FGL catalog it decomposed into three point sources 3FGL J1654.0-4617, 3FGL J1651.5-4626 and 3FGL J1652.2-4649. The TeV contours also show an extended and fragmented emission region, but significantly offset to the north.

The combined SED shows a soft TeV component, which smoothly connects to the GeV flux points measured in this analysis. The flux points of the source 3FHL J1652.2-4633e are not compatible in the lower part of the overlapping energy range, because the 3FHL source is essentially a different emission region than the TeV source. The emission region is very complex and no clear conclusion about the origin of the GeV nor the TeV emission can be drawn.



# Summary and Outlook

” *After the survey is before the survey.*

— Freely adapted from Sepp Herberger

## 4.1 Summary

### The H.E.S.S. Galactic Plane Survey

In the first part (Chap. 2) of this work we presented a re-analysis of the complete H.E.S.S. Galactic Plane Survey (HGPS) dataset, taken by the H.E.S.S. telescopes between 2004 and 2013. The dataset comprises  $\sim 2700$  h of observations in the region between  $\ell = 250^\circ$  and  $65^\circ$  in longitude and  $b = \pm 3^\circ$  in latitude. The distribution of observation time translates into a flux sensitivity of better than 2% Crab for the largest part of the surveyed region, with a lower energy threshold of typically  $> 200$  GeV.

Using a Poisson maximum likelihood modeling approach we generated a catalog of Galactic TeV gamma-ray sources in multiple steps. We excluded the GC region and shell-type supernova remnants from the analysis because of their complex morphologies. Next we globally modeled the large-scale emission in the Galactic plane and split the HGPS region into smaller, manageable regions of interest (ROI). The emission in every ROI was then modeled as superposition of Gaussian components, requiring a detection significance of  $TS = 30$  for every component. In the next step we manually classified those components and merged them into astrophysical VHE gamma-ray sources. For every source we measured total flux, position, size and spectrum. Finally we associated the sources to objects from multiwavelength (MWL) counterpart catalogs.

In this analysis we found in total 78 sources, including the ones that were cut-out in the first step. The sources cover a flux range of 0.6% Crab to 103% Crab and have angular sizes between point-like and  $\sim 1^\circ$ . An analysis of the flux and size distribution of the sources and comparison against a simple sensitivity model, showed the HGPS is complete above 10% Crab for gamma-ray sources of all ( $< 1^\circ$ )

sizes. In particular it is complete with respect to small and bright sources, which are not affected by the HGPS sensitivity.

The association of HGPS sources with other MWL catalogs yielded a total number of 31 2FHL, 64 3FGL, 47 ATNF and 51 SNRCat objects. We only found 11 HGPS sources without MWL association, of which 4 still had a GeV counterpart. Seven sources remain *dark*, without any counterpart at all. 31 HGPS sources could be firmly identified. Among those were 12 PWN, 8 SNRs, 8 composite and 3 binary objects.

A comparison of the latitude distribution of the sources showed good agreement with the distribution of sources of the 2FHL, 3FGL, ATNF and SNRCat catalogs as well as the distribution of Galactic CO gas. In particular no significant differences at high latitudes were observed, indicating that the HGPS did not miss a large population of high latitude sources, albeit its reduced sensitivity off the Galactic plane.

The comparison of the longitude distribution of the sources against the distribution of CO gas showed general agreement, with an enhanced density of both in the inner Galaxy. A slightly enhanced density of gamma-ray sources in directions of the *Scutum* and between *Norma* and *Crux-Centaurus* spiral arm tangents could be observed, but no strong conclusion could be drawn because of the limited sample size.

An analysis of the log N - log S histogram of the sources in the flux range above 10% Crab yielded a slope of the distribution of  $-1.3 \pm 0.2$ . A value compatible with a 2-dimensional distribution of the sources in the Galactic disk. The power law extrapolation of the curve to lower fluxes allowed us to estimate an upper limit on the Galactic TeV source population of 600 sources above 1% Crab, even though with a large statistical error of a factor of  $\sim 2$ .

### **The H.E.S.S. Galactic Plane Survey compared to *Fermi*-LAT Observations**

In the second part (Chap. 3) of this work we compared the results from the HGPS analysis against *Fermi*-LAT observations of the same region. For this we used 84 months of *Fermi*-LAT data above 10 GeV, where the energy threshold was chosen as a compromise between sufficient signal statistics and angular resolution to limit source confusion. From this data we first generated flux maps in three energy bands; 10 – 30 GeV, 30 – 100 GeV and 100 – 2000 GeV. Those we combined into RGB images using a color mapping based on a reference power law with a spectral index of  $\Gamma - 2.3$ . Next we measured latitude and longitude flux profiles on the HGPS sky maps as well as *Fermi*-LAT images above 100 GeV in the region between  $b = \pm 2.5^\circ$ . Finally we estimated GeV flux points for all HGPS sources, by fitting the HGPS source morphology template to the GeV data in five different energy bands as well as the full energy range of 10 GeV to 2 TeV.

The qualitative comparison of the *Fermi*-LAT RGB images with significance contours of the HGPS measurement revealed 4 compact emission regions not detected at TeV energies. Three of those are associated to the known objects *Puppis A*, *MSH 15-56* and *Eta Carinae*, one is associated to the unidentified source *3FHL J1553.8-5325e*.

The comparison of the longitude flux profiles showed in general good agreement between the HGPS and *Fermi*-LAT measurement above 100 GeV. The largest differences were found in the region between  $\ell = 310^\circ$  and  $\ell = 270^\circ$  which showed increased gamma-ray emission in the *Fermi*-LAT profile, caused by extended underlying emission components with radii  $\sim 2.5^\circ$ . The origin of these emission regions is not known, but a confusion with the Galactic diffuse background model seems likely.

The determination of flux points for all HGPS sources yielded significant GeV emission with  $\sqrt{TS} > 5$  in the energy range between 10 GeV and 2000 GeV for 55 objects. Among those were 9 sources that did not have an associated 3FHL object. A closer inspection of those cases showed that the GeV flux points were compatible with the TeV spectra in most cases, but source confusion as well as confusion with the Galactic diffuse emission likely prevented the detection of a separate 3FHL source. For the remaining 23 HGPS sources we estimated GeV flux upper limits.

## 4.2 Outlook

### The H.E.S.S. Galactic Plane Survey

The method used for the re-analysis of the HGPS data presented in Chapter 2 of this work evolved from previous attempts to deal with a few challenges and bottlenecks during the creation of the catalog. Among the most important ones are the problem of *source confusion*, modeling of underlying *large scale emission* and modeling of *complex source morphologies*. In this analysis we handled those problems partly by manual intervention and the a priori decision to exclude complex emission regions such as the Galactic center region and shell-type SNRs. Even if most of the challenges will remain in future TeV catalog analyses, they can likely be tackled better with improved analysis methods.

The first obvious improvement is to use better event reconstruction methods such as semi-analytical model based shower reconstruction (de Naurois and Rolland, 2009) or template based methods (Parsons and Hinton, 2014). Those advanced methods typically have better angular resolution and improved sensitivity in general (factor of  $\sim 2$ ). The better angular resolution helps to separate close by sources and better sensitivity allows for a better analysis of weak objects.

In this analysis we used image based modeling for source detection and measuring positions, flux and sizes and the *adaptive ring* background estimate. The spectra were determined in a second step using a region based measurement and a *reflected region* background estimate. This procedure corresponds to the classical approach of analyzing TeV gamma-ray data. Even though it is an established method for the analysis of individual sources, it showed its limitations in the analysis of the survey dataset. The use of the *adaptive ring* background estimation subtracts large scale features in the data.

In GeV astronomy the standard analysis method involves a combined spectral and spatial likelihood fitting (also referred to as *cube style* analysis) using three dimensional models. This method typically shows better sensitivity in source detection and also helps to deal with the problem of source confusion, because it allows to separate nearby sources taking spectral information into account. One requirement for the use of the combined spatial and spectral analysis is the development of improved and energy-dependent background models.

### **The H.E.S.S. Galactic Plane Survey compared to *Fermi*-LAT Observations**

The obvious next step to continue the analysis in the second part of this work is to combine the GeV and TeV flux points in  $\chi^2$  likelihood fit. This would allow us to determine curvatures and peaks in the SED as well as identifying single or multiple components in the SEDs. This approach could be even taken further by combining GeV with TeV data in a *joint likelihood fit*. This will be possible in future with the standardization of data formats, as outlined in the introduction (Chapter 1) and the development of new open source analysis software such as *Gammapy*.

### **The CTA Galactic Plane Survey**

The next generation instrument and successor of current IACTs, is the Cherenkov Telescope Array (CTA). It will consist of a southern array of telescopes located in Chile and a northern array, located in La Palma. The proposed layout for the southern array includes 4 large,  $\sim 15$  mid sized and  $\sim 70$  small sized telescopes. The proposed layout for the northern array consists of 4 large,  $\sim 15$  mid sized telescope. The target sensitivity curve of CTA already been shown in Fig. 1.2. For 100 hrs observation time the sensitivity will be one order of magnitude better than the H.E.S.S. instrument. The sensitivity curve also extends to lower energies and closes the sensitivity gap to the *Fermi*-LAT instrument.

One of the key science projects of CTA will be an extended (in sensitivity as well as energy range and survey region) Galactic plane survey (Dubus et al., 2013). Figure B.14 shows a significance ( $\sqrt{TS}$ ) image of a simulated CTA dataset for the

HGPS region. For comparison a significance image of the HGPS is shown in Fig. B.13 with exactly the same color scale. The CTA survey image was created using the Galactic plane survey dataset from the first CTA data challenge<sup>1</sup>. It comprises  $\sim 1000$  hrs of observation time from the southern array and a selected energy range of 300 GeV to 100 TeV.

By qualitatively comparing both images one can see that even with  $\approx 30\%$  of the observation time of the HGPS, CTA will perform a much more sensitive survey of the Galactic plane. More sources are detected, among those are a few weak, shell-like SNRs at higher latitude. For comparison Fig. B.15 shows again a  $\sqrt{TS}$  image but using the same background model as it was used for the simulation. This image clearly demonstrates that with improved background estimation methods CTA, but also H.E.S.S., will be able to better study the large scale diffuse emission in the Galaxy.

---

<sup>1</sup><https://forge.in2p3.fr/projects/data-challenge-1-dc-1/wiki>



# Tables

# A

## Contents

---

A.1	HGPS Source Catalog Morphological Results . . . . .	100
A.2	HGPS Source Catalog Spectral Results . . . . .	104
A.3	HGPS Sources 3FHL Associations . . . . .	108
A.4	HGPS Sources GeV Flux Points . . . . .	112

---

**Tab. A.1.:** HGPS source catalog – summary of map-based measurements. The quantities are computed as described in Sect. 2.3.6. The values for sources marked with an asterisk are taken from external references, see Table 2.1 for details.

Name	Spatial Model	GLON deg	GLAT deg	$R_{95}$ deg	Size deg	$F(> 1 \text{ TeV})$ $10^{-12} \text{ cm}^{-2} \text{ s}^{-1}$	$F(> 1 \text{ TeV})$ % Crab	$\sqrt{TS}$
HESS J0835–455	3-Gaussian	263.96	–3.05	0.09	$0.58 \pm 0.052$	$15.36 \pm 0.53$	$67.7 \pm 2.4$	39.4
HESS J0852–463*	Shell	266.29	–1.24	–	1.00	$23.39 \pm 2.35$	$103.2 \pm 10.3$	–
HESS J1018–589 A	Gaussian	284.35	–1.67	0.03	$0.00 \pm 0.012$	$0.30 \pm 0.05$	$1.3 \pm 0.2$	8.7
HESS J1018–589 B	Gaussian	284.22	–1.77	0.12	$0.15 \pm 0.026$	$0.83 \pm 0.17$	$3.7 \pm 0.8$	7.6
HESS J1023–575	Gaussian	284.19	–0.40	0.05	$0.17 \pm 0.009$	$2.56 \pm 0.17$	$11.3 \pm 0.8$	21.4
HESS J1026–582	Gaussian	284.85	–0.52	0.12	$0.13 \pm 0.039$	$0.69 \pm 0.19$	$3.0 \pm 0.9$	7.3
HESS J1119–614	Gaussian	292.13	–0.53	0.06	$0.10 \pm 0.014$	$0.87 \pm 0.13$	$3.8 \pm 0.6$	10.2
HESS J1302–638	Gaussian	304.18	–1.00	0.02	$0.01 \pm 0.009$	$0.40 \pm 0.05$	$1.7 \pm 0.2$	16.6
HESS J1303–631	2-Gaussian	304.24	–0.35	0.04	$0.18 \pm 0.015$	$5.26 \pm 0.27$	$23.2 \pm 1.2$	54.5
HESS J1356–645	Gaussian	309.79	–2.50	0.08	$0.23 \pm 0.020$	$5.53 \pm 0.53$	$24.4 \pm 2.3$	17.3
HESS J1418–609	Gaussian	313.24	0.14	0.04	$0.11 \pm 0.011$	$3.01 \pm 0.31$	$13.3 \pm 1.4$	21.9
HESS J1420–607	Gaussian	313.58	0.27	0.03	$0.08 \pm 0.006$	$3.28 \pm 0.24$	$14.5 \pm 1.1$	27.6
HESS J1427–608	Gaussian	314.42	–0.16	0.04	$0.05 \pm 0.009$	$0.74 \pm 0.10$	$3.3 \pm 0.5$	10.5
HESS J1442–624*	Shell	315.43	–2.29	–	$0.30 \pm 0.020$	$2.44 \pm 0.67$	$10.8 \pm 3.0$	–
HESS J1457–593	Gaussian	318.35	–0.42	0.15	$0.33 \pm 0.045$	$2.50 \pm 0.40$	$11.0 \pm 1.8$	12.5
HESS J1458–608	Gaussian	317.95	–1.70	0.17	$0.37 \pm 0.031$	$2.44 \pm 0.30$	$10.8 \pm 1.3$	11.5
HESS J1503–582	Gaussian	319.57	0.29	0.14	$0.28 \pm 0.033$	$1.89 \pm 0.28$	$8.3 \pm 1.2$	10.8
HESS J1507–622	Gaussian	317.97	–3.48	0.06	$0.18 \pm 0.017$	$2.99 \pm 0.31$	$13.2 \pm 1.4$	17.0
HESS J1514–591	3-Gaussian	320.32	–1.19	0.03	$0.14 \pm 0.026$	$6.43 \pm 0.21$	$28.4 \pm 0.9$	42.0

Tab. A.1.: continued.

Name	Spatial Model	GLON	GLAT	$R_{95}$	Size	$F(> 1 \text{ TeV})$	$F(> 1 \text{ TeV})$	$\sqrt{TS}$
		deg	deg	deg	deg	$10^{-12} \text{ cm}^{-2} \text{ s}^{-1}$	% Crab	
HESS J1534–571*	Shell	323.70	–1.02	–	$0.40 \pm 0.040$	$1.98 \pm 0.23$	$8.7 \pm 1.0$	–
HESS J1554–550	Gaussian	327.16	–1.08	0.03	$0.02 \pm 0.009$	$0.36 \pm 0.06$	$1.6 \pm 0.3$	9.1
HESS J1614–518*	Shell	331.47	–0.60	–	$0.42 \pm 0.010$	$5.87 \pm 0.42$	$25.9 \pm 1.9$	–
HESS J1616–508	2-Gaussian	332.48	–0.17	0.12	$0.23 \pm 0.035$	$8.48 \pm 0.44$	$37.4 \pm 1.9$	34.3
HESS J1626–490	Gaussian	334.82	–0.12	0.14	$0.20 \pm 0.035$	$1.65 \pm 0.33$	$7.3 \pm 1.5$	8.4
HESS J1632–478	Gaussian	336.39	0.26	0.08	$0.18 \pm 0.020$	$2.93 \pm 0.51$	$12.9 \pm 2.3$	14.8
HESS J1634–472	Gaussian	337.12	0.26	0.06	$0.17 \pm 0.013$	$2.90 \pm 0.37$	$12.8 \pm 1.6$	17.8
HESS J1640–465	2-Gaussian	338.28	–0.04	0.05	$0.11 \pm 0.034$	$3.33 \pm 0.19$	$14.7 \pm 0.8$	41.1
HESS J1641–463	Gaussian	338.52	0.08	0.05	$0.04 \pm 0.013$	$0.27 \pm 0.06$	$1.2 \pm 0.3$	6.9
HESS J1646–458	Gaussian	339.33	–0.78	0.15	$0.50 \pm 0.030$	$5.48 \pm 0.46$	$24.2 \pm 2.0$	18.6
HESS J1702–420	Gaussian	344.23	–0.19	0.08	$0.20 \pm 0.025$	$3.91 \pm 0.65$	$17.3 \pm 2.9$	15.0
HESS J1708–410	Gaussian	345.67	–0.44	0.03	$0.06 \pm 0.006$	$0.88 \pm 0.09$	$3.9 \pm 0.4$	17.0
HESS J1708–443	Gaussian	343.07	–2.32	0.14	$0.28 \pm 0.031$	$2.28 \pm 0.32$	$10.1 \pm 1.4$	11.0
HESS J1713–381	Gaussian	348.62	0.38	0.05	$0.09 \pm 0.017$	$0.65 \pm 0.13$	$2.9 \pm 0.6$	11.6
HESS J1713–397*	Shell	347.31	–0.46	–	0.50	$16.88 \pm 0.82$	$74.4 \pm 3.6$	–
HESS J1714–385	Gaussian	348.42	0.14	0.04	$0.03 \pm 0.011$	$0.25 \pm 0.05$	$1.1 \pm 0.2$	8.6
HESS J1718–374*	Point-Like	349.72	0.17	–	–	$0.12 \pm 0.04$	$0.6 \pm 0.2$	–
HESS J1718–385	Gaussian	348.88	–0.48	0.06	$0.12 \pm 0.015$	$0.80 \pm 0.14$	$3.5 \pm 0.6$	11.6
HESS J1729–345	Gaussian	353.39	–0.02	0.13	$0.19 \pm 0.031$	$0.86 \pm 0.17$	$3.8 \pm 0.8$	8.4
HESS J1731–347*	Shell	353.54	–0.67	–	$0.27 \pm 0.020$	$2.01 \pm 0.15$	$8.8 \pm 0.6$	–

Tab. A.1.: continued.

Name	Spatial Model	GLON deg	GLAT deg	$R_{95}$ deg	Size deg	$F(> 1 \text{ TeV})$ $10^{-12} \text{ cm}^{-2} \text{ s}^{-1}$	$F(> 1 \text{ TeV})$ % Crab	$\sqrt{TS}$
HESS J1741–302*	Point-Like	358.28	0.05	–	–	$0.16 \pm 0.04$	$0.7 \pm 0.2$	–
HESS J1745–290*	Point-Like	359.94	–0.04	–	–	$1.70 \pm 0.08$	$7.5 \pm 0.3$	–
HESS J1745–303	Gaussian	358.64	–0.56	0.11	$0.18 \pm 0.020$	$0.94 \pm 0.21$	$4.1 \pm 0.9$	13.7
HESS J1746–285*	Point-Like	0.14	–0.11	–	–	$0.15 \pm 0.05$	$0.7 \pm 0.2$	–
HESS J1746–308	Gaussian	358.45	–1.11	0.15	$0.16 \pm 0.036$	$0.68 \pm 0.22$	$3.0 \pm 1.0$	8.7
HESS J1747–248	Gaussian	3.78	1.71	0.06	$0.06 \pm 0.012$	$0.29 \pm 0.05$	$1.3 \pm 0.2$	8.1
HESS J1747–281*	Point-Like	0.87	0.08	–	–	$0.60 \pm 0.13$	$2.6 \pm 0.6$	–
HESS J1800–240	Gaussian	5.96	–0.42	0.13	$0.32 \pm 0.039$	$2.44 \pm 0.35$	$10.8 \pm 1.5$	12.6
HESS J1801–233*	Gaussian	6.66	–0.27	–	$0.17 \pm 0.030$	$0.45 \pm 0.10$	$2.0 \pm 0.4$	–
HESS J1804–216	2-Gaussian	8.38	–0.09	0.15	$0.24 \pm 0.034$	$5.88 \pm 0.27$	$25.9 \pm 1.2$	34.2
HESS J1808–204	Gaussian	10.01	–0.24	0.07	$0.06 \pm 0.014$	$0.19 \pm 0.04$	$0.8 \pm 0.2$	6.4
HESS J1809–193	3-Gaussian	11.11	–0.02	0.21	$0.40 \pm 0.048$	$5.27 \pm 0.29$	$23.2 \pm 1.3$	26.6
HESS J1813–126	Gaussian	17.31	2.49	0.19	$0.21 \pm 0.032$	$1.08 \pm 0.24$	$4.8 \pm 1.1$	6.1
HESS J1813–178	Gaussian	12.82	–0.03	0.02	$0.05 \pm 0.004$	$1.98 \pm 0.15$	$8.7 \pm 0.7$	26.4
HESS J1818–154	Gaussian	15.41	0.16	0.04	$0.00 \pm 0.046$	$0.17 \pm 0.04$	$0.7 \pm 0.2$	5.6
HESS J1825–137	3-Gaussian	17.53	–0.62	0.20	$0.46 \pm 0.032$	$18.41 \pm 0.56$	$81.2 \pm 2.5$	76.5
HESS J1826–130	Gaussian	18.48	–0.39	0.10	$0.15 \pm 0.021$	$0.86 \pm 0.17$	$3.8 \pm 0.7$	9.4
HESS J1826–148	Gaussian	16.88	–1.29	0.02	$0.01 \pm 0.004$	$1.28 \pm 0.04$	$5.7 \pm 0.2$	58.1
HESS J1828–099	Gaussian	21.49	0.38	0.05	$0.05 \pm 0.011$	$0.43 \pm 0.07$	$1.9 \pm 0.3$	8.9
HESS J1832–085	Gaussian	23.21	0.29	0.05	$0.02 \pm 0.012$	$0.21 \pm 0.05$	$0.9 \pm 0.2$	5.9

Tab. A.1.: continued.

Name	Spatial Model	GLON	GLAT	$R_{95}$	Size	$F(> 1 \text{ TeV})$	$F(> 1 \text{ TeV})$	$\sqrt{TS}$
		deg	deg	deg	deg	$10^{-12} \text{ cm}^{-2} \text{ s}^{-1}$	% Crab	
HESS J1832–093	Gaussian	22.48	–0.16	0.03	$0.00 \pm 0.012$	$0.17 \pm 0.03$	$0.8 \pm 0.1$	6.8
HESS J1833–105	Gaussian	21.50	–0.90	0.03	$0.02 \pm 0.017$	$0.39 \pm 0.07$	$1.7 \pm 0.3$	11.4
HESS J1834–087	2-Gaussian	23.26	–0.33	0.06	$0.21 \pm 0.037$	$3.34 \pm 0.24$	$14.7 \pm 1.1$	21.0
HESS J1837–069	3-Gaussian	25.15	–0.09	0.05	$0.36 \pm 0.031$	$12.05 \pm 0.45$	$53.1 \pm 2.0$	41.5
HESS J1841–055	2-Gaussian	26.71	–0.23	0.17	$0.41 \pm 0.033$	$10.16 \pm 0.42$	$44.8 \pm 1.9$	33.9
HESS J1843–033	2-Gaussian	28.90	0.07	0.20	$0.24 \pm 0.063$	$2.88 \pm 0.30$	$12.7 \pm 1.3$	16.0
HESS J1844–030	Gaussian	29.41	0.09	0.04	$0.02 \pm 0.013$	$0.26 \pm 0.05$	$1.1 \pm 0.2$	7.3
HESS J1846–029	Gaussian	29.71	–0.24	0.03	$0.01 \pm 0.013$	$0.45 \pm 0.05$	$2.0 \pm 0.2$	13.8
HESS J1848–018	Gaussian	30.92	–0.21	0.12	$0.25 \pm 0.032$	$1.74 \pm 0.35$	$7.7 \pm 1.6$	12.0
HESS J1849–000	Gaussian	32.61	0.53	0.06	$0.09 \pm 0.015$	$0.53 \pm 0.09$	$2.3 \pm 0.4$	9.1
HESS J1852–000	Gaussian	33.11	–0.13	0.18	$0.28 \pm 0.042$	$1.30 \pm 0.25$	$5.7 \pm 1.1$	9.0
HESS J1857+026	2-Gaussian	36.06	–0.06	0.10	$0.26 \pm 0.056$	$3.77 \pm 0.40$	$16.6 \pm 1.8$	16.8
HESS J1858+020	Gaussian	35.54	–0.58	0.07	$0.08 \pm 0.016$	$0.53 \pm 0.11$	$2.3 \pm 0.5$	8.4
HESS J1908+063	Gaussian	40.55	–0.84	0.13	$0.49 \pm 0.027$	$6.53 \pm 0.50$	$28.8 \pm 2.2$	19.0
HESS J1911+090*	Point-Like	43.26	–0.19	–	–	$0.15 \pm 0.03$	$0.6 \pm 0.1$	–
HESS J1912+101*	Shell	44.46	–0.13	–	$0.49 \pm 0.040$	$2.49 \pm 0.35$	$11.0 \pm 1.5$	–
HESS J1923+141	Gaussian	49.08	–0.40	0.10	$0.12 \pm 0.019$	$0.78 \pm 0.15$	$3.5 \pm 0.7$	7.3
HESS J1930+188	Gaussian	54.06	0.27	0.05	$0.02 \pm 0.025$	$0.29 \pm 0.09$	$1.3 \pm 0.4$	5.8
HESS J1943+213	Gaussian	57.78	–1.30	0.05	$0.03 \pm 0.022$	$0.32 \pm 0.10$	$1.4 \pm 0.4$	5.9

**Tab. A.2.:** HGPS source catalog – summary of spectral measurements. The quantities are computed as described in Sect. 2.3.7. The values for sources marked with an asterisk are taken from external references, see Table 2.1 for details.

Name	$R_{\text{spec}}$	$E_{\text{min}}$	$F(> 1 \text{ TeV})$	$\Gamma$	$\lambda$	Contain.	Contam.	CF
	deg	TeV	$10^{-12} \text{ cm}^{-2} \text{ s}^{-1}$		$\text{TeV}^{-1}$	%	%	%
HESS J0835–455	0.50	0.3	$17.43 \pm 1.40$	$1.35 \pm 0.08$	$0.08 \pm 0.01$	37	0	271.4
HESS J0852-463*	1.00	0.3	$23.39 \pm 2.35$	$1.81 \pm 0.08$	$0.15 \pm 0.03$	–	–	–
HESS J1018–589 A	0.15	0.4	$0.21 \pm 0.03$	$2.24 \pm 0.13$	–	92	42	63.5
HESS J1018–589 B	0.25	0.5	$0.70 \pm 0.09$	$2.20 \pm 0.09$	–	70	32	96.8
HESS J1023–575	0.27	0.4	$2.41 \pm 0.13$	$2.36 \pm 0.05$	–	70	5	135.5
HESS J1026–582	0.22	0.5	$0.66 \pm 0.09$	$1.81 \pm 0.10$	–	70	11	126.9
HESS J1119–614	0.18	0.4	$0.92 \pm 0.09$	$2.64 \pm 0.12$	–	70	4	137.9
HESS J1302–638	0.15	0.4	$0.39 \pm 0.03$	$2.59 \pm 0.09$	–	90	40	67.4
HESS J1303–631	0.29	0.4	$5.21 \pm 0.35$	$2.04 \pm 0.06$	$0.07 \pm 0.01$	70	5	136.2
HESS J1356–645	0.37	0.5	$4.39 \pm 0.39$	$2.20 \pm 0.08$	–	70	0	142.8
HESS J1418–609	0.19	0.4	$2.69 \pm 0.15$	$2.26 \pm 0.05$	–	70	6	134.7
HESS J1420–607	0.15	0.4	$2.77 \pm 0.15$	$2.20 \pm 0.05$	–	70	4	138.5
HESS J1427–608	0.15	0.4	$0.48 \pm 0.09$	$2.85 \pm 0.22$	–	84	5	113.3
HESS J1442-624*	0.41	0.4	$2.44 \pm 0.67$	$1.59 \pm 0.22$	$0.29 \pm 0.10$	–	–	–
HESS J1457–593	0.50	0.5	$4.31 \pm 0.56$	$2.52 \pm 0.14$	–	67	10	135.1
HESS J1458–608	0.50	0.5	$1.40 \pm 0.35$	$1.81 \pm 0.14$	–	58	1	170.2
HESS J1503–582	0.45	0.4	$3.07 \pm 0.24$	$2.68 \pm 0.08$	–	70	8	131.1
HESS J1507–622	0.29	0.5	$2.60 \pm 0.21$	$2.22 \pm 0.07$	–	70	0	142.9
HESS J1514–591	0.22	0.4	$5.72 \pm 0.42$	$2.05 \pm 0.06$	$0.05 \pm 0.01$	70	0	142.8

Tab. A.2.: continued.

Name	$R_{\text{spec}}$	$E_{\text{min}}$	$F(> 1 \text{ TeV})$	$\Gamma$	$\lambda$	Contain.	Contam.	CF
	deg	TeV	$10^{-12} \text{ cm}^{-2} \text{ s}^{-1}$		$\text{TeV}^{-1}$	%	%	%
HESS J1534-571*	0.47	0.4	$1.98 \pm 0.23$	$2.51 \pm 0.09$	–	–	–	–
HESS J1554–550	0.15	0.4	$0.29 \pm 0.06$	$2.19 \pm 0.17$	–	92	0	108.6
HESS J1614-518*	0.49	0.3	$5.87 \pm 0.42$	$2.42 \pm 0.06$	–	–	–	–
HESS J1616–508	0.36	0.3	$7.99 \pm 0.55$	$2.32 \pm 0.06$	–	70	2	139.9
HESS J1626–490	0.32	0.3	$2.13 \pm 0.26$	$2.47 \pm 0.11$	–	70	11	126.9
HESS J1632–478	0.30	0.3	$2.32 \pm 0.16$	$2.52 \pm 0.06$	–	70	34	93.9
HESS J1634–472	0.28	0.3	$2.87 \pm 0.15$	$2.31 \pm 0.05$	–	70	31	98.8
HESS J1640–465	0.16	0.3	$2.84 \pm 0.73$	$2.12 \pm 0.13$	$0.24 \pm 0.09$	70	4	137.6
HESS J1641–463	0.15	0.3	$0.22 \pm 0.03$	$2.47 \pm 0.11$	–	90	58	47.4
HESS J1646–458	0.50	0.3	$5.81 \pm 0.73$	$2.54 \pm 0.13$	–	39	2	254.4
HESS J1702–420	0.32	0.2	$4.45 \pm 0.36$	$2.09 \pm 0.07$	–	70	14	122.9
HESS J1708–410	0.15	0.2	$0.65 \pm 0.05$	$2.54 \pm 0.07$	–	81	9	112.8
HESS J1708–443	0.44	0.2	$3.32 \pm 0.37$	$2.17 \pm 0.08$	–	70	0	142.9
HESS J1713–381	0.16	0.2	$0.52 \pm 0.07$	$2.74 \pm 0.12$	–	70	15	121.4
HESS J1713-397*	0.60	0.2	$16.88 \pm 0.82$	$2.06 \pm 0.02$	$0.08 \pm 0.01$	–	–	–
HESS J1714–385	0.15	0.2	$0.21 \pm 0.03$	$2.52 \pm 0.12$	–	91	47	57.9
HESS J1718-374*	0.10	0.2	$0.12 \pm 0.04$	$2.80 \pm 0.27$	–	–	–	–
HESS J1718–385	0.20	0.2	$0.62 \pm 0.14$	$0.98 \pm 0.22$	$0.09 \pm 0.03$	70	23	110.4
HESS J1729–345	0.30	0.2	$0.82 \pm 0.09$	$2.43 \pm 0.09$	–	70	25	108.0
HESS J1731-347*	0.30	0.2	$2.01 \pm 0.15$	$2.32 \pm 0.06$	–	–	–	–

Tab. A.2.: continued.

Name	$R_{\text{spec}}$	$E_{\text{min}}$	$F(> 1 \text{ TeV})$	$\Gamma$	$\lambda$	Contain.	Contam.	CF
	deg	TeV	$10^{-12} \text{ cm}^{-2} \text{ s}^{-1}$		$\text{TeV}^{-1}$	%	%	%
HESS J1741-302*	0.10	0.4	$0.16 \pm 0.04$	$2.30 \pm 0.20$	–	–	–	–
HESS J1745-290*	0.10	–	$1.70 \pm 0.08$	$2.14 \pm 0.02$	$0.09 \pm 0.02$	–	–	–
HESS J1745–303	0.29	0.2	$1.09 \pm 0.08$	$2.57 \pm 0.06$	–	70	30	99.6
HESS J1746-285*	0.09	0.3	$0.15 \pm 0.05$	$2.17 \pm 0.24$	–	–	–	–
HESS J1746–308	0.26	0.2	$0.30 \pm 0.09$	$3.27 \pm 0.22$	–	70	23	110.2
HESS J1747–248	0.15	0.2	$0.27 \pm 0.04$	$2.36 \pm 0.14$	–	83	0	120.5
HESS J1747-281*	0.10	0.3	$0.60 \pm 0.13$	$2.40 \pm 0.11$	–	–	–	–
HESS J1800–240	0.50	0.2	$2.90 \pm 0.31$	$2.47 \pm 0.09$	–	70	17	118.9
HESS J1801-233*	0.20	0.3	$0.45 \pm 0.10$	$2.66 \pm 0.27$	–	–	–	–
HESS J1804–216	0.38	0.2	$5.12 \pm 0.23$	$2.69 \pm 0.04$	–	70	8	131.6
HESS J1808–204	0.15	0.2	$0.19 \pm 0.03$	$2.19 \pm 0.14$	–	85	27	86.1
HESS J1809–193	0.50	0.2	$5.37 \pm 0.45$	$2.38 \pm 0.07$	–	54	16	154.2
HESS J1813–126	0.34	0.2	$1.04 \pm 0.21$	$1.99 \pm 0.14$	–	70	0	143.6
HESS J1813–178	0.15	0.2	$2.12 \pm 0.40$	$1.64 \pm 0.12$	$0.14 \pm 0.04$	89	14	96.6
HESS J1818–154	0.15	0.2	$0.23 \pm 0.05$	$2.21 \pm 0.15$	–	95	29	74.6
HESS J1825–137	0.50	0.2	$19.15 \pm 1.85$	$2.15 \pm 0.06$	$0.07 \pm 0.02$	47	3	203.6
HESS J1826–130	0.25	0.2	$1.14 \pm 0.16$	$2.04 \pm 0.10$	–	70	41	84.4
HESS J1826–148	0.15	0.2	$0.84 \pm 0.08$	$2.32 \pm 0.07$	–	95	10	94.5
HESS J1828–099	0.15	0.2	$0.38 \pm 0.05$	$2.25 \pm 0.12$	–	89	11	100.3
HESS J1832–085	0.15	0.2	$0.23 \pm 0.04$	$2.38 \pm 0.14$	–	94	27	77.7

Tab. A.2.: continued.

Name	$R_{\text{spec}}$	$E_{\text{min}}$	$F(> 1 \text{ TeV})$	$\Gamma$	$\lambda$	Contain.	Contam.	CF
	deg	TeV	$10^{-12} \text{ cm}^{-2} \text{ s}^{-1}$		$\text{TeV}^{-1}$	%	%	%
HESS J1832–093	0.15	0.2	$0.16 \pm 0.04$	$2.54 \pm 0.22$	–	95	25	78.9
HESS J1833–105	0.15	0.2	$0.26 \pm 0.06$	$2.42 \pm 0.19$	–	94	2	104.6
HESS J1834–087	0.34	0.2	$2.47 \pm 0.22$	$2.61 \pm 0.07$	–	70	8	131.2
HESS J1837–069	0.50	0.2	$11.55 \pm 0.49$	$2.54 \pm 0.04$	–	63	8	145.6
HESS J1841–055	0.50	0.2	$11.58 \pm 1.36$	$2.21 \pm 0.07$	$0.09 \pm 0.03$	51	10	178.3
HESS J1843–033	0.38	0.2	$3.04 \pm 0.20$	$2.15 \pm 0.05$	–	70	15	121.0
HESS J1844–030	0.15	0.2	$0.28 \pm 0.04$	$2.48 \pm 0.12$	–	94	28	77.0
HESS J1846–029	0.15	0.2	$0.48 \pm 0.05$	$2.41 \pm 0.09$	–	94	10	95.8
HESS J1848–018	0.39	0.3	$1.11 \pm 0.15$	$2.57 \pm 0.11$	–	70	26	105.9
HESS J1849–000	0.16	0.3	$0.58 \pm 0.07$	$1.97 \pm 0.09$	–	70	9	129.9
HESS J1852–000	0.44	0.3	$1.21 \pm 0.15$	$2.17 \pm 0.10$	–	70	25	106.8
HESS J1857+026	0.41	0.3	$4.00 \pm 0.29$	$2.57 \pm 0.06$	–	70	11	127.6
HESS J1858+020	0.15	0.3	$0.47 \pm 0.06$	$2.39 \pm 0.12$	–	72	14	120.6
HESS J1908+063	0.50	0.3	$8.35 \pm 0.57$	$2.26 \pm 0.06$	–	41	2	240.9
HESS J1911+090*	0.10	0.3	$0.15 \pm 0.03$	$3.14 \pm 0.24$	–	–	–	–
HESS J1912+101*	0.56	0.7	$2.49 \pm 0.35$	$2.56 \pm 0.09$	–	–	–	–
HESS J1923+141	0.21	0.4	$0.69 \pm 0.11$	$2.55 \pm 0.17$	–	70	3	138.7
HESS J1930+188	0.15	0.5	$0.32 \pm 0.07$	$2.59 \pm 0.26$	–	92	8	100.3
HESS J1943+213	0.15	0.6	$0.39 \pm 0.08$	$2.83 \pm 0.22$	–	91	1	109.0

**Tab. A.3.:** HGPS source catalog – summary of associations with 3FHL sources. Source class as well as identified objects are listed for both catalogs.

Name HGPS	Source Class HGPS	Identified Object	Name 3FHL	Source Class 3FHL	TeV Association 3FHL
HESS J0835-455	PWN	Vela X	3FHL J0835.3-4510	PSR	Vela Pulsar
HESS J0852-463	SNR	Vela Junior	3FHL J0851.9-4620e	SNR	RX J0852.0-4622
HESS J1018-589 A	Binary	1FGL J1018.6-5856	3FHL J1018.8-5857	HMB	HESS J1018-589 A
HESS J1018-589 B	Unid	–	3FHL J1016.2-5857	psr	HESS J1018-589 B
HESS J1023-575	Unid	–	3FHL J1023.3-5747e	sfr	Westerlund 2
HESS J1026-582	Unid	–	–	–	–
HESS J1119-614	Composite	PSR J1119-6127	3FHL J1119.0-6127	PSR	SNR G292.2-00.5
HESS J1302-638	Binary	PSR B1259-63	3FHL J1303.0-6350	HMB	PSR B1259-63
HESS J1303-631	PWN	PSR J1301-6305	3FHL J1303.0-6312e	PWN	HESS J1303-631
HESS J1356-645	PWN	PSR J1357-6429	3FHL J1355.1-6420e	PWN	HESS J1356-645
HESS J1418-609	PWN	PSR J1418-6058	3FHL J1418.6-6058	PSR	Kookaburra (Rabbit)
HESS J1420-607	PWN	PSR J1420-6048	3FHL J1420.3-6046e	PWN	HESS J1420-607
HESS J1427-608	Unid	–	3FHL J1427.9-6054	–	HESS J1427-608
HESS J1442-624	SNR	RCW 86	3FHL J1443.0-6227e	SNR	RCW 86
HESS J1457-593	Unid	–	–	–	–
HESS J1458-608	Unid	–	3FHL J1459.4-6052	PSR	HESS J1458-608
HESS J1503-582	Unid	–	–	–	–
HESS J1507-622	Unid	–	3FHL J1507.9-6228e	unknown	HESS J1507-622
HESS J1514-591	PWN	MSH 15-52	3FHL J1514.2-5909e	PWN	MSH 15-52
HESS J1534-571	SNR	G323.7-01.0	–	–	–
HESS J1554-550	PWN	G327.1-01.1	–	–	–

Tab. A.3.: continued.

Name HGPS	Source Class HGPS	Identified Object	Name 3FHL	Source Class 3FHL	TeV Association 3FHL
HESS J1614-518	Unid	–	3FHL J1615.3-5146e	spp	HESS J1614-518
HESS J1616-508	Unid	–	3FHL J1616.2-5054e	PWN	HESS J1616-508
HESS J1626-490	Unid	–	3FHL J1626.3-4915	–	–
HESS J1632-478	Unid	–	3FHL J1631.6-4756e	pwn	HESS J1632-478
HESS J1632-478	Unid	–	3FHL J1633.0-4746e	spp	HESS J1632-478
HESS J1634-472	Unid	–	–	–	–
HESS J1640-465	Composite	G338.3-0.0	3FHL J1640.6-4633	spp	HESS J1640-465
HESS J1641-463	Unid	–	3FHL J1641.1-4619	spp	HESS J1641-463
HESS J1646-458	Unid	–	3FHL J1648.5-4610	PSR	–
HESS J1702-420	Unid	–	–	–	–
HESS J1708-410	Unid	–	–	–	–
HESS J1708-443	Unid	–	3FHL J1709.7-4429	PSR	–
HESS J1713-381	Unid	–	3FHL J1714.0-3811	snr	CTB 37B
HESS J1713-397	SNR	RX J1713.7-3946	3FHL J1713.5-3945e	SNR	RX J1713.7-3946
HESS J1714-385	Composite	CTB 37A	3FHL J1714.4-3829	snr	CTB 37A
HESS J1718-374	SNR	G349.7+0.2	3FHL J1718.0-3726	snr	SNR G349.7+00.2
HESS J1718-385	Unid	–	–	–	–
HESS J1729-345	Unid	–	–	–	–
HESS J1731-347	SNR	G353.6-0.7	–	–	–
HESS J1741-302	Unid	–	–	–	–
HESS J1745-290	Unid	–	3FHL J1745.6-2900	spp	Galactic Centre

Tab. A.3.: continued.

Name HGPS	Source Class HGPS	Identified Object	Name 3FHL	Source Class 3FHL	TeV Association 3FHL
HESS J1745-303	Unid	–	3FHL J1745.8-3028e	–	HESS J1745-303
HESS J1746-285	Unid	–	3FHL J1746.2-2852	pwn	HESS J1746-285
HESS J1746-308	Unid	–	–	–	–
HESS J1747-248	Unid	–	3FHL J1748.0-2446	glc	Terzan 5
HESS J1747-281	PWN	G0.9+0.1	–	–	–
HESS J1800-240	Unid	–	3FHL J1800.5-2343e	SNR	W 28
HESS J1800-240	Unid	–	3FHL J1800.7-2357	–	HESS J1800-240B
HESS J1801-233	SNR	W 28	3FHL J1801.6-2327	snr	W 28
HESS J1804-216	Unid	–	3FHL J1803.1-2148	PSR	–
HESS J1804-216	Unid	–	3FHL J1804.7-2144e	snr	HESS J1804-216
HESS J1808-204	Unid	–	–	–	–
HESS J1809-193	Unid	–	3FHL J1811.5-1927	psr	–
HESS J1813-126	Unid	–	3FHL J1813.4-1245	PSR	HESS J1813-126
HESS J1813-178	Composite	PSR J1813-1749	–	–	–
HESS J1818-154	PWN	G015.4+00.1	–	–	–
HESS J1825-137	PWN	PSR J1826-1334	3FHL J1824.5-1351e	PWN	HESS J1825-137
HESS J1826-130	Unid	–	3FHL J1826.1-1256	PSR	HESS J1826-130
HESS J1826-148	Binary	LS 5039	3FHL J1826.2-1451	HMB	LS 5039
HESS J1828-099	Unid	–	–	–	–
HESS J1832-085	Unid	–	–	–	–
HESS J1832-093	Unid	–	–	–	–

Tab. A.3.: continued.

Name HGPS	Source Class HGPS	Identified Object	Name 3FHL	Source Class 3FHL	TeV Association 3FHL
HESS J1833-105	Composite	G21.5-0.9	3FHL J1833.6-1034	PSR	HESS J1833-105
HESS J1834-087	Composite	W41	3FHL J1834.5-0846e	spp	HESS J1834-087
HESS J1837-069	PWN	PSR J1838-0655	3FHL J1836.5-0651e	pwn	HESS J1837-069
HESS J1837-069	PWN	PSR J1838-0655	3FHL J1838.9-0704e	pwn	HESS J1837-069
HESS J1841-055	Unid	–	3FHL J1838.9-0537	PSR	–
HESS J1841-055	Unid	–	3FHL J1839.4-0553	–	–
HESS J1841-055	Unid	–	3FHL J1840.9-0532e	PWN	HESS J1841-055
HESS J1843-033	Unid	–	–	–	–
HESS J1844-030	Unid	–	–	–	–
HESS J1846-029	Composite	PSR J1846-0258	–	–	–
HESS J1848-018	Unid	–	–	–	–
HESS J1849-000	PWN	PSR J1849-0001	–	–	–
HESS J1852-000	Unid	–	–	–	–
HESS J1857+026	Unid	–	3FHL J1857.7+0246e	pwn	HESS J1857+026
HESS J1858+020	Unid	–	–	–	–
HESS J1908+063	Unid	–	3FHL J1907.9+0602	PSR	–
HESS J1911+090	SNR	W49B	3FHL J1911.0+0905	snr	W 49B
HESS J1912+101	Unid	–	–	–	–
HESS J1923+141	Unid	–	3FHL J1923.2+1408e	SNR	W 51
HESS J1930+188	Composite	G54.1+0.3	–	–	–
HESS J1943+213	Unid	–	3FHL J1943.9+2117	bcu	HESS J1943+213

**Tab. A.4.:** HGPS source catalog – GeV band flux points. The indices correspond to the following energy ranges: 1: 10 – 20 GeV, 2: 20 – 50 GeV, 3: 50 – 150 GeV, 4: 150 – 500 GeV and 5: 500 – 2000 GeV. Flux upper limits are given when  $\sqrt{TS} < 1$  for the corresponding energy band. The flux points for *HESS J0835-455* are not listed, because the fit to the data fails for technical reasons. The region is dominated by the emission from the *Vela Pulsar* which is two orders of magnitude higher than the flux of an average GeV source.

Name	$F_1$	$\sqrt{TS}_1$	$F_2$	$\sqrt{TS}_2$	$F_3$	$\sqrt{TS}_3$	$F_4$	$\sqrt{TS}_4$	$F_5$	$\sqrt{TS}_5$
HESS J0835-455	– ± –	–	– ± –	–	– ± –	–	– ± –	–	– ± –	–
HESS J0852-463	$6.22 \pm 0.55$	15.5	$5.27 \pm 0.47$	18.9	$3.32 \pm 0.34$	19.0	$1.12 \pm 0.20$	11.6	$0.55 \pm 0.15$	8.9
HESS J1018-589	$1.63 \pm 0.29$	11.9	$0.70 \pm 0.20$	7.3	$0.22 \pm 0.11$	4.5	$0.07 \pm 0.06$	3.3	<0.13	-0.0
HESS J1018-589	$2.80 \pm 0.36$	12.7	$1.02 \pm 0.23$	7.8	$0.37 \pm 0.13$	5.5	$0.08 \pm 0.07$	2.3	$0.05 \pm 0.06$	2.0
HESS J1023-575	$3.92 \pm 0.44$	14.4	$1.93 \pm 0.30$	11.2	$0.48 \pm 0.15$	5.6	$0.37 \pm 0.13$	6.3	$0.08 \pm 0.07$	2.4
HESS J1026-582	$4.78 \pm 0.48$	17.3	$0.94 \pm 0.23$	6.5	$0.13 \pm 0.10$	1.9	$0.10 \pm 0.08$	2.7	<0.16	0.9
HESS J1119-614	$1.30 \pm 0.26$	8.4	$0.91 \pm 0.22$	7.7	$0.28 \pm 0.13$	4.2	$0.16 \pm 0.08$	4.5	$0.04 \pm 0.05$	1.9
HESS J1302-638	<0.33	0.6	$0.29 \pm 0.13$	4.7	$0.16 \pm 0.11$	2.8	<0.08	-0.2	– ± –	–
HESS J1303-631	$1.40 \pm 0.37$	4.7	$2.07 \pm 0.34$	9.6	$0.61 \pm 0.18$	5.7	$0.39 \pm 0.14$	5.8	<0.14	0.6
HESS J1356-645	$0.65 \pm 0.24$	3.5	$0.77 \pm 0.21$	5.8	$0.32 \pm 0.13$	4.4	$0.13 \pm 0.09$	3.1	$0.06 \pm 0.07$	2.2
HESS J1418-609	$5.23 \pm 0.52$	15.8	$1.21 \pm 0.27$	6.7	$0.84 \pm 0.21$	6.8	$0.24 \pm 0.11$	4.1	$0.10 \pm 0.07$	3.3
HESS J1420-607	$3.82 \pm 0.45$	13.0	$0.97 \pm 0.23$	6.9	$0.72 \pm 0.19$	7.1	$0.28 \pm 0.12$	5.0	$0.06 \pm 0.07$	1.8
HESS J1427-608	$0.60 \pm 0.22$	4.0	$0.45 \pm 0.17$	4.4	$0.04 \pm 0.06$	1.6	<0.20	0.9	– ± –	–
HESS J1442-624	$0.57 \pm 0.19$	4.4	$0.58 \pm 0.17$	6.4	$0.35 \pm 0.13$	5.5	$0.08 \pm 0.07$	2.5	$0.04 \pm 0.06$	1.1
HESS J1457-593	<0.98	-0.1	$0.58 \pm 0.35$	1.8	<0.40	0.2	<0.15	-0.7	$0.08 \pm 0.08$	1.5
HESS J1458-608	$1.33 \pm 0.38$	4.2	$0.87 \pm 0.27$	4.1	<0.31	0.6	<0.13	-0.6	$0.12 \pm 0.09$	2.6
HESS J1503-582	$1.05 \pm 0.43$	2.8	$0.59 \pm 0.28$	2.5	$0.28 \pm 0.17$	2.1	$0.12 \pm 0.09$	1.9	<0.17	0.8
HESS J1507-622	$0.81 \pm 0.23$	5.1	$0.81 \pm 0.19$	7.4	$0.41 \pm 0.14$	5.8	$0.15 \pm 0.08$	4.6	<0.15	0.2
HESS J1514-591	$3.14 \pm 0.40$	12.9	$2.05 \pm 0.30$	12.8	$1.10 \pm 0.21$	10.7	$0.47 \pm 0.14$	7.8	$0.16 \pm 0.09$	4.3

Tab. A.4.: continued.

Name	$F_1$	$\sqrt{TS_1}$	$F_2$	$\sqrt{TS_2}$	$F_3$	$\sqrt{TS_3}$	$F_4$	$\sqrt{TS_4}$	$F_5$	$\sqrt{TS_5}$
HESS J1534-571	$0.53 \pm 0.25$	2.6	$<0.39$	0.6	$0.19 \pm 0.12$	2.3	$0.21 \pm 0.10$	4.3	$0.08 \pm 0.07$	2.3
HESS J1554-550	$0.27 \pm 0.15$	2.7	$<0.15$	0.0	$<0.14$	-0.1	$<0.06$	-0.2	$<0.07$	-0.1
HESS J1614-518	$1.90 \pm 0.38$	6.7	$1.49 \pm 0.28$	8.1	$0.83 \pm 0.21$	7.0	$0.43 \pm 0.14$	5.9	$0.03 \pm 0.06$	1.2
HESS J1616-508	$6.52 \pm 0.73$	11.4	$4.89 \pm 0.54$	12.9	$1.61 \pm 0.30$	8.1	$0.55 \pm 0.17$	5.1	$0.11 \pm 0.09$	1.8
HESS J1626-490	$1.82 \pm 0.49$	4.3	$0.73 \pm 0.30$	2.9	$0.38 \pm 0.19$	2.6	$0.31 \pm 0.13$	3.7	$0.06 \pm 0.07$	1.5
HESS J1632-478	$7.25 \pm 0.66$	15.1	$3.89 \pm 0.46$	12.4	$1.73 \pm 0.29$	9.3	$0.84 \pm 0.20$	7.4	$0.14 \pm 0.10$	2.8
HESS J1634-472	$4.41 \pm 0.62$	9.0	$2.53 \pm 0.41$	8.1	$1.15 \pm 0.25$	6.6	$0.34 \pm 0.14$	3.7	$0.09 \pm 0.08$	1.7
HESS J1640-465	$3.07 \pm 0.47$	9.0	$2.11 \pm 0.33$	10.3	$1.10 \pm 0.22$	9.5	$0.13 \pm 0.09$	2.6	$0.09 \pm 0.07$	2.7
HESS J1641-463	$1.32 \pm 0.31$	6.3	$0.54 \pm 0.20$	4.3	$0.16 \pm 0.15$	2.1	$0.03 \pm 0.05$	1.4	$<0.21$	1.0
HESS J1646-458	$7.93 \pm 0.98$	9.1	$5.62 \pm 0.69$	10.0	$2.41 \pm 0.42$	7.4	$0.46 \pm 0.19$	3.1	$0.16 \pm 0.12$	1.9
HESS J1702-420	$0.55 \pm 0.43$	1.4	$0.54 \pm 0.29$	2.1	$0.50 \pm 0.20$	3.4	$0.30 \pm 0.14$	3.1	$0.10 \pm 0.09$	1.7
HESS J1708-410	$<0.53$	0.9	$0.11 \pm 0.13$	1.0	$0.10 \pm 0.11$	1.4	$<0.14$	0.9	$<0.07$	-0.3
HESS J1708-443	$25.34 \pm 0.93$	52.0	$3.57 \pm 0.39$	15.0	$0.22 \pm 0.15$	2.0	$0.17 \pm 0.10$	2.6	$0.04 \pm 0.06$	1.3
HESS J1713-381	$1.93 \pm 0.37$	7.0	$1.03 \pm 0.24$	6.6	$0.51 \pm 0.16$	5.4	$<0.11$	0.2	$0.03 \pm 0.05$	1.5
HESS J1713-397	$3.42 \pm 0.49$	8.5	$3.91 \pm 0.41$	13.9	$1.60 \pm 0.25$	10.0	$0.66 \pm 0.16$	7.5	$0.18 \pm 0.09$	3.8
HESS J1714-385	$2.10 \pm 0.35$	9.5	$0.58 \pm 0.21$	4.2	$0.25 \pm 0.13$	3.8	$<0.06$	-0.4	$0.03 \pm 0.05$	1.6
HESS J1718-374	$2.11 \pm 0.32$	11.1	$0.61 \pm 0.17$	6.6	$0.28 \pm 0.11$	5.4	$<0.06$	-0.4	$0.06 \pm 0.06$	2.9
HESS J1718-385	$0.56 \pm 0.25$	2.7	$0.39 \pm 0.19$	2.7	$0.08 \pm 0.09$	1.2	$<0.17$	0.9	$<0.09$	-0.4
HESS J1729-345	$<1.17$	0.8	$0.36 \pm 0.28$	1.4	$0.31 \pm 0.17$	2.2	$<0.12$	-0.8	$<0.17$	0.8
HESS J1731-347	$0.56 \pm 0.29$	2.1	$0.51 \pm 0.21$	3.1	$0.14 \pm 0.12$	1.5	$<0.08$	-0.6	$0.06 \pm 0.06$	2.1
HESS J1741-302	$<0.26$	-0.6	$0.14 \pm 0.12$	1.7	$<0.08$	-0.6	$<0.07$	-0.3	$- \pm -$	-

Tab. A.4.: continued.

Name	$F_1$	$\sqrt{TS_1}$	$F_2$	$\sqrt{TS_2}$	$F_3$	$\sqrt{TS_3}$	$F_4$	$\sqrt{TS_4}$	$F_5$	$\sqrt{TS_5}$
HESS J1745-290	$11.15 \pm 0.67$	29.7	$3.07 \pm 0.37$	16.7	$0.88 \pm 0.19$	9.6	$0.14 \pm 0.09$	3.2	<0.13	0.7
HESS J1745-303	$2.40 \pm 0.49$	5.8	$1.52 \pm 0.35$	5.6	$0.38 \pm 0.17$	2.9	$0.36 \pm 0.14$	3.8	$0.08 \pm 0.08$	1.7
HESS J1746-285	$7.53 \pm 0.63$	19.8	$1.67 \pm 0.31$	9.0	$0.18 \pm 0.14$	1.8	<0.15	0.3	<0.08	-0.3
HESS J1746-308	$0.97 \pm 0.35$	3.3	$0.55 \pm 0.25$	2.7	<0.31	0.6	$0.14 \pm 0.11$	2.0	$0.08 \pm 0.08$	2.0
HESS J1747-248	$0.86 \pm 0.21$	6.4	$0.19 \pm 0.11$	2.8	<0.19	0.8	<0.05	-0.4	<0.06	-0.2
HESS J1747-281	$0.26 \pm 0.24$	1.3	$0.26 \pm 0.15$	2.5	$0.13 \pm 0.10$	2.5	<0.06	-0.5	<0.07	-0.3
HESS J1800-240	$14.22 \pm 0.91$	22.0	$6.64 \pm 0.58$	16.2	$1.91 \pm 0.32$	8.8	$0.24 \pm 0.13$	2.6	<0.16	-0.0
HESS J1801-233	$2.86 \pm 0.34$	13.2	$1.08 \pm 0.21$	8.1	$0.25 \pm 0.11$	3.7	$0.05 \pm 0.06$	1.6	<0.05	-0.7
HESS J1804-216	$9.29 \pm 0.73$	17.6	$5.61 \pm 0.50$	16.8	$2.48 \pm 0.32$	12.7	$0.58 \pm 0.17$	5.5	$0.25 \pm 0.11$	4.5
HESS J1808-204	$0.19 \pm 0.20$	1.1	<0.23	0.7	<0.16	1.0	<0.06	-0.3	<0.12	-0.1
HESS J1809-193	$3.46 \pm 0.73$	5.4	$0.61 \pm 0.44$	1.5	$0.71 \pm 0.26$	3.5	$0.21 \pm 0.14$	2.0	<0.09	-0.7
HESS J1813-126	- ± -	-	<0.48	1.0	<0.27	0.6	<0.04	-1.2	$0.04 \pm 0.05$	1.6
HESS J1813-178	$0.98 \pm 0.29$	4.4	$0.41 \pm 0.18$	3.2	$0.30 \pm 0.14$	3.4	$0.10 \pm 0.08$	2.3	$0.04 \pm 0.05$	1.9
HESS J1818-154	$0.47 \pm 0.22$	2.8	$0.08 \pm 0.09$	1.3	<0.16	-0.1	<0.06	-0.3	- ± -	-
HESS J1825-137	$10.30 \pm 1.02$	12.4	$8.43 \pm 0.74$	15.1	$4.51 \pm 0.47$	14.0	$1.61 \pm 0.27$	9.3	$0.43 \pm 0.16$	4.4
HESS J1826-130	$3.63 \pm 0.49$	9.7	$1.19 \pm 0.30$	5.3	$0.35 \pm 0.17$	2.8	<0.20	0.3	$0.10 \pm 0.08$	2.2
HESS J1826-148	$1.06 \pm 0.24$	7.5	$0.74 \pm 0.19$	8.2	$0.46 \pm 0.14$	7.7	$0.13 \pm 0.08$	4.8	<0.08	-0.1
HESS J1828-099	<0.38	0.2	<0.27	0.9	$0.06 \pm 0.07$	1.4	<0.13	-0.2	<0.06	-0.2
HESS J1832-085	<0.57	0.9	<0.38	0.8	<0.14	-0.4	$0.04 \pm 0.06$	1.6	<0.07	-0.2
HESS J1832-093	<0.50	0.3	$0.16 \pm 0.14$	1.6	<0.06	-0.8	<0.11	0.2	- ± -	-
HESS J1833-105	$0.87 \pm 0.23$	5.9	$0.28 \pm 0.13$	3.8	$0.13 \pm 0.09$	3.4	<0.07	-0.3	<0.06	-0.1

Tab. A.4.: continued.

Name	$F_1$	$\sqrt{TS_1}$	$F_2$	$\sqrt{TS_2}$	$F_3$	$\sqrt{TS_3}$	$F_4$	$\sqrt{TS_4}$	$F_5$	$\sqrt{TS_5}$
HESS J1834-087	$3.49 \pm 0.59$	7.1	$2.94 \pm 0.43$	9.0	$1.18 \pm 0.26$	6.6	$0.33 \pm 0.13$	3.8	<0.10	-0.3
HESS J1837-069	$15.34 \pm 1.04$	19.4	$10.91 \pm 0.74$	20.6	$4.83 \pm 0.47$	15.7	$1.15 \pm 0.23$	8.1	$0.18 \pm 0.12$	2.2
HESS J1841-055	$10.78 \pm 0.93$	14.2	$7.08 \pm 0.65$	14.2	$3.38 \pm 0.41$	12.0	$0.52 \pm 0.19$	3.7	$0.28 \pm 0.13$	3.5
HESS J1843-033	$1.74 \pm 0.52$	3.7	$0.74 \pm 0.34$	2.5	$0.67 \pm 0.21$	4.4	<0.21	0.1	$0.07 \pm 0.09$	1.1
HESS J1844-030	$0.33 \pm 0.22$	2.0	<0.23	-0.1	<0.09	-0.5	<0.09	-0.2	$0.04 \pm 0.05$	1.9
HESS J1846-029	$0.51 \pm 0.22$	3.2	$0.26 \pm 0.14$	3.0	<0.07	-0.6	$0.03 \pm 0.05$	1.6	<0.07	-0.2
HESS J1848-018	$3.29 \pm 0.63$	6.1	$1.45 \pm 0.40$	4.4	$0.47 \pm 0.23$	2.5	<0.22	0.2	<0.10	-0.7
HESS J1849-000	$0.33 \pm 0.23$	1.7	$0.28 \pm 0.15$	2.6	<0.17	0.2	<0.05	-0.9	$0.03 \pm 0.05$	1.3
HESS J1852-000	$2.48 \pm 0.55$	5.1	$1.19 \pm 0.36$	3.8	$0.41 \pm 0.21$	2.4	<0.19	0.1	<0.24	0.8
HESS J1857+026	$3.69 \pm 0.59$	7.6	$2.09 \pm 0.40$	7.0	$0.96 \pm 0.23$	5.8	$0.43 \pm 0.14$	4.9	<0.07	-0.6
HESS J1858+020	$1.05 \pm 0.27$	5.4	$0.22 \pm 0.14$	2.1	<0.20	0.4	$0.09 \pm 0.07$	2.4	- ± -	-
HESS J1908+063	$6.50 \pm 0.78$	10.1	$1.95 \pm 0.45$	5.1	$0.87 \pm 0.26$	4.3	$0.34 \pm 0.16$	3.0	$0.11 \pm 0.10$	1.7
HESS J1911+090	$4.94 \pm 0.44$	21.8	$2.19 \pm 0.29$	16.5	$0.47 \pm 0.14$	7.7	$0.15 \pm 0.09$	4.2	<0.06	-0.1
HESS J1912+101	$1.06 \pm 0.34$	3.7	$0.43 \pm 0.21$	2.5	$0.22 \pm 0.13$	2.3	$0.07 \pm 0.08$	1.4	- ± -	-
HESS J1923+141	$10.01 \pm 0.61$	30.3	$3.54 \pm 0.37$	17.7	$1.07 \pm 0.20$	10.7	$0.15 \pm 0.09$	3.3	$0.06 \pm 0.06$	2.0
HESS J1930+188	$0.49 \pm 0.19$	3.9	$0.13 \pm 0.11$	1.8	<0.10	-0.2	<0.13	0.2	- ± -	-
HESS J1943+213	$0.55 \pm 0.17$	6.0	$0.47 \pm 0.13$	8.2	$0.22 \pm 0.09$	5.7	$0.04 \pm 0.05$	2.1	<0.06	-0.1



# Survey Images

# B

## Contents

---

B.1	HGPS Flux Image . . . . .	118
B.2	HGPS Model Flux Image . . . . .	119
B.3	HGPS Large Scale Model and Discarded Components Flux Image . . . . .	120
B.4	HGPS Residual $\sqrt{TS}$ Image . . . . .	121
B.5	HGPS Sources and MWL Associations . . . . .	122
B.6	HGPS Cut-out Regions, Exclusion Regions and Modeling ROIs . . . . .	126
B.7	<i>Fermi</i> -LAT RGB Flux Image . . . . .	127
B.8	<i>Fermi</i> -LAT RGB 3FHL Model Flux Image . . . . .	128
B.9	<i>Fermi</i> -LAT RGB 3FHL Model Residual Flux Image . . . . .	129
B.10	HGPS $\sqrt{TS}$ Image . . . . .	130
B.11	CTA Simulated $\sqrt{TS}$ Image (Ring Background) . . . . .	131
B.12	CTA Simulated $\sqrt{TS}$ Image (Template Background) . . . . .	132

---

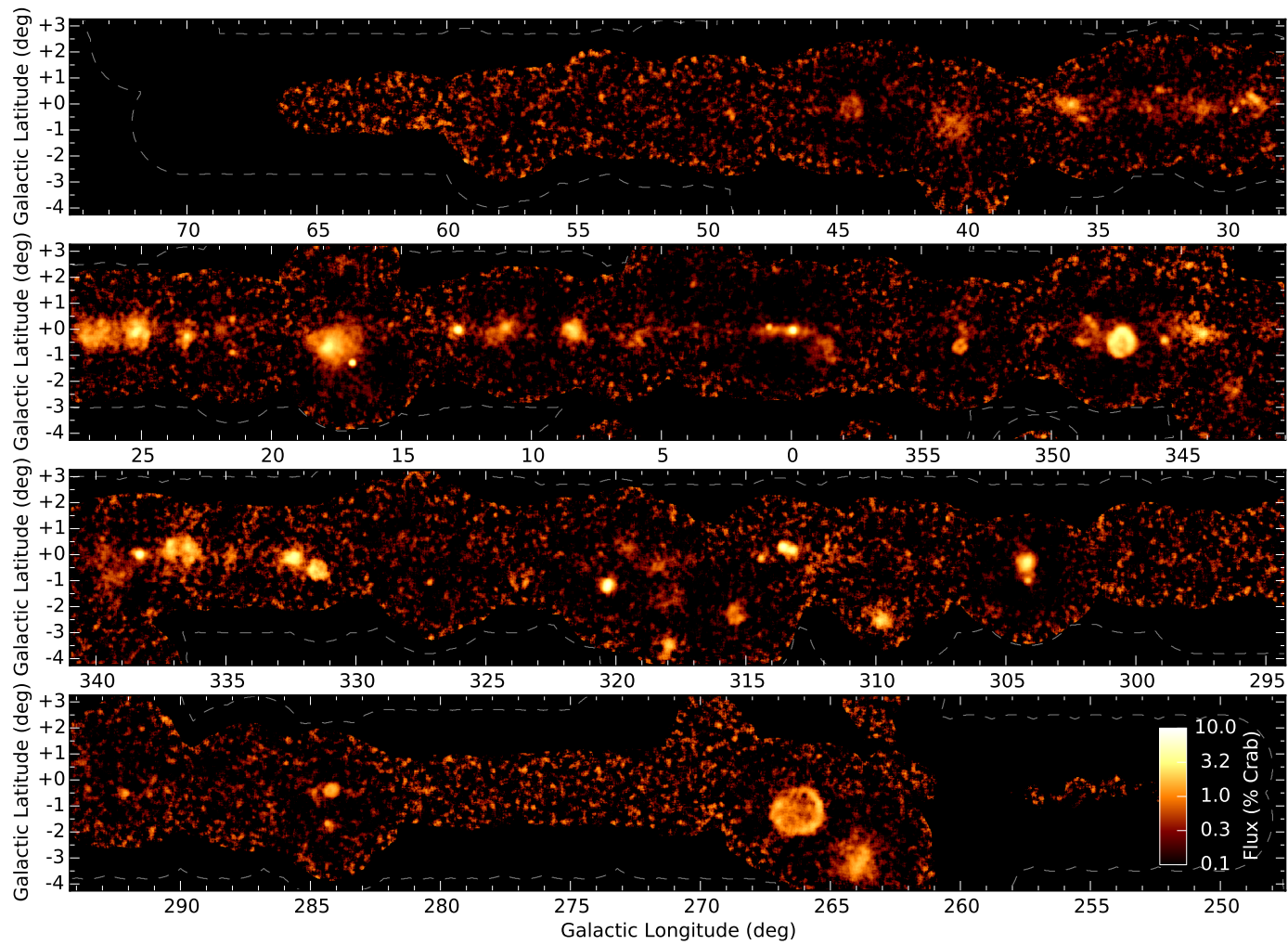


**Fig. B.1.:** HGPS Flux Image – Integral flux above 1 TeV using a correlation radius  $R_c = 0.1^\circ$  and assuming spectral index  $\Gamma = 2.3$ , in units of % Crab. The map is only filled where the point-source sensitivity for a  $5\text{-}\sigma$  detection (c.f. Fig. 2.2) is better (lower) than 2.5% Crab.

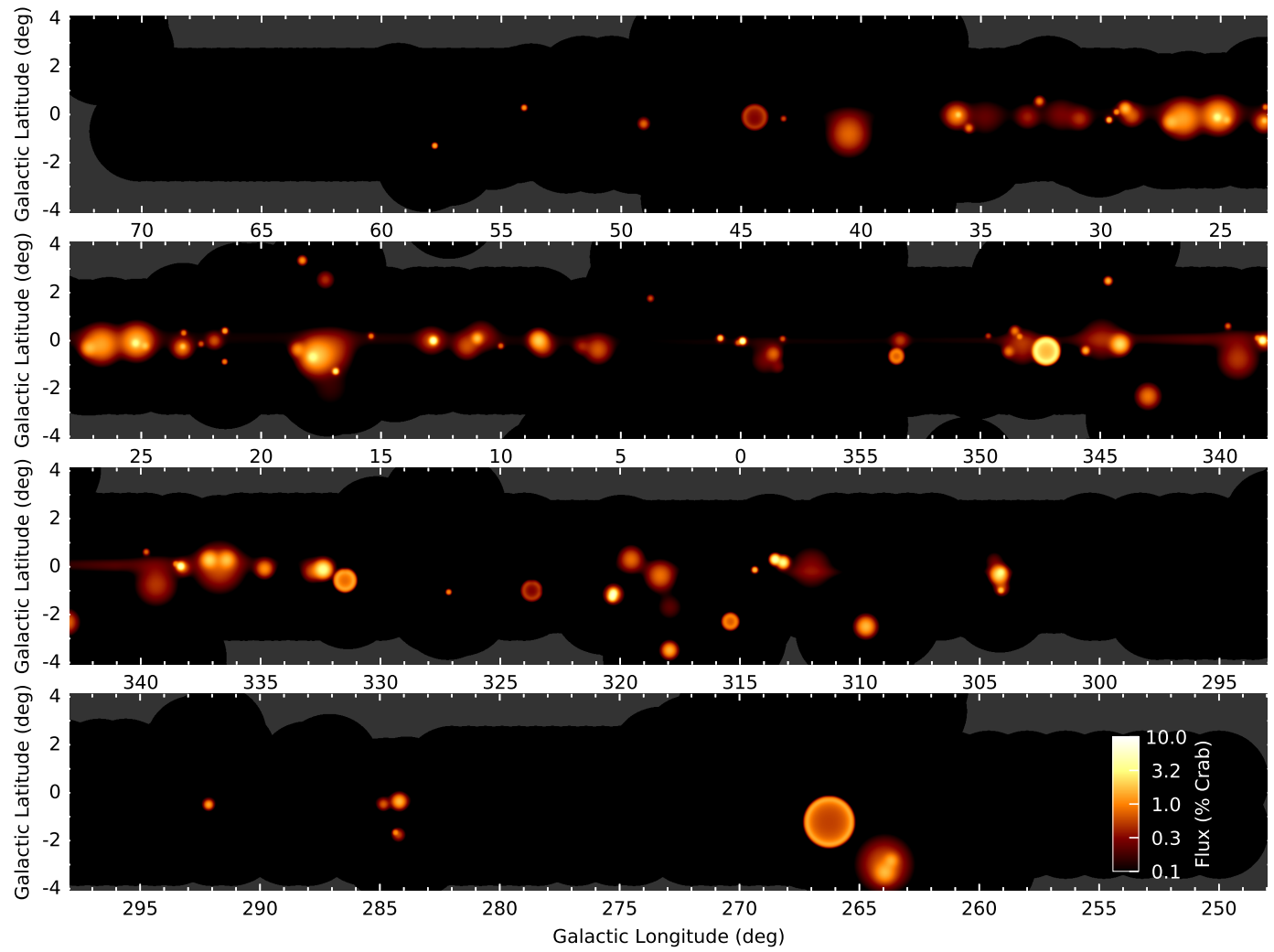


**Fig. B.2.:** HGPS Model Flux Image – Integral flux above 1 TeV using a correlation radius  $R_c = 0.1^\circ$  and assuming spectral index  $\Gamma = 2.3$ , in units of % Crab. For a better comparison the colorscale is equivalent to Fig. B.1.

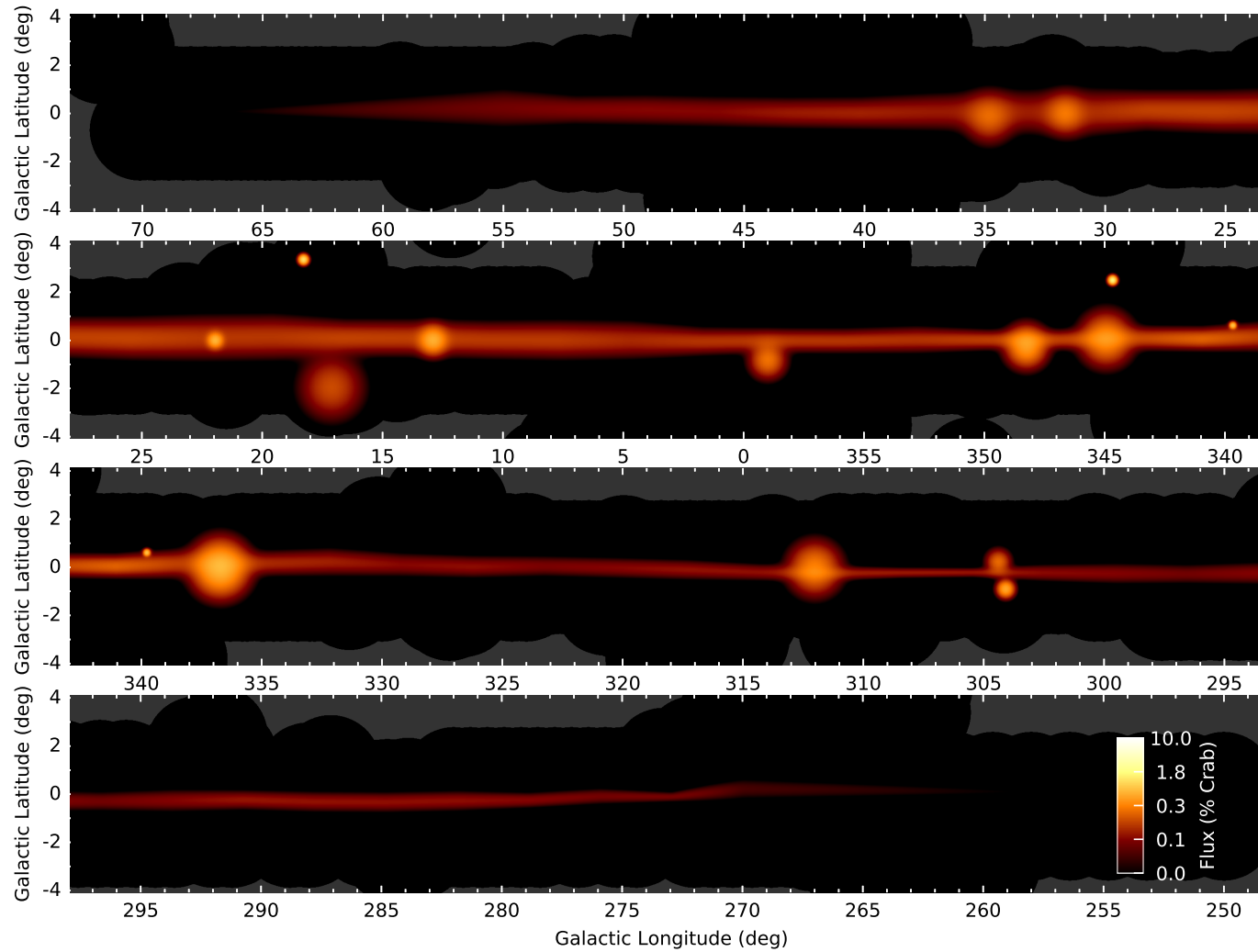


**Fig. B.3.:** HGPS Large Scale Model and Discarded Components Flux Image – Integral flux above 1 TeV using a correlation radius  $R_c = 0.1^\circ$  and assuming spectral index  $\Gamma = 2.3$ , in units of % Crab. The colorscale was adapted to enhance the faint emission.

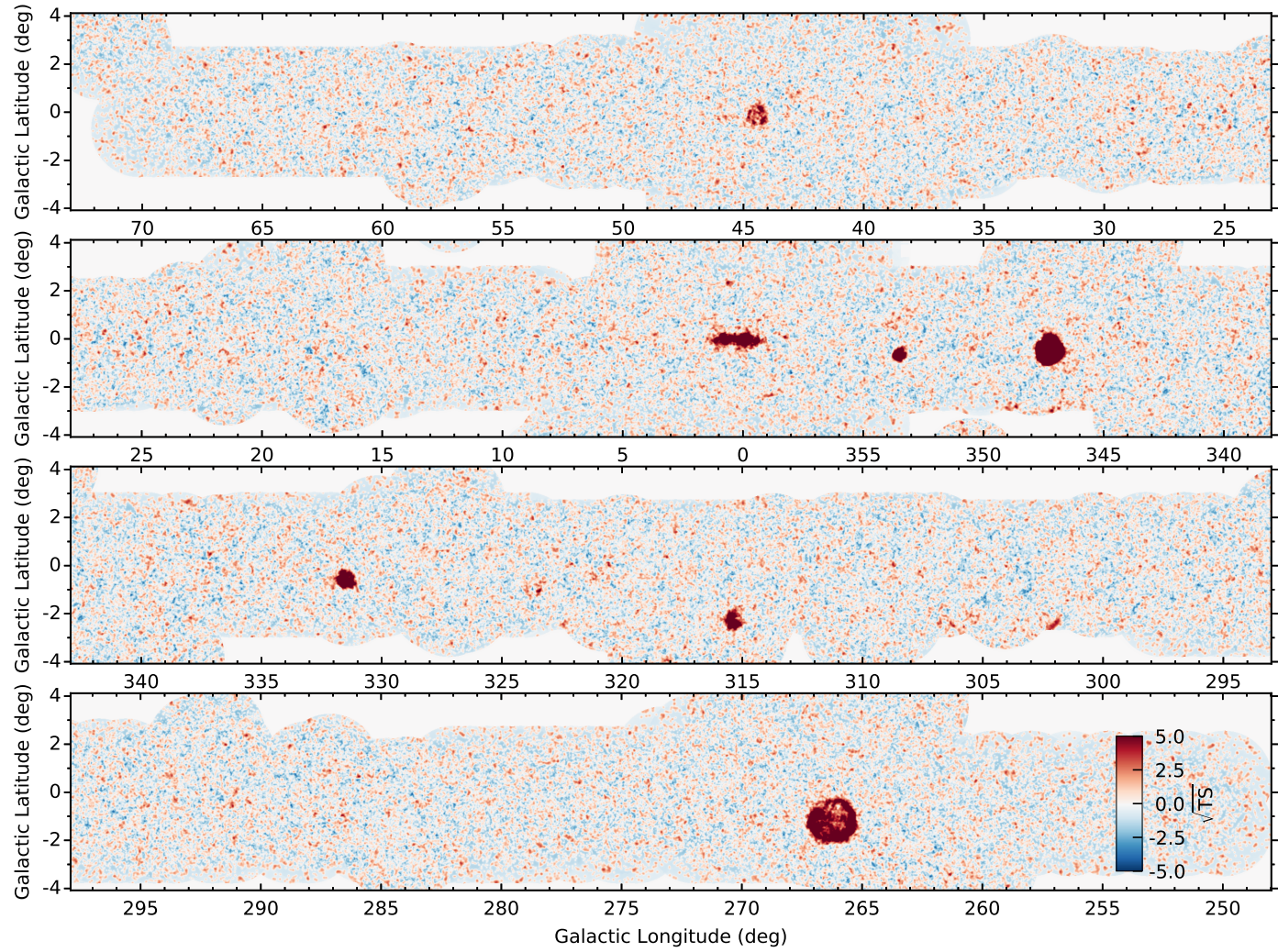


**Fig. B.4.:** HGPS residual  $\sqrt{TS}$  image – The image is computed assuming a point source morphology. The cut-out emission regions stand out with significant residuals (cf. Fig. B.9).

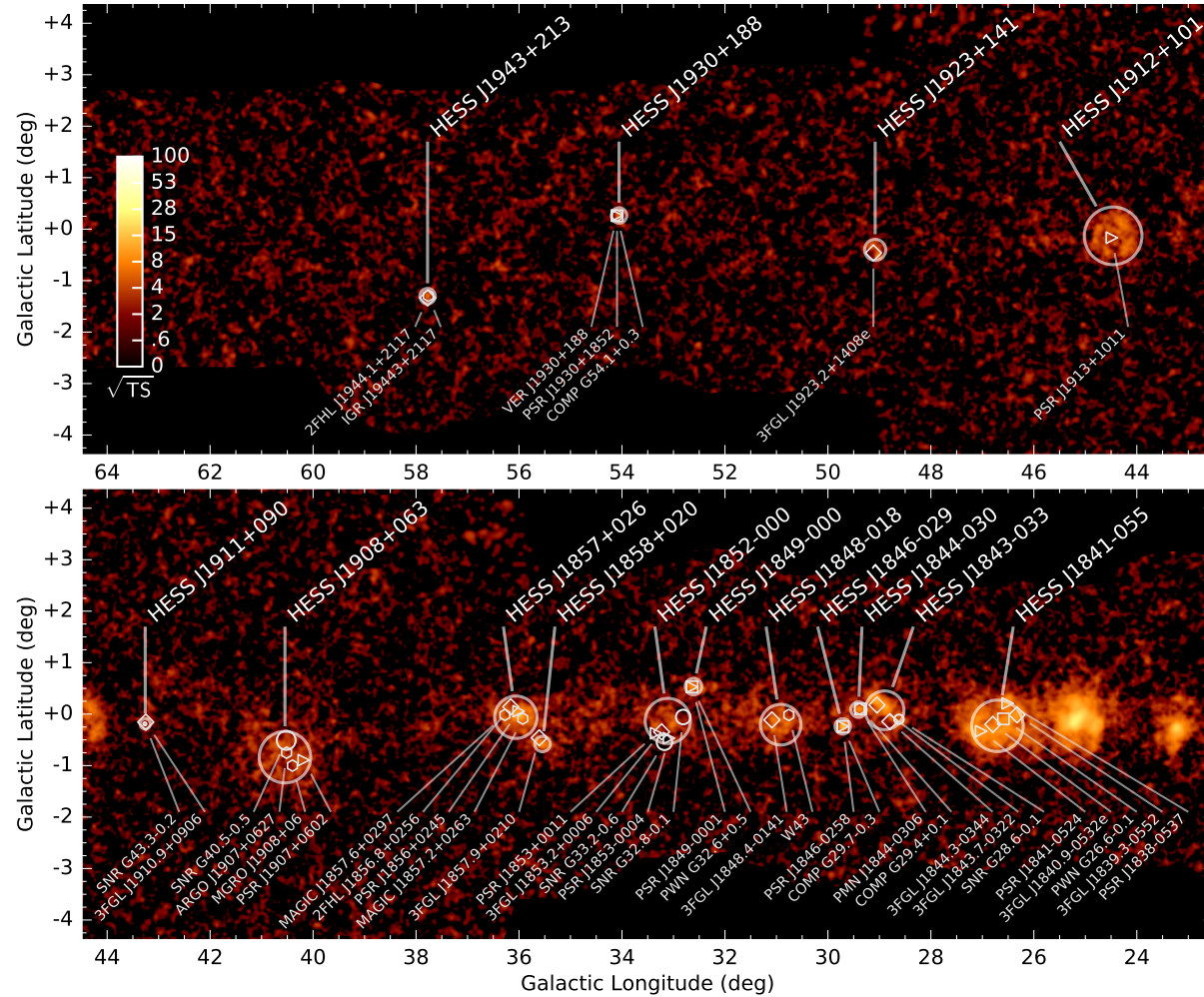


**Fig. B.5.:** HGPS sources and MWL associations (1 of 4) – The background image shows  $\sqrt{TS}$  of the VHE gamma-ray excess in the Galactic plane assuming a point source morphology. All HGPS catalog sources are shown on top with transparent circles that correspond to the measured size of the source. Source names are labelled above the Galactic plane. Associations for the sources are shown with white markers and labels below the Galactic plane. The various object categories and the association criteria applied are detailed in Sect. 2.3.8.

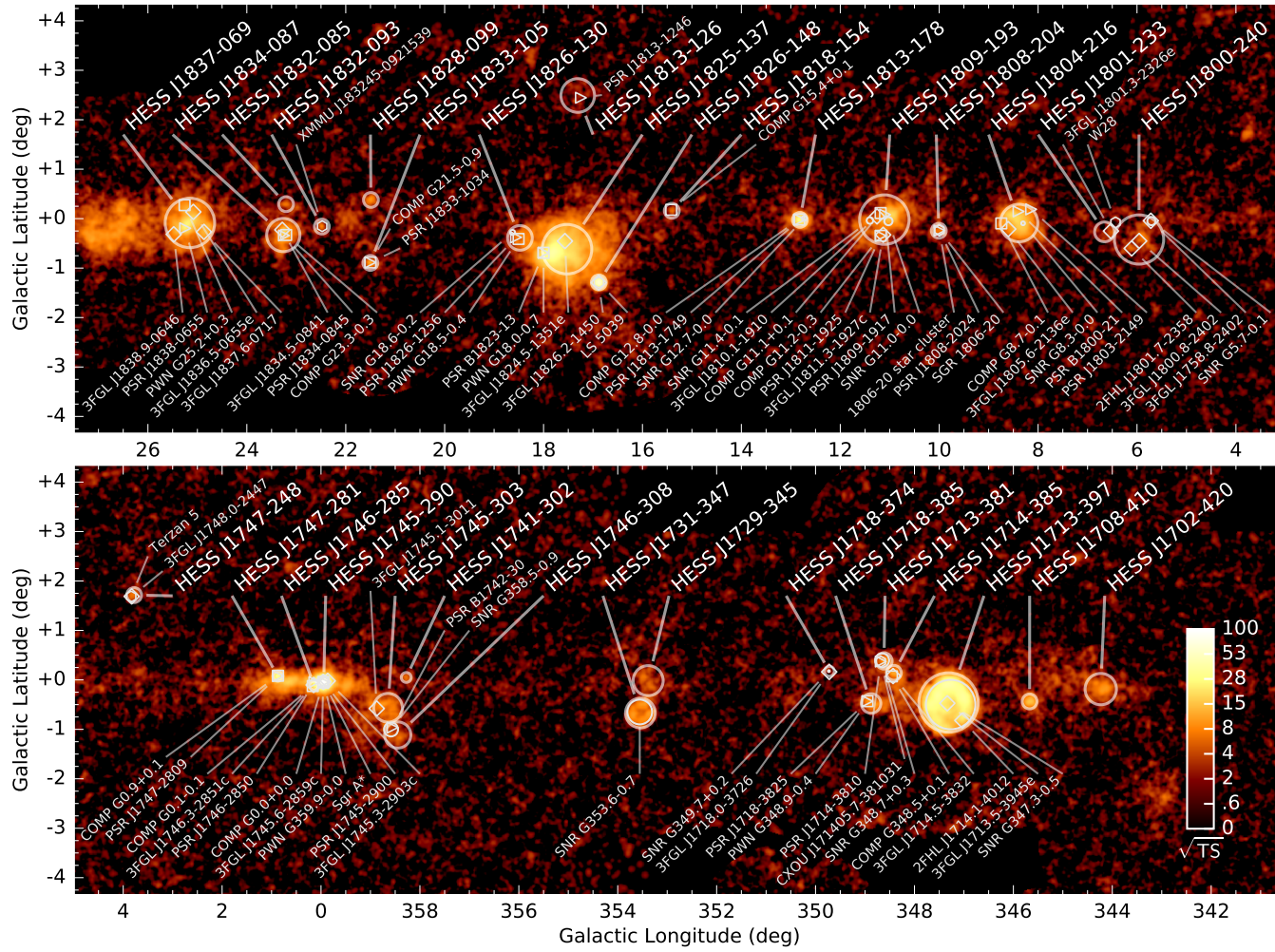


Fig. B.6.: HGPS sources and MWL associations (2 of 4) – Fig. B.5 continued.

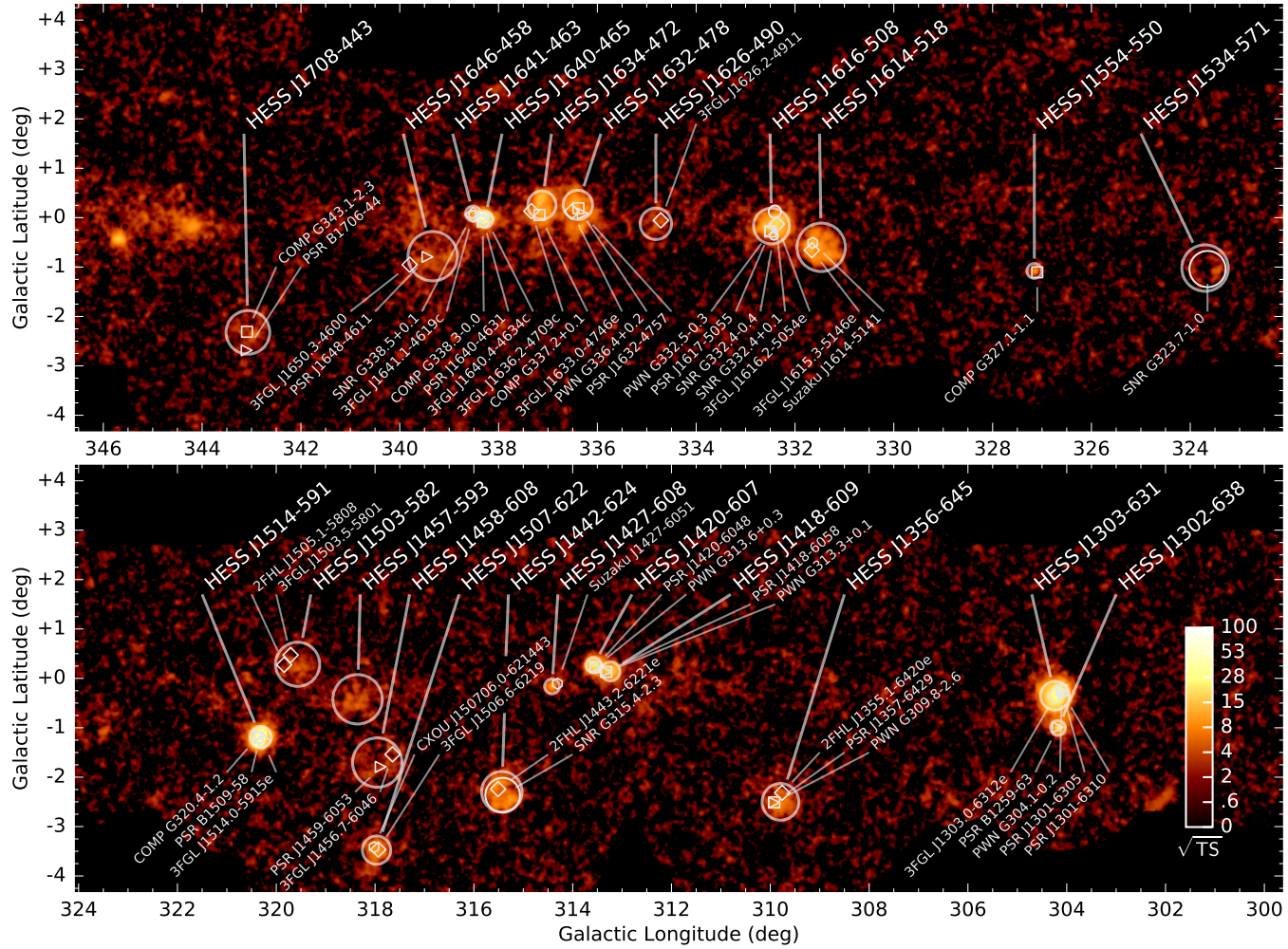


Fig. B.7.: HGPS sources and MWL associations (3 of 4) – Fig. B.5 continued.

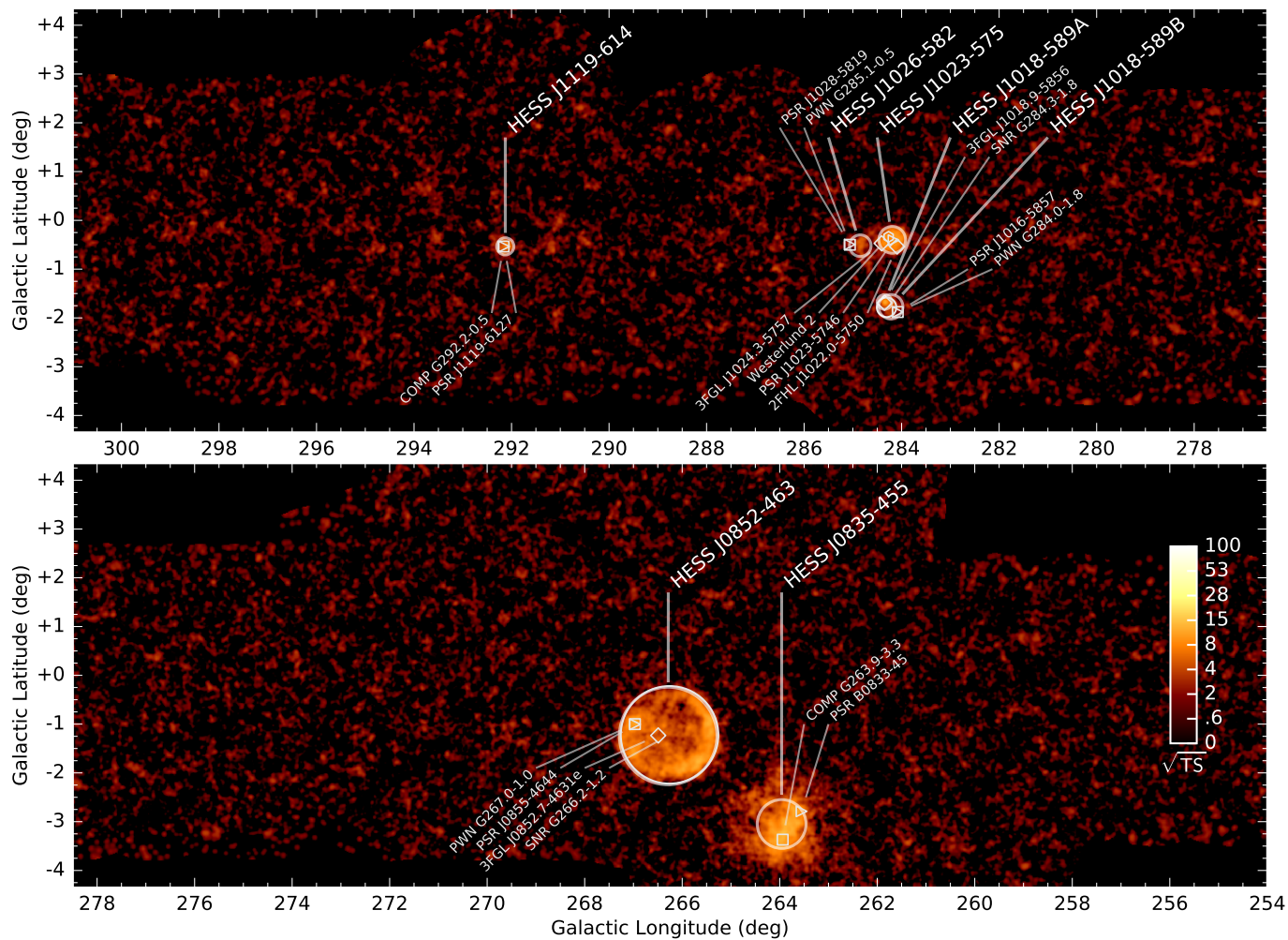
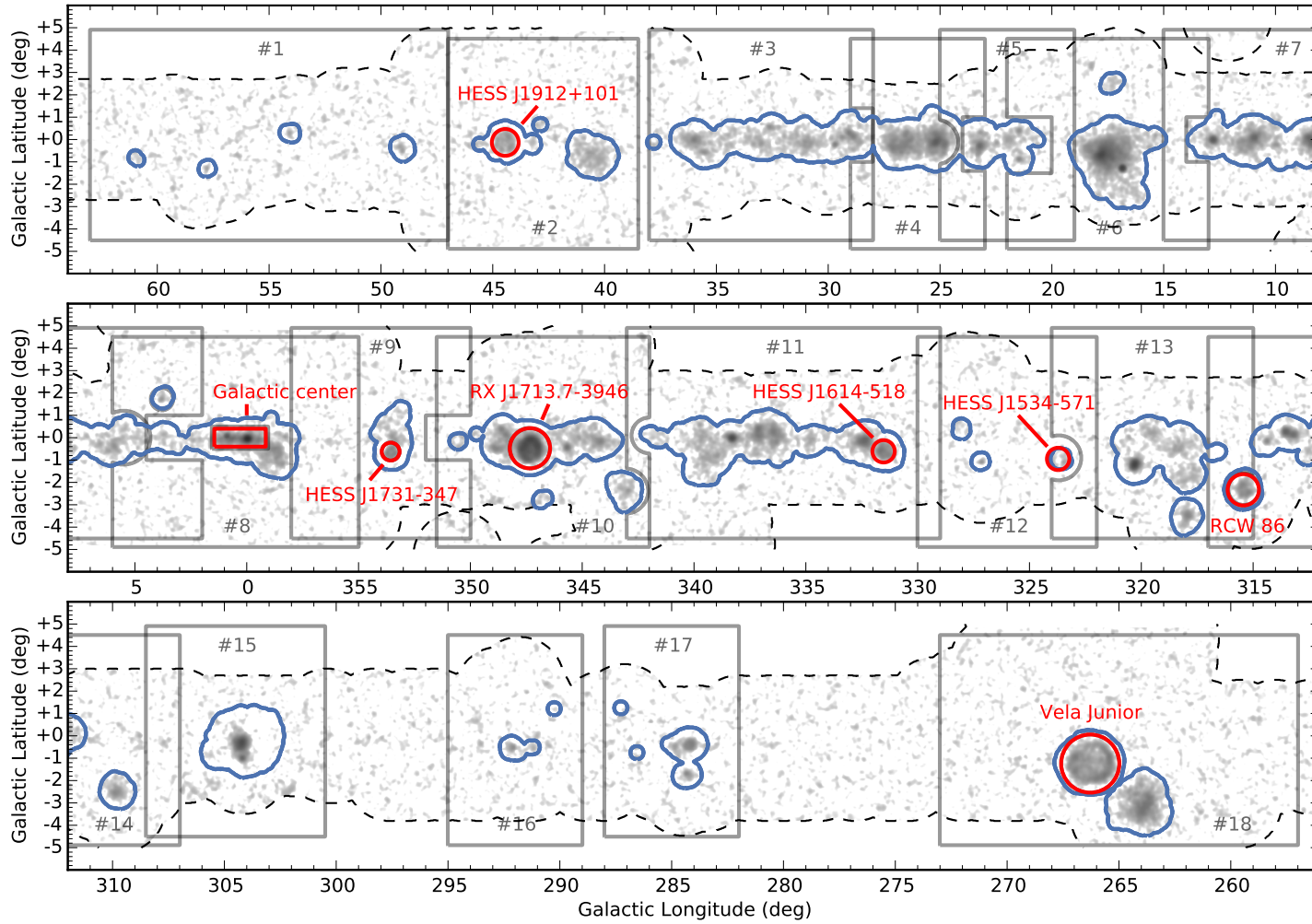
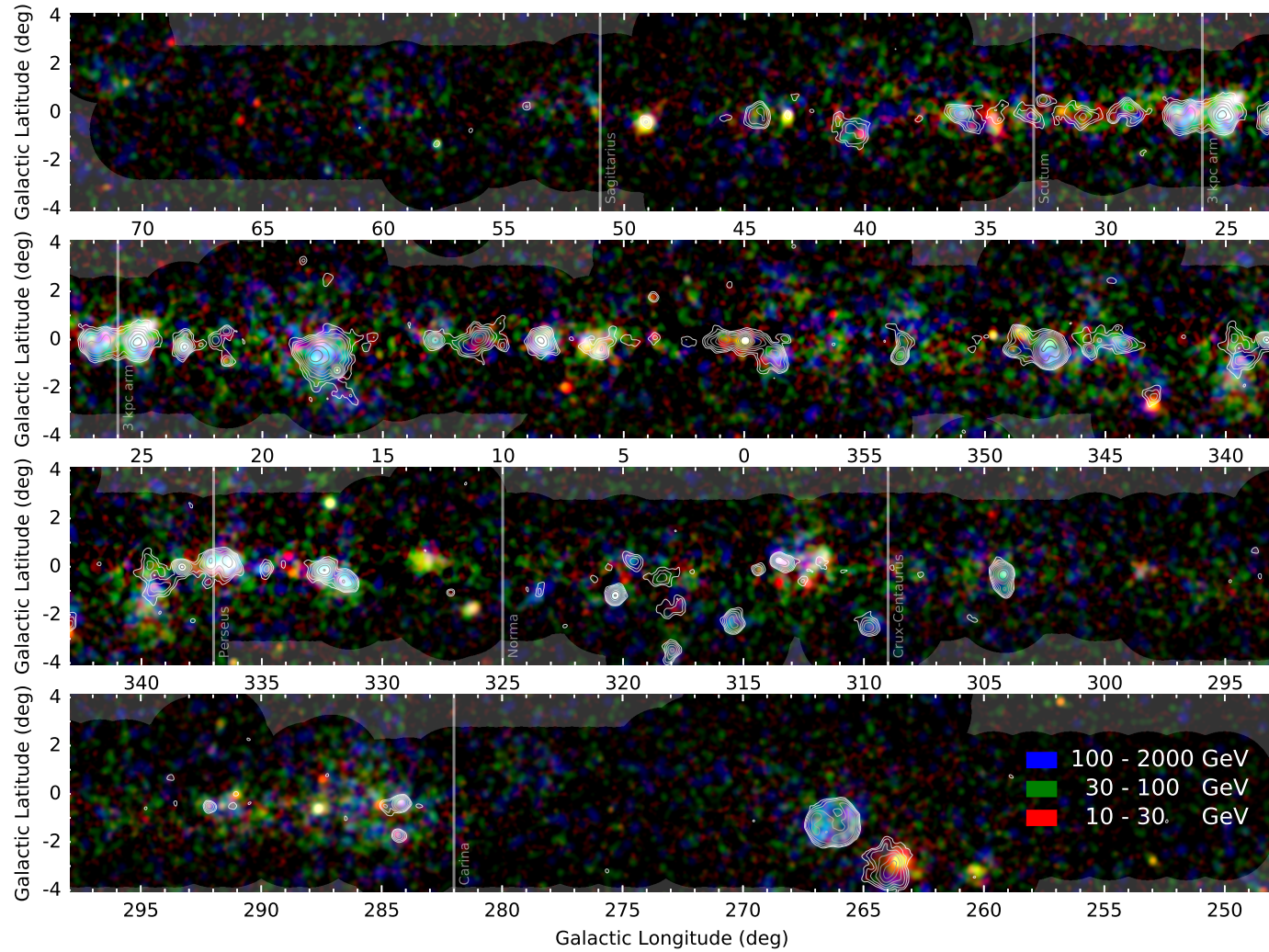


Fig. B.8.: HGPS sources and MWL associations (4 of 4) – Fig. B.5 continued.



**Fig. B.9.:** HGPS Cut-out Regions, Exclusion Regions and Modeling ROIs – The background image displays significance ( $R_c = 0.1^\circ$ ) in inverse grayscale.



**Fig. B.10.:** *Fermi*-LAT RGB flux image – For a qualitative comparison the contours of the HGPS significance map with a correlation radius of  $0.1^\circ$  are overlaid. The outer contour corresponds to a level of  $3\sigma$ , the innermost contour to  $30\sigma$ . The image is smoothed with a Gaussian of width  $0.2^\circ$  in all energy bands. The transparent vertical lines indicate the positions of spiral arm tangents from Vallée (2014).

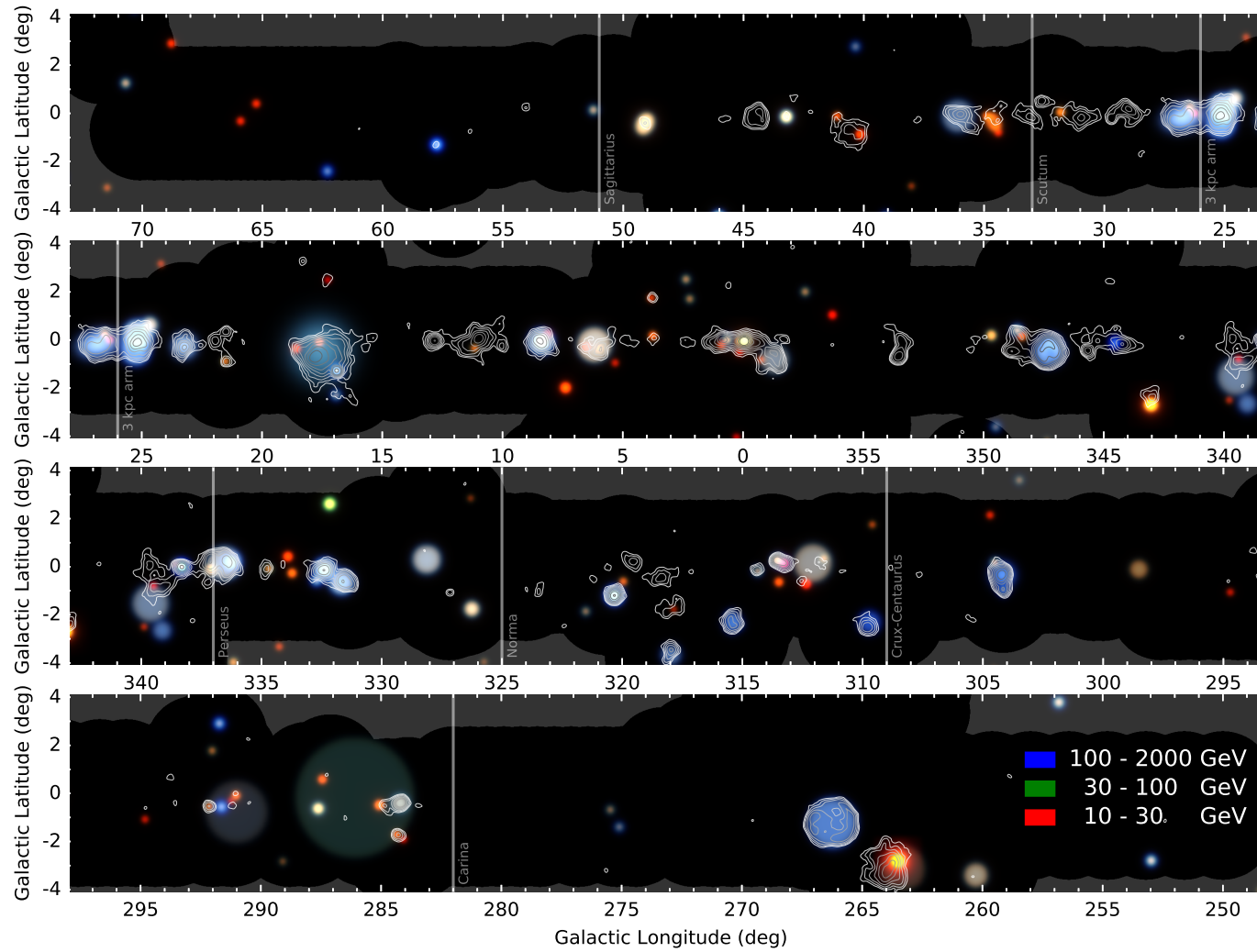


**Fig. B.11.:** *Fermi*-LAT RGB 3FHL model flux Image and HGPS significance contours – See caption of Fig. B.10 for further details.

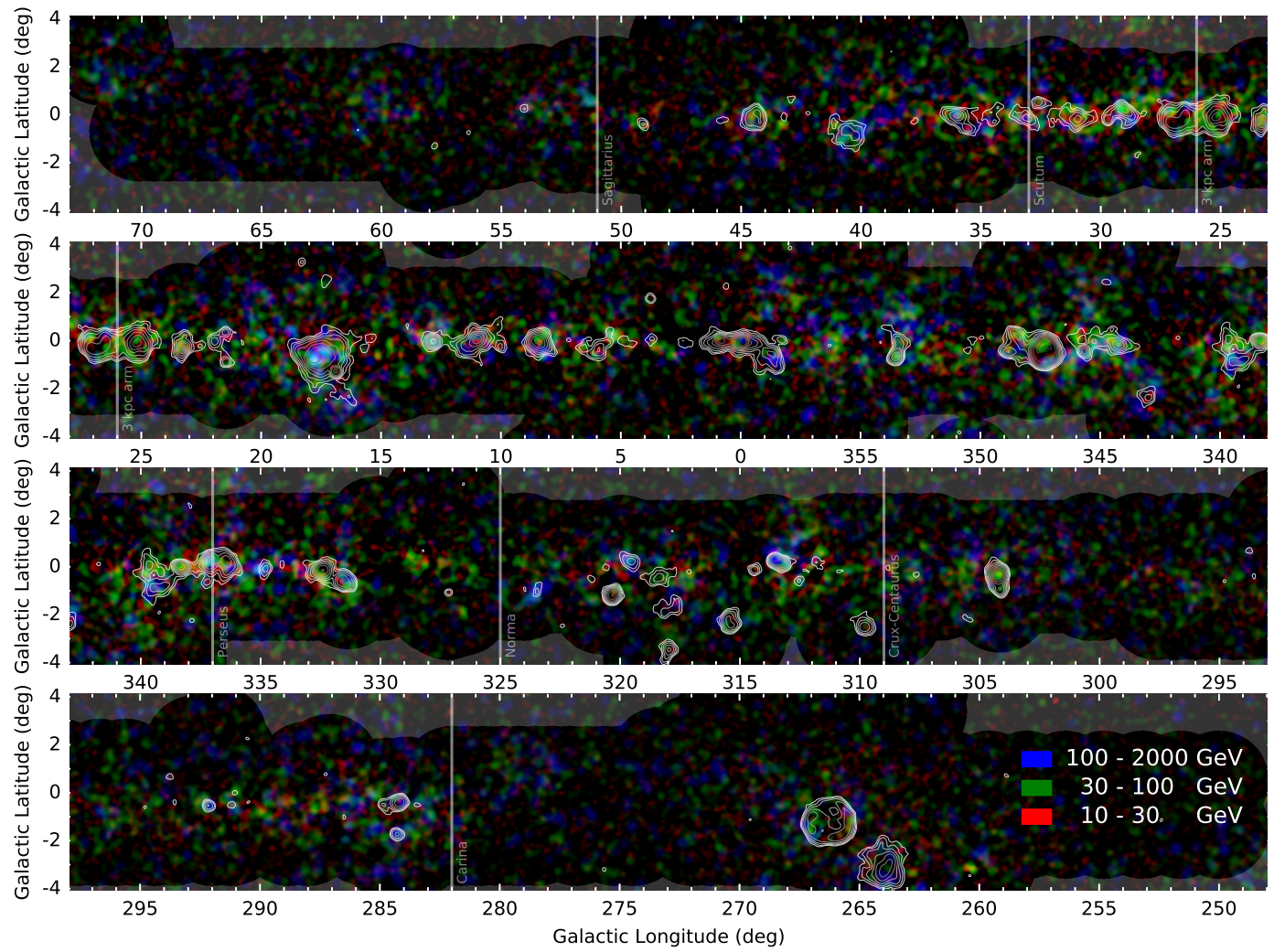


**Fig. B.12.:** *Fermi*-LAT RGB 3FHL model residual flux image and HGPS significance contours – See caption of Fig. B.10 for further details.

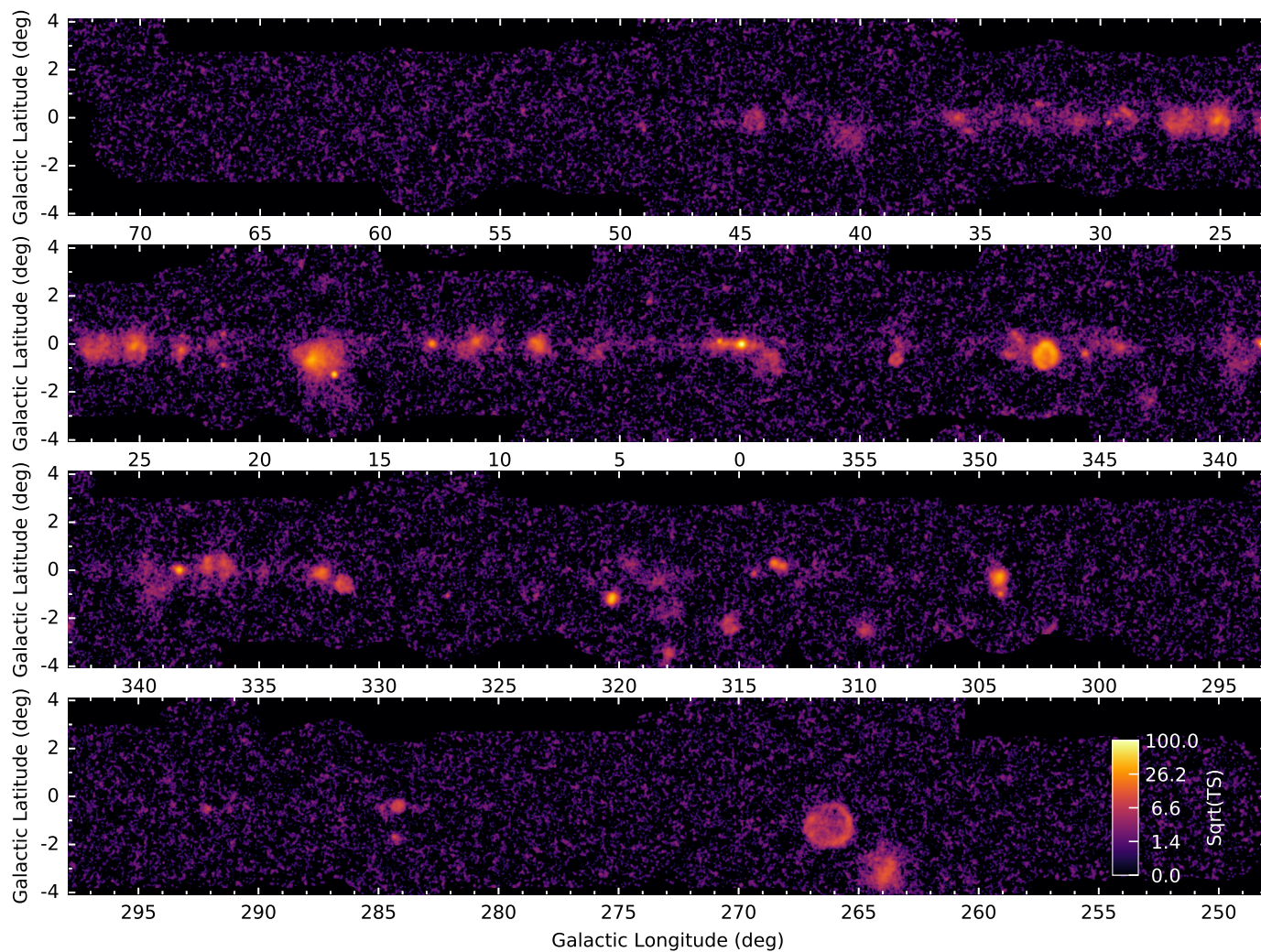


**Fig. B.13.:** H.E.S.S. survey  $\sqrt{TS}$  image – The background was estimated using the adaptive ring method and parameters as described in Sec. 2.2.5. The  $\sqrt{TS}$  image was computed using the method described in Sec. 2.2.5 assuming a H.E.S.S. point source morphology.

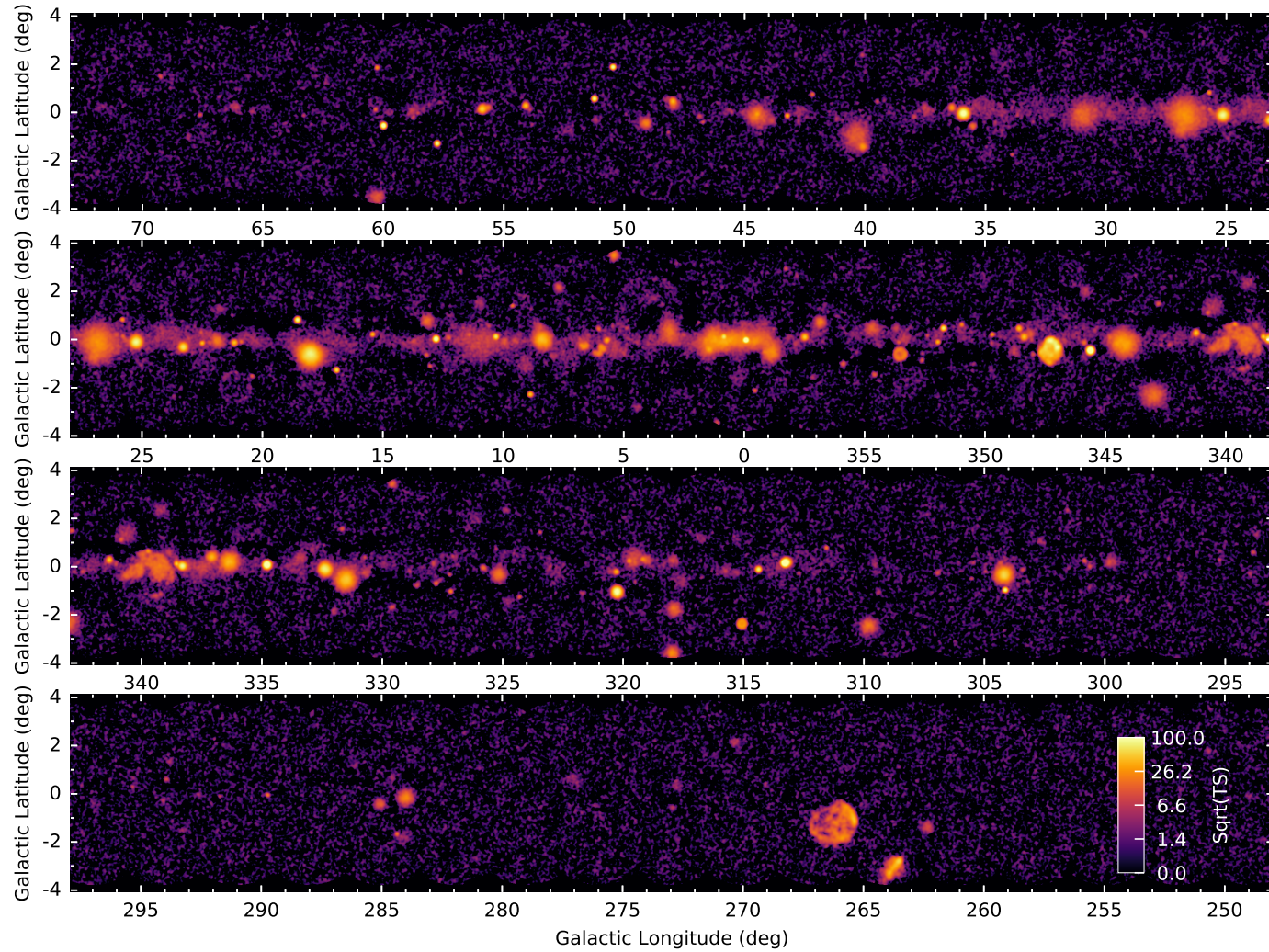


**Fig. B.14.:** Simulated CTA survey  $\sqrt{TS}$  image between 300 GeV and 100 TeV – The background was estimated using the same adaptive ring method and parameters as described in Sec. 2.2.5. The  $\sqrt{TS}$  image was computed using the method described in Sec. 2.2.5 assuming a CTA point source morphology.

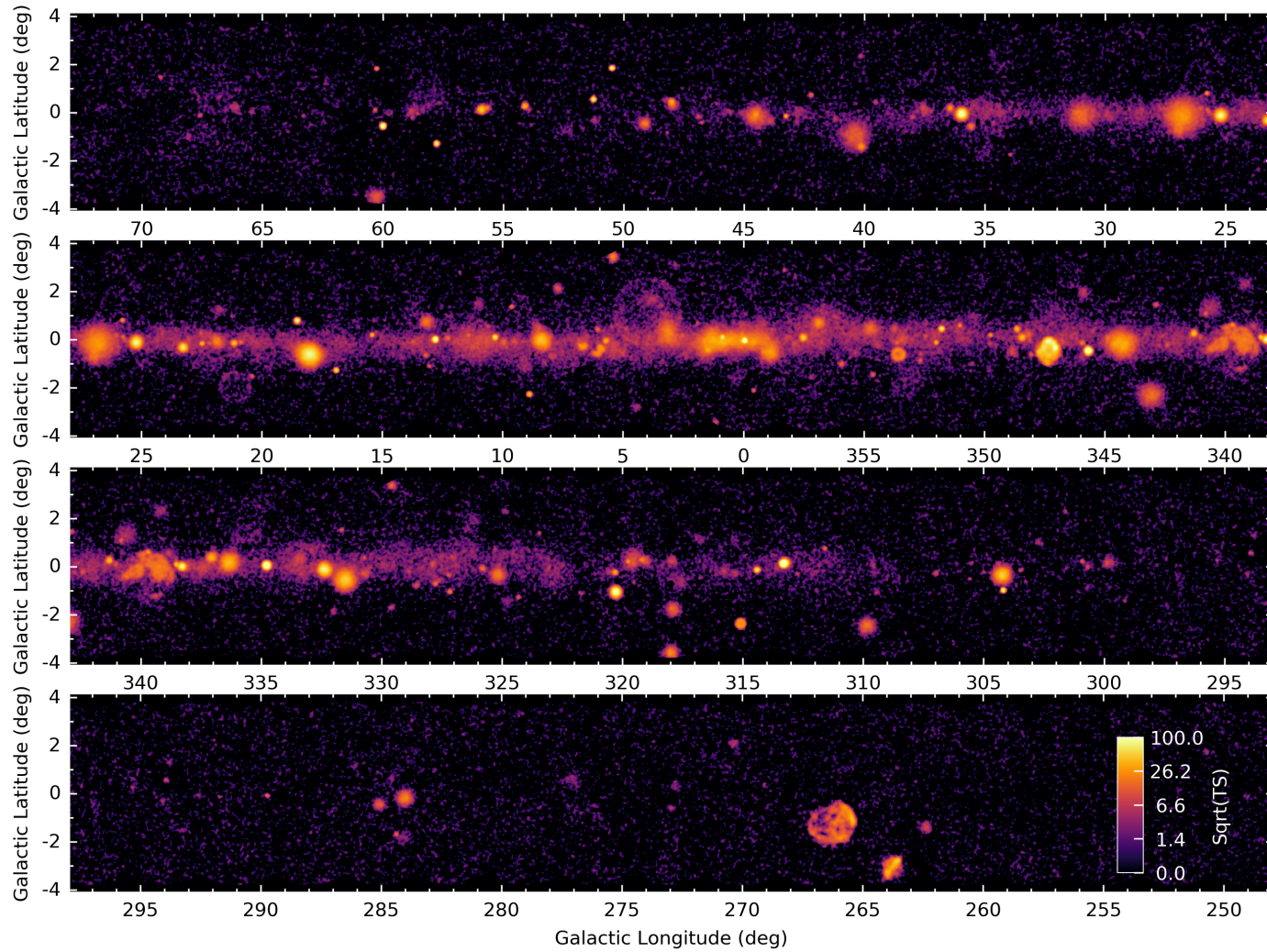


**Fig. B.15.:** Simulated CTA survey  $\sqrt{TS}$  image between 300 GeV and 100 TeV – The background model was estimated using the *template background* method, which corresponds to the same model as used for the simulation. The  $\sqrt{TS}$  image was computed using the method described in Sec. 2.2.5 assuming a CTA point source morphology.

# Individual source images and SEDs

## Contents

---

C.1	RGB Image and Spectrum of <i>HESS J1026-582</i> . . . . .	134
C.2	RGB Image and Spectrum of <i>HESS J1632-478</i> and <i>HESS J1634-472</i> . . . . .	134
C.3	RGB Image and Spectrum of <i>HESS J1702-420</i> . . . . .	134
C.4	RGB Image and Spectrum of <i>HESS J1746-308</i> . . . . .	135
C.5	RGB Image and Spectrum of <i>HESS J1813-178</i> . . . . .	135
C.6	RGB Image and Spectrum of <i>HESS J1843-033</i> . . . . .	135
C.7	RGB Image and Spectrum of <i>HESS J1848-018</i> . . . . .	136
C.8	RGB Image and Spectrum of <i>HESS J1852-000</i> . . . . .	136
C.9	RGB Image and Spectrum of <i>HESS J1858+020</i> . . . . .	136
C.10	RGB Image and Spectrum of <i>HESS J1534-571</i> . . . . .	137
C.11	RGB Image and Spectrum of <i>HESS J1731-347</i> . . . . .	137
C.12	RGB Image and Spectrum of <i>HESS J1912+101</i> . . . . .	137

---

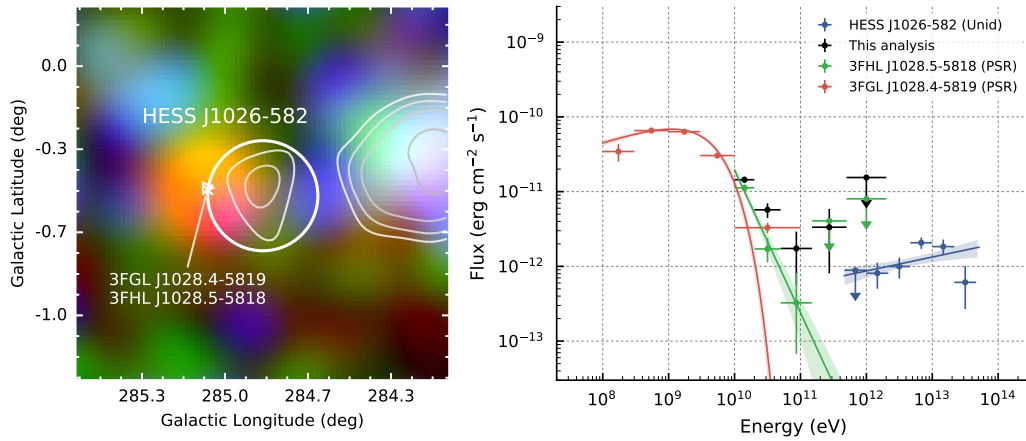


Fig. C.1.: Fermi-LAT RGB image and spectrum of *HESS J1026-582*.

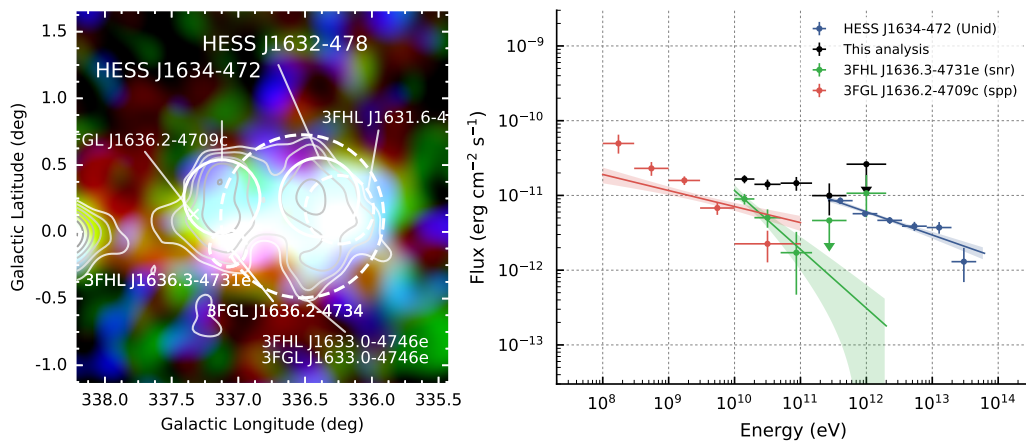


Fig. C.2.: Fermi-LAT RGB image and spectrum of *HESS J1632-478* and *HESS J1634-472*.

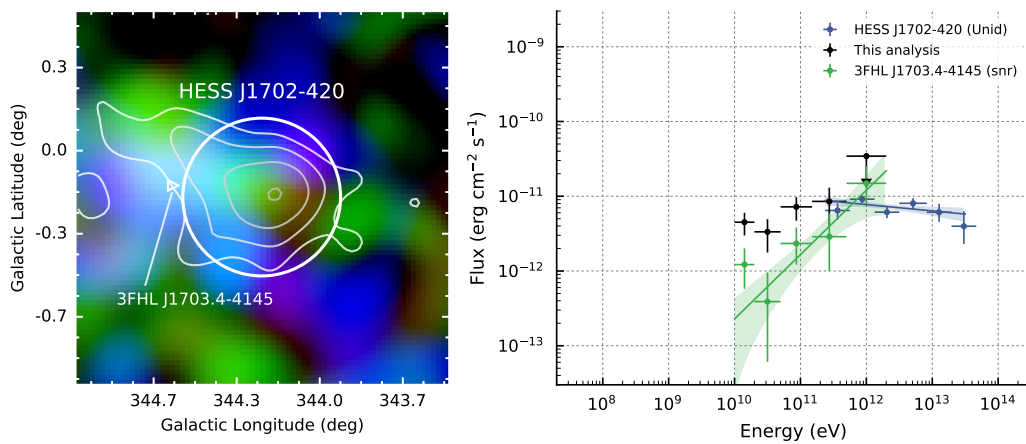


Fig. C.3.: Fermi-LAT RGB image and spectrum of *HESS J1702-420*.

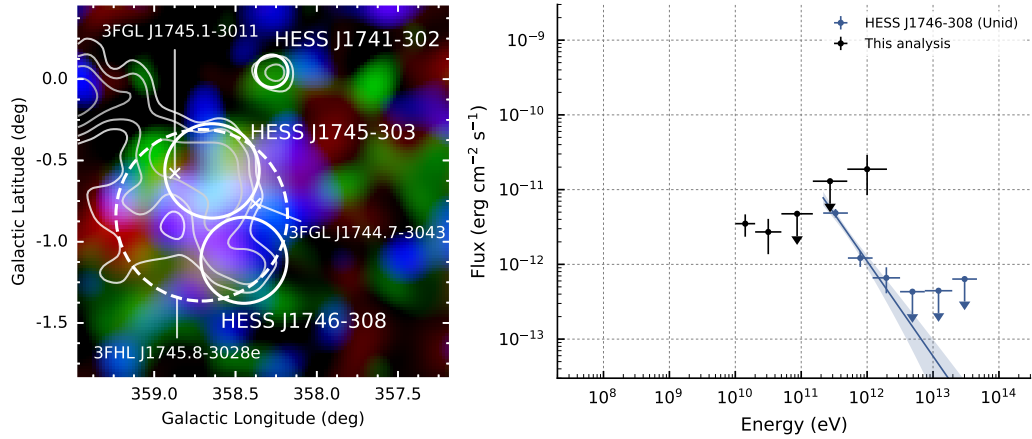


Fig. C.4.: Fermi-LAT RGB image and spectrum of *HESS J1746-308*.

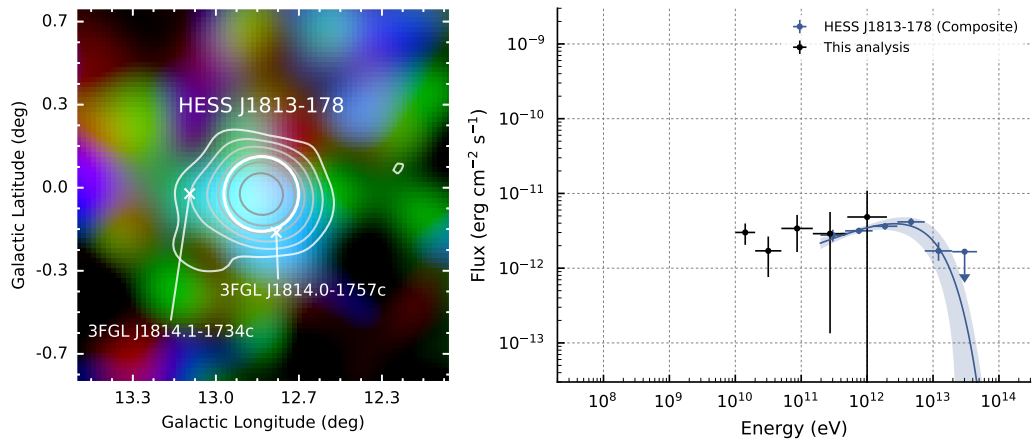


Fig. C.5.: Fermi-LAT RGB image and spectrum of *HESS J1813-178*.

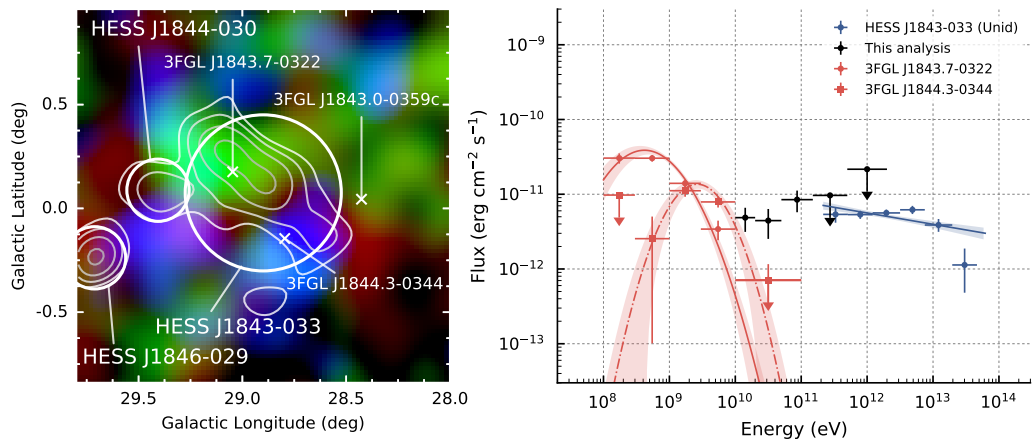


Fig. C.6.: Fermi-LAT RGB image and spectrum of *HESS J1843-033*.

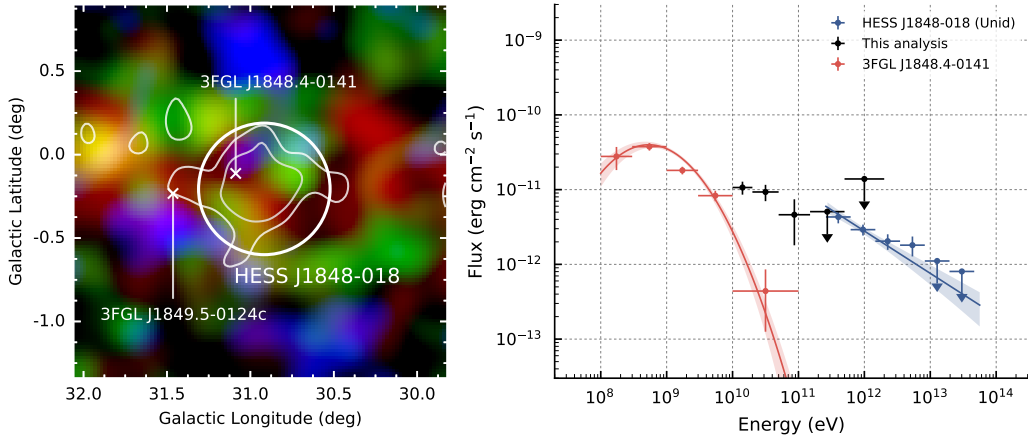


Fig. C.7.: Fermi-LAT RGB image and spectrum of *HESS J1848-018*.

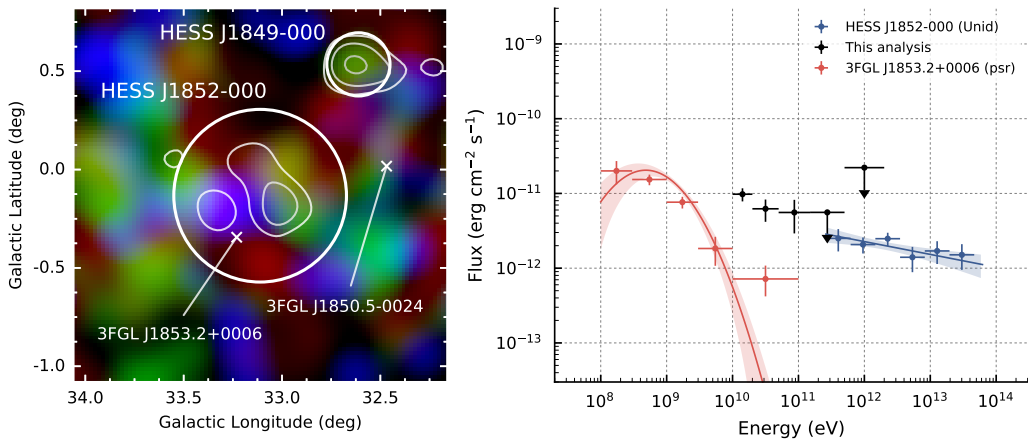


Fig. C.8.: Fermi-LAT RGB image and spectrum of *HESS J1852-000*.

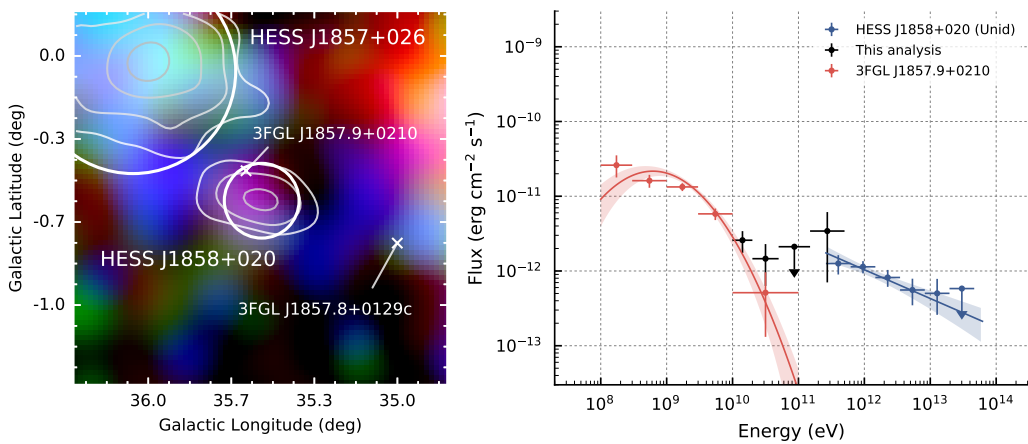


Fig. C.9.: Fermi-LAT RGB image and spectrum of *HESS J1858+020*.

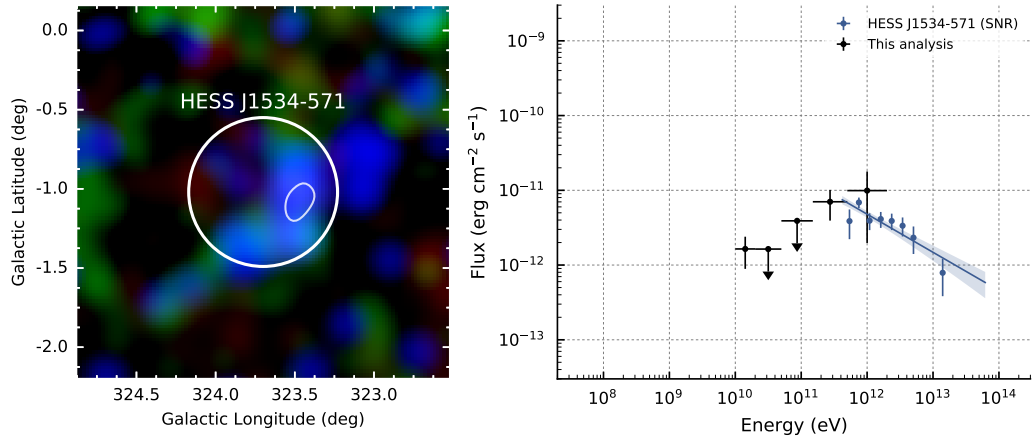


Fig. C.10.: Fermi-LAT RGB image and spectrum of *HESS J1534-571*.

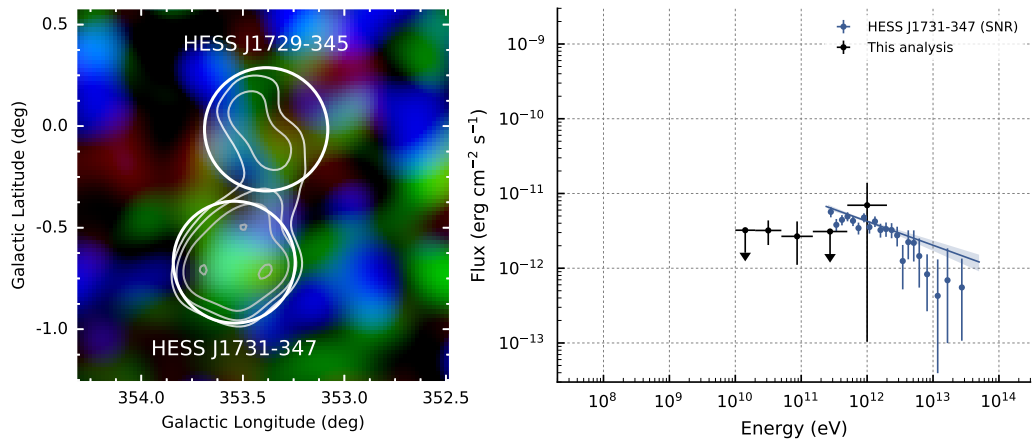


Fig. C.11.: Fermi-LAT RGB image and spectrum of *HESS J1731-347*.

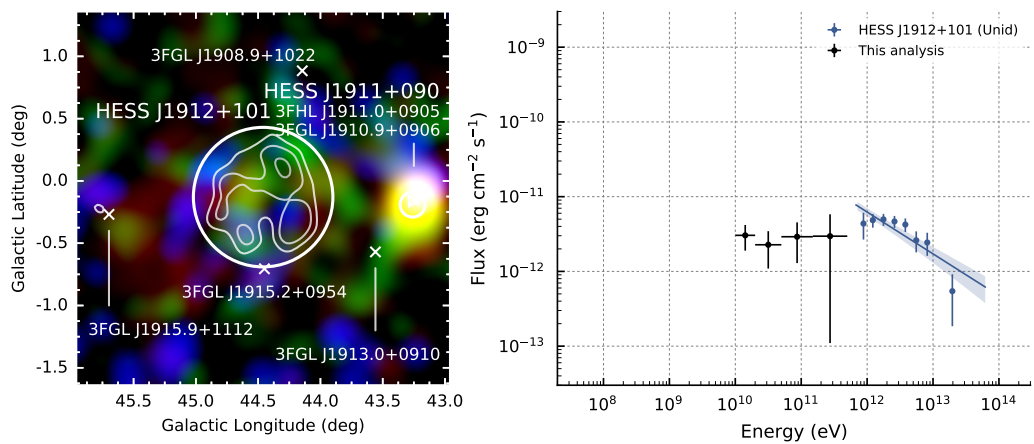


Fig. C.12.: Fermi-LAT RGB image and spectrum of *HESS J1912+101*. The last flux point is missing, because no event above 500 GeV was measured in the analysis region.



# Bibliography

## Literature

- Abdo, A. A., M. Ackermann, M. Ajello, et al. (2009). „Fermi/Large Area Telescope Bright Gamma-Ray Source List“. In: *ApJS* 183, pp. 46–66. arXiv: [0902.1340](#) (cit. on pp. 38, 68).
- Abeysekara, A. U., A. Albert, R. Alfaro, et al. (2017). „The 2HWC HAWC Observatory Gamma-Ray Catalog“. In: *ApJ* 843, 40, p. 40. arXiv: [1702.02992 \[astro-ph.HE\]](#) (cit. on p. 85).
- Abramowski, A., F. Aharonian, F. Ait Benkhali, et al. (2014a). „Diffuse Galactic gamma-ray emission with H.E.S.S.“ In: *Phys. Rev. D* 90.12, 122007, p. 122007 (cit. on pp. 28, 31).
- Abramowski, A., F. Aharonian, F. Ait Benkhali, et al. (2014b). „HESS J1640-465 - an exceptionally luminous TeV  $\gamma$ -ray supernova remnant“. In: *MNRAS* 439, pp. 2828–2836. arXiv: [1401.4388 \[astro-ph.HE\]](#) (cit. on p. 50).
- Abramowski, A., F. Aharonian, F. Ait Benkhali, et al. (2014c). „H.E.S.S. observations of the Crab during its March 2013 GeV gamma-ray flare“. In: *A&A* 562, L4, p. L4. arXiv: [1311.3187 \[astro-ph.HE\]](#) (cit. on p. 21).
- Acciari, V. A., E. Aliu, T. Arlen, et al. (2010). „Discovery of Very High Energy  $\gamma$ -ray Emission from the SNR G54.1+0.3“. In: *ApJ* 719, pp. L69–L73. arXiv: [1005.0032 \[astro-ph.HE\]](#) (cit. on p. 50).
- Acero, F., F. Aharonian, A. G. Akhperjanian, et al. (2010a). „First detection of VHE  $\gamma$ -rays from SN 1006 by HESS“. In: *A&A* 516, A62, A62. arXiv: [1004.2124 \[astro-ph.HE\]](#) (cit. on p. 21).
- Acero, F., F. Aharonian, A. G. Akhperjanian, et al. (2010b). „Localizing the VHE  $\gamma$ -ray source at the Galactic Centre“. In: *MNRAS* 402, pp. 1877–1882. arXiv: [0911.1912 \[astro-ph.GA\]](#) (cit. on p. 38).
- Acero, F., M. Ackermann, M. Ajello, et al. (2013). „Constraints on the Galactic Population of TeV Pulsar Wind Nebulae Using Fermi Large Area Telescope Observations“. In: *ApJ* 773, 77, p. 77. arXiv: [1306.5735 \[astro-ph.HE\]](#) (cit. on pp. 63, 83–85, 88).
- Acero, F., M. Ackermann, M. Ajello, et al. (2015). „Fermi Large Area Telescope Third Source Catalog“. In: *ApJS* 218, 23, p. 23. arXiv: [1501.02003 \[astro-ph.HE\]](#) (cit. on pp. 43, 44, 68).

- Acero, F., M. Ackermann, M. Ajello, et al. (2016). „Development of the Model of Galactic Interstellar Emission for Standard Point-source Analysis of Fermi Large Area Telescope Data“. In: *ApJS* 223, 26, p. 26. arXiv: [1602.07246 \[astro-ph.HE\]](#) (cit. on p. 67).
- Ackermann, M., M. Ajello, A. Albert, et al. (2012). „The Fermi Large Area Telescope on Orbit: Event Classification, Instrument Response Functions, and Calibration“. In: *ApJS* 203, 4, p. 4. arXiv: [1206.1896 \[astro-ph.IM\]](#) (cit. on p. 64).
- Ackermann, M., A. Albert, W. B. Atwood, et al. (2014). „The Spectrum and Morphology of the Fermi Bubbles“. In: *ApJ* 793, 64, p. 64. arXiv: [1407.7905 \[astro-ph.HE\]](#) (cit. on p. 63).
- Ackermann, M., M. Ajello, W. B. Atwood, et al. (2016). „2FHL: The Second Catalog of Hard Fermi-LAT Sources“. In: *The Astrophysical Journal Supplement Series* 222.1, p. 5 (cit. on pp. 21, 44).
- Ackermann, M., M. Ajello, L. Baldini, et al. (2017). „Search for Extended Sources in the Galactic Plane Using Six Years of Fermi-Large Area Telescope Pass 8 Data above 10 GeV“. In: *ApJ* 843, 139, p. 139 (cit. on pp. 63, 69, 77–79).
- Aharonian, F., A. Akhperjanian, J. Barrio, et al. (2001). „Evidence for TeV gamma ray emission from Cassiopeia A“. In: *A&A* 370, pp. 112–120. eprint: [astro-ph/0102391](#) (cit. on p. 19).
- Aharonian, F., A. Akhperjanian, M. Beilicke, et al. (2002a). „An unidentified TeV source in the vicinity of Cygnus OB2“. In: *A&A* 393, pp. L37–L40. eprint: [astro-ph/0207528](#) (cit. on p. 19).
- Aharonian, F., A. G. Akhperjanian, K.-M. Aye, et al. (2004a). „Calibration of cameras of the H.E.S.S. detector“. In: *Astroparticle Physics* 22, pp. 109–125 (cit. on p. 23).
- Aharonian, F., A. G. Akhperjanian, A. R. Bazer-Bachi, et al. (2005a). „Detection of TeV  $\gamma$ -ray emission from the shell-type supernova remnant RX J0852.0-4622 with HESS“. In: *A&A* 437, pp. L7–L10. eprint: [arXiv:astro-ph/0505380](#) (cit. on p. 50).
- Aharonian, F., A. G. Akhperjanian, K.-M. Aye, et al. (2005b). „Discovery of extended VHE gamma-ray emission from the asymmetric pulsar wind nebula in MSH 15-52 with HESS“. In: *A&A* 435, pp. L17–L20. eprint: [arXiv:astro-ph/0504120](#) (cit. on p. 50).
- Aharonian, F., A. G. Akhperjanian, K.-M. Aye, et al. (2005c). „Discovery of the binary pulsar PSR B1259-63 in very-high-energy gamma rays around periastron with HESS“. In: *A&A* 442, pp. 1–10. eprint: [astro-ph/0506280](#) (cit. on p. 50).
- Aharonian, F., A. G. Akhperjanian, K.-M. Aye, et al. (2005d). „Discovery of the binary pulsar PSR B1259-63 in very-high-energy gamma rays around periastron with HESS“. In: *A&A* 442, pp. 1–10. eprint: [astro-ph/0506280](#) (cit. on p. 82).
- Aharonian, F., A. G. Akhperjanian, K.-M. Aye, et al. (2005e). „Very high energy gamma rays from the composite SNR G 0.9+0.1“. In: *A&A* 432, pp. L25–L29. eprint: [arXiv:astro-ph/0501265](#) (cit. on pp. 31, 50).
- Aharonian, F., A. G. Akhperjanian, A. R. Bazer-Bachi, et al. (2006a). „3.9 day orbital modulation in the TeV  $\gamma$ -ray flux and spectrum from the X-ray binary LS 5039“. In: *A&A* 460, pp. 743–749. eprint: [arXiv:astro-ph/0607192](#) (cit. on p. 50).

- Aharonian, F., A. G. Akhperjanian, A. R. Bazer-Bachi, et al. (2006b). „Discovery of the two ”wings” of the Kookaburra complex in VHE  $\gamma$ -rays with HESS“. In: *A&A* 456, pp. 245–251. eprint: [arXiv:astro-ph/0606311](#) (cit. on p. 50).
- Aharonian, F., A. G. Akhperjanian, A. R. Bazer-Bachi, et al. (2006c). „Energy dependent  $\gamma$ -ray morphology in the pulsar wind nebula HESS J1825-137“. In: *A&A* 460, pp. 365–374. eprint: [arXiv:astro-ph/0607548](#) (cit. on p. 50).
- Aharonian, F., A. G. Akhperjanian, A. R. Bazer-Bachi, et al. (2006d). „First detection of a VHE gamma-ray spectral maximum from a cosmic source: HESS discovery of the Vela X nebula“. In: *A&A* 448, pp. L43–L47. eprint: [arXiv:astro-ph/0601575](#) (cit. on pp. 7, 50).
- Aharonian, F., A. G. Akhperjanian, A. R. Bazer-Bachi, et al. (2006e). „Observations of the Crab nebula with HESS“. In: *A&A* 457.3, pp. 899–915 (cit. on pp. 23, 47, 59).
- Aharonian, F., A. G. Akhperjanian, A. R. Bazer-Bachi, et al. (2006f). „The H.E.S.S. Survey of the Inner Galaxy in Very High Energy Gamma Rays“. In: *The Astrophysical Journal* 636.2, p. 777 (cit. on pp. 7, 20, 47, 84, 85, 87).
- Aharonian, F., A. G. Akhperjanian, U. Barres de Almeida, et al. (2008a). „Discovery of a VHE gamma-ray source coincident with the supernova remnant CTB 37A“. In: *A&A* 490, pp. 685–693. arXiv: [0803.0702](#) (cit. on pp. 50, 60).
- Aharonian, F., A. G. Akhperjanian, A. R. Bazer-Bachi, et al. (2008b). „Discovery of very high energy gamma-ray emission coincident with molecular clouds in the W 28 (G6.4-0.1) field“. In: *A&A* 481, pp. 401–410. arXiv: [0801.3555](#) (cit. on pp. 31, 50).
- Aharonian, F., A. G. Akhperjanian, U. Barres de Almeida, et al. (2008c). „Discovery of very-high-energy  $\gamma$ -ray emission from the vicinity of PSR J1913+1011 with HESS“. In: *A&A* 484, pp. 435–440. arXiv: [0802.3841](#) (cit. on p. 88).
- Aharonian, F., A. G. Akhperjanian, U. Barres de Almeida, et al. (2008d). „HESS very-high-energy gamma-ray sources without identified counterparts“. In: *A&A* 477, pp. 353–363. arXiv: [0712.1173](#) (cit. on pp. 20, 60, 83, 84).
- Aharonian, F. A., A. M. Atoyan, and T. Kifune (1997). „Inverse Compton gamma radiation of faint synchrotron X-ray nebulae around pulsars“. In: *MNRAS* 291, pp. 162–176 (cit. on p. 7).
- Aharonian, F. A., A. G. Akhperjanian, M. Beilicke, et al. (2002b). „A search for TeV gamma-ray emission from SNRs, pulsars and unidentified GeV sources in the Galactic plane in the longitude range between -2 deg and 85 deg.“ In: *A&A* 395, pp. 803–811. eprint: [astro-ph/0209360](#) (cit. on pp. 20, 21).
- Aharonian, F. A., A. G. Akhperjanian, K.-M. Aye, et al. (2004b). „High-energy particle acceleration in the shell of a supernova remnant“. In: *Nature* 432, pp. 75–77. eprint: [astro-ph/0411533](#) (cit. on p. 6).
- Aharonian, F. A., A. G. Akhperjanian, K.-M. Aye, et al. (2004c). „High-energy particle acceleration in the shell of a supernova remnant“. In: *Nature* 432, pp. 75–77. eprint: [arXiv:astro-ph/0411533](#) (cit. on p. 50).
- Ajello, M., W. B. Atwood, L. Baldini, et al. (2017). „3FHL: The Third Catalog of Hard Fermi-LAT Sources“. In: *ApJS* 232, 18, p. 18. arXiv: [1702.00664](#) [[astro-ph.HE](#)] (cit. on pp. 65, 68, 69, 71, 78, 82).

- Albert, J., E. Aliu, H. Anderhub, et al. (2006). „MAGIC Observations of Very High Energy  $\gamma$ -Rays from HESS J1813-178“. In: *ApJ* 637, pp. L41–L44. eprint: [astro-ph/0512283](#) (cit. on p. 85).
- Aliu, E., S. Archambault, T. Aune, et al. (2014). „Long-term TeV and X-Ray Observations of the Gamma-Ray Binary HESS J0632+057“. In: *ApJ* 780, 168, p. 168. arXiv: [1311.6083 \[astro-ph.HE\]](#) (cit. on p. 21).
- Araya, M. (2017). „Detection of GeV Gamma-Rays from HESS J1534-571 and Multiwavelength Implications for the Origin of the Nonthermal Emission“. In: *ApJ* 843, 12, p. 12. arXiv: [1705.03902 \[astro-ph.HE\]](#) (cit. on pp. 86, 87).
- Astropy Collaboration, T. P. Robitaille, E. J. Tollerud, et al. (2013). „Astropy: A community Python package for astronomy“. In: *A&A* 558, A33, A33. arXiv: [1307.6212 \[astro-ph.IM\]](#) (cit. on p. 35).
- Atwood, W. B., A. A. Abdo, M. Ackermann, et al. (2009). „The Large Area Telescope on the Fermi Gamma-Ray Space Telescope Mission“. In: *ApJ* 697, pp. 1071–1102. arXiv: [0902.1089 \[astro-ph.IM\]](#) (cit. on p. 64).
- Berge, D., S. Funk, and J. Hinton (2007). „Background modelling in very-high-energy  $\gamma$ -ray astronomy“. In: *A&A* 466, pp. 1219–1229. eprint: [arXiv:astro-ph/0610959](#) (cit. on pp. 26, 39, 40).
- Bernlöhr, K. (2008). „Simulation of imaging atmospheric Cherenkov telescopes with CORSIKA and sim\_telarray“. In: *Astroparticle Physics* 30, pp. 149–158. arXiv: [0808.2253](#) (cit. on p. 24).
- Blandford, R. and D. Eichler (1987). „Particle acceleration at astrophysical shocks: A theory of cosmic ray origin“. In: *Phys. Rep.* 154, pp. 1–75 (cit. on pp. 6, 8).
- Blumenthal, G. R. and R. J. Gould (1970). „Bremsstrahlung, Synchrotron Radiation, and Compton Scattering of High-Energy Electrons Traversing Dilute Gases“. In: *Reviews of Modern Physics* 42, pp. 237–271 (cit. on p. 10).
- Bolz, O. (2004). „Absolute Energiekalibration der abbildenden Cherenkov-Teleskope des H.E.S.S. Experimente und Ergebnisse erster Beobachtungen des Supernova-Überrests RX J1713.7-3946“. PhD thesis. Ruprecht-Karls-Universität Heidelberg (cit. on p. 24).
- Caraveo, P. A. (2014). „Gamma-Ray Pulsar Revolution“. In: *ARA&A* 52, pp. 211–250. arXiv: [1312.2913 \[astro-ph.HE\]](#) (cit. on p. 7).
- Carrigan, S., F. Brun, R. C. G. Chaves, et al. (2013a). „Charting the TeV Milky Way: H.E.S.S. Galactic plane survey maps, catalog and source populations“. In: *ArXiv e-prints*. arXiv: [1307.4868 \[astro-ph.HE\]](#) (cit. on p. 20).
- Carrigan, S., F. Brun, R. C. G. Chaves, et al. (2013b). „The H.E.S.S. Galactic Plane Survey - maps, source catalog and source population“. In: *ArXiv e-prints*. arXiv: [1307.4690 \[astro-ph.HE\]](#) (cit. on p. 20).
- Cash, W. (1979). „Parameter estimation in astronomy through application of the likelihood ratio“. In: *ApJ* 228, pp. 939–947 (cit. on p. 13).
- Chaves, R. C. G. and for the H.E.S.S. Collaboration (2009). „Extending the H.E.S.S. Galactic Plane Survey“. In: *ArXiv e-prints*. arXiv: [0907.0768 \[astro-ph.HE\]](#) (cit. on p. 20).

- Chaves, R. C. G., E. de Oña Wilhemi, and S. Hoppe (2008). „The H.E.S.S. Galactic Plane Survey“. In: *American Institute of Physics Conference Series*. Ed. by F. A. Aharonian, W. Hofmann, and F. Rieger. Vol. 1085. American Institute of Physics Conference Series, pp. 219–222 (cit. on p. 20).
- Condon, B., M. Lemoine-Goumard, F. Acero, and H. Katagiri (2017). „Detection of Two TeV Shell-type Remnants at GeV Energies with FERMI-LAT: HESS J1731-347 and SN 1006“. In: *ApJ* 851, 100, p. 100. arXiv: [1711.05499 \[astro-ph.HE\]](#) (cit. on pp. 65, 87, 88).
- de Naurois, M. and L. Rolland (2009). „A high performance likelihood reconstruction of  $\gamma$ -rays for imaging atmospheric Cherenkov telescopes“. In: *Astroparticle Physics* 32, pp. 231–252. arXiv: [0907.2610 \[astro-ph.IM\]](#) (cit. on pp. 24, 95).
- Deil, C. (2012). „The H.E.S.S. view of the Milky Way in TeV light“. In: *The Spectral Energy Distribution of Galaxies - SED 2011*. Ed. by R. J. Tuffs and C. C. Popescu. Vol. 284. IAU Symposium, pp. 365–370 (cit. on pp. 20, 25).
- Deil, C., R. Zanin, J. Lefaucheur, et al. (2017a). „Gammapy - A prototype for the CTA science tools“. In: *ArXiv e-prints*. arXiv: [1709.01751 \[astro-ph.IM\]](#) (cit. on pp. 14, 35).
- Deil, C., C. Boisson, K. Kosack, et al. (2017b). „Open high-level data formats and software for gamma-ray astronomy“. In: *6th International Symposium on High Energy Gamma-Ray Astronomy*. Vol. 1792. American Institute of Physics Conference Series, p. 070006. arXiv: [1610.01884 \[astro-ph.IM\]](#) (cit. on p. 13).
- Diehl, R., H. Halloin, K. Kretschmer, et al. (2006). „Radioactive  $^{26}\text{Al}$  from massive stars in the Galaxy“. In: *Nature* 439, pp. 45–47. eprint: [astro-ph/0601015](#) (cit. on p. 6).
- Donath, A., C. Deil, M. P. Arribas, et al. (2015). *Gammapy - A Python package for  $\gamma$ -ray astronomy*. arXiv: [1509.07408 \[astro-ph.IM\]](#) (cit. on pp. 14, 35).
- Donath, Axel (2014). „Towards the H.E.S.S. Galactic Plane Survey Gamma-Ray Source Catalog“. MA thesis. Heidelberg: Ruprecht-Karls-Universität (cit. on pp. 20, 25).
- Dubus, G. (2013). „Gamma-ray binaries and related systems“. In: *A&A Rev.* 21, 64, p. 64. arXiv: [1307.7083 \[astro-ph.HE\]](#) (cit. on p. 8).
- Dubus, G., J. L. Contreras, S. Funk, et al. (2013). „Surveys with the Cherenkov Telescope Array“. In: *Astroparticle Physics* 43, pp. 317–330. arXiv: [1208.5686 \[astro-ph.HE\]](#) (cit. on p. 96).
- Fermi, ENRICO (1949). „On the Origin of the Cosmic Radiation“. In: *Phys. Rev.* 75 (8), pp. 1169–1174 (cit. on p. 8).
- Ferrand, G. and S. Safi-Harb (2012). „A census of high-energy observations of Galactic supernova remnants“. In: *Advances in Space Research* 49, pp. 1313–1319. arXiv: [1202.0245 \[astro-ph.HE\]](#) (cit. on pp. 43, 58).
- Freeman, P., S. Doe, and A. Siemiginowska (2001). „Sherpa: a mission-independent data analysis application“. In: *Society of Photo-Optical Instrumentation Engineers (SPIE) Conference Series*. Vol. 4477, pp. 76–87 (cit. on p. 35).
- Fujinaga, T., K. Mori, A. Bamba, et al. (2013). „An X-Ray Counterpart of HESS J1427-608 Discovered with Suzaku“. In: *PASJ* 65, 61, p. 61. arXiv: [1301.5274 \[astro-ph.HE\]](#) (cit. on p. 83).
- Funk, S. (2015). „Ground- and Space-Based Gamma-Ray Astronomy“. In: *Annual Review of Nuclear and Particle Science* 65, pp. 245–277 (cit. on pp. 4, 6, 11, 12, 79).

- Funk, S., J. A. Hinton, Y. Moriguchi, et al. (2007). „XMM-Newton observations of HESS J1813-178 reveal a composite Supernova remnant“. In: *A&A* 470, pp. 249–257. eprint: [astro-ph/0611646](#) (cit. on p. 50).
- Funk, S., O. Reimer, D. F. Torres, and J. A. Hinton (2008). „The GeV-TeV Connection in Galactic  $\gamma$ -Ray Sources“. In: *ApJ* 679, 1299-1314, pp. 1299–1314. arXiv: [0710.1584](#) (cit. on p. 62).
- Funk, Stefan (2005). „A new population of very high-energy gamma-ray sources detected with H.E.S.S. in the inner part of the Milky Way“. eng. PhD thesis. Heidelberg: Ruprecht-Karls Universität (cit. on p. 9).
- Gaensler, B. M. and P. O. Slane (2006). „The Evolution and Structure of Pulsar Wind Nebulae“. In: *ARA&A* 44, pp. 17–47. eprint: [astro-ph/0601081](#) (cit. on p. 7).
- Gast, H., F. Brun, S. Carrigan, et al. (2011). „Exploring the Galaxy at TeV energies: Latest results from the H.E.S.S. Galactic Plane Survey.“ In: *International Cosmic Ray Conference 7*, p. 158 (cit. on p. 20).
- Ginzburg, V. L. and S. I. Syrovatskii (1964). *The Origin of Cosmic Rays* (cit. on p. 6).
- Green, D. A. (1991). „Limitations imposed on statistical studies of Galactic supernova remnants by observational selection effects“. In: *PASP* 103, pp. 209–220 (cit. on p. 53).
- Green, D. A. (2014). „A catalogue of 294 Galactic supernova remnants“. In: *Bulletin of the Astronomical Society of India* 42, pp. 47–58. arXiv: [1409.0637 \[astro-ph.HE\]](#) (cit. on p. 43).
- Hahn, J., R. de los Reyes, K. Bernlöhr, et al. (2014). „Impact of aerosols and adverse atmospheric conditions on the data quality for spectral analysis of the H.E.S.S. telescopes“. In: *Astroparticle Physics* 54, pp. 25–32. arXiv: [1310.1639 \[astro-ph.IM\]](#) (cit. on p. 23).
- H.E.S.S. Collaboration, A. Abramowski, F. Acero, et al. (2011a). „A new SNR with TeV shell-type morphology: HESS J1731-347“. In: *A&A* 531, A81, A81. arXiv: [1105.3206 \[astro-ph.HE\]](#) (cit. on pp. 31, 50, 87).
- H.E.S.S. Collaboration, A. Abramowski, F. Acero, et al. (2011b). „Discovery of the source HESS J1356-645 associated with the young and energetic PSR J1357-6429“. In: *A&A* 533, A103, A103. arXiv: [1108.2855 \[astro-ph.HE\]](#) (cit. on p. 50).
- H.E.S.S. Collaboration, A. Abramowski, F. Acero, et al. (2012). „Identification of HESS J1303-631 as a pulsar wind nebula through  $\gamma$ -ray, X-ray, and radio observations“. In: *A&A* 548, A46, A46. arXiv: [1210.6513 \[astro-ph.HE\]](#) (cit. on p. 50).
- H.E.S.S. Collaboration, A. Abramowski, F. Aharonian, et al. (2014). „HESS J1818-154, a new composite supernova remnant discovered in TeV gamma rays and X-rays“. In: *A&A* 562, A40, A40. arXiv: [1310.6956 \[astro-ph.HE\]](#) (cit. on p. 50).
- H.E.S.S. Collaboration, A. Abramowski, F. Aharonian, et al. (2015a). „Discovery of variable VHE  $\gamma$ -ray emission from the binary system 1FGL J1018.6-5856“. In: *A&A* 577, A131, A131. arXiv: [1503.02711 \[astro-ph.HE\]](#) (cit. on p. 50).
- H.E.S.S. Collaboration, A. Abramowski, F. Aharonian, et al. (2015b). „H.E.S.S. detection of TeV emission from the interaction region between the supernova remnant G349.7+0.2 and a molecular cloud“. In: *A&A* 574, A100, A100. arXiv: [1412.2251 \[astro-ph.HE\]](#) (cit. on pp. 31, 50).

- H.E.S.S. Collaboration, A. Abramowski, F. Acero, et al. (2015c). „H.E.S.S. reveals a lack of TeV emission from the supernova remnant Puppis A“. In: *A&A* 575, A81, A81. arXiv: [1412.6997 \[astro-ph.HE\]](#) (cit. on p. 77).
- H.E.S.S. Collaboration, A. Abramowski, F. Aharonian, et al. (2015d). „Probing the gamma-ray emission from HESS J1834-087 using H.E.S.S. and Fermi LAT observations“. In: *A&A* 574, A27, A27. arXiv: [1407.0862 \[astro-ph.HE\]](#) (cit. on p. 50).
- HESS Collaboration, A. Abramowski, F. Aharonian, et al. (2016). „Acceleration of petaelectronvolt protons in the Galactic Centre“. In: *Nature* 531, pp. 476–479. arXiv: [1603.07730 \[astro-ph.HE\]](#) (cit. on p. 8).
- H.E.S.S. Collaboration, A. Abramowski, F. Aharonian, et al. (2016a). „Acceleration of petaelectronvolt protons in the Galactic Centre“. In: *Nature* 531, pp. 476–479. arXiv: [1603.07730 \[astro-ph.HE\]](#) (cit. on p. 31).
- H.E.S.S. Collaboration, H. Abdalla, A. Abramowski, et al. (2016b). „Deeper H.E.S.S. Observations of Vela Junior (RX J0852.0-4622): Morphology Studies and Resolved Spectroscopy“. In: *ArXiv e-prints*. arXiv: [1611.01863 \[astro-ph.HE\]](#) (cit. on pp. 30, 31, 50).
- H.E.S.S. Collaboration, A. Abramowski, F. Aharonian, et al. (2016c). „Detailed spectral and morphological analysis of the shell type SNR RCW 86“. In: *ArXiv e-prints*. arXiv: [1601.04461 \[astro-ph.HE\]](#) (cit. on pp. 31, 50).
- H.E.S.S. Collaboration, H. Abdalla, A. Abramowski, et al. (2016d). „Extended VHE gamma-ray emission towards SGR1806-20, LBV1806-20, and stellar cluster Cl\*1806-20“. In: *ArXiv e-prints*. arXiv: [1606.05404 \[astro-ph.HE\]](#) (cit. on p. 60).
- H.E.S.S. Collaboration, H. Abdalla, H. Abdalla, et al. (2016e). „H.E.S.S. observations of RX J1713.7-3946 with improved angular and spectral resolution; evidence for gamma-ray emission extending beyond the X-ray emitting shell“. In: *ArXiv e-prints*. arXiv: [1609.08671 \[astro-ph.HE\]](#) (cit. on p. 31).
- H.E.S.S. Collaboration, H. Abdalla, A. Abramowski, et al. (2016f). „The supernova remnant W49B as seen with H.E.S.S. and Fermi-LAT“. In: *ArXiv e-prints*. arXiv: [1609.00600 \[astro-ph.HE\]](#) (cit. on pp. 31, 50).
- H.E.S.S. Collaboration, H. Abdalla, A. Abramowski, et al. (2017a). *A search for new supernova remnant shells in the Galactic plane with H.E.S.S.* (Cit. on pp. 31, 50).
- H.E.S.S. Collaboration, H. Abdalla, A. Abramowski, et al. (2017b). „Characterising the VHE diffuse emission in the central 200 parsecs of our Galaxy with H.E.S.S.“. In: *ArXiv e-prints*. arXiv: [1706.04535 \[astro-ph.HE\]](#) (cit. on pp. 30, 31).
- H.E.S.S. Collaboration, H. Abdalla, A. Abramowski, et al. (2017c). *HESS J1741-302: a hidden accelerator in the Galactic plane* (cit. on p. 31).
- H.E.S.S. Collaboration, H. Abdalla, A. Abramowski, et al. (2017d). „The population of TeV pulsar wind nebulae in the H.E.S.S. Galactic Plane Survey“. In: *ArXiv e-prints*. arXiv: [1702.08280 \[astro-ph.HE\]](#) (cit. on p. 53).
- H.E.S.S. Collaboration, : H. Abdalla, et al. (2018). „A search for new supernova remnant shells in the Galactic plane with H.E.S.S.“ In: *ArXiv e-prints*. arXiv: [1801.06020 \[astro-ph.HE\]](#) (cit. on pp. 15, 86, 88, 90).
- H.E.S.S. Collaboration, H. Abdalla, A. Abramowski, et al. (2018). *The H.E.S.S. Galactic Plane Survey*. *A&A* forthcoming (cit. on p. 19).

- Hinton, J. A. and W. Hofmann (2009). „Teraelectronvolt Astronomy“. In: *ARA&A* 47, pp. 523–565. arXiv: [1006.5210 \[astro-ph.HE\]](https://arxiv.org/abs/1006.5210) (cit. on pp. 9, 46).
- Hoppe, S. (2008a). „The H.E.S.S. survey of the inner Galactic plane“. In: *International Cosmic Ray Conference 2*, pp. 579–582. arXiv: [0710.3528](https://arxiv.org/abs/0710.3528) (cit. on p. 20).
- Hoppe, Stefan (2008b). „Emitters of VHE  $\gamma$ -radiation as revealed by the H.E.S.S. Galactic plane survey“. PhD thesis. Universität Heidelberg, Max-Planck-Institut für Kernphysik (cit. on p. 42).
- James, F. (1994). „MINUIT Function Minimization and Error Analysis: Reference Manual Version 94.1“. In: (cit. on p. 14).
- Katagiri, H., R. Enomoto, L. T. Ksenofontov, et al. (2005). „Detection of Gamma Rays around 1 TeV from RX J0852.0-4622 by CANGAROO-II“. In: *ApJ* 619, pp. L163–L166. eprint: [astro-ph/0412623](https://arxiv.org/abs/astro-ph/0412623) (cit. on p. 19).
- Kniffen, D. A., R. C. Hartman, D. J. Thompson, G. F. Bignami, and C. E. Fichtel (1974). „Gamma radiation from the Crab Nebula above 35 MeV“. In: *Nature* 251, pp. 397–399 (cit. on p. 7).
- Leroy, N. (2004). „Observations, avec les telescopes H.E.S.S., du rayonnement gamma emis par le Noyau Actif de Galaxie PKS 2155-304, au-dela de 100 GeV“. PhD thesis. Ecole Polytechnique (cit. on p. 24).
- Leser, E., S. Ohm, M. Füßling, et al. (2017). „First Results of Eta Car Observations with H.E.S.S.II“. In: *ArXiv e-prints*. arXiv: [1708.01033 \[astro-ph.HE\]](https://arxiv.org/abs/1708.01033) (cit. on p. 77).
- Li, J., D. F. Torres, K.-S. Cheng, et al. (2017). „GeV Detection of HESS J0632+057“. In: *ApJ* 846, 169, p. 169. arXiv: [1707.04280 \[astro-ph.HE\]](https://arxiv.org/abs/1707.04280) (cit. on p. 65).
- Longair, M.S. (2011). *High Energy Astrophysics*. Cambridge University Press (cit. on p. 8).
- Lupton, R., M. R. Blanton, G. Fekete, et al. (2004). „Preparing Red-Green-Blue Images from CCD Data“. In: *PASP* 116, pp. 133–137. eprint: [astro-ph/0312483](https://arxiv.org/abs/astro-ph/0312483) (cit. on p. 73).
- Manchester, R. N., G. B. Hobbs, A. Teoh, and M. Hobbs (2005). „The Australia Telescope National Facility Pulsar Catalogue“. In: *AJ* 129, pp. 1993–2006 (cit. on pp. 43, 58).
- Marandon, V., A. Djannati-Atai, R. Terrier, et al. (2008). „A closer look at HESS J1837-069 following the pulsar discovery“. In: *American Institute of Physics Conference Series*. Ed. by F. A. Aharonian, W. Hofmann, and F. Rieger. Vol. 1085. American Institute of Physics Conference Series, pp. 320–323 (cit. on p. 50).
- Meyer, M., D. Horns, and H.-S. Zechlin (2010). „The Crab Nebula as a standard candle in very high-energy astrophysics“. In: *A&A* 523, A2, A2. arXiv: [1008.4524 \[astro-ph.HE\]](https://arxiv.org/abs/1008.4524) (cit. on pp. 73, 74).
- Momcheva, Ivelina and Erik Tollerud (2015). „Software Use in Astronomy: an Informal Survey“. In: arXiv: [1507.03989 \[astro-ph.IM\]](https://arxiv.org/abs/1507.03989) (cit. on p. 14).
- Muraishi, H., T. Tanimori, S. Yanagita, et al. (2000). „Evidence for TeV gamma-ray emission from the shell type SNR RX J1713.7-3946“. In: *A&A* 354, pp. L57–L61. eprint: [astro-ph/0001047](https://arxiv.org/abs/astro-ph/0001047) (cit. on p. 19).
- NASA (2012). *The Multiwavelength Milky Way*. URL: [https://mwmw.gsfc.nasa.gov/mmw\\_sci.html](https://mwmw.gsfc.nasa.gov/mmw_sci.html) (visited on June 30, 2017) (cit. on p. 3).

- Ohm, S., C. van Eldik, and K. Egberts (2009). „ $\gamma$ /hadron separation in very-high-energy  $\gamma$ -ray astronomy using a multivariate analysis method“. In: *Astroparticle Physics* 31, pp. 383–391. arXiv: [0904.1136 \[astro-ph.IM\]](#) (cit. on p. 24).
- Parsons, R. D. and J. A. Hinton (2014). „A Monte Carlo template based analysis for air-Cherenkov arrays“. In: *Astroparticle Physics* 56, pp. 26–34. arXiv: [1403.2993 \[astro-ph.IM\]](#) (cit. on p. 95).
- Pence, W. D., L. Chiappetti, C. G. Page, R. A. Shaw, and E. Stobie (2010). „Definition of the Flexible Image Transport System (FITS), version 3.0“. In: *A&A* 524, A42+ (cit. on p. 13).
- Piron, F., A. Djannati-Atai, M. Punch, et al. (2001). „Temporal and spectral gamma-ray properties of Mkn 421 above 250 GeV from CAT observations between 1996 and 2000“. In: *A&A* 374, pp. 895–906. eprint: [arXiv:astro-ph/0106196](#) (cit. on pp. 39, 42).
- Planck Collaboration, R. Adam, P. A. R. Ade, et al. (2016). „Planck 2015 results. X. Diffuse component separation: Foreground maps“. In: *A&A* 594, A10, A10. arXiv: [1502.01588](#) (cit. on pp. 21, 51, 52, 81).
- Reimer, O., K. Reitberger, A. Reimer, and H. Takahashi (2015). „Eta Carinae’s first full orbit in the Fermi era“. In: *IAU General Assembly 22*, 2256629, p. 2256629 (cit. on p. 77).
- Reynolds, S. P. (2008). „Supernova Remnants at High Energy“. In: *ARA&A* 46, pp. 89–126 (cit. on p. 7).
- Robitaille, T. P., E. J. Tollerud, P. Greenfield, et al. (2013). „Astropy: A community Python package for astronomy“. In: *A&A* 558, A33, A33 (cit. on p. 14).
- Stewart, I. M. (2009). „Maximum-likelihood detection of sources among Poissonian noise“. In: *A&A* 495, pp. 989–1003. arXiv: [0901.3276](#) (cit. on pp. 14, 28).
- Stycz, Kornelia (2016). „VHE Gamma-ray sources at the resolution limit of H.E.S.S.“. PhD thesis. Humboldt-Universität Berlin (cit. on p. 38).
- Su, M., T. R. Slatyer, and D. P. Finkbeiner (2010). „Giant Gamma-ray Bubbles from Fermi-LAT: Active Galactic Nucleus Activity or Bipolar Galactic Wind?“ In: *ApJ* 724, pp. 1044–1082. arXiv: [1005.5480 \[astro-ph.HE\]](#) (cit. on p. 63).
- Tam, P. H. T., S. J. Wagner, O. Tibolla, and R. C. G. Chaves (2010). „A search for VHE counterparts of Galactic Fermi bright sources and MeV to TeV spectral characterization“. In: *A&A* 518, A8, A8. arXiv: [0911.4333 \[astro-ph.HE\]](#) (cit. on p. 62).
- Temim, T., P. Slane, D. Castro, et al. (2013). „High-energy Emission from the Composite Supernova Remnant MSH 15-56“. In: *ApJ* 768, 61, p. 61. arXiv: [1303.2425 \[astro-ph.HE\]](#) (cit. on p. 77).
- Thompson, D. J., C. E. Fichtel, D. A. Kniffen, and H. B. Ogelman (1975). „SAS-2 high-energy gamma-ray observations of the VELA pulsar“. In: *ApJ* 200, pp. L79–L82 (cit. on p. 7).
- Tibolla, O., S. Kaufmann, and K. Kosack (2014). „XMM-Newton and Chandra X-ray follow-up observations of the VHE gamma-ray source HESS J1507-622“. In: *A&A* 567, A74, A74. arXiv: [1405.5564 \[astro-ph.HE\]](#) (cit. on p. 90).
- Tsuchiya, K., R. Enomoto, L. T. Ksenofontov, et al. (2004). „Detection of Sub-TeV Gamma Rays from the Galactic Center Direction by CANGAROO-II“. In: *ApJ* 606, pp. L115–L118. eprint: [astro-ph/0403592](#) (cit. on p. 19).

- Vallée, J. P. (2014). „Catalog of Observed Tangents to the Spiral Arms in the Milky Way Galaxy“. In: *ApJS* 215, 1, p. 1. arXiv: [1409.4801](https://arxiv.org/abs/1409.4801) (cit. on pp. 52, 53, 58, 80, 81, 127).
- Völk, H. J. and K. Bernlöhr (2009). „Imaging very high energy gamma-ray telescopes“. In: *Experimental Astronomy* 25, pp. 173–191. arXiv: [0812.4198](https://arxiv.org/abs/0812.4198) (cit. on p. 5).
- Weekes, T. C., M. F. Cawley, D. J. Fegan, et al. (1989). „Observation of TeV gamma rays from the Crab nebula using the atmospheric Cerenkov imaging technique“. In: *ApJ* 342, pp. 379–395 (cit. on pp. 7, 19).
- Weinstein, A. (2009). „The VERITAS Survey of the Cygnus Region of the Galactic Plane“. In: *ArXiv e-prints*. arXiv: [0912.4492](https://arxiv.org/abs/0912.4492) [[astro-ph.HE](https://arxiv.org/abs/0912.4492)] (cit. on pp. 20, 21).
- W.Hofmann (2012). *The H.E.S.S. Telescopes*. URL: <https://www.mpi-hd.mpg.de/hfm/HESS/pages/about/telescopes/> (visited on Feb. 26, 2018) (cit. on p. 22).
- Wilks, Samuel S (1938). „The large-sample distribution of the likelihood ratio for testing composite hypotheses“. In: *The Annals of Mathematical Statistics* 9.1, pp. 60–62 (cit. on p. 13).
- Woosley, S. and T. Janka (2005). „The physics of core-collapse supernovae“. In: *Nature Physics* 1, pp. 147–154. eprint: [astro-ph/0601261](https://arxiv.org/abs/astro-ph/0601261) (cit. on p. 6).
- Yoshikoshi, T., T. Kifune, S. A. Dazeley, et al. (1997). „Very High Energy Gamma Rays from the VELA Pulsar Direction“. In: *ApJ* 487, pp. L65–L68. eprint: [astro-ph/9707203](https://arxiv.org/abs/astro-ph/9707203) (cit. on p. 19).

# Acknowledgements

First I would like to thank my referee and supervisor **Prof. Werner Hofmann** for giving me the opportunity to work on such an interesting and relevant project as the H.E.S.S. Galactic plane survey. I would also like to thank my co-referee **Prof. Stefan Wagner**.

Especially I would like to thank **Christoph Deil** for the supervision of this thesis, for many interesting and fruitful discussions. His numerous ideas and critical comments greatly improved the quality of the work presented in this thesis.

I would also like to thank my collaborators of the HGPS project **Vincent Marandon, Francois Brun, Ryan Chaves** and **Régis Terrier**. I also thank **Arjun Vorunganti, Roberta Zanin** and **Rubén López-Coto** for their contributions and help with the HGPS / *Fermi*-LAT project.

I would like to thank the whole **H.E.S.S. working group at the MPIK** for a very pleasant working atmosphere, especially my office mates **Johannes King** and **Alison Mitchell**. I would also like to thank **Ruth Crespo** for her support in administrative issues.

Finally I would like to thank **Anna Hellein** for her support, patience and inspiration. I would also like to thank **my parents, my sister** and her family for encouraging and supporting me throughout my whole studies. Many thanks also go to **Jonas, Marcel, Freya & Max** for many memorable and future hiking, climbing, cooking, biking, handicraft, music and physics adventures.



## Colophon

This thesis was typeset with  $\text{\LaTeX}2_{\epsilon}$ . It uses the *Clean Thesis* style developed by Ricardo Langner. The design of the *Clean Thesis* style is inspired by user guide documents from Apple Inc.

Download the *Clean Thesis* style at <http://cleanthesis.der-ric.de/>.